An Experimental Study of Automotive Underbody Diffusers

By Lydia Jowsey

Doctoral Thesis
Submitted in partial fulfilment of the requirements
for the award of
Doctor of Philosophy of Loughborough University
2013

For Stef,

Non ti dimenticherò mai

Abstract

Aerodynamics has always been a driving force in motorsport and road vehicle design and development, and continues to play an important role. A significant advancement in race car aerodynamics was the development of the vehicle underbody to produce downforce, in particular the implementation of the diffuser. This thesis concentrates on the performance flow mechanisms found in simple rear diffusers commonly seen in motorsport applications. There is little published work on these mechanisms, especially the influence of the more commonly used multiple-channel diffusers.

A simple diffuser-equipped bluff body was tested in the Loughborough University scale wind tunnel, investigating the performance of plane and multi-channel diffusers using force, pressure and PIV measurements. Ten diffuser angles and eight ride heights were investigated for plane, two-channel, three-channel and four-channel diffuser configurations.

The plane diffuser showed similar trends in lift and drag to published data of increased downforce and drag with decreasing ride height to a maximum, followed by a sharp decreased in downforce due to ground proximity. The optimum angle for downforce was found to be between 13° and 16°, with the pressure measurements highlighting local separation present at the diffuser inlet above 13° and a completely stalled diffuser above 25°. The presence of a vortex was confirmed by the PIV data as well as an underbody upwash within the diffuser. At 25°, the vortex was much weaker than lower angles with signs of asymmetry. As the ride height was increased the vortex strength increased and reduced levels of separation were observed.

The multiple-channel diffusers showed similar trends in lift and drag to the plane diffusers, and increased downforce production above 13°, up to 13% for the mid-range (16°-19°) angles. Area pressure measurements indicated that the gains occurred through improved diffuser pumping and pressure recovery in both the inside and outside channels. In the PIV data, all the multi-channel diffusers exhibited a similar flow field distribution to the plane diffuser. The two-channel diffusers highlighted reduced levels of separation due to the presence of the splitter plates, improving attachment and increasing downforce. The splitter plates had a similar effect in the three- and four-channel diffuser outer channels but with high levels of separation in the inside channels. Additionally, the four-channel diffuser had developed a “secondary vortex” in the outside channel, emanating from flow off the main vortex, accounting for the increased downforce in the force measurements.

Acknowledgements

Firstly, I'd like to thank my supervisor, Martin Passmore for all his help, guidance, support and generally putting up with me during this long PhD process.

To the best technician I could ever wish to have in Rob Hunter for all his help with my model and testing, along with Keith Coulthard, Peter Stinchcombe and Stacey Prentice.

Finally, to my mum, dad, Rat and all of my other friends and family, especially Mark for their love and support to finally reach the end of this chapter, thank you.

Table of Contents

Table of Figures

Table of Tables

Table of Equations

Nomenclature

Symbol	***Description***	***Unit***
A	Frontal area	m^2
AR	Area ratio	
ARP	Area ratio parameter	
C_D	Drag coefficient	
$C_{D(d)}$	Drag coefficient for dual-channel diffuser	
$C_{D(f)}$	Drag coefficient for four-channel diffuser	
$C_{D(p)}$	Drag coefficient for plane diffuser	
$C_{D(t)}$	Drag coefficient for three-channel diffuser	
ΔC_D	Difference in drag coefficient	
C_L	Lift coefficient	
C_LA	Lift coefficient Area	m^2
C_{Lr}	Rear lift coefficient	
$C_{L(d)}$	Lift coefficient for dual-channel diffuser	
$C_{L(f)}$	Lift coefficient for four-channel diffuser	
$C_{L(p)}$	Lift coefficient for plane diffuser	
$C_{L(t)}$	Lift coefficient for three-channel diffuser	
ΔC_L	Difference in lift coefficient	
C_{MX}	Roll moment coefficient	
C_{MY}	Pitching moment coefficient	
C_{MZ}	Yaw moment coefficient	
C_Y	Side force coefficient	
C_P	Pressure coefficient	
$\overline{\overline{C_{Pd}}}$	Diffuser pressure coefficient	
$\overline{\overline{C_{Pf}}}$	Underbody pressure coefficient	
C_P^*	Maximum pressure recovery for fixed area ratios	
C_P^{**}	Maximum pressure recovery for fixed length ratios	
D	Drag force	N
$F_{T(max)}$	Maximum tractive force	N
h_1	Ride height	m
h_1/H	Non-dimensional ride height	
h_2	Exit height	m
H	Model height	m
l	Model length	m

L	Lift force	N
N	Diffuser length	m
N/h_1	Non-dimensional diffuser length	
N_R	Normal reaction force	N
Q	Q-factor/Peak ratio	
Re	Reynolds number	
V	Velocity	ms^{-1}
V_x	Velocity component in x-direction	ms^{-1}
V_y	Velocity component in y-direction	ms^{-1}
W	Model width	m
w	Diffuser width	m
x	Distance along the diffuser	m
α	Diffuser angle	°
ρ	Air density	$1.165kgm^{-3}$
$ø_i$	Inner wall angle	°
$ø_o$	Outer wall angle	°
μ	Coefficient of friction	

Chapter 1 - Introduction

1.1 Overview

Aerodynamics has always been a driving force in both motorsport and road vehicle design and development, and continues to play an important role. Before 1967 the motorsport industry and particularly the focus in Formula 1 (F1) was to optimise the cars for low drag by streamlining the cars and reducing the frontal area. This increased the speeds on the straights, but drag reduction was not enough to increase the cornering speeds. However, the appearance of wings on a Jim Hall Chaparral 2E car in the 1966 Can-Am Series [1] changed the focus to downforce production and in 1968 F1 teams started implementing simple aluminium wings. These were swiftly banned after a series of accidents, only to be reintroduced in regulated form in 1969 [4]. Teams continued to develop the wing concept until Jim Hall again showcased a new idea in Can-Am in 1970; that of applying large powered fans to remove air from the underside of the car with skirts that sealed the underside from the outer freestream air. This led to low pressures on the whole underside producing large levels of downforce that acted to "suck" the car to the ground. As the F1 rules [2] stated that aerodynamic devices were forbidden from moving relative to the car it rendered the Jim Hall concept illegal. The Brabham "fan car" [3] tried to get around this by stating the fans primary purpose was for engine cooling, but after winning one race it was banned. Despite this, the principle of using the underbody to produce downforce was now established and in 1978 Colin Chapman and the designers at Lotus successfully introduced the ground effect concept [4]. The design of the car had the whole centre structure shaped as an inverted wing, generating low pressures over a very large area, enabling levels of downforce never before seen in motorsport. The increase in cornering speeds and reduced braking distances saw the idea implemented by

rival teams and became commonplace in F1. By 1981, the FIA had banned the use of movable side skirts to try to increase the ground clearance in a bid to reduce cornering speeds and in 1983 the "flat-bottom" regulation was introduced and underbody aerodynamic devices such as the venturi tunnels were no longer legal [2]. A few years later turbocharged engines were introduced and the shift of focus was purely on downforce production at the rear to get the power down on the road, and drag was deemed almost irrelevant. During the 1990s, more gradual aerodynamic development was seen with the main changes focusing on reduced levels of downforce for safety reasons, particularly after the death of Ayrton Senna in 1994. After which a stepped underbody [2] was introduced to reduce downforce and cornering speeds as well as a 10mm wooden "plank" fitted to the underbody prior to the diffuser to monitor ride height changes, with a wear limit of 1mm throughout each race. Further changes to reduce levels of downforce for the 1998 season through more restrictive dimensions of aerodynamic devices led to designers trying to find more innovative ways of creating downforce and the appearance of barge boards and winglets was born. This vein of aerodynamic development continued through until 2008 but the largest regulation change in a decade was implemented for the 2009 season, with wholesale aerodynamic changes to reduce downforce levels and wake size in order to improve overtaking. The front wings became lower, wider with a 6° driver-adjustable front wing flap and rear wings became taller and narrower, while the diffuser moved rearwards with a fixed maximum exit height. Despite these changes, there was not the expected extreme reduction in cornering speeds and increased lap times, primarily due to the innovative introduction of the "double decker" diffusers which incorporated a second diffuser "channel" above the centre channel that effectively lowered the pressure at the inlet, increasing the pressure recovery and downforce. The driver-adjustable wings were replaced by the Drag Reduction System (DRS) for the 2011 season, which altered the angle of the rear wing, reducing drag and producing a temporary speed advantage. Additionally, the teams introduced "blown diffusers" where the exhaust ducts directed air into the diffuser resulting in increased downforce, but these were banned by the FIA for 2012.

Similar to the aerodynamic development in motorsport, road vehicle design has seen sweeping changes over the last few decades. Initially, the shape of road cars was more related to styling than any drag or lift distribution. But as the influence of performance figures, fuel economy and CO_2 emissions became increasingly important, the aerodynamic design became more significant. Subsequently, the primary focus has and is still on drag reduction, the levels of lift present are still deemed important, but on more of a lift distribution and stability basis rather than large levels of downforce. The drag coefficient for the first automotive vehicles in the early 1900s were around 0.61 [11] whereas over the last few decades vehicle design has progressed such that drag

coefficients have reduced massively. The C_D for a 1980 Peugeot 305 GL was 0.44 [5] whereas more recently developments in drag reduction have resulted in values as low as 0.26 for the 2009 Toyota Prius [6]. Just as fuel economy and CO_2 emissions have driven drag decreases in the past, future powertrain developments may further increase the need for reduced drag. This is due to the influence drag has on the range capability of electric and alternative fuel (e.g. Hydrogen fuel cell) technologies; a reduction in drag giving increased mileage possible for the same power consumption and hence making it a more attractive and realistic option for consumers. Whereas high levels of downforce have been key in the development of motorsport aerodynamics, the overall lift and its distribution is more important in road vehicle design due to its influence on handling and stability.

This thesis will concentrate on the performance and flow mechanisms found in simple rear diffusers commonly seen in motorsport applications. In these cases they are used to produce large levels of downforce to aid cornering performance, and drag is generally seen as less of a concern. They are also seen on high performance road cars where they can be used to cure lift stability issues. Despite the emphasis on high performance vehicles, it has been seen that the use of low angle diffusers can actually reduce drag levels and therefore may be applicable to the standard road vehicle in the drive for drag reduction. There is little published work on the mechanisms involved in automotive diffuser performance despite their common application, and additionally even less on the use of multiple channel diffusers; those most widely used.

The experiments will cover realistic diffuser geometries for both road and race car applications in simple form and will not investigate the design and development of diffusers. The aim is more to investigate and highlight the aerodynamic mechanisms involved, the trends they create and therefore the overall understanding of underbody diffusers.

1.2 Influence of aerodynamic drag on performance

The influence of aerodynamic drag on the performance of a vehicle is important for both road and race cars, affecting the power required and time to accelerate, as well as the fuel economy. With road vehicles the concern is to balance the customers conflicting requirements for ‘good’ performance (in terms of acceleration and top speed) with good fuel economy. In addition there is a pressing need to reduce CO_2 emissions both from customers and increasingly from legislation [7]. With race cars the primary significance is the excess power available to accelerate the car as quickly as possible, with fuel efficiency less of a concern.

The drag is normally presented as a non-dimensional coefficient defined as:

$$C_D = \frac{D}{\frac{1}{2}\rho V^2 A}$$ **Equation 1.2.1**

Where D is the drag force (N), ρ is the air density (kgm^{-3}), V is the vehicle velocity (ms^{-1}) and A is the frontal area (m^2).

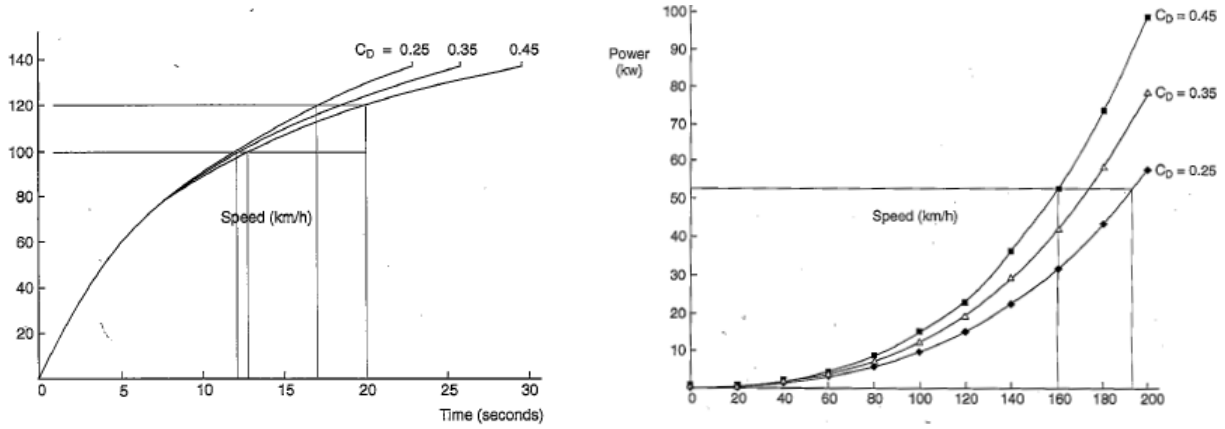

(a) Acceleration **(b) Power**

Figure 1.2.1(a) & (b) – Influence of drag on acceleration and power [9]

Figure 1.2.1 (a) and (b) shows an example of the influence of drag on power requirement and acceleration times. As the drag coefficient is decreased the time taken to accelerate a vehicle to a specific speed is reduced. The gains are relatively small at low speed but become increasingly important at high speed. This is particularly advantageous in racing cars because it enables the driver to out-pace an opponent along a straight or out of a corner. For road cars, acceleration times are used as a performance figure for marketing and therefore can be advantageous when marketing a vehicle. Figure 1.2.1 (b) shows the power required to overcome the aerodynamic drag for three values of C_D. Again the impact is more significant at higher speeds where the reduction in power for a reduction in C_D of 0.2 is about 40%. Reducing the power improves fuel economy which has become increasingly important in road vehicle design. Table 1.3.1 shows the influence of drag coefficient on fuel consumption for a small saloon car driving the EPA cycles. Reducing the drag coefficient from 0.45 to 0.316 gave a fuel consumption improvement of 7% (Urban), 18% (Highway) and 11% (Composite).

EPA Cycle	**Fuel Consumption (Litres/100km)**		**Percentage Improvement**
	Baseline (C_D at 0° = 0.45)	**Modified Vehicle (C_D at 0° = 0.316)**	
Urban	6.88	6.42	7
Highway	6.37	5.25	18
Composite	6.64	5.90	10

Table 1.2.1 – Influence of drag on fuel consumption [9]

Vehicle manufacturers also have to abide by strict emissions legislation, which coupled with the consumer demand for improved fuel consumption, due to increased fuel costs, adds further pressure on drag reduction. Currently the legislation in Europe states that by 2012 the average CO_2 emissions across a manufacturer fleet must be no more than 130g/km. Furthermore by 2020 and 2025 these limits are expected to reduce to 80g/km and 60g/km respectively [7]. A study by Hoffman [37] found that a reduction of ten drag counts (0.01 C_D) gave a saving of 0.04ltr/100km/vehicle which relates to 1.2 billion litres of fuel per year or approximately 2.88billion kilos of CO_2 per year.

1.3 Influence of aerodynamic lift on performance

While the aerodynamic drag is important in some applications, particularly race-cars, the aerodynamic lift forces can be equally if not more important. Lift coefficient is defined as:

$$C_L = \frac{L}{\frac{1}{2}\rho V^2 A} \qquad \textbf{Equation 1.3.1}$$

Where L is the drag force (N), ρ is the air density (kgm^{-3}), V is the vehicle velocity (ms^{-1}) and A is the frontal area (m^2).

In racing, improvements in acceleration times can be extremely important for competitiveness, especially on a short circuit and are related to the tractive force at the tyres. At high speeds the acceleration tends to be limited by the excess engine power available and is therefore influenced by the aerodynamic drag. However, at low speeds, the tractive force available tends to be limited by the amount of tangential force the wheels can transmit to the road without spinning [9] and this maximum tractive force ($F_{T(max)}$) is determined by μN_R where μ is the limiting coefficient of friction and N_R is the normal reaction force.

Increasing the normal reaction on the tyres will aid in increasing the maximum possible tractive force and hence improve the acceleration. However, achieving this by increasing the vehicle weight is counterproductive because as well as increasing the tractive force, the inertia of the vehicle is increased requiring further tractive force. If the normal reaction is increased by aerodynamic means, through the generation of downforce, then no increase in inertia is experienced and acceleration is improved. In practice, very high powered racing cars can also be adhesion limited at high speeds, so the advantages of increased aerodynamic downforce are particularly useful when considering increased acceleration when exiting corners. This improvement in acceleration in an adhesion limited car is illustrated by Table 1.3.1. It shows that

the acceleration time from rest to 44ms^{-1} improves by almost 20% from 6.06s without downforce to 5.0s with downforce.

Measurement	With downforce (C_L = -1.96)	With no downforce
Time from rest to 44ms^{-1} (160kmh^{-1})	5s	6.06s
Final rate of acceleration (i.e. at 44ms^{-1})	10.02ms^{-1}	5.52ms^{-1}
Amount of power transmitted at 44ms^{-1}	353kW	229kW

Table 1.3.1 – The affect of downforce on acceleration of an adhesion-limited race car [9]

The influence of lift on braking is similar to that of acceleration and the influence of the normal load on braking distances is shown in Figure 1.3.1. As the aerodynamic downforce is increased the braking distances are reduced. For example, when braking from 300kmh^{-1} the distance reduces from 160m to 130m with C_L=-1.0 and reduces by a further 20m (to 110m) at C_L=-2.0.

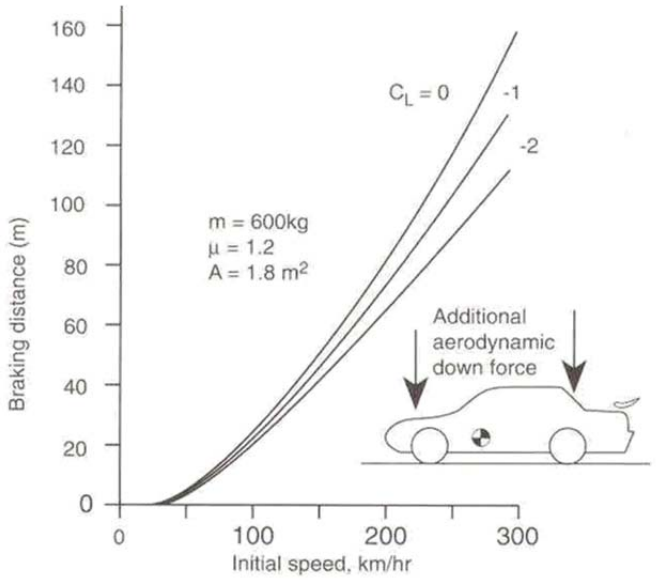

Figure 1.3.1 – Influence of downforce on braking distances [10]

While the importance of lift in acceleration and braking is clear, by far the strongest motivation to increase the aerodynamic downforce is because of its effect on cornering speeds. In the same way that the increase in normal load can improve longitudinal traction, it also increases the maximum lateral or cornering force. This increase in maximum lateral force is accompanied with an increase in maximum lateral acceleration and hence the maximum speed around a given corner. An example of the effect of aerodynamic downforce is illustrated in Figure 1.3.2, where $k_{c(max)}$ is the coefficient of limiting friction. The value of 1.4 is typical for racing slicks in the dry, while 1.0 is for grooved tyres in wet conditions.

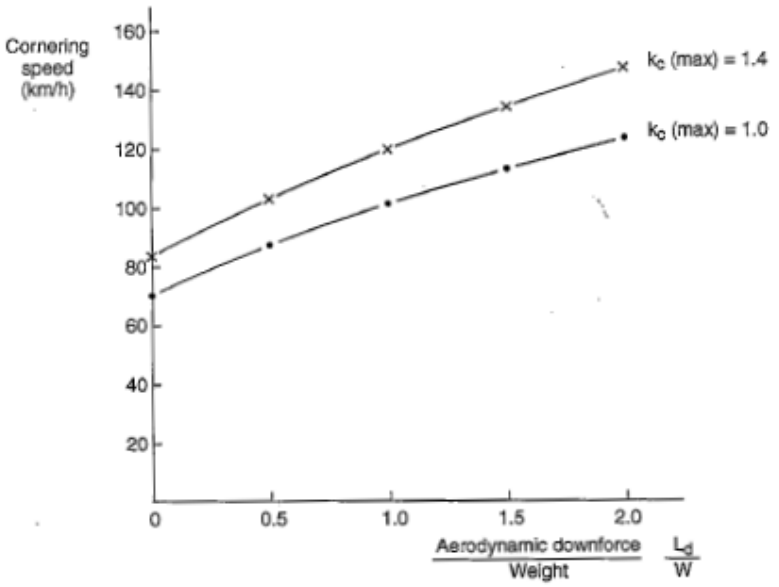

Figure 1.3.2 - Influence of downforce on cornering speeds for a corner of radius 40m [9]

As a result of increased downforce, a modern Formula 1 car is capable of developing in the order of 3.5g of lateral acceleration. Figure 1.3.3 highlights how this lateral acceleration changes with changes in downforce for a Formula 1 car. Here the results are presented as the product C_LA, a value of 2.2 therefore corresponds to a C_L value of approximately 1.5 for a typical race car with frontal area 1.5m^2 and C_LA=3.8m^2 corresponds to a C_L of approximately 2.5. Lateral acceleration increases with both corner radius and C_LA. At corners of low radii (e.g. 50m) increased downforce (C_LA=2.2-3.8m^2) gives an improvement in lateral acceleration such that the maximum cornering speed increases by 4.5% (1.4ms^{-1}). However, at much larger radii corners (e.g. 150m) the improvement is much more pronounced with an 18% increase in maximum cornering speed.

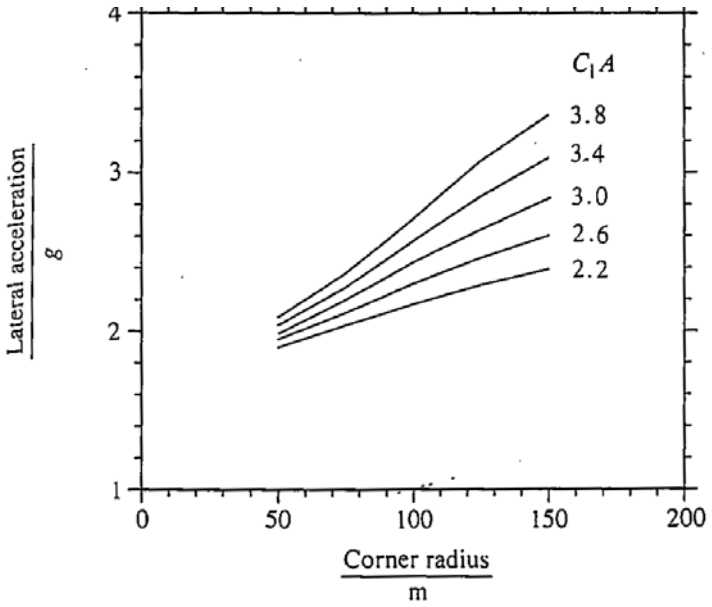

Figure 1.3.3 – The effect of aerodynamic downforce on cornering force [45]

While the benefits of increased overall downforce are clear, it is also essential to consider the downforce distribution between front and rear wheels. This distribution influences the cornering ability of the vehicle because the relationship between the centre of pressure (for lift) and the centre of gravity determines the understeer/oversteer characteristics. Applying large amounts of downforce at the rear, for example, will not improve cornering if the front wheels are traction limited because the car will heavily understeer. To achieve good balance, all the aerodynamic devices (front wings, diffusers and rear wings) need to be carefully designed, and optimised as a package to enable the car to be 'tuned' for different circuits based on their specific aerodynamic requirements, often a compromise between high straight line speeds (low drag) and high cornering speeds (high downforce).

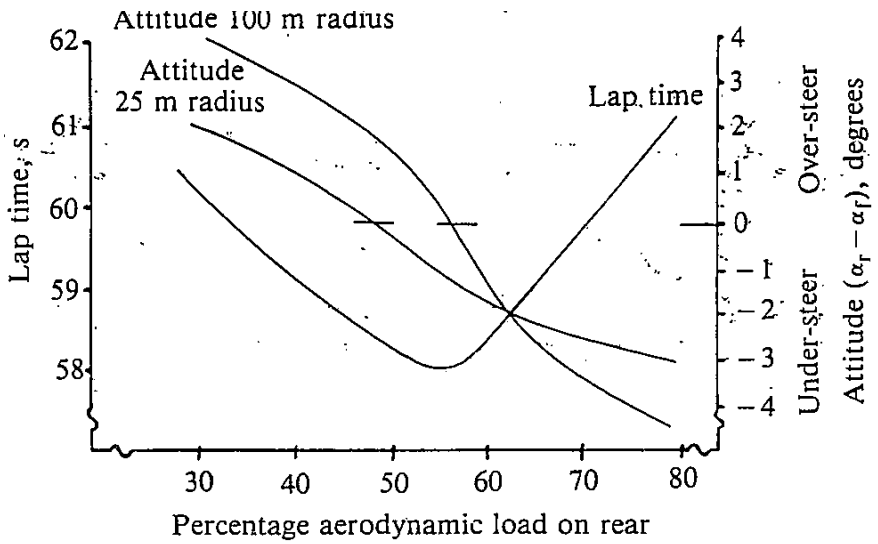

Figure 1.3.4 – Effect of aerodynamic balance on lap time and cornering attitude for a Formula 1 car [44]

The effect that the aerodynamic balance has on lap times and cornering attitude of a Formula 1 car from a study by Dominy and Dominy [44] is depicted in Figure 1.3.4. It should be noted that the intersection point around 62.5% load on rear is not significant and is merely a consequence of axis-scaling. Additionally, the characteristics shown are for a specific car and circuit combination. Each circuit has a different combination of corners (high and low speed) and straights with varying lengths. This results in a different vehicle setup in terms of aerodynamics (front and rear wings) and suspension. Figure 1.3.4 highlights the importance of aerodynamic balance such that for the optimum lap time (for this car-circuit combination), the ideal aero load on the rear is between 50% and 60%. Above and below this value the lap times typically increase. This paper also shows that in practice, this lift distribution actually means that the car is close to neutral steer.

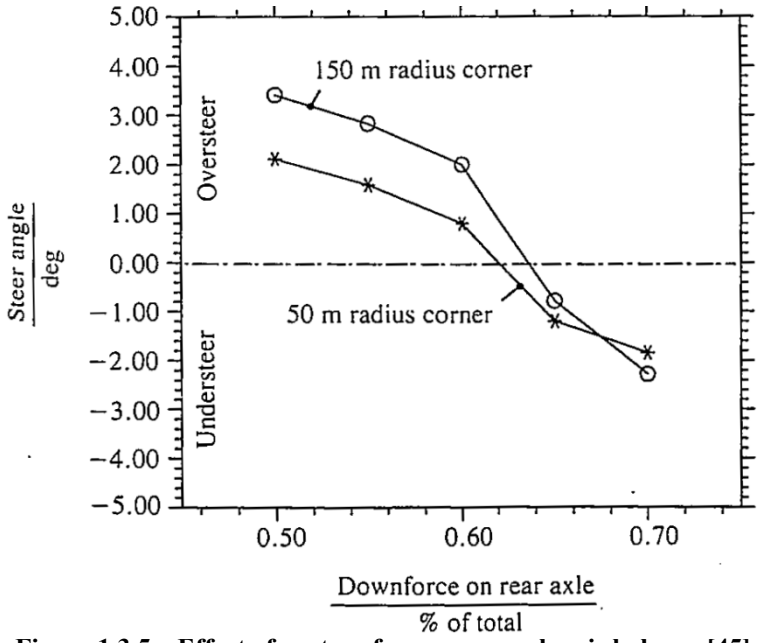

Figure 1.3.5 – Effect of centre of pressure on chassis balance [45]

A further study by Dominy [45] shows a racecar's understeer/oversteer characteristic with changes in the position of centre of pressure as shown in Figure 1.3.5. As the centre of pressure moves towards the rear the car's dynamic behaviour changes from oversteer to neutral steer to understeer. As the optimum performance (lowest lap time) of the car requires a near neutral attitude on cornering, this figure highlights how difficult it is to optimise the vehicle for a particular race because neutral steer is achieved with a different downforce distribution around different radii corners.

1.4 Diffuser Applications

Aerodynamic devices have been shown to be highly effective in improving the performance of racing cars, and the influence of aerodynamic balance has already been highlighted in this chapter. However, to gain further understanding the individual contributions of each aerodynamic device are also important to consider. There is little published data on the overall and specific aerodynamic loads, particularly on recent racing designs, however Wright [8] stated that the front wing contributes 25-30% of the overall lift, the underbody 40% and the rear wing 30-35%. In terms of drag, the rear wing accounts for about 25-30% , the wheels 40% and the remaining 30-35% is made up of drag from the front wing and main over and underbody.

The underbody contribution to the overall downforce can only be achieved through careful diffuser design due to the strictly implemented regulations. Additionally, the advantage of diffuser based downforce is that despite the vortex drag and drag due to ground proximity produced in the diffuser, the downforce-drag ratios available through diffusers have been

suggested to reach as high as 300:1 [12] significantly higher than that available through the application of wings.

The application of diffusers to road cars is less common because the often rough underbody forward of a rear diffuser renders any shaping largely ineffective and the increase in cost and weight associated with fitting a smooth underbody makes it an uninviting option for manufacturers, though it can reduce drag [43]. The possibility of thermal problems and increased difficulty in maintenance of driveline components may also be of influence. Diffusers may, however, become more common in the continuing drive to reduce CO_2 as well as offering an alternative aerodynamic balance solution to a rear spoiler. Additionally, with the future of road-vehicle powertrain likely to be hybrid, electric and fuel-cell technology, the greater influence of drag on range capabilities may increase the diffuser use, particularly as the revised powertrain may make a smoother underbody more viable. The primary road-vehicle application of diffusers is currently on high performance road cars where they can improve high speed stability [42].

1.4.1 Conical Diffusers

Diffusers, in particular conical diffusers, have been in use in aeronautical applications for many years prior to their implementation on road and race vehicles. The use of these diffusers can provide an insight into the potential performance parameters that may affect an automotive underbody diffuser as there has been much research into the performance of conical diffusers and the parameters and additional components that can improve pressure recovery.

A series of reports into aeronautical diffusers were published by ESDU [25], [51], [52], [53], [54] and [55] collating data from a variety of sources. These studies covered several parameters that affect the performance of different diffuser types including conical diffusers, plane-walled single-plane expansion diffusers, plane-walled two-plane expansion diffusers and annular diffusers. They defined a diffuser as “a section of closed duct along which mean static pressure of a flowing fluid increases as a result of decreasing kinetic energy of the flow without energy input from an external source”. Such diffusers have been used to improve the performance of compressors and to achieve gas velocity reduction between compressors and combustion chambers in gas turbines. Diffuser performance is expressed in terms of the static pressure rise across the diffuser and sometimes in terms of total pressure loss and outlet flow conditions. Contour plots of static pressure recovery were plotted for the conical diffuser, enabling all major geometrical variables to be evaluated in a single figure, as shown in Figure 1.4.1.

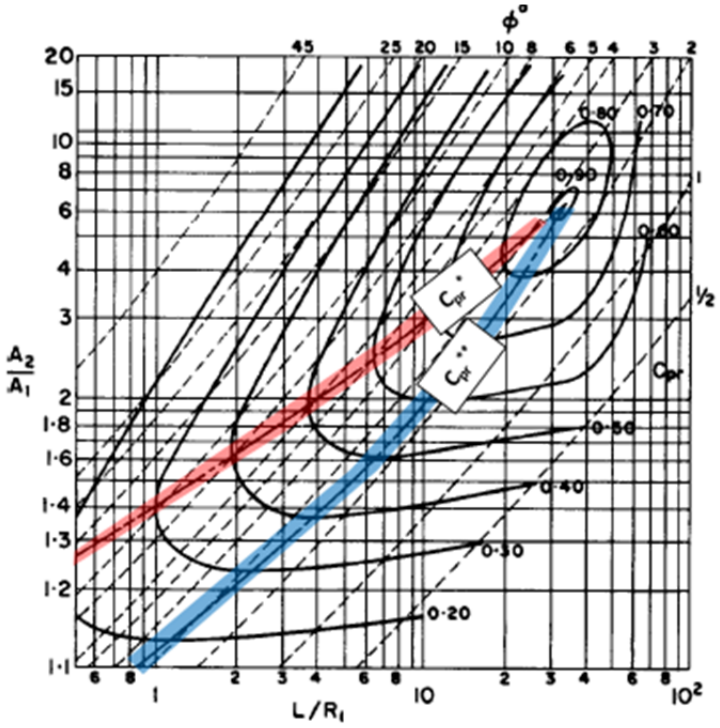

Figure 1.4.1 – Contour plot of pressure recovery for a conical diffuser [25]

Two optimum pressure recovery lines were identified on the contour plot; one of maximum pressure recovery for fixed area ratio (C_{pr}**) and one for maximum pressure recovery for fixed length ratios (C_{pr}*). The C_{pr}** line produced improved pressure recovery compared to that of the C_{pr}* line. For annular diffusers, the maximum static pressure recovery occurred when the inner wall angle ($ø_i$) was one or two degrees greater than the outer wall angle ($ø_o$), as it gave a flow passage convergent in axial cross section. It was noted by the authors that as the boundary layer grew the diffusers were less able to withstand the longitudinal pressure gradient and therefore more likely to separate.

In addition to straight-walled conical diffusers, ESDU [25] report on the effect of wall curvature showing that the curvature changed the pressure gradient as well as the development of the boundary layer. Three main types of wall curvature were assessed; bell-shaped diffusers, trumpet-shaped diffuser and inflected-wall diffusers.

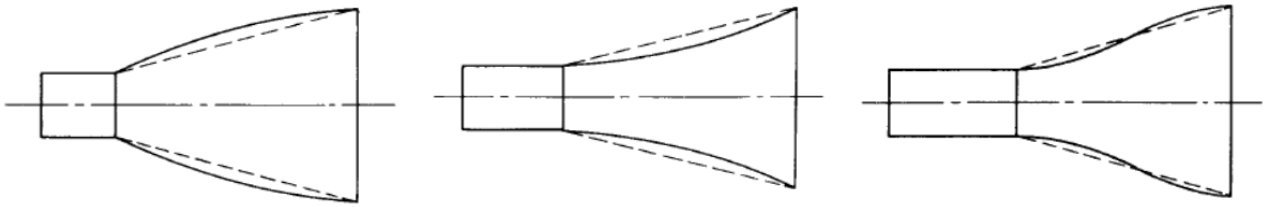

(a) (b) (c)

Figure 1.4.2 – (a) Bell-shaped, (b) trumpet-shaped and (c) inflected-shaped diffuser [25]

The bell-shaped diffuser (Figure 1.4.2a) was found to increase the longitudinal pressure gradient near the diffuser inlet in the region where the flow is most able to resist a high pressure gradient without separation, and then decreases the pressure gradient to reduce separation further along the diffuser. They also found that if separation was imminent near the first half of the diffuser, the curvature would in fact cause separation and that the high angles present at inlet meant that sharp corners should be avoided. The trumpet shaped diffuser (Figure 1.4.2b) was found to reduce the pressure gradient early in the diffuser, resulting in delayed separation, but further downstream the increased wall angle was likely to cause separation. Additionally, the initial boundary layer development was sometimes found to cause a reduction in effective area due to the slow increase in area near the inlet. Tests showed that if little or no separation was present in the straight-walled diffuser, then the bell diffuser had better pressure recovery while if separation was present the trumpet diffuser gave a performance improvement. An improvement on the design of the trumpet-shaped diffuser was found in the form of the inflected-shaped diffuser (Figure 1.4.2c). The advantages of this design were that it was found to alleviate problems of separation when the wall angle is very high near the exit.

An investigation into the effect of cross-sectional shape found that the maximum pressure recovery was similar for all cross-sections of diffusers but that the geometry at which the maximum was achieved varied. For asymmetric geometries, the maximum was achieved at higher area and length ratios than for plane-walled single-plane expansion geometries. For square-sectioned diffusers that expand in two planes, the maximum pressure recovery was found to occur at the same wall angle and area ratio as the asymmetric geometries. It was also found that the plane of expansion normal to the plane of the velocity profile gives the best performance for diffusers with a predominantly 2-dimensional velocity profile at the inlet. The shape and finish of the inlet and upstream conditions were found to influence the local static pressure variations as well as the overall diffuser performance. It was established that if a diffuser operates with large amounts of separation or with high inlet flow speeds then a smooth, rounded inlet should be implemented. This could be particularly significant for automotive applications and model designs.

Rough and imperfect surfaces were shown to decrease the static pressure recovery but in many cases showed that the changes were small. The diffusers most likely to be affected were those whose geometries lay on or near the flow regime boundaries (shown in Figure 1.4.3) especially those between attached and significantly separated flows. In these regions, when the boundary

layer was laminar, the surface roughness promoted a transition to turbulent and resulted in the diffuser being more able to withstand the pressure gradient.

The most problematic surface conditions were imperfections that caused asymmetry leading to asymmetric separation. It was found that symmetric or near symmetric inlet velocity profiles gave the best diffuser performance, particularly in the case of rectangular section diffusers where asymmetry in the inlet profile can lead to premature separation.

The position of the roughness is also important; roughness downstream of the entry promotes mixing and improves flow symmetry and stability. Additionally, the presence of roughness starting just upstream of the normal separation and improve performance. Surface roughness all over the diffuser was found to be detrimental to performance, especially for diffusers operating in the attached or slightly separated flow regimes due to increased friction and more rapid thickening of the boundary layers. For geometries which, if smooth, would have flow near to separation or just separated, the surface roughness in only the downstream part of the diffuser can improve performance especially in terms of stability of outlet conditions.

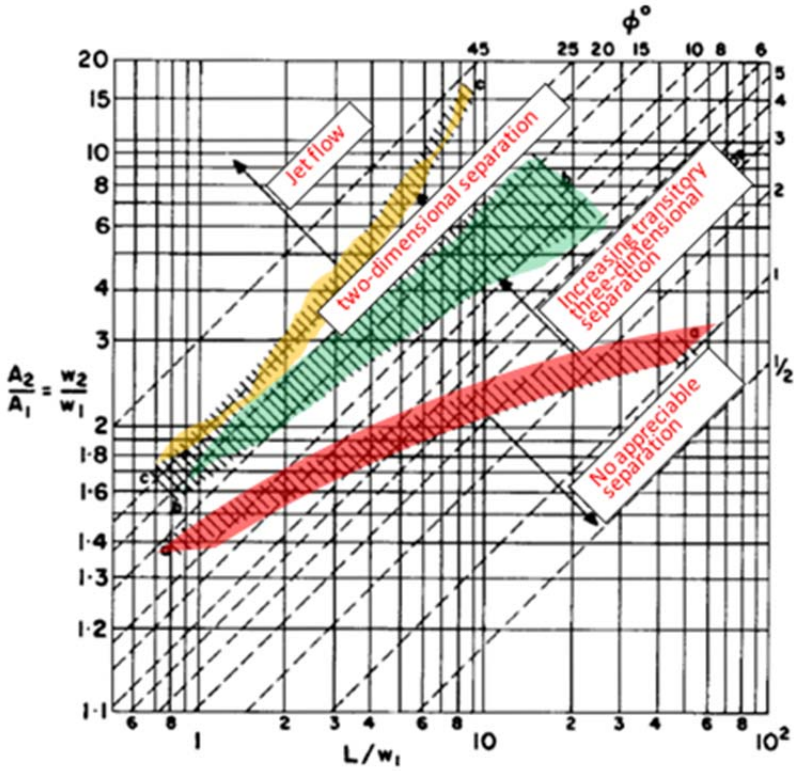

Figure 1.4.3 – Flow regimes for straight-walled plane-expansion diffusers [25]

The affect of swirling inlet flow was found to affect diffuser performance differently depending on the flow regime in which they lie. For diffusers in the attached flow regime it was found to have little effect on their performance. However, for a diffuser with transitory separation the

optimum performance line (C_{pr}*) was shifted to higher divergence angles. It was suggested that the optimum swirl occurred when the mean swirl angle was equal to the total divergence angle of the diffuser (Figure 1.4.4). At these conditions a pressure recovery improvement of up to 15% was observed.

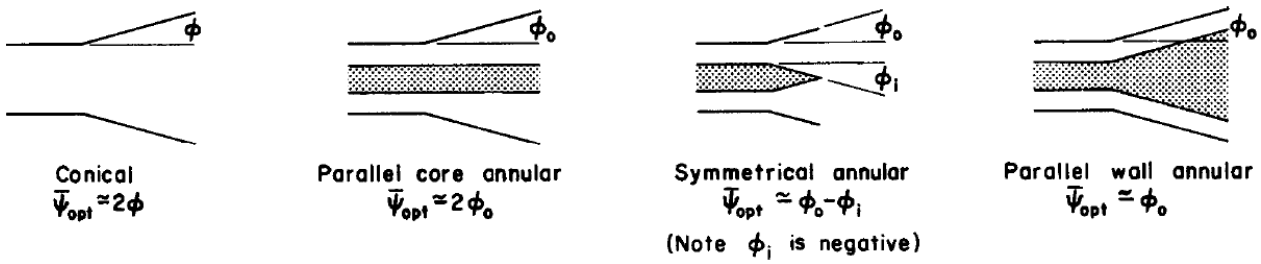

Figure 1.4.4 – Optimum mean swirl angle for various diffusers [25]

With the presence of inlet swirl and in the absence of flow separation, the angular momentum was found to be conserved along the diffuser length but no obvious performance advantage was observed, especially if the swirl was produced deliberately because swirl generation produces energy losses.

The main cause of poor performance of any diffuser geometry was identified as separation of the flow, which then reduces the effective area ratio and produces a non-uniform exit flow. An investigation was undertaken to try and establish how this separation could be prevented, delayed or stabilised to improve the performance of diffusers, especially where large angles were implemented. Splitters and vanes were used to assess the possible improvements available. Splitters are plates that extend the full length of the diffuser and it was found that even if severe separation occurred, it was confined by the splitter plates and did not interfere with the flow in other passages. Vanes only extend over a portion of the diffuser length but were also found to improve performance. This was partly attributed to the splitting of the diffuser channel but additionally the wakes and vortices that were shed from the edges promoted mixing. Vortex generators were implemented upstream of the diffuser inlet which shed small vortices. These improved the mixing near the diffuser walls, delaying separation and improving performance.

This study conducted by ESDU provides a large quantity of information on the factors affecting the performance of conical, annular, single-plane and two-plane expansion diffusers. Although automotive diffusers are not identical to those described here, the improvements in performance seen in these diffusers may provide insights into possible improvements in automotive diffusers. Automotive diffusers are primarily three-dimensional due to the presence of vortices, although

the centreline of the diffuser, where separation occurs, can be thought of as close to two-dimensional. The ability of the different types of conical diffusers to withstand the adverse pressure gradient may well be applicable to those in automotive diffusers. The presence of splitter plates in the diffuser resulted in the confinement of any separation present in the flow while the vanes and vortex generators improved the performance. Due to the three-dimensional behaviour of underbody diffusers the implementation of splitters and vanes may provide further performance improvement.

1.4.2 Automotive Diffusers

At this point it is necessary to consider the general downforce mechanisms and behaviour of the automotive underbody diffusers and how they may differ from the conical diffusers. Published work on automotive diffusers has largely concentrated on detailed studies of simple plane diffusers [13], [14], [15], [16], [17], [21] and [22]. A diffuser, in this instance, can be described as a passage of increasing area that is used to reduce the velocity of the flow, thereby recovering pressure. Despite the fact that the primary function of a diffuser is to recover pressure, when used in automotive applications, the conditions to which these diffusers are subjected results in some additional mechanisms (i.e. ground interaction) that affect the performance. Previous studies [16], [17], [19] have identified three important mechanisms involved in the operation of underbody diffusers as follows:

- The interaction with the ground
- The phenomenon of *diffuser pumping*
- The upsweep of the underbody

A symmetrical body in free air has zero lift [16], however as the body is brought into ground proximity, the flow along the underside of the body is constrained causing a greater flow acceleration. This increased flow acceleration produces a decrease in static pressure creating suction on the underbody and hence producing downforce. As the ride height is reduced the underside flow is further constrained resulting in the pressure recovery after the front edge radius being suppressed and consequently the downforce increases. This increase continues until a point where, at a very small ride height, the effects of fluid viscosity become dominant and no further increase in downforce is achieved. Clearly the interaction with the ground is not a diffuser phenomenon but its interaction with the diffuser performance is a critical one.

The phenomenon of diffuser pumping was first discussed in relation to automotive plane diffusers by Sovran [19] and further investigated by Cooper et al [16], [17]. The phenomenon occurs because the exit pressure of an automotive diffuser is essentially fixed by the vehicle base pressure. As the diffuser recovers pressure along its length the fixing of the outlet pressure effectively reduces the diffuser inlet pressure and it is said to have *pumped down* the underbody pressures. The depression at the diffuser inlet is a significant source of downforce and has the effect of also reducing the underbody pressures forward of the diffuser inlet, increasing the underbody flow rate, as can be seen from the pressure results in Figure 1.4.5. This reduction in pressure on the flat underbody has been found to produce a larger proportion of downforce than the diffuser, but it is the diffuser that controls how much the pressures are "pumped down".

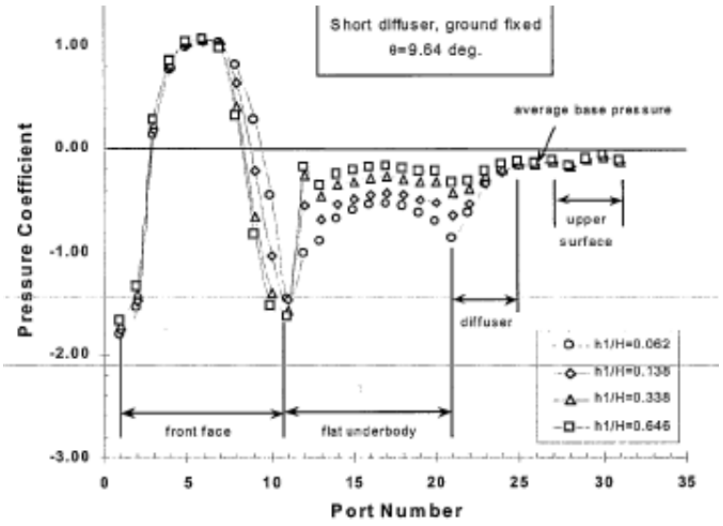

Figure 1.4.5 - Pressure distributions from [16]

The angled upsweep on a diffuser aids in downforce production in a similar way to that of an inverted wing. A diffuser without endplates may also be compared to an inverted fastback vehicle. In the fastback vehicle the presence of twin trailing vortices generates a *downwash* over the rear slant which helps maintain flow attachment [18]. When inverting this scenario to that of a diffuser, the vortices now create an *up-wash* of the flow field, aiding the flow attachment and ultimately increasing the downforce produced. The presence of end plates on the diffuser suppresses the cross flow and may reduce the size of these vortices. However, the depression at the diffuser inlet, results in flow being drawn in from the sides at this point which aids in the vortex production. These vortices are then enclosed within the endplates of the diffuser. When operating in close proximity to the ground the development of the vortices may be modified.

Cooper, Bertenyi et al [16] completed the most thorough set of measurements on a diffuser-equipped bluff body in published data. Their main objective was to identify the physics of the underbody flows of vehicles with plane underbody diffusers. The model that was used was of bluff body design with 25% and 75% length diffusers and diffuser angles between 0° and 15°.

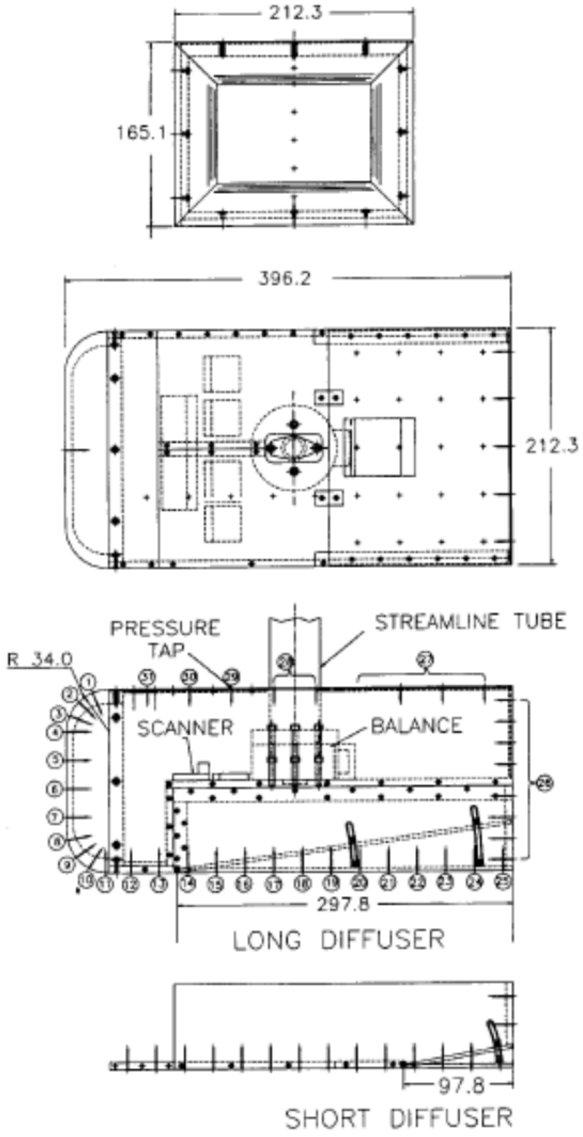

Figure 1.4.6 – Cooper model description [16]

This model was tested at nine angles and 22 ride heights, with three different ground plane simulations at 30ms^{-1}. Both force and centre-line pressure measurements were taken. Only the results for the 25% diffuser were discussed and it was found that for a fixed angle, as the ride height was decreased, the downforce increased to a maximum and below this small ride height the downforce decreased rapidly. This was attributed to viscous effects close to the ground where the sum of the boundary layer thickness on the underbody and the ground was a large percentage of the ride height. At large ride heights ($h1/H > 0.2$), the drag was reduced with the diffuser angle

because at high ride height the diffuser area ratio is close to one, and essentially the model is acting as a body in free air. This is similar to the drag variation seen in fastback vehicles where increasing the back slant angle from 0° reduces drag up to an angle of about 12°-15°. The drag was however, increased by the diffuser at low ride heights over the region in which the downforce production increases rapidly, but a drag reduction over the flat floor was observed for small diffuser angles (1°-5°) highlighting the potential for application as a drag reduction mechanism. The range over which the diffuser reduces drag is small (0°-5°) compared to the fastback data (0°-15°). For the overbody, the "area ratio" is 1, irrespective of the angle but for the diffuser the area ratio increased rapidly with angle. Similar to the lift variation, the drag variation was comparable for both ground simulations with a slight difference at very small ride heights where viscous effects were more significant in the fixed ground simulation.

The pressure distributions supported the idea of diffuser pumping with a depression at the inlet of the diffuser and the pressure-based coefficients calculated from the pressure distributions showed good correlation with the force measurements. These pressure-based coefficients identified that the flat underbody contributed most of the downforce with the diffuser producing the small additional amount. Contour plots or 'diffuser maps' were also plotted, from the pressure-based coefficients, to enable an optimum diffuser performance line to be established, similar to those plotted for conical diffusers [25] and Figure 1.4.1. This optimum performance line (or C_p^*) represents the diffuser geometries that give maximum pressure recovery at fixed non-dimensional length. The diffuser maps showed that as the area ratio parameter was increased from zero, the diffuser-based downforce increased to a maximum and then decreased. The investigation by Cooper et al gives a broad insight into the mechanisms of an underbody diffuser and provides a starting point for further investigation into both the flow mechanisms and influence of varying parameters.

Cooper et al [17] continued an initial study [16] by investigating the influence of diffuser length on performance and using pressure data to indentify more clearly the three downforce mechanisms already suggested by previously published data. Centreline pressure data was examined and found that a change in downforce in the flat floor configuration was observed as the ride height was altered such that at very high ride heights (representative of freestream) the model lift coefficient was close to zero but that as ride height was reduced this became increasing negative, identifying the downforce production due to ground proximity. This effect is summarised in Figure 1.4.7.

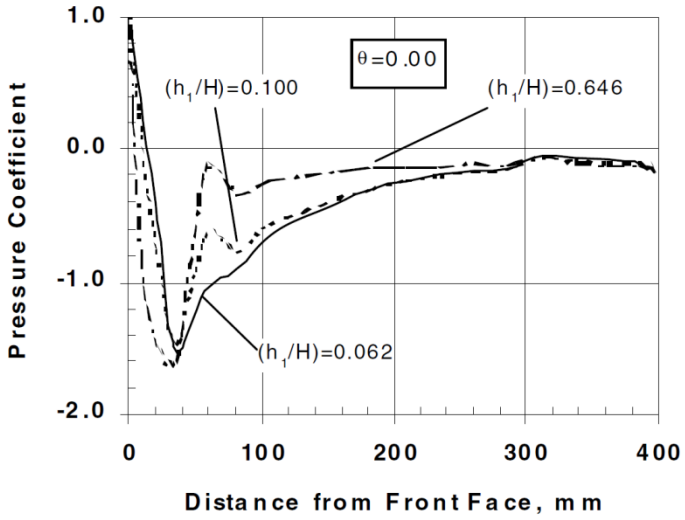

Figure 1.4.7 – 0° pressure distribution with changing ride height [17]

Moving from the flat floor to a diffuser angle of 9.64° provided insight into the diffuser pumping contribution. As the ride height was decreased the area ratio increased from close to unity and caused progressively greater pressure recovery in the diffuser. This resulted in the negative depression at inlet to increase due to the fixed base pressure, causing a higher flow velocity over the flat underbody. The increased flow velocity lowered the observed pressure distribution, leading to higher downforce. Cooper et al used the "ground interaction" and "diffuser pumping" effects to illustrate the relative contributions to the overall downforce in the schematic shown in Figure 1.4.8. Additionally it was noted that the third downforce mechanism 'underbody upsweep' was not an independent mechanism when the model was in close ground proximity.

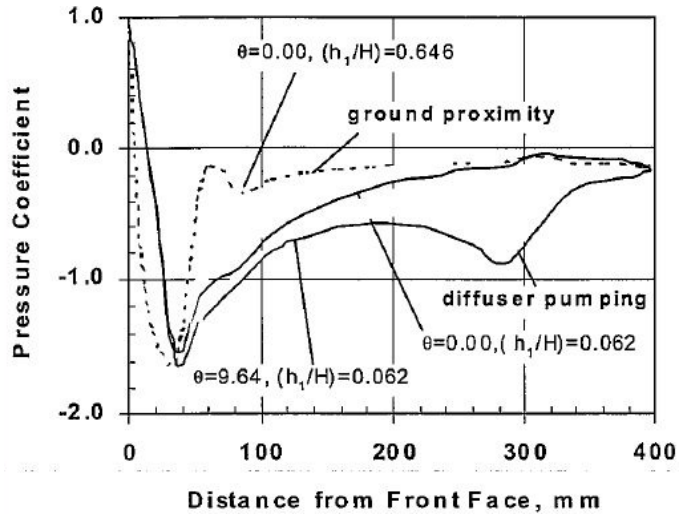

Figure 1.4.8 – Mechanisms of downforce generation [17]

It was found that the changes in the lift distribution were determined by the changes observed in the mean-effective underbody pressure coefficient, where the more negative the greater the downforce produced. CFD was used to predict the relationship between the underbody pressure

recovery ($\overline{\overline{C_{pf}}}$) and diffuser pressure recovery ($\overline{\overline{C_{pd}}}$) and then calculated for the experimental data. The ratio of $\overline{\overline{C_{pf}}}$ and $\overline{\overline{C_{pd}}}$ was calculated for both diffuser lengths and the ratio of mean effective pressure was insensitive to ride height and area ratio parameter, and the relationship was found to be essentially linear. As such, at a specific area ratio, as the diffuser length was increased to improve the overall pressure recovery coefficient, this made $\overline{\overline{C_{pd}}}$ more negative and consequently $\overline{\overline{C_{pf}}}$ became negative even faster.

Performance maps were generated of diffuser pressure recovery coefficient derived from the centreline pressure distributions of the model with a 25% diffuser for both ground simulations. They exhibited similar distributions with some significant differences; such as the fixed ground contours were closed whereas the moving ground were open at high non-dimensional lengths. Additionally, the location of maximum pressure recovery occurred at a lower area ratio and higher non-dimensional length with moving ground. Comparison of contours of near maximum pressure recovery showed that a specific pressure recovery could be achieved at a smaller geometric area ratio with moving ground. This was found to be because the effective area ratio for a given geometric area ratio was always greater in the moving ground thanks to the reduced distortion in the velocity profile from the reduced boundary layer thickness. Additionally, higher diffuser lengths could be tolerated more with the moving ground.

A correlation was found between lift coefficient (C_L) and the diffuser pressure recovery coefficient ($\bar{C}_p$) such that when $\bar{C}_p$ increases locally, the lift coefficient becomes more negative locally and vice versa. The contours of lift coefficient showed similar distributions to those of the pressure recovery contours, except that the maximum occurred at lower area ratios and non-dimensional lengths.

When considering the mean-effective underbody pressure coefficient, it was found that when the diffuser length was short, the flat underbody component contributed a greater amount and at a specific diffuser length, a maximum occurred and decreased as the length was further increased. Underbody mean-effective pressure coefficient was plotted against diffuser length fraction and found that the optimum diffuser length changed with changes in area ratio and ride height, but it generally occurred about N/L=0.5. The optimum area ratio was found to increase with decreasing ride height while the maximum downforce increased with increasing area ratio up to (AR-1) = 2.02, decreasing at values above this optimum.

The two studies undertaken by Cooper et al provide a large quantity of information concerning the performance of plane underbody diffusers using force and centreline pressure measurements.

George [23] carried out tests on a diffuser equipped bluff body (without endplates) over a range of pitch angles with and without a rough underbody and wheels. Force measurements and flow visualisation showed the formation of vortices which were fed by edge surface separation. When the pitch angle was changed (incrementally in 5° steps) vortices formed at low angles of attack and as the angle was increased the vortices moved forward and were strengthened. They also induced an inflow which prevented the formation of a separation bubble. Even at the extreme angle of 35° pitch (equating to 55° relative to freestream within the 20° diffuser) where a separation bubble formed upstream, the flow reattached further down due to the strong vortices. When underbody roughness strips were added at a pitch angle of -10°, the flow was seen to remain attached due to the presence of strong vortex structures. As the pitch angle was increased to 5°, separation behind the roughness strips increased reducing the strength of the vortices. It was also noted that the presence of the roughness strips resulted in detrimental drag figures. The addition of wheels helped trigger and stabilise the vortex formation and at zero pitch angle the small separations present were reduced, vortex strength increased resulting in the increased downforce observed. It was suggested that if relatively high levels of downforce were required, strakes should be used on the underbody to trigger vortex flow, similar to vortex generators used to maintain diffuser flow on Formula 1 cars of the time. Additionally, the influence of ground simulation was investigated and found that the moving ground tended towards increased drag and downforce. This investigation gives a good general overview of the effect of pitch angle on diffuser performance, as well as underbody roughness and wheel presence. However, the complexity of the model (with wheels and large diffuser angles) begs the question of the relevance of the configurations to practical cases.

George and Donis [22] present a comprehensive paper that includes results from several different model types. In each case, force and pressure measurements are reported along with the results of the surface flow visualisations. The first model configuration Figure 1.4.9(a) is describing a ‘plenum’ model. The model is formed from a simple bluff body with a hollow underside and skirts at the front, side and rear. The results showed that the pressures under the model were controlled by the pressures around the skirt edge and by the size of the ground clearance gap allowing the local flow movement.

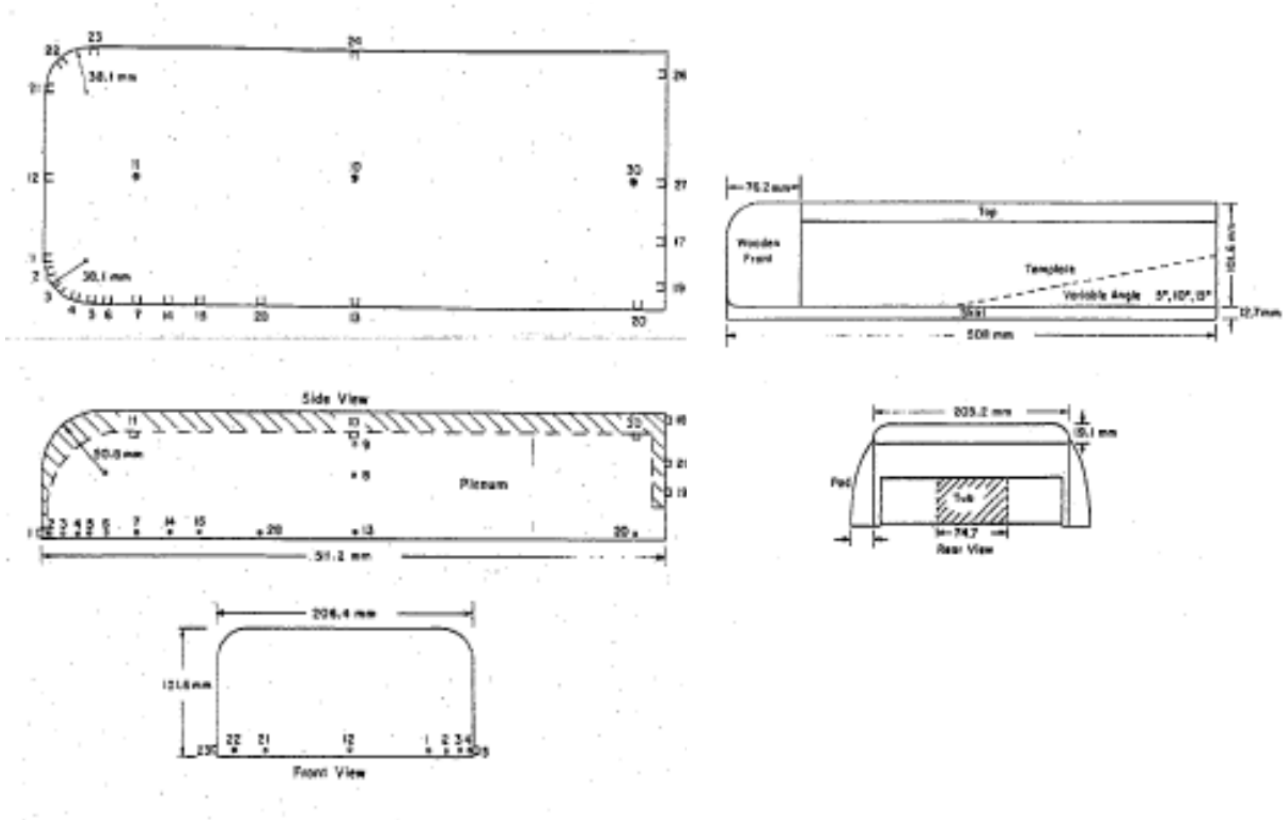

(a) **(b)**

Figure 1.4.9(a) and (b) - Plenum and venturi model configurations [22]

The 'venturi' model (Figure 1.4.9(b)) was essentially a long (50% length) diffuser equipped with 5°, 10° and 15° diffusers and adjustable full length side skirts allowing the gap between skirt and ground to be varied. The 5° diffuser with skirts sealed to the ground produced maximum downforce compared to open skirt clearance and gave a 'classical attached 2D flow'. The pressure results showed areas of low pressure on the side, suggesting the formation of longitudinal vortices under the model. Despite these vortices being weak, it was noted by the authors that they prevented stalling of the flow. The 10° and 15° diffusers exhibited different behaviour to that of the 5°, as they both stalled with the skirts fully sealed, instead they produced higher levels of downforce with open skirts. This differing behaviour was attributed to the formation of longitudinal vortices originating from the skirt edges. They likened these flow characteristics to those on a fastback vehicle in that the vortices aided attachment.

The results for 9.5mm skirt clearance showed a region of separation on the ground plane, which was attributed to the vortices causing a flow away from the ground up towards the underbody. This separation was more pronounced for the 15° diffuser than the 10°. Additionally, it was observed that with inflow under the skirts, increasing the diffuser angle created stronger vortices which increased downforce, but that at very large ride heights the 'vortex phenomenon'

disappeared. The 15° diffuser produced maximum downforce at higher ride heights then the 10° diffuser, which was owing to the fact that the 15° diffuser obtained its larger forces due to the stronger vortices generated.

Alternative modified venturi configurations were tested which included addition of such components as side pods, centre 'tubs' and L-skirts. The addition of side pods increased the downforce, which was attributed to the high velocity, low pressure inflow having a wider area to operate in, whereas the introduction of a centre tub decreased the downforce due to reduced effective diffuser area. These results imply that the width of the diffuser channel and sides may have a direct impact on the diffuser performance. The L-skirts increased downforce while the labyrinth skirts reduced the downforce production. The presence of wheel 'bumps' disrupted the vortex formation resulting in reduced downforce. Overall, George and Donis provided a broad range of results concerning the influence of configuration and ride height on diffuser performance. The identification of a pair of longitudinal vortices aids in the understanding of downforce production. The work on alternative configurations provides a starting point for future work.

Howell [21] performed a study exploring road-vehicle models and typical overbody geometry. He investigated simple wheelless models representative of road car shapes with interchanging rear end shapes and an underbody diffuser. The backlight angles used were varied from 0° to 40° and the 18% length diffuser was capable of diffusers angles from 0° to 20° at 5° intervals. The lift results for the effect of diffuser angle showed that as the diffuser angle was increased, the downforce increased to a maximum at 15°, then decreased at 20°. Additionally, as the ride height was reduced the downforce was seen to increase to a maximum at a very small critical ride height, which varied slightly for different diffuser angles. The results for effect of backlight angle found that with no diffuser, the drag reduced to a minimum at 15° backlight angle and increased to a maximum at 30°. As the diffuser angle was increased to 5°, the drag was seen to reduce over all backlight angles and the peak drag was significantly reduced. As the diffuser angle was increased further, it was noted that increasing the diffuser angle increased the initial drag but reduced the drag peak. The 15° diffuser was observed to give the lowest overall drag and the 20° diffuser increased drag for all backlight angles. Additionally it was found that the influence of increasing the diffuser angle at each backlight angle resulted in reduced lift values. Howell's investigation provides information regarding the interaction of the diffuser with the base pressure and overbody profile. This is important when considering model geometry for an independent diffuser study.

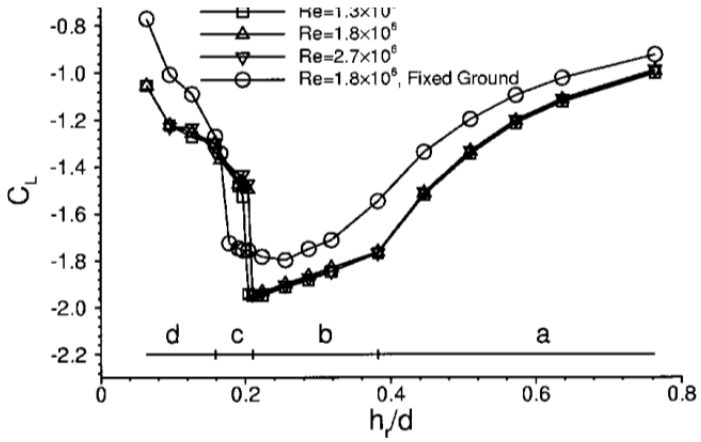

Figure 1.4.10 – Lift coefficient vs. non-dimensional ride height for 17° diffuser [14]

Senior and Zhang [14] concentrated on investigating a 17° diffuser angle at a range of ride heights between 0.01m and 0.199m. The model used had dimensions 1.315m (length), 0.314m (width) and 0.324m (height) with a 41% length diffuser. They used force measurements, pressure measurements and surface visualisation techniques to enable the flow behaviour to be examined. They identified four distinct regions of force behaviour:

Region a – 'downforce enhancement'

Region b – 'maximum downforce'

Region c – 'downforce reduction'

Region d – 'low downforce'

They observed (Figure 1.4.10) that in *region a,* the downforce was weak but increased with decreasing ride height until a limiting ride height, similar to that observed by [16]. A change in the gradient of the downforce curve below the limiting ride height was attributed to the introduction of new flow physics close to the ground. *Region b* was characterised by a "plateau" in the downforce curve where it was observed that the flow remained relatively constant around the model. The maximum downforce and drag occurred at $h_1/H = 0.105$. As the ride height was reduced (into *region c*) the downforce reduced dramatically and continued to reduce with further reduction of ride height. The pressure results showed a suction peak at the inlet of the diffuser which increased with reducing ride height until a maximum suction at $h_1/H = 0.105$, corresponding with the maximum downforce seen with the force measurements. Below this ride height the suction peak decreased and signs of flow separation in the first half of the diffuser were observed.

The flow visualisation results show that in *region a*, the flow was symmetric about the centre plane of the diffuser with slight separation observed across the diffuser inlet. The presence of S-

shaped lines on the diffuser surface identified a pair of streamwise vortices (confirmed by areas of low pressure near the side plates) and the curvature of these lines was seen to reduce as the flow decelerated toward the base of the model and flow on the side plate implied the vortices became detached from the surface. As the ride height was reduced the S-lines were observed to be more pronounced and stretched further down the length of the diffuser which was attributed to the strength of the vortex increasing. In *region b*, the flow remained symmetric but flow separation was observed with the formation of a separation bubble at the centre of the diffuser. As the ride height was reduced further, the adverse pressure gradient became increasingly steep until further separation was observed at a critical ride height. Downstream of the inlet, the flow visualisations suggested that the counter rotating vortices were increasing in diameter, and becoming a more dominant feature of the flow.

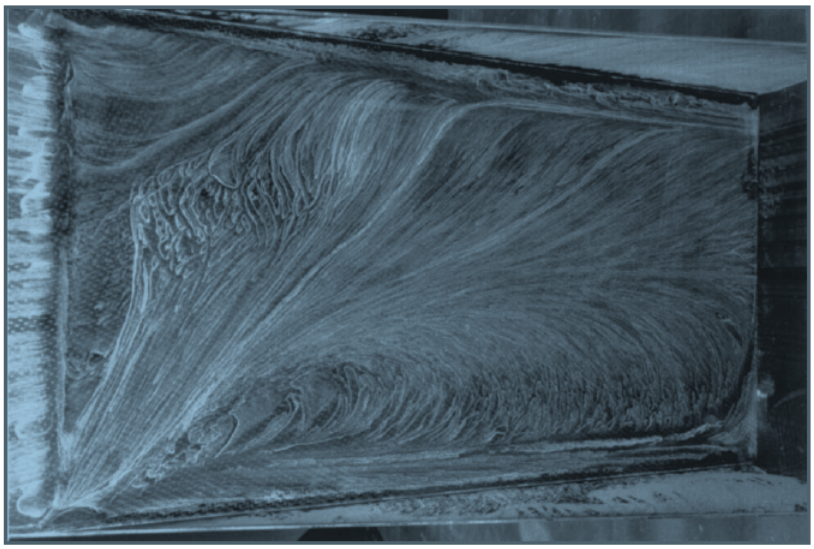

Figure 1.4.11 – Surface flow visualisation of vortex breakdown [14]

When the ride height was reduced to much smaller ride heights in *region c* and *d* flow asymmetry and separation at inlet was observed. This asymmetry produced flow that ran from the bottom corner diagonally across the diffuser channel causing the detachment of one of the vortices shown in Figure 1.4.11. Senior and Zhang completed a relatively thorough investigation on one diffuser angle in terms of flow visualisation results that offer a good basis for further investigation to surface flow measurements.

Ruhrmann and Zhang [15] investigated a diffuser equipped bluff body with five diffuser angles (5°, 10°, 15°, 17° and 20°) and at a range of ride heights. Although measurements were taken using load cells, pressure tappings and surface flow visualisations, the majority of the report focussed on the flow visualisations results. The force measurements showed two types of flow

regimes; one for low angles (5°) and one for larger angles (15°, 17° and 20°). In addition the 10° diffuser appeared as a transitional angle between the two regimes, exhibiting characteristics from both. The higher angles exhibited characteristics as seen by the same model at 17° in [14]. The flow visualisations produced interesting results for all angles at the different force regions in terms of separation and vortex characteristics. In the maximum downforce region, the 5° diffuser experienced no separation bubble formation whereas the 10° diffuser showed a closed separation bubble downstream of the inlet, closing just before the diffuser exit.

Upstream of the exit, the vortices were seen to begin to breakdown due to reducing swirl. They observed that the high angle diffusers produced similar results, with an open separation bubble. The separated flow was entrained into the vortices which reduced the axial momentum and it was observed that at higher ride heights the adverse pressure gradient was weak and two dimensional separation did not occur. The separation bubble was prevented from forming due to two counter rotating vortices which dominated the flow. As the ride height was reduced the pressure at the inlet decreased and low pressure regions formed at the corner where the vortices originate. For the 20°, vortex breakdown was observed. This was characterised by the swirl becoming less evident and the vortex diameter getting larger. Asymmetry was observed on the 15° diffuser and was attributed to several effects. The separation point cannot travel further upstream than the inlet due to the favourable pressure gradient ahead of the inlet and the low pressures either side of the inlet cause large asymmetry. They found that the direction of asymmetry was random but once it was established it did not change sides. Additionally, the separation bubble was swept to one side and recirculation was observed. This recirculating flow region was also observed in the pressure contour plot as a region of constant pressure. Maps of diffuser performance (Figure 1.4.12), similar to those plotted for conical diffusers [25], showing the different operating regions of diffuser angles with respect to area ratio.

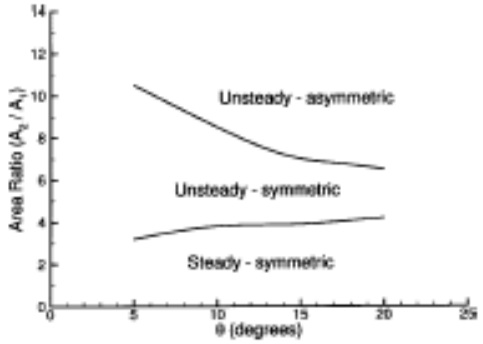

Figure 1.4.12 – Diffuser Map of Performance [15]

It was found that the change from "steady-symmetric" flow occurred at a similar area ratio for all angles and this change was controlled by the adverse pressure gradient. They also noted that the narrowing of the "unsteady-symmetric" region at high angles shows that the streamwise adverse pressure gradient is not the main factor in transition to asymmetric flow. Ruhrmann and Zhang concluded that the main cause of downforce reduction was vortex breakdown in small diffuser angles and a combination of flow separation and vortex breakdown in larger diffuser angles. This investigation provides good information on the flow mechanisms at work within different angles from the flow visualisation results and provides a good basis for further work.

A further investigation of a 17° diffuser was undertaken by Zhang, Senior and Ruhrmann [13]. The primary measurement technique used was 3-component Laser Doppler Anemometry (LDA) but additional measurements were taken including force, pressure and surface flow measurements. Three types of trailing vortices were observed; a) concentrated, symmetric with high axial speed core, b) diffused, symmetric with low axial speed core and c) diffused and asymmetric. At very high ride height, representative of near freestream, the LDA measurements imply a highly 3-dimensional inlet flow. Similar to the findings of [15], the flow was symmetric about the centre plane for the diffuser and local low pressure lead to strong entrainment either side of the model. LDA measurements of the flow immediately behind the diffuser exit indicated a highly concentrated vortex forming from the edge of the side plate. This vortex was seen to have a high axial speed core but measurements could not be taken at the centre of the vortex due to problems with seeding. These vortices were formed by flow entrained underneath the side plated and wound into a vortex with the flow between the two vortices forming an 'upwash' as explained by [16]. The force measurements exhibited characteristics very similar to [14] with the same four regions of downforce behaviour. The pressure distributions showed suction peaks at the diffuser inlet that became more pronounced as the ride height was reduced. Separation was observed at the inlet at a critical height of $h_1/H = 0.176$ where a sudden change in the downforce curve indicated a loss of downforce. As the ride height was reduced from near freestream into region a ($h_1/H = 0.192$) the vortices were observed to move inboard and become larger with a high axial speed core. An additional secondary vortex flow was noticed which started at the junction between the upswept surface and side plate. As the ride height was reduced further (into region b) the vortices increase substantially in size but exhibited lower axial core speed.

The presence of asymmetric vortices was observed as the ride height entered region c, with the flow in the cross plane dominated by one vortex only. In this ride height region the downforce production mechanisms were dominated by the flow separation at the inlet and vortex

breakdown. At the lowest ride heights (region d) very close to the ground, the mass flow entering the diffuser was seen to decrease substantially suggesting that the boundary layers had merged and comprised a large percentage of the ride height, restricting the flow to the diffuser. The exit flow was observed to be dominated by flow reversal and weak circulating cross-flow and flow entrainment between the side plates and the ground was greatly reduced. Overall, Zhang et al completed a relatively good study on a 17° diffuser giving some useful LDA results that provide further information concerning the behaviour of the vortices. The force, pressure and surface flow visualisations were all consistent with those found by [14] and [15].

Breslouer and George [26] investigated a 25% length diffuser-equipped bluff body similar to that of Cooper et al [16], [17] with the presence of non-rotating wheels with a similar ratio of wheel thickness to body thickness of Formula 1 cars. Force measurements as well as flow visualisation techniques were used to assess the performance of two diffuser angles (0° and 9°). Initial tests were carried out to make a comparison with [16] at a variety of similar ride heights and compared well except at the lowest ride heights where the boundary layer conditions varied between the two configurations. A second set of tests were undertaken examining the influence of presence of the wheels. Both front and rear wheels were tested separately, as well as all four wheels at a variety of distances away from the model centreline. The results found that the formation of vortices was diminished because the wheels reduced the ability of the flow to form tightly rotating vortices. This was attributed to the wake of the wheels being confined to the region behind and having no lateral motion of the flow. The fact that there was no lateral flow movement was itself attributed to flow acceleration between the wheel and endplates, such that the pressure difference between the diffuser channel and model sides was reduced and therefore less inflow would be expected, reducing vortex formation. In the case of all four wheels, the downforce was reduced further due to a turbulent low energy region between the front and rear wheels. This investigation, although useful in theory, provides little insight into the performance behaviour of diffusers interaction with wheels. The data presented was not complete enough to draw conclusions on behaviour and the lack of pressure data compounded this issue. Additionally, the results appear to contradict those observed in [22].

1.5 Objectives

Several investigations have considered the performance of automotive underbody diffusers. A range of diffuser angles have been tested from 0° to a maximum of 20°, although the majority of results are for angles below 15°. The ride height range in which these angles have been tested is

from 4mm to 199mm (h_1/H = 0.01 to 0.646, where H=310mm). All these investigations have focussed on the single plane diffuser channel configuration while the use of multiple channel configurations and their performance is an unknown quantity despite their application in many racing formulae.

The first aim of this set of experiments is to investigate the lift, drag and efficiency of a plane diffuser over a range of diffuser angles and ride heights. The diffuser angles chosen represent a wide range of operation from 0° (flat floor) to 30°, the higher angles representative of those utilised on high performance racing cars not previously investigated in published literature. The ride heights used are representative of both road and race car proportions to enable a realistic set of measurements for real world scenarios. Initially, comparison will be made with previously published data to ascertain confidence in the experimental technique, however the primary concern for the plane diffuser is to identify the controlling mechanisms within the flow that lead to the performance changes with parametric changes. This enables a base line configuration to be established to which further configurations can be compared.

Secondly, the effect of longitudinal splitter plates will be examined through the use of multiple-channel diffuser configurations, in the form of two-, three- and four-channel diffusers. These experiments will repeat those performed for the plane diffuser and comparisons of performance change to the plane diffuser made.

Chapter 2 - Experimental Method

2.1 Model Description

The base model, depicted in Figure 2.1.1, is a generic bluff body equipped with a 25% length diffuser. The overall dimensions are length of 800mm, width of 400mm and a height of 310mm giving a blockage ratio of 5%.

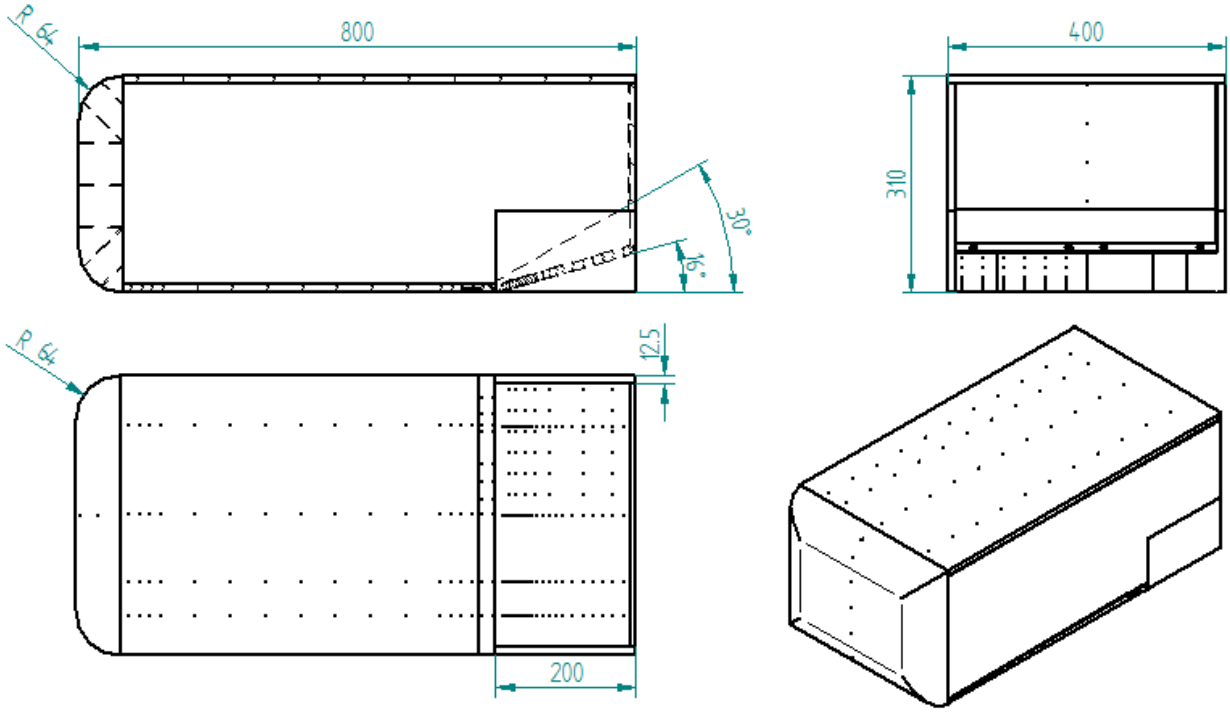

Figure 2.1.1 - Model schematic of plane configuration

The body is a simple bluff body design similar to that used by Cooper et al [16]. The choice of a simple body of this type ensures that the overbody flow is not affected by the geometry changes in the underbody, largely due to the large base area.

The model dimensions were chosen to have a similar length:width:height ratio to that used by Cooper et al [16] to enable a comparison to be made for the force and pressure measurements. A comparison between the two models is shown in . The Reynolds number based on the square root of frontal area and model length at a nominal test velocity of 40ms^{-1} are 9.97x10^5 and 2.27x10^6 respectively. These are consistent with the recommendations in SAE J 1252 Standard [29] that states that a Reynolds number (frontal area) should be around 1.0x10^6.

	Length	Width	Height	Length:Width:Height			Blockage	Re. no. (L)	Re. no. (√S)
Cooper, 1998	0.396	0.212	0.165	2.40	1.29	1.00	4.3%	8.3x10^5	3.98x10^5
Jowsey, 2006	0.800	0.400	0.310	2.58	1.29	1.00	5.0%	2.27x10^6	9.97x10^5

Table 2.1.1 – Comparison of Cooper Model and Jowsey Model

The front radius was chosen based on work done by Cooper et al, to enable flow to be attached and again ensuring that that performance change was not related to effects related to separation around the front edge radius.

The underbody diffuser comprises 25% of the model length which is of comparable size to those used in many racing applications. It is also a size that would be a realistic application on a road car. Using a 25% diffuser also ensured that the diffuser behaviour could be distinguished from that of the flat underbody, upstream of the diffuser inlet. This is particularly important in trying to establish the mechanisms involved in downforce production, especially between the multiple channel diffusers.

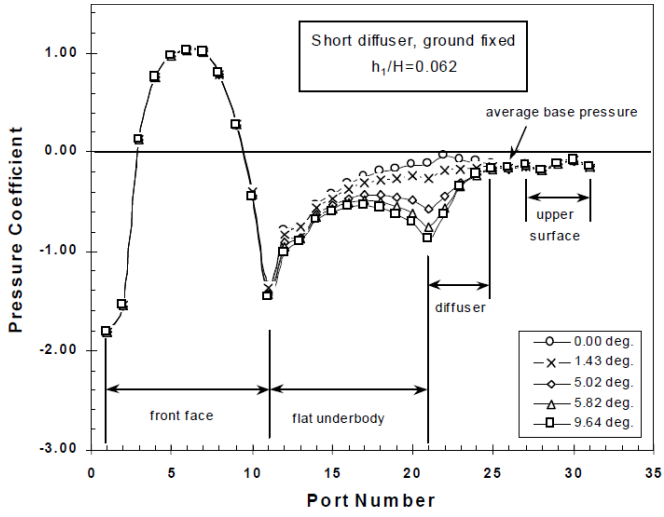

Figure 2.1.2 – Pressure distribution for 25% length diffuser by Cooper et al

To fulfil the need for adjustment of ten diffuser angles, a diffuser plate, of length 200mm, was used, hinged at the inlet using an arrangement (Figure 2.1.3) with a flexible plastic hinge to reduce the likelihood of a backward facing step at different diffuser angles, shown schematically in Figure 2.1.4. The diffuser plate was hinged to a 50mm flat extension which was then attached to the main model body. This whole system is removed for different configurations so that the diffuser inlet remains under the same conditions each time. The flat extension was attached such that if any step was present it was a forward facing step and hence would not cause separation of the underbody prior to diffuser inlet.

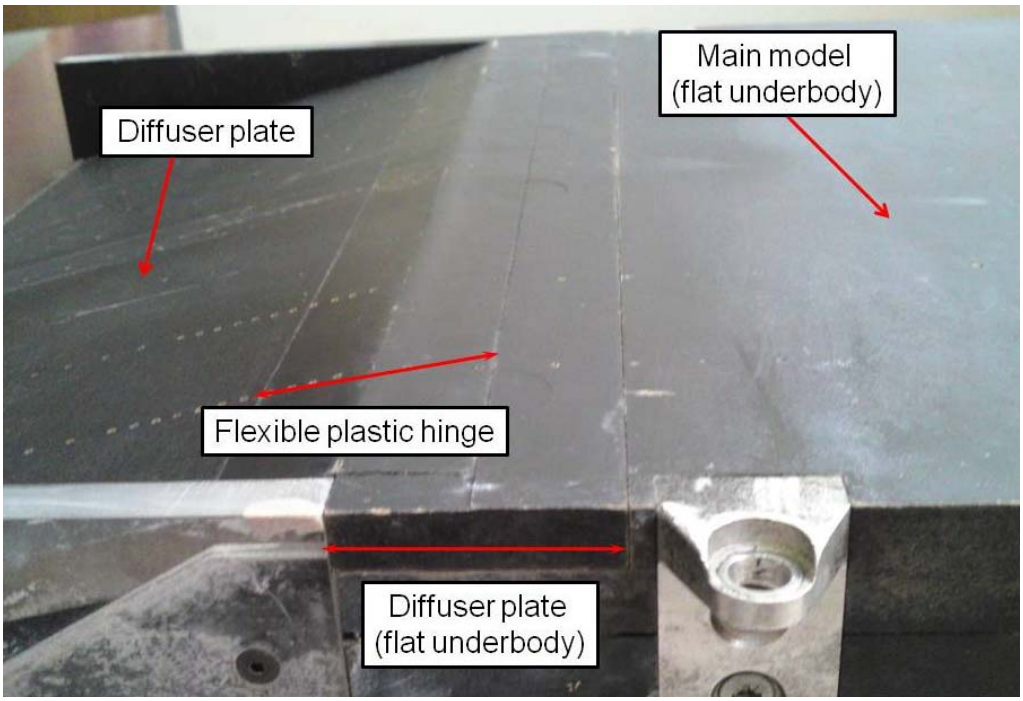

Figure 2.1.3 - Diffuser plate and "hinged" arrangement

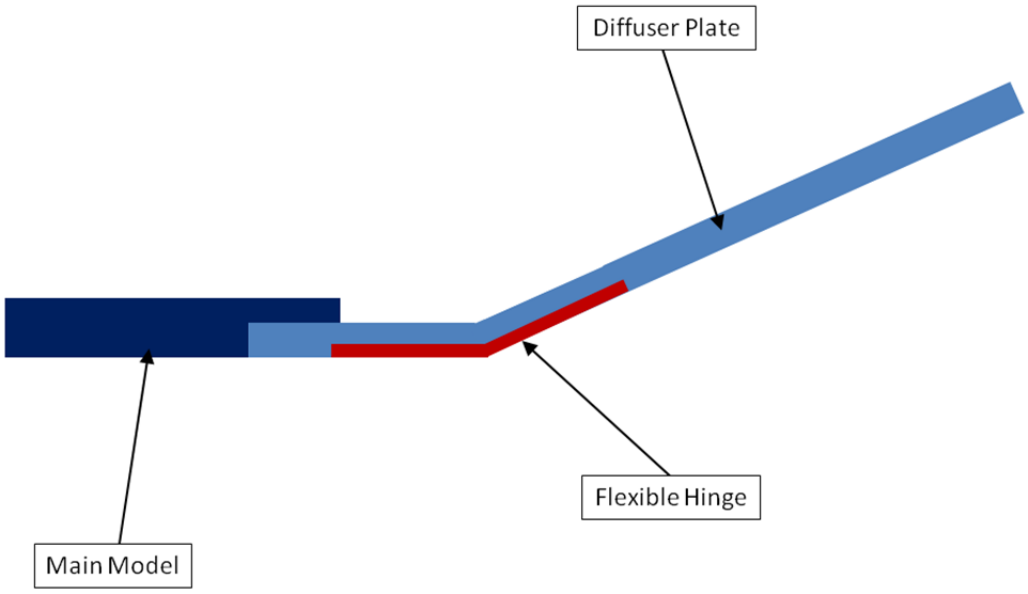

Figure 2.1.4 - Schematic of diffuser plate arrangement

When the diffuser angle is changed, the diffuser plate is set using a screw attachment on each side of the model and to ensure a consistent setup, a positive location is provided for each angle (Figure 2.1.5) via a threaded insert in the diffuser plate arm. For the multiple channel diffusers, each part of the diffuser plate has to be changed individually and has a separate positive location for each part.

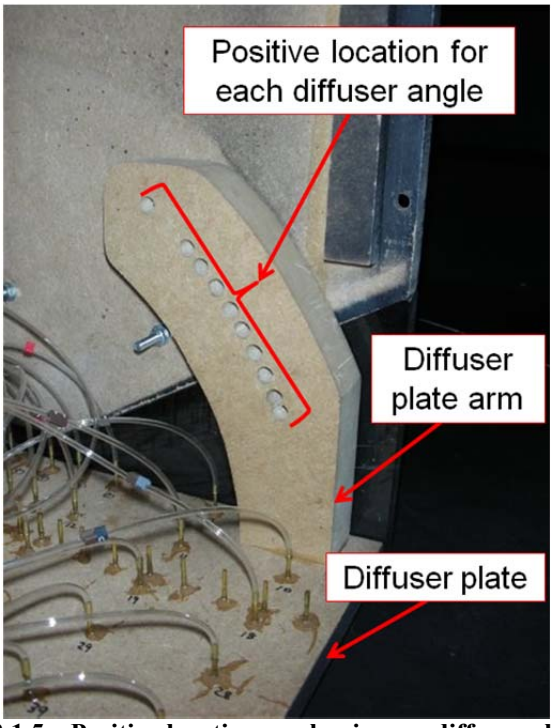

Figure 2.1.5 – Positive location mechanism on diffuser plate arm

At each angle, the back plate of the model is also changed to allow for the change in height of the base section, with the 0° and 25° back plates shown in Figure 2.1.6. Each back is located using a screw mechanism at four points on the rear of the model.

Similarly, at angles above 10°, the diffuser plate was not long enough to reach the back face, so additional pieces are added as shown in Figure 2.1.7. Initial tests were performed with and without tape on the join between the diffuser plate and addons. The results suggested no significant difference between configurations Therefore for improved ease and time of configuration changes, it was decided to run without the addition of tape.

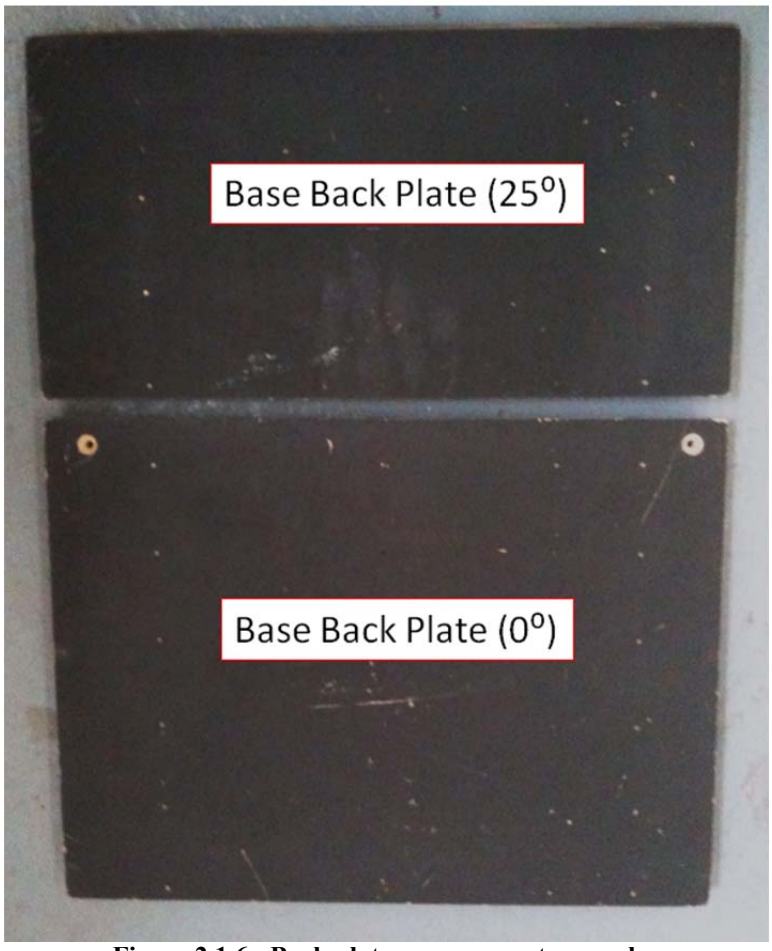

Figure 2.1.6 - Back plate arrangement examples

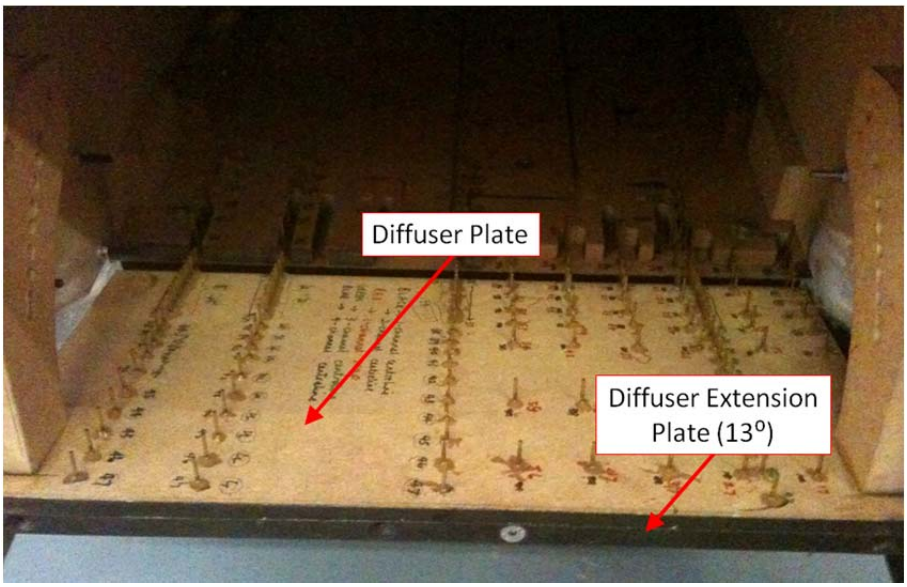

Figure 2.1.7 - Diffuser extender plates arrangement

In the split channel configuration, a "splitter plate" was fixed inside the model, and a split diffuser plate and hinge employed shown in Figure 2.1.8. A similar arrangement is used for the three- and four-channel diffusers. A schematic of the four diffuser configurations is shown in Figure 2.1.9.

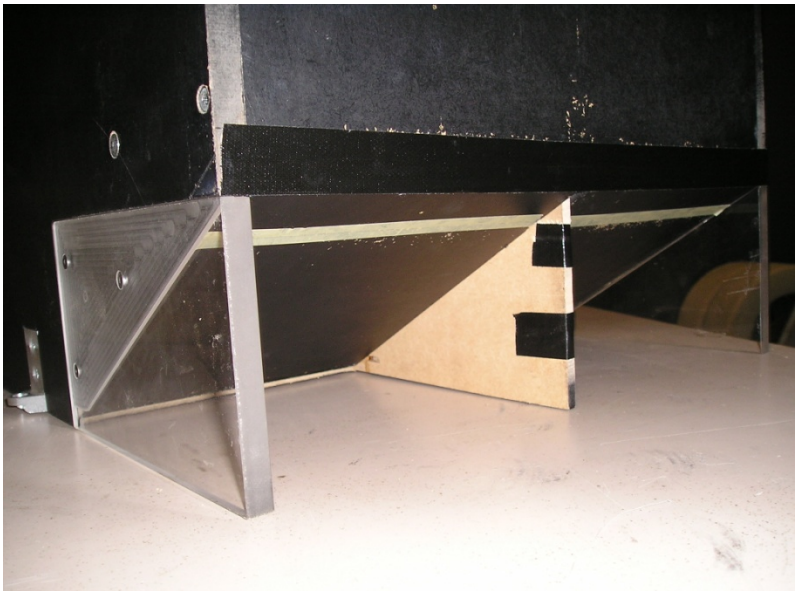

Figure 2.1.8 – Two-channel diffuser plate model configuration

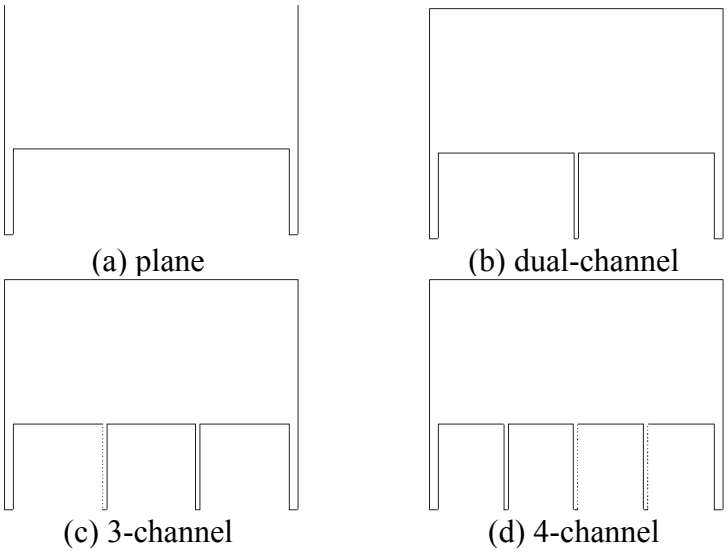

Figure 2.1.9 (a)–(e) – Schematic of different diffuser configurations

Pressure tappings were placed along the model centreline, equivalent to the plane diffuser centreline and is shown in Figure 2.1.10 along with the numbering system used. Tappings 1-9 are on the front face of the model, 10-26 on the flat underbody, 27-47 on the diffuser plate, 48-51 on the model base section and 52-62 on the overbody.

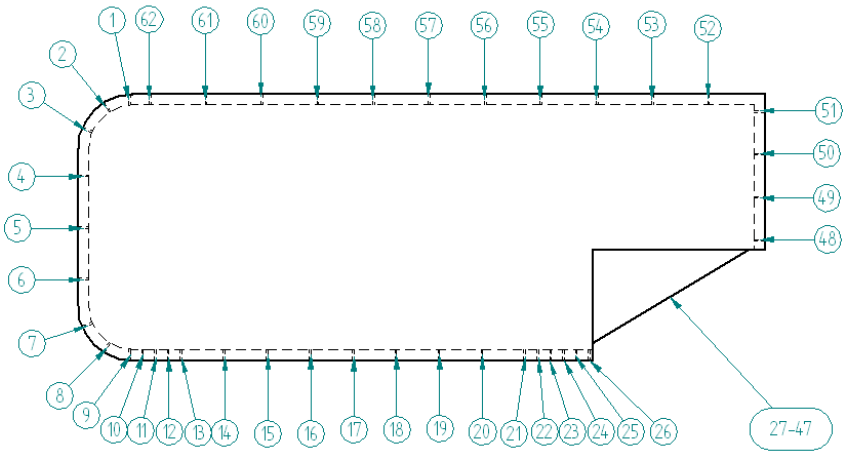

Figure 2.1.10 – Pressure tapping numbering system

In order to make comparisons between plane and multi-channel configurations, the same distribution of tappings in Figure 2.1.10 were placed along the channel centreline positions. These were placed at the model quarterline (two-channel), 1/3 model width (three-channel) and 1/8 model width (four-channel) as shown in .

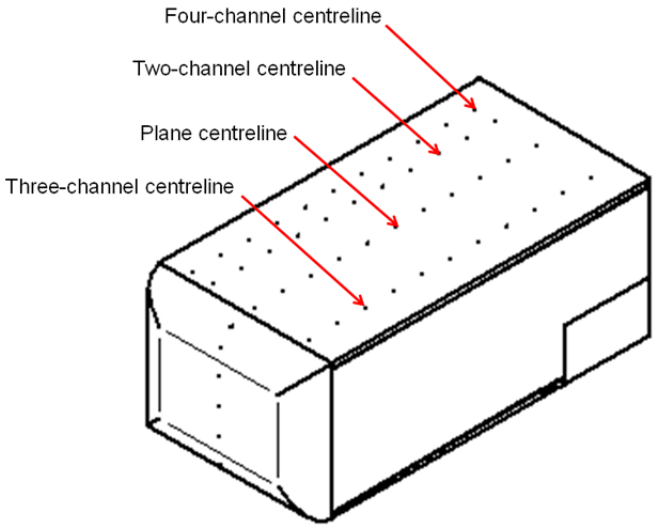

Figure 2.1.11 – Pressure tapping centreline positions for different diffuser channel configurations

The distribution of tappings in the diffuser area are shown in Figure 2.1.12 for plane and multi-channel diffusers. As well as the channel-centreline tappings, additional tappings across a width of each channel were places to investigate the pressure distribution across the diffuser and investigate the vortex structures present in the diffuser channels.

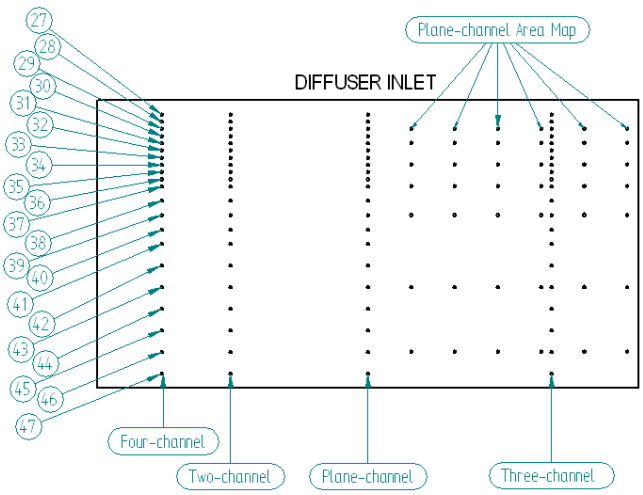

(a) Plane diffuser plate

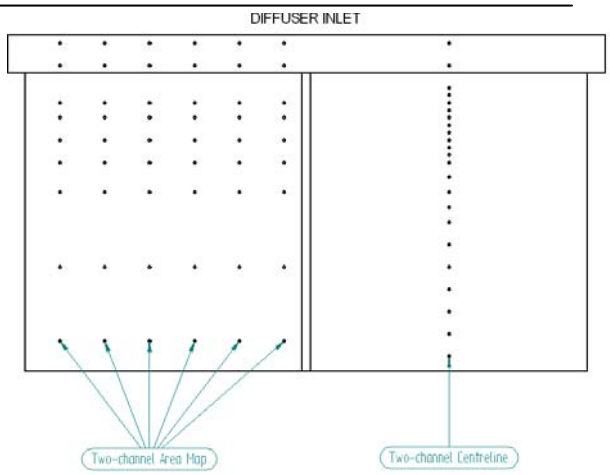

(b) Two-channel diffuser plate

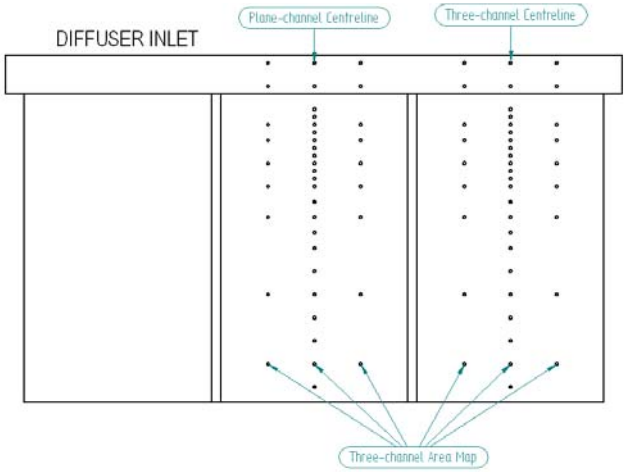

(c) Three-channel diffuser plate

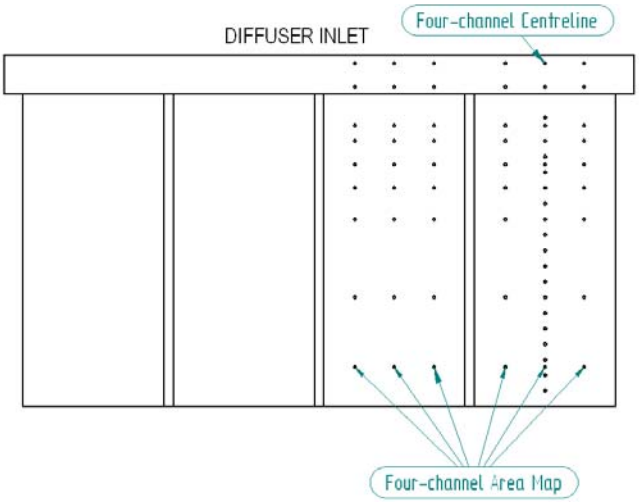

(d) Four-channel diffuser plate

Figure 2.1.12 – Area map pressure tappings

Results will be presented in the form of non-dimensional coefficients as a function of diffuser angle (α), non dimensional ride height, (h_1/H), where H is the overall height of the body, non dimensional diffuser length (N/h_1) and diffuser area ratio given by the equation:

$$Area\ Ratio = 1 + \left(\frac{N}{h_1}\right) tan \propto$$

Equation 2.1.1

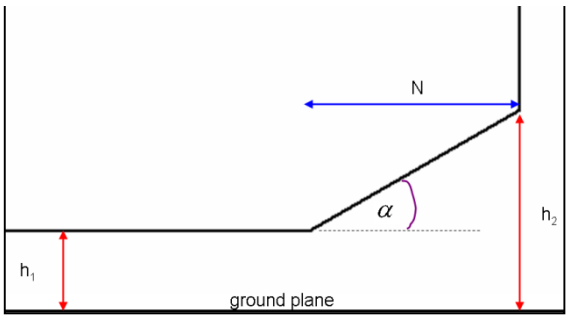

Figure 2.1.13 – Diffuser Geometry

The use of area ratio is advantageous because it takes into account all the variables associated with a diffuser such as ride height (h_1), diffuser length (N) and diffuser angle (α). The initial definition of area ratio is the ratio of the area at exit to the area at inlet, which translates (in the diffuser case) to a ratio of heights as shown in Figure 2.1.13.

$$\text{Area Ratio (AR)} = \frac{A_2}{A_1} = \frac{h_2}{h_1} \qquad \textbf{Equation 2.1.2}$$

From this equation and using the geometry shown in Figure 2.1.13 the final equation for area ratio can be found as shown in Equation 2.1.5.

$$h_2 = h_1 + N \tan \alpha \qquad \textbf{Equation 2.1.3}$$

$$AR = \frac{h_1 + N\tan\alpha}{h_1} \qquad \textbf{Equation 2.1.4}$$

$$AR = 1 + \frac{N}{h_1}\tan\alpha \qquad \textbf{Equation 2.1.5}$$

2.2 Wind Tunnel Description

The experimental programme was performed in the Loughborough University open circuit, closed working section wind tunnel shown schematically in Figure 2.2.1 and fitted with an underfloor 6-component balance and fixed floor. Air is drawn from the outside environment through the inlet, into the contraction with a contraction ratio of 7.4:1 up to the working section which was designed to accommodate a 25% scale passenger car or a 33% scale race car. Dimensions of 1.92m (width), 1.32m (height) and 3.6m (length), with additional corner fillets of 0.15m by 0.15m give a working area of 2.49m^2. A nominal test velocity of 40ms^{-1} is used although the tunnel has an operating range of velocities up to 45ms^{-1}.

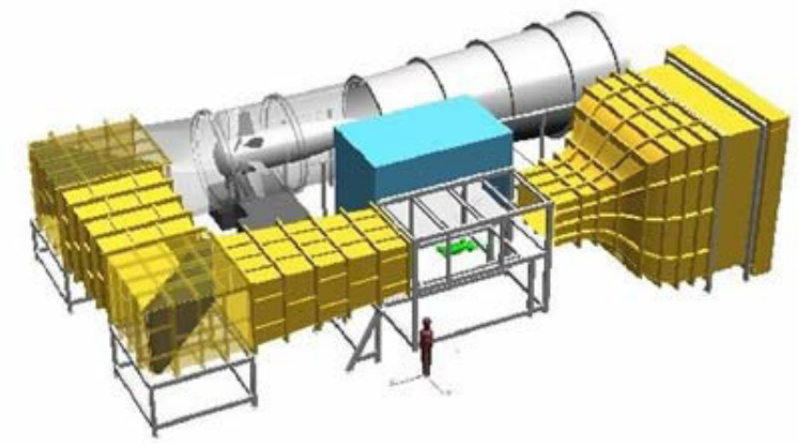

Figure 2.2.1 – Loughborough University Scale Wind Tunnel

The flow quality of the tunnel was reported by Johl [39]. The turbulence intensity was measured as 0.15% at 40ms^{-1}, and a working section velocity uniformity within 0.3% deviation from mean velocity. The boundary layer was found to have a thickness of 60mm, displacement thickness of 9.4mm and momentum thickness of 5.5mm.

2.2.1 Ground Plane Simulation

Given that the Loughborough wind tunnel is not equipped with a moving ground plane and that there has been much debate regarding the ground simulation when performing wind tunnel testing on automotive models. It is appropriate at this point to address the question of using a fixed floor in this study of underbody diffusers. The primary problem with fixed floor is due to the boundary layer development on the floor, similar to that occurring on a flat plate, which exists due to the motion of the flow close to the stationary floor that is not present on the road. The presence of this boundary layer produces an altered velocity profile under the model and interacts with the model's underside boundary layer. This effect is more pronounced the closer the model is to the wind tunnel floor and results produced may vary from the real "on-road" conditions and will be discussed further in Section 2.2.2.

There are many variations of ground plane simulation with some examples shown in Figure 2.2.2. The two main types of simulation used are boundary layer control using suction and/or blowing and a full moving ground plane.

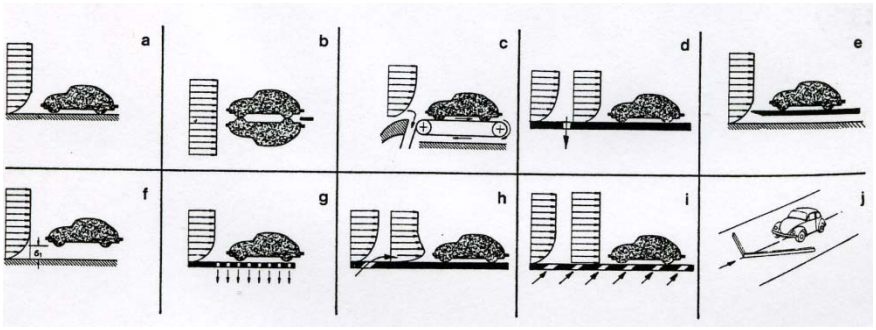

Figure 2.2.2 – Wind Tunnel Ground Simulation Configurations [11]

Boundary layer suction (Figure 2.2.2d and g) is used to remove the low momentum flow and reduce the boundary layer thickness, while boundary layer blowing (Figure 2.2.2h and i) is used to re-energise the boundary layer by blowing high energy air into the flow. The most realistic simulation of on-road conditions is that using the moving ground plane (Figure 2.2.2c). This utilises a moving belt system that either spans the whole working section width (full belt) or the model wheelbase (partial belt) which run at the same speed as tunnel freestream. For a more realistic simulation, rotating wheels in contact with the belt are often implemented.

In an ideal situation, a moving belt system with suction would be used to try and replicate real world scenario. However, as Loughborough University's wind tunnel is not equipped with a moving ground the effects of using a fixed floor with a diffuser-equipped model have been investigated.

2.2.2 Evaluation of Ground Simulation Options

Cogotti [24] performed an investigation into the influence of ground simulation using a modified SAE reference model, equipped with a diffuser. Four different ground simulation configurations were used; moving ground and rotating wheels, moving ground only, rotating wheels only, and fixed ground. It was found that for fixed ground, the increase in drag due to the increase of ground clearance was overestimated while the increase in drag caused by increase of diffuser angle was underestimated. The rear lift was underestimated when using the fixed ground or rotating wheels but overestimated with the moving ground only. It was concluded that if a "complete dynamic simulation" (i.e. moving ground ***and*** rotating wheels) could not be implemented, then the next best solution was probably the completely static condition.

More conclusive and detailed investigations were performed by Howell [21], Cooper, Fediw et al [20], George and Donis [22] Cooper, Bertynyi et al [16].

Howell [21] investigated the influence of ground plane simulation on a diffuser-equipped model with varying backlight angle. He used three different ground simulations; fixed ground, stationary belt and moving belt. It was found that the fixed ground and stationary belt produced very similar results in both drag and lift variation and whilst the variation of lift and drag was similar with the moving belt, the absolute values varied such that it produced higher drag and lower lift. These similarities in drag and lift trends observed were said to be "defined with acceptable accuracy by the stationary belt, and by implication, the fixed ground". It was concluded that, for examining the trends and flow mechanisms of underbody aerodynamics a fixed ground was adequate, but should absolute values for drag and lift be required (for example when developing a real vehicle) then a moving ground simulation is necessary.

Cooper et al [20] tested a vehicle model with three different underbody configurations over four different ground simulations; fixed ground with no boundary layer control, fixed ground with suction and tangential blowing, full-width moving belt and partial belt. Aerodynamic coefficients were compared for all ground simulations. The drag coefficients were observed to increase in a similar fashion with ride height for all ground simulations. Using the fixed ground as a comparison, the use of tangential blowing resulted in a slight increase in drag whereas the use of moving ground resulted in a reduction in drag with the narrow belt producing the least drag. The lift coefficients also produced comparable trends between ground simulations, with the use of moving ground producing reduced coefficients compared to that of the fixed condition. When considering the incremental coefficients, the drag changes were found to be identical within measuring accuracy for all ground simulations whereas the incremental lift coefficients gave identical results for the two moving ground conditions but these varied from the fixed ground simulations. These results support the conclusion by Howell [21] that as the trends observed were comparable, the fixed ground would be adequate for investigations looking at parametric changes.

George and Donis [22] conducted tests using a model with a variety of underbody configurations using both a fixed ground and a moving belt system. They observed differences in magnitude of aerodynamic coefficients for fixed and moving ground simulations, with an increase of between 5 and 15% in lift coefficient and a slightly smaller increase in drag. However, the trends observed were very similar and it was concluded that although the influence of a moving ground is significant, it does not affect the flow qualitatively. Similar to [21] and [20], George and Donis stated that, when investigating the trends and understanding of flows a fixed ground is satisfactory but a moving ground is necessary if absolute data is required.

Cooper et al [16] conducted a thorough investigation into plane automotive diffusers using a simplified bluff body and made useful comparisons of results with and without moving ground plane. They show general trend similarity for both lift and drag coefficients, consistent with [21], [20]. As expected this difference was less pronounced at larger ride heights where the influence of ground interaction is not as significant. Additionally, Cooper plotted loci of optimum diffuser downforce and optimum total (model) downforce for both ground simulations. For the optimum diffuser loci, it shows similar trends but different optimum area ratios for fixed and moving ground; with the fixed floor producing an optimum at a higher area ratio. The loci of optimum total downforce shows similar trends as with the diffuser optimum and for a given area ratio the fixed ground configuration under predicted the downforce by approximately 10%. However, the optimum area ratios are almost identical for both ground simulations. These results reiterate the view that optimising a particular vehicle with a fixed floor may not provide acceptable results for real-world simulations, but that a study that aims to investigate the relationship between diffuser parameters is valid.

The investigation by Senior and Zhang [14] used a diffuser-equipped bluff body undertaking the majority of the experiment using a moving ground plane, but did perform a short fixed ground test. The one result that they present shows similar trends between fixed and moving ground and this is consistent with the work of the other authors discussed. However, they conclude that because the magnitudes are different a fixed floor cannot be used.

2.2.3 Instrumentation and Measurement Techniques

Several different measurement techniques have been employed to obtain data; balance acquired force and moment measurements, pressure measurements, cobra probe measurements and Particle Image Velocimetry (PIV).

2.2.3.1 Underfloor Balance

The tunnel is equipped with a 6-component underfloor balance measuring lift, drag, side force, roll moment, pitching moment and yaw moment with load range basic accuracy shown in Table 2.2.1.

Component	Balance Load Range	Accuracy (% Full Scale)
Lift	±500N	0.010
Drag	±120N	0.005
Side Force	±420N	0.010
Roll Moment	±150Nm	0.010
Pitching Moment	±60Nm	0.010
Yaw Moment	±45Nm	0.015

Table 2.2.1 – Balance load range and accuracy

The model is mounted to the balance via M8 threaded bar, which is attached to magnetised posts on the balance bed. The model sits on lock nuts on the bar, enabling the ride height to be changed by altering the nut height. Forces and moments are then transmitted from the model through the pins and measured by the balance.

Repeatability tests were performed at different times during testing, following a complete removal and reinstallation of the model. The repeatability data is shown in Figure 2.2.3 and Figure 2.2.4 for lift and drag respectively. From these graphs it can be seen that the average repeatability is ±0.005 for C_d and ±0.02 for C_l., although at certain ride heights it was more than this, primarily at lower ride heights where viscous effects may be at work.

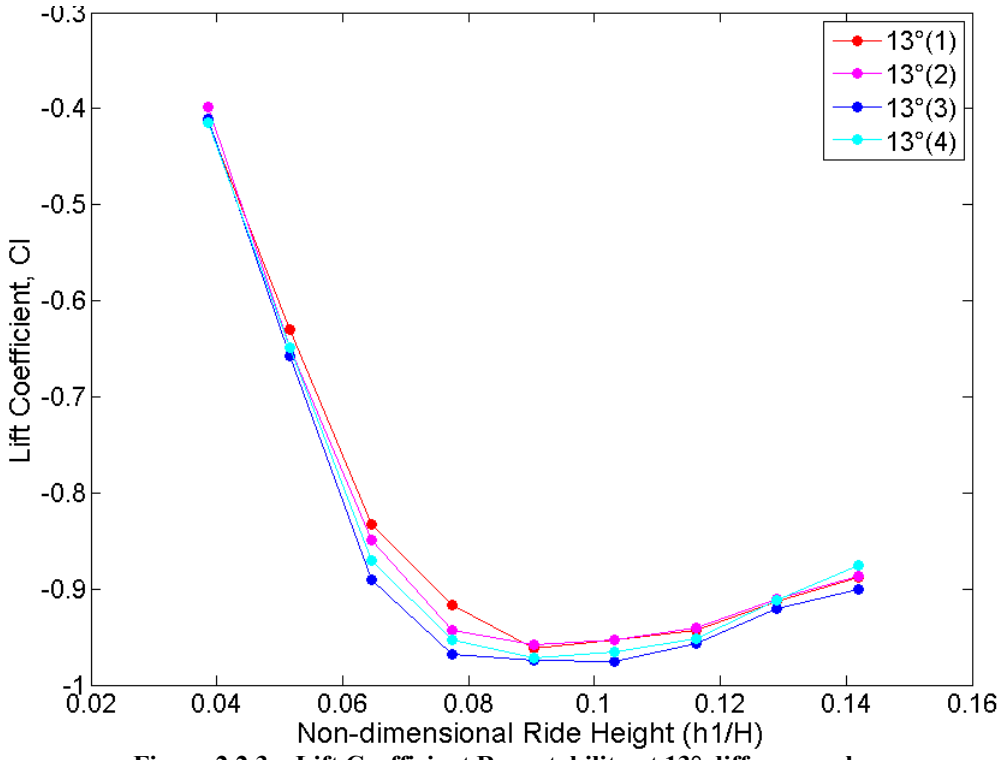

Figure 2.2.3 – Lift Coefficient Repeatability at 13° diffuser angle

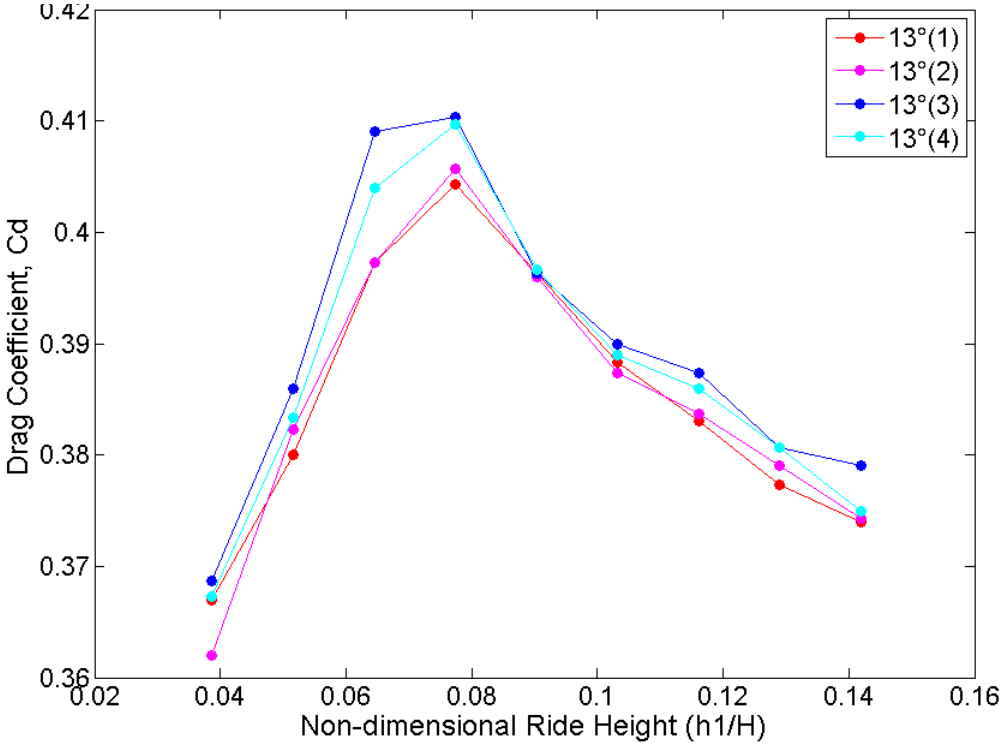

Figure 2.2.4 – Drag Coefficient Repeatability at 13° diffuser angle

2.2.3.2 Pressure Measurements

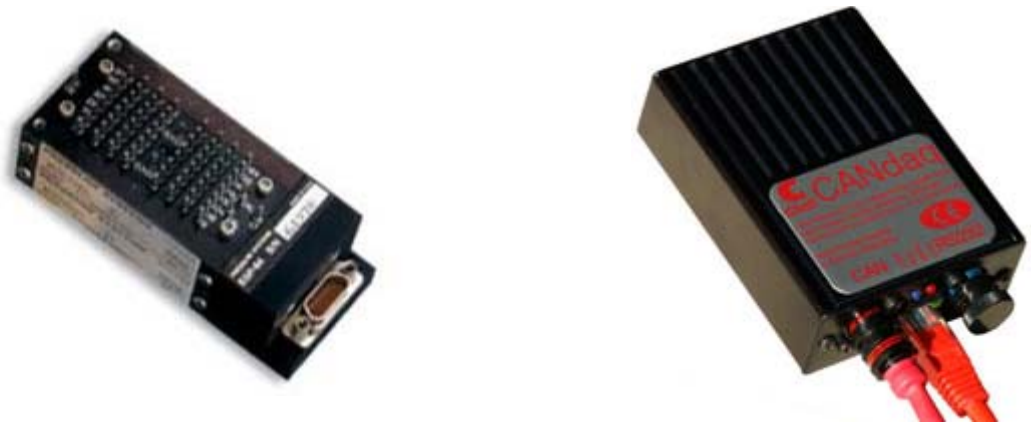

Figure 2.2.5 - PSI DTC 64 channel pressure scanner and CANdaq [30]

To collect pressure data a PSI high speed 64 channel DTC scanner and CANdaq control unit was used as shown in Figure 2.2.5. The scanner consists of 64 pressure transducers that sample the pressure at each point simultaneously, at a required frequency up to a maximum of 300Hz. It calculates the pressure difference relative to a reference static pressure taken from the wind tunnel pitot outputting pressure in millimetres of water. The scanner has a range of ±2kPa (≈232mm of water) with digital temperature compensation, the accuracy stated as ±0.06% of full scale [30] equating to 0.15mm of water.

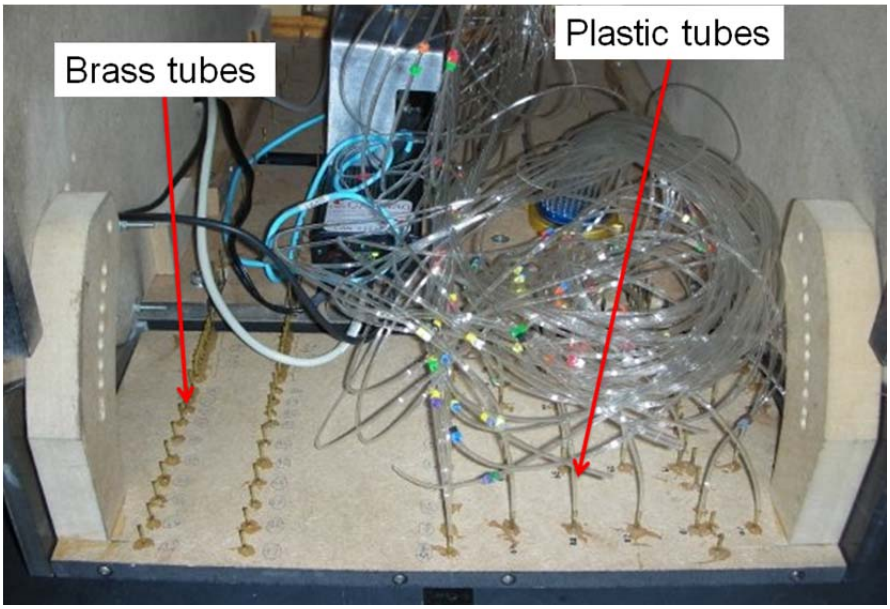

Figure 2.2.6 – Brass and plastic tubing setup

In order to measure the pressure distribution on the model, brass tubes (1.6mm OD/0.9mm ID) were inserted at specified positions flush with the model surface and plastic tubing (2.5mm OD/1.5mm ID) was then used to connect the brass tubes to the tapping disconnect on the scanner as shown in Figure 2.2.6. A schematic of the scanner setup (

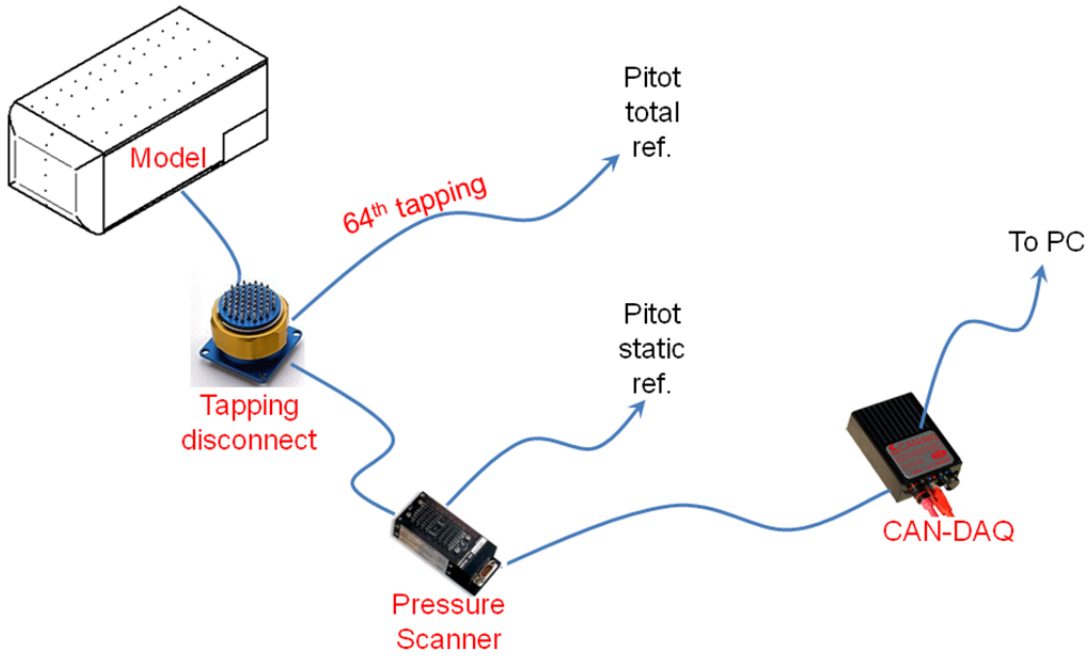

Figure 2.2.7) shows how each of the scanner components are related. All of the equipment is placed inside the model and the diagram is for illustrative purposes. The plastic tubes from the model, are connected to port numbers 1-63 on one side of the disconnect while the 64th port is connected to the wind tunnel pitot total pressure. This enables ease of data manipulation since

measurements from the scanner ports 1-63 need only be divided by the 64th port to obtain pressure coefficient as shown in

$$C_p = \frac{P - P_\infty}{\frac{1}{2}\rho V_\infty^2}$$
$$= \frac{P_{\text{Static}} - P_{\text{Reference}}}{P_{\text{Dynamic}}}$$
$$= \frac{\text{Tapping Data}, P_n}{\text{Tapping 64}, P_{64}}$$

Equation 2.2.1

The other side of the disconnect is attached via plastic tubes to the pressure scanner. A reference static pressure is taken from the wind tunnel pitot and inputted into the scanner reference port. The scanner and CanDaq are connect together and communication between the computer and CanDaq is via a cross-over Ethernet cable.

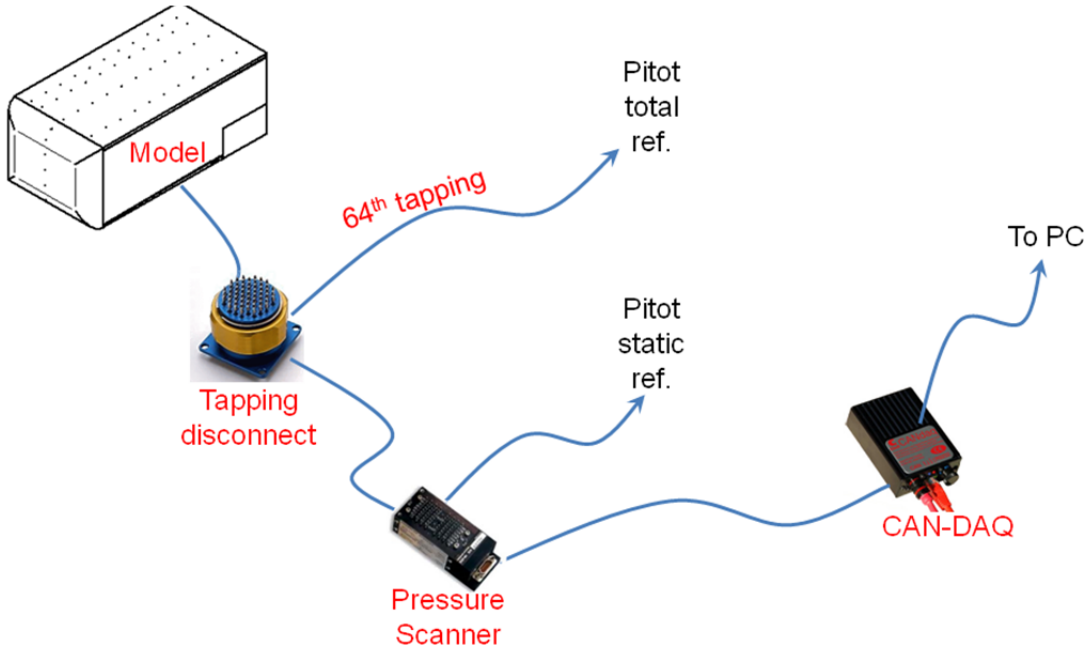

Figure 2.2.7 – Scanner schematic

2.2.3.3 Particle Image Velocimetry (PIV) Measurements

PIV was utilised to investigate the flow structures generated in the diffuser. Details of the setup and results can be found in Section 3.5. The laser used in this experiment was a Nd-Yag New Wave Solo III-15 Laser with a repetition rate of 15Hz and a beam diameter of 4mm. The camera was a LaVision ImagerIntense CCD Camera with 1376x1040 pixels, pixel size of 6.45µm x 6.45

µm, scan rate of 16MHz, controlled by DaVis software. The seeding system used was an olive oil based atomiser system.

PIV is a laser-based measurement technique that uses a dual-pulsed laser firing through optics creating a "light sheet", the size and orientation of which can be manipulated by changing the optic on the front of the laser head. The light sheet is orientated in such a way as to illuminate the plane of interest for a particular experimental setup (Figure 2.2.8). In order for the flow to be examined, it has to be seeded with particles, in this case with an olive oil based atomizer seeding system, with an average particle size of 1µm [32]. The laser then illuminates the particles in the flow allowing a CCD camera to capture images.

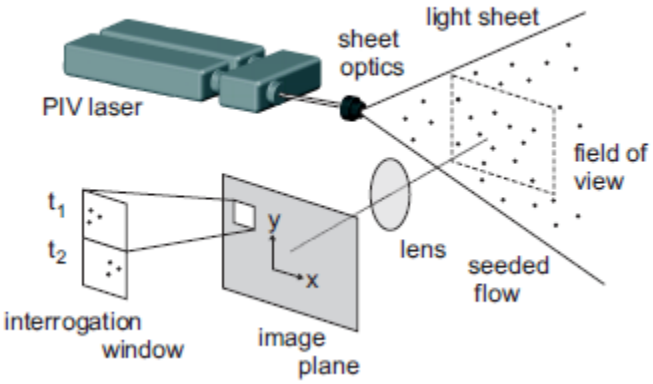

Figure 2.2.8 – PIV example setup [31]

The size of the examined area or Field of View (FoV) is controlled by the size of the lens focal length implemented by the user. In this experiment a 35mm lens was used allowing 2/3 of the model width to be seen so that two of the three diffuser channels in the 3-channel configuration could be examined. This equates to a FoV of about 270x200mm. The camera needs to be situated (ideally) normal to the light sheet, although functions exist in the calibration software for off-axis positioning. During an operation the camera takes two images, one at each laser pulse, resulting in image pairs representative of the flow between a time 't' (at the first pulse) and 't+δt' (at the second pulse) with the time difference named the "inter-frame time". This time is specified by the user and is dependent on experiment setup and wind speed. It has to be significantly short for each image to contain the same flow but long enough for the particles to have shifted a reasonable amount. For a "through plane" setup where the flow is travelling through the light sheet thickness, the inter-frame time can be estimated using:

$$t = \frac{d}{v}$$ **Equation 2.2.2**

Where d is the percentage of light sheet thickness and v is the tunnel wind speed. However, to enable the same flow to be in each image, only a small percentage of the flow should have left the light sheet (e.g. 10%) so the inter-frame time should be based on 10% thickness. An example of images with different inter-frame time is shown in Figure 2.2.9

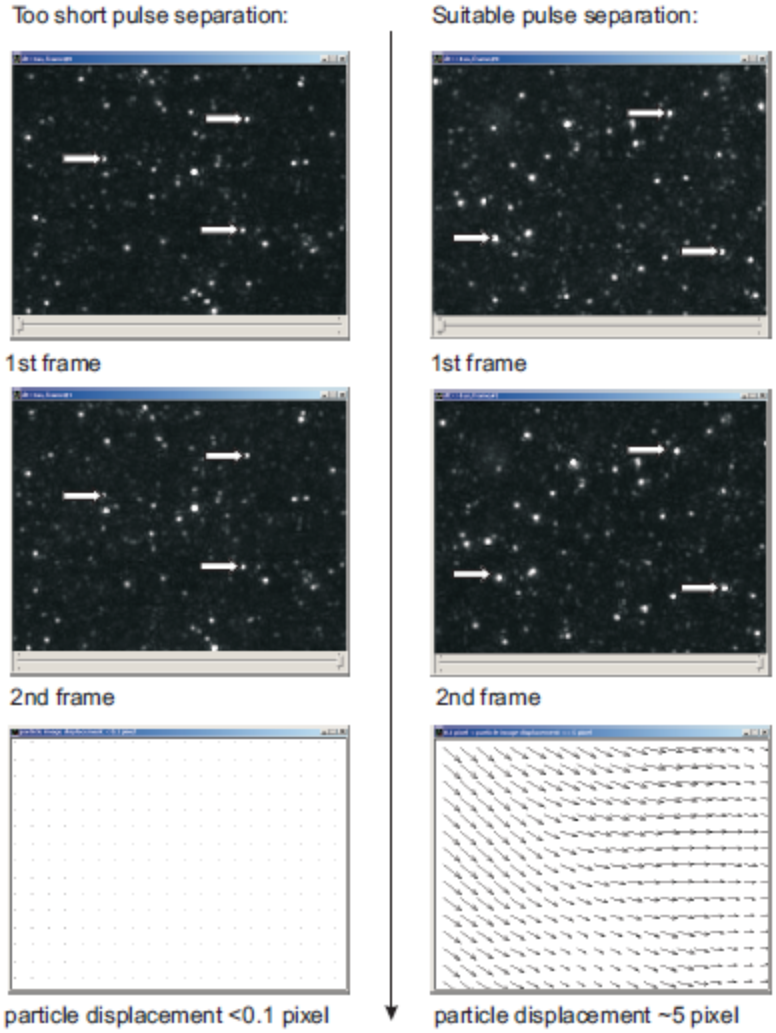

Figure 2.2.9 – Inter-frame time flow example [31]

In order to calculate the velocity vectors a cross-correlation process is used that calculates a vector field from the two single-exposure images. The images are divided into "interrogation cells" (the size of which is defined by the user) and each cell is evaluated using cross-correlation (Figure 2.2.10). The highest peak in each cell is deemed most likely be the displacement vector and a velocity vector map is created using these vectors and the inter-frame time.

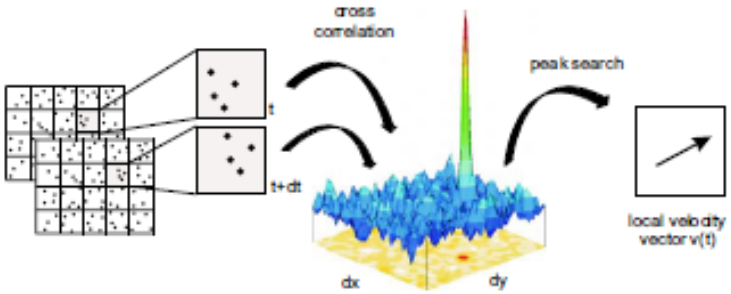

Figure 2.2.10 – Cross-correlation Process [31]

The distance travelled by a particle (used to calculate the vectors) has a maximum threshold magnitude based on the "One Quarter Rule" described by Keane and Adrian [34]. This states that the distance of 'pixel shift' should be less than one quarter of the cell dimension. For example, for an interrogation window size 32x32 pixels the pixel shift should be less than eight pixels. The pixel shift can be tuned by altering the inter-frame time. In a 'through-plane' setup, because the flow travels through the light sheet, the particle displacements in-sheet during the inter-frame time are small. Although this is not ideal, increasing the inter-frame time would result in the particles having travelled completely through the light sheet. However, the smaller the displacement the smaller the relative errors become. For this reason the PIV images are being used as a comparison to each other rather than a magnitude correlation to force and pressure measurements.

Another important parameter is the 'peak locking' factor. This is when the particle displacements across the whole vector field tend towards integer values, which can cause errors in the mean and turbulence statistics. Peak locking tends to occur when the particle size is too small for the sub-pixel curve fitting method. For the Gaussian fit used in DaVis, a particle size of greater than 2 pixels is required to reduce the bias towards integer values.

Figure 2.2.11 shows two example distributions with and without peak locking. The first graph in each column shows how the curve fit is applied, the second is the complete velocity distribution and the third is a histogram of the decimal place of the velocity component, $\overline{V_1}$. This essentially "cuts out the integer value", i.e. V_xV_y = 2.13px becomes V_xV_y = 0.13px. If a distribution was peak locked there would be a greater proportion of the histogram at, or near 0 and 1, represented by a U-shaped distribution shown in Figure 2.2.11. In experimental setups where the overall displacements are small (e.g.± 2pixels) the $\overline{V_1}$ histogram can falsely suggest the distributions are peak locked. In these situations, the complete velocity distribution and a $\overline{V_{0.5}}$ histogram need to be examined. The $\overline{V_{0.5}}$ histogram is similar to the $\overline{V_1}$ except that it covers decimal places 0-0.5,

i.e. as well as removing the integer value, it subtracts 0.5px and calculates the modulus. This gives a more accurate evaluation of distributions with small particle shifts.

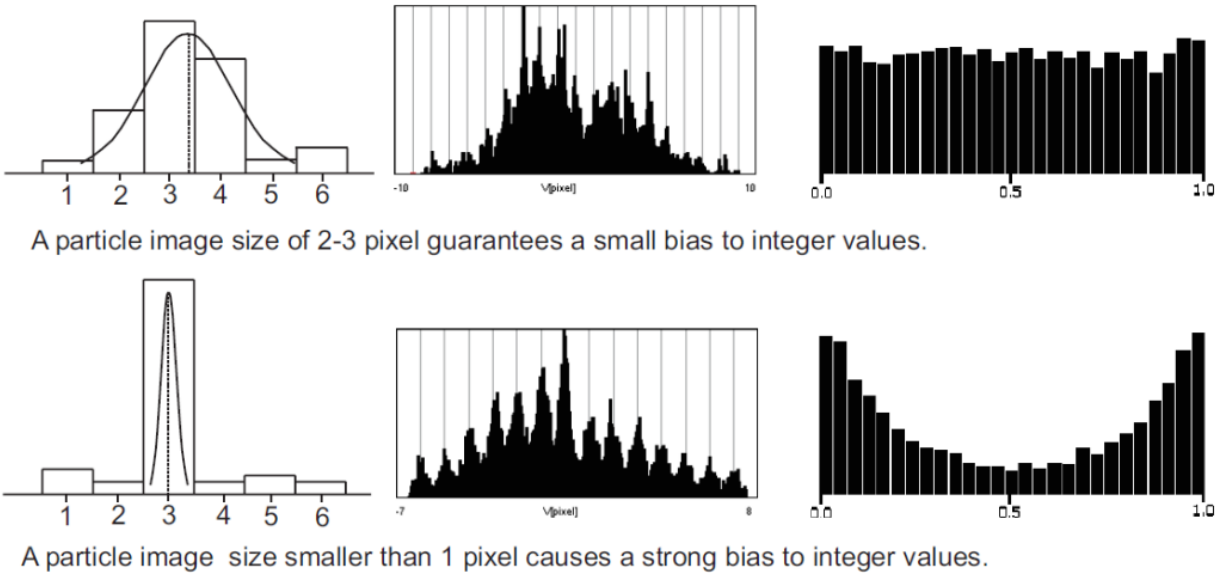

Figure 2.2.11 – Peak Locking example [31]

When processing the vectors using the cross-correlation process, several other factors need to be taken into account such as interrogation cell size, number of passes, window overlap as well as the filters and statistics to improve the quality of the data. The interrogation cell size changes the amount of vectors created in the field of view, such that for each cell, one vector will be defined. For example, for an image size of 1280x1024 pixels with an interrogation cell size 64x64 would be divided into 20x16 interrogation cells (assuming 0% overlap) giving 320 vectors. With a smaller cell size of 32x32 pixels there would be 40x32 cells and 1280 vectors.

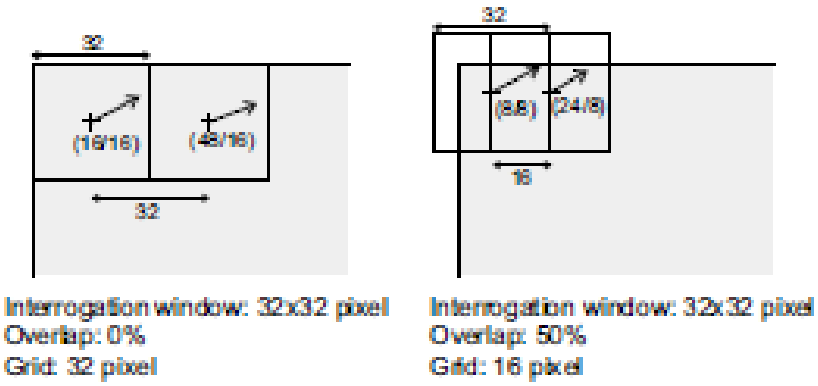

Figure 2.2.12 – Window overlap example of 50% [31]

The window overlap defines the overlap between an interrogation cell and its neighbours, an example of 50% overlap is shown in Figure 2.2.12. Using the 32x32 pixel example in Fig Above, using a 50% overlap would result in a smaller grid size of 16x16pixel, and the first (top left)

vector would now be positioned at (8,8) equivalent to half the grid size. This would result in 4988 vectors therefore increasing spatial resolution and accuracy of vectors.

An additional way of improving the quality of the data is to use adaptive multi-pass processing. This uses several passes with decreasing interrogation cell size; the size, number of passes and window overlap are defined by the user. The first pass with the initial interrogation cell size produces a reference vector field. The second pass has a window size half that of the first and the interrogation cell is adaptively shifted based on the vector calculated in the first pass. This process is summarised in Figure 2.2.13 and is used to calculate the vector more accurately by ensuring that the correlation is performed on the same particles even when a small cell size is used where less particles enter or exit the cell. This improves the spatial resolution of the vector and helps to reduce the number of spurious vectors.

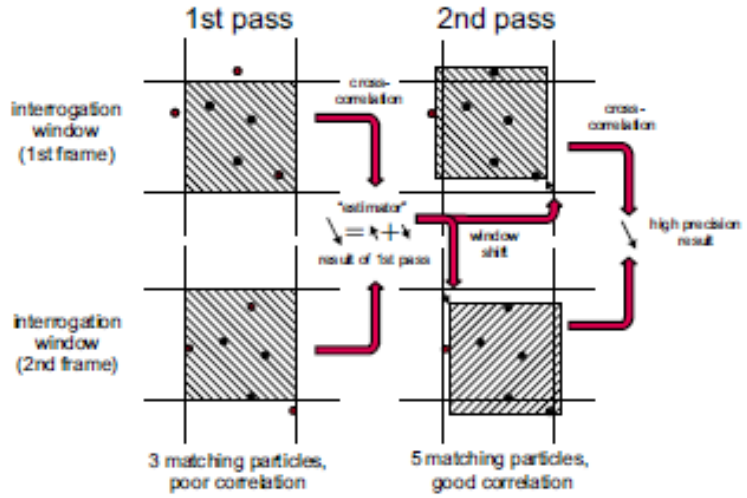

Figure 6.9: Adaptive multi-pass with constant interrogation window size.

Figure 2.2.13 – Adaptive Multi-pass Processing [31]

Post-processing has an important role in ensuring quality data and to reduce spurious vectors. The two main post-processing used in this experiment were Q-factor and median filter. The Q-factor or "Peak Ratio" is a ratio of the 1st and 2nd correlation peaks (Figure 2.2.14) defined in Equation 2.2.3 where P_1 = 1st peak and P_2 = 2nd peak. In general Q-factors above 1.5-2.0 give confidence in the vector [31] but ratios close to 1 suggest that the highest peak is a "false random peak".

$$Q = \frac{P_1 - min}{P_2 - min} > 1 \qquad \textbf{Equation 2.2.3}$$

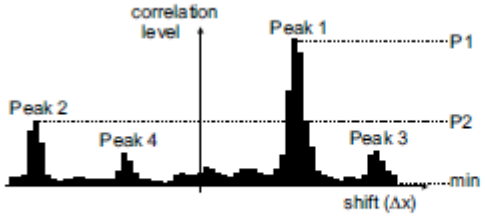

Figure 6.17: Peak ratio or Q-factor.

The peak ratio factor Q is defined as $Q = \frac{P1-min}{P2-min} > 1$,

Figure 2.2.14 – Peak Ratio [31]

The median filter calculates a 'median vector' based on the eight neighbouring vectors and then compares it to the middle vector (Figure 2.2.15) which is rejected if it is outside the allowed range shown in Equation 2.2.4 where U_{median} (or V_{median}) = median value of all U (or V) components of neighbouring vectors and U_{rms} (or V_{rms}) = deviation of U (or V) components of neighbouring vectors.

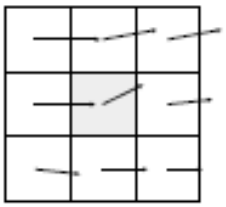

Figure 6.18: Local median filter.

Figure 2.2.15 – Median Filter [31]

$$U_{median} - U_{rms} \leq U \leq U_{median} + U_{rms}$$
$$V_{median} - V_{rms} \leq V \leq V_{median} + V_{rms}$$

Equation 2.2.4

Chapter 3 - Plane Diffuser Performance

In this chapter the results are presented from initial experiments using the plane diffuser configuration only. These comprise force, pressure and PIV results which will be compared against published data and used as baseline measurements for comparison with the multi-channel diffusers in Chapter 4.

3.1 Reynolds Number Sensitivity

The decision to use a simplified bluff body ensures that the results from the diffuser study have general applicability. Using this type of simple geometry can also avoid generating Reynolds number sensitivity that might arise if there is significant detail on the model.

To check that the model once equipped with the diffuser is not over sensitive to Reynolds number, a sweep was conducted by running the tunnel from $5ms^{-1}$ to $45ms^{-1}$ in steps of $2.5ms^{-1}$. This corresponds to a Reynolds number range of $3.16x10^5$ to $2.52x10^6$ based on model length. The results are shown in Figure 3.1.1 - Figure 3.1.3 for all diffuser angles at a single ride height of 44mm ($h_1/H = 0.1419$).

There is some variation in lift coefficient with Reynolds number for all diffuser angles, through they do settle to reasonably stable values for Reynolds numbers above $2x10^6$. This is consistent with the SAE J1252 Standard recommending automotive model testing should be conducted at Reynolds numbers above $1x10^6$ based on the square root of frontal area as $2x10^6$ corresponds to $0.96x10^6$ based on frontal area.

Two configurations (22° and 25°) show large Reynolds number sensitivity in the range tested suggesting a large change in separation characteristics as the Reynolds number is increased. This could be due to changes in the boundary layer conditions, such that these angles are on the transition between fully attached and partially separated, and hence are more Reynolds number sensitive.

Many of the configurations show a small progressive increase in downforce with increasing Reynolds number, this may be a consequence of the fixed floor boundary layer thinning with increasing Reynolds number, allowing improved underbody flow.

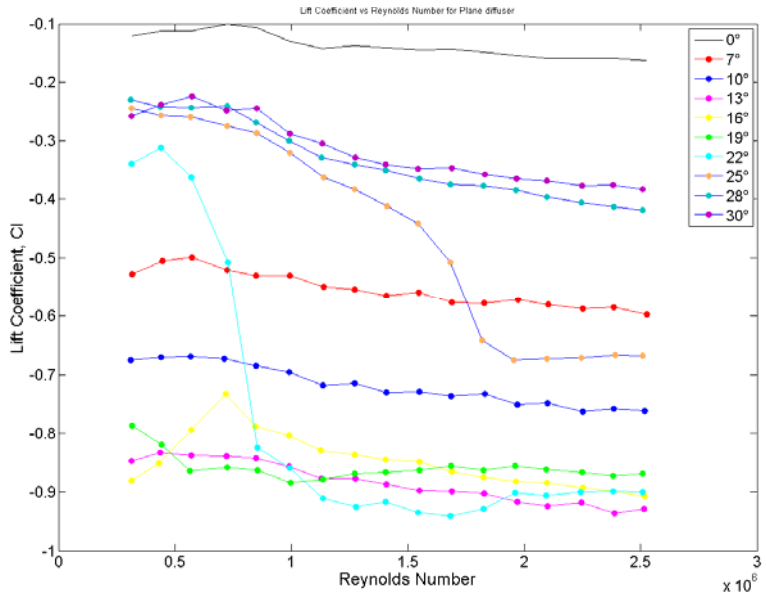

Figure 3.1.1 - Graph of Lift Coefficient vs. Reynolds Number (based on length) for Plane diffuser

The variation of front and rear lift are shown in Figure 3.1.2 and Figure 3.1.3. There is some variation in lift coefficient with Reynolds number for all diffuser angles with the rear lift showing similar trends to that of the overall lift. The point at which the values stabilise occurs at 2.125x106 and 1.8x106 compared to around 2.0x106 for the overall lift. This highlights that the rear lift is more Reynolds sensitive, due to the presence of the diffuser and the changing adverse pressure gradient affecting the boundary layer development and separation characteristics.

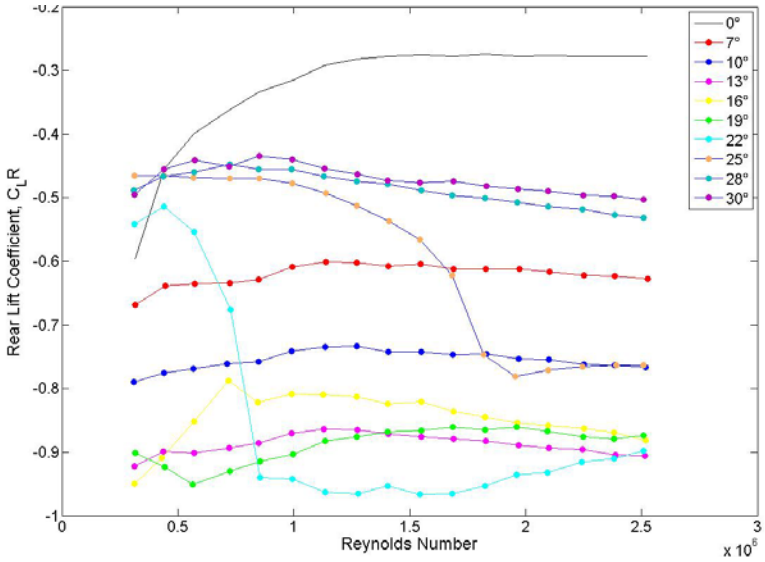

Figure 3.1.2 - Graph of Rear Lift Coefficient vs. Reynolds Number (based on length) for Plane diffuser

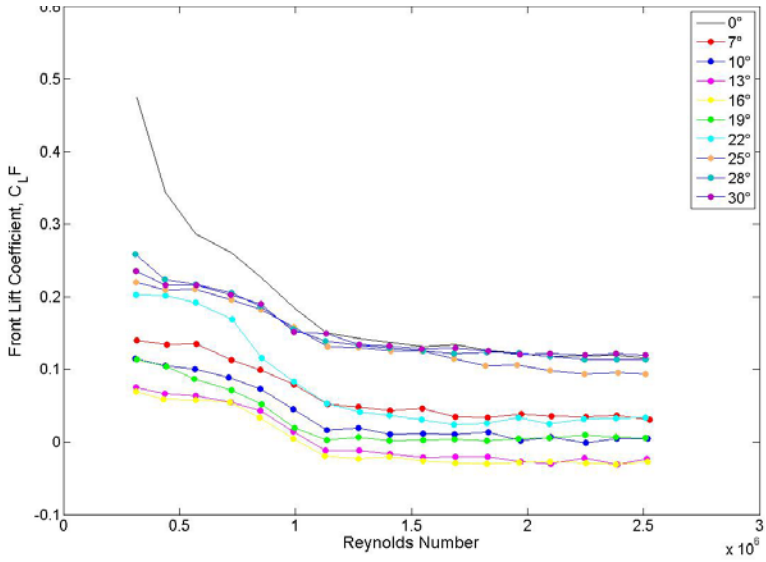

Figure 3.1.3 - Graph of Front Lift Coefficient vs. Reynolds Number (based on length) for Plane diffuser

In order to further examine the Reynolds sensitivity of the different diffuser angles, the lift coefficient was plotted against diffuser angle for a fixed Reynolds number, as shown in Figure 3.1.4. There is some variation in lift coefficient with diffuser angle for all Reynolds numbers. For most Reynolds numbers, the variation is similar for a fixed diffuser angle at low angles. As the diffuser angle is increased further (around 16°) the lift variation increased. Two configurations (22° and 25°) show the greatest variation in lift coefficient highlighting their Reynolds sensitivity over the speeds covered here. These configurations are the same as those identified in Figure 3.1.1 as exhibiting Reynolds sensitivity.

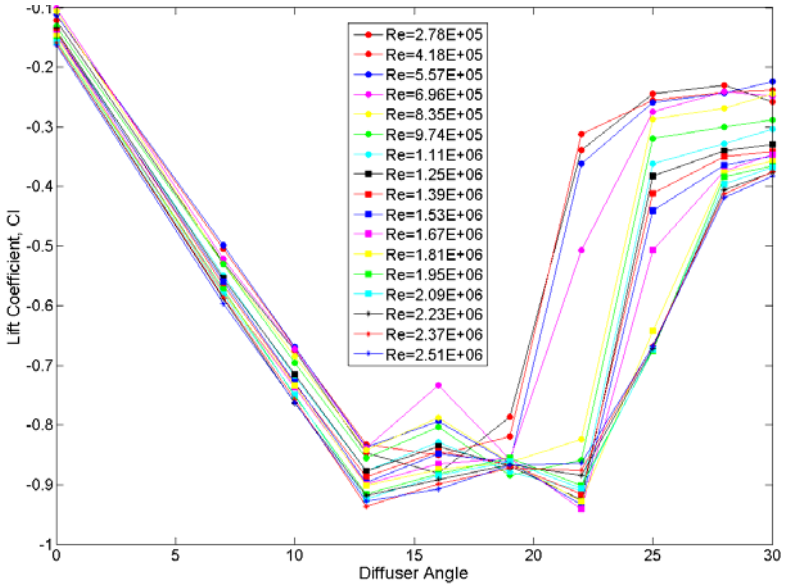

Figure 3.1.4 - Graph of Lift Coefficient vs. Diffuser Angle for Each Length-based Reynolds Number for Plane Diffuser

3.2 Yaw Tests

In real world applications, vehicles do not only run at zero yaw angle due to the ambient wind conditions, and in racing applications there may be significant slip angle. For this reason, the variation of several aerodynamic coefficients; lift coefficient (C_L), drag coefficient (C_D), side force coefficient (C_Y), roll moment coefficient (C_{MX}), pitching moment coefficient (C_{MY}), and yaw moment coefficient (C_{MZ}) with yaw angle is shown in Figure 3.2.1 for a 10° (a) and 28° (b) diffuser angle to represent a low and high angle diffuser.

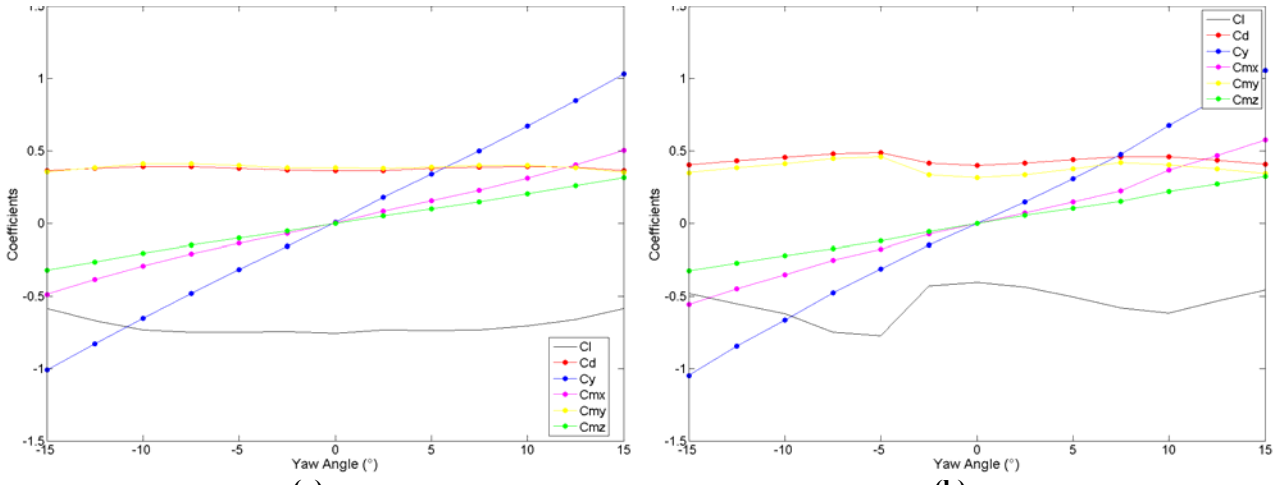

(a) **(b)**

Figure 3.2.1 - Graph of coefficients against Yaw Angle for (a) 10° and (b) 28° plane diffuser

At 10° diffuser angle there is no variation in coefficients between ±5° yaw and only a small variation in lift between ±5° and ±15° yaw, with all variation symmetrical about zero yaw. All

low angles (0°-13°) exhibit this behaviour, attributed to the fact that these angles are thought to be largely attached with small vortex structures and hence the presence of cross-flow through increased yaw angles doesn't affect the flow development. Only at large values of yaw, where it is assumed that asymmetry in flow causes a reduction in lift coefficient.

As the diffuser angle is increased (16°-22°, not shown) the coefficient variation is still symmetrical about zero yaw but peaks at ±5° are observed signifying a Reynolds number sensitivity and change in lift coefficient. This can be attributed to the fact that these angles are assumed to be in a range of attachment to partial separation.

At 28°, representative of the large diffuser angles (25°-30°) the variation becomes less symmetrical with peaks observed at ±5° and ±10° suggesting that the angles are not consistently affected by the cross flow due to separation present.

3.3 Lift and Drag Variation

An initial investigation was undertaken using a plane diffuser configuration in order to establish a set of baseline measurements that could be compared with both previously published data and further diffuser configurations. Figure 3.3.1 shows the variation of lift coefficient with non-dimensional ride height for all the ten diffuser angles tested.

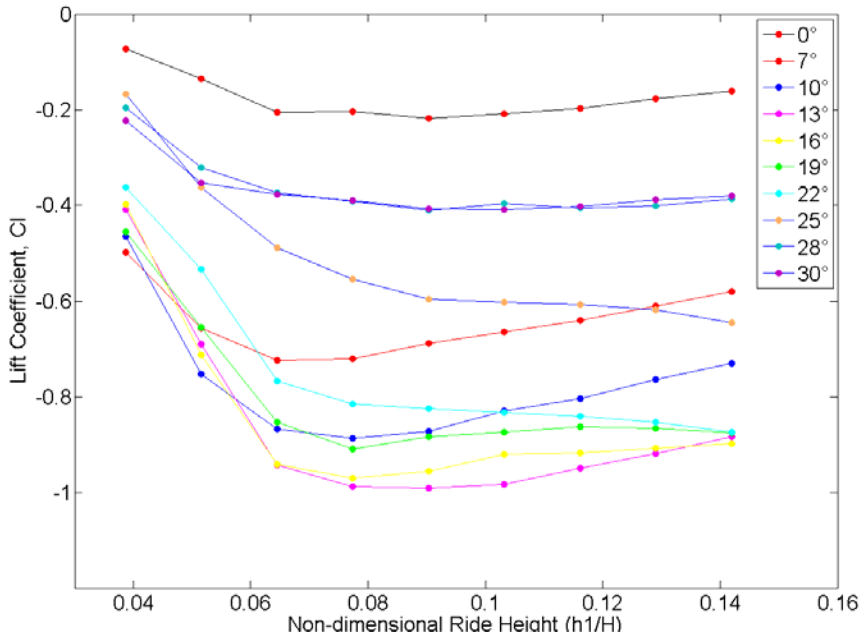

Figure 3.3.1 - Graph of lift coefficient against non-dimensional ride height for plane diffusers

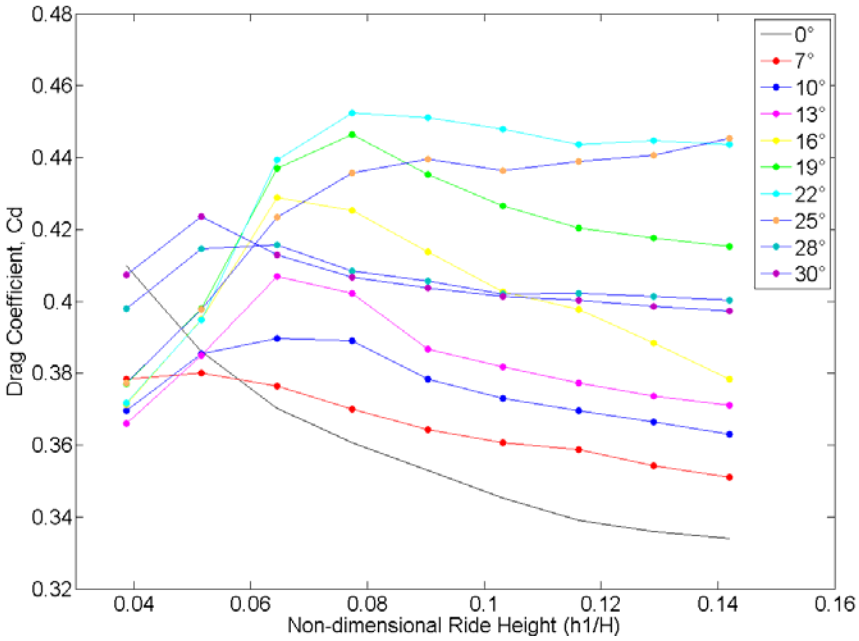

Figure 3.3.2 - Graph of drag coefficient against non-dimensional ride height for plane diffusers

All diffusers show a general trend of increased downforce with decreasing ride height to a maximum, followed by a sharp decrease. This decrease is attributed to close ground proximity where the boundary layer is a large proportion of the ride height and so viscous effects reduce underbody flow, reducing downforce as observed by [16] and [14]. This is supported by the drag variation where relatively low levels of drag are observed compared with higher ride heights, suggesting that large levels of separation aren't present, and the large downforce reduction is due to lack of flow.

As the diffuser angle is increased from the flat floor (0°), an increase in downforce is observed to a maximum at 13°, the increase in drag in the same range is attributed to an increase in strength of the vortex pair shown in [14]. Angles between 16° and 22° show a progressive decrease in downforce, suggesting separation of the flow at the diffuser inlet as the local longitudinal pressure gradient becomes more severe. Flow visualisation by [14] identified a separation bubble present in similar conditions. The progressive reduction arises as the separation bubble grows and consequently the reattachment length increases. This is supported by the drag variation, as increased levels of drag are observed in this angle range with a maximum at 22°. The increased drag arises from increased strength of the vortex structures as well as the increased separation. As the diffuser angle is increased further to 25°, both downforce and drag are reduced as the centreline separation is assumed to no longer reattach, and only a weak is vortex present. At 28° and 30°, the diffuser is completely stalled with much reduced drag and downforce, the two

configurations producing very similar results. The downforce remains significantly higher than for the flat floor as the underbody upsweep continues to contribute.

The minimum downforce is seen with the flat-floor configuration which despite having no diffuser still produces downforce with a lift coefficient of -0.2, the negative value can be attributed to the proximity to ground. To put this into context, results from full scale testing in the MIRA wind tunnel showed a 2007 Ford Fiesta and a 2008 Ford Mondeo to have lift coefficients of 0.124 and 0.221 respectively. The ride height range used in the following experiments is between 4% and 14% of the total body height. Cooper et al [16] demonstrates zero lift at h1/H=0.6 (60%), and as the diffuser angle was increased the ride height at which the maximum lift coefficient was observed to increase. The plot shows that lift coefficient increases, due to only being at a maximum of 14% body height. As higher angles are examined here it could be expected that at only 0-14% body height these angles would not have reached their maximum C_L.

The 13° diffuser produces the greatest downforce with a lift coefficient of around -1. This represents a significant amount of downforce when considering that an aerodynamically optimised racing car that includes a diffuser, front and rear wings and an optimised overbody would typically produce a coefficient of about -3 [8].

The general downforce variation with changing ride height is observed as an increase in downforce with decreasing ride height until $h_1/H = 0.0387$ to 0.0516. At these low ride heights viscous effects associated with close ground proximity are much more pronounced. For example, the displacement thickness in the working section is 9.4mm [39] and is therefore 78% and 59% of the ride height respectively. This essentially chokes the underbody flow as seen by [14] and [16] and consequently a large reduction in downforce is observed.

A simple comparison of results with that published by Cooper et al [16] is shown in Figure 3.3.3. The tests here are conducted at slightly different diffuser angles so the comparison is limited to the overall lift coefficient for five angles that are sufficiently close for comparison.

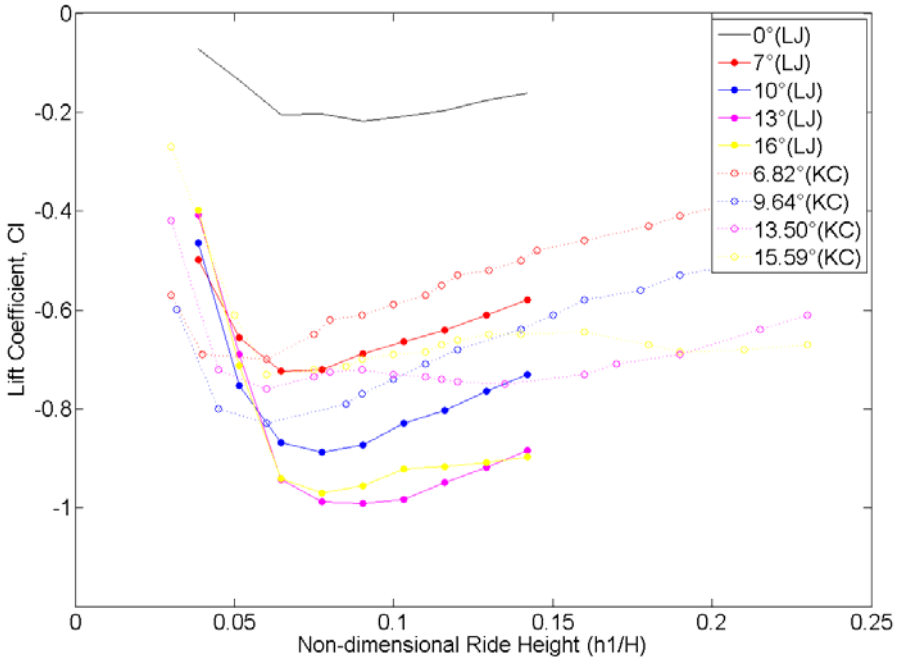

Figure 3.3.3 – Comparison graph of lift coefficient against non-dimensional ride height for plane diffusers and Cooper data

The measured diffuser characteristics compare well to those reported by Cooper et al. The general trend of lift coefficient is almost identical with a progressive increase in downforce with reducing ride height until the optimum is reached, below which the viscous effect reduces the underbody flow. Additionally, the gradients of the curves are almost identical. The primary difference is that the optimum downforce reported here occurs at higher non-dimensional ride heights than those reported by Cooper et al. This arises because the model, tunnel and blockage ratios are different and the onset boundary layers are unlikely to be the same.

The four downforce regions observed by Senior and Zhang [14] of 'downforce enhancement' ($h_1/H \geq 0.192$), 'maximum downforce' ($0.15 \leq h_1/H < 0.192$), 'downforce reduction' ($0.08 \leq h_1/H < 0.15$) and 'low downforce' ($h_1/H < 0.08$) were not repeated identically in Figure 3.3.1, and the ride height regions at which the different regions were observed did not correlate. Although a less broad range of ride heights were tested here, all angles exhibited 'maximum downforce', 'downforce reduction; and 'low downforce' with the addition of 'downforce enhancement' observed for the low angles. When comparing the region d ($h_1/H < 0.08$) in [14] with the corresponding ride height region in Figure 3.3.1, it shows markedly different results. This region was identified as 'low downforce', whereas in Figure 3.3.1 it covers the 'low downforce' region and the majority of the 'maximum downforce' region. This difference can be attributed to the differences in the model, particularly the length:width:height ratio as described in Table 3.3.1.

	Length (m)	Width (m)	Height (m)	L:W:H Ratio	Blockage (%)	Re (L)	Re (√A)	Diffuser Length (%)
Jowsey	0.800	0.400	0.310	2.58:1.29:1.00	5%	$2.27x10^6$	$9.97x10^5$	25
Zhang et al	1.315	0.314	0.324	4.06:0.97:1.00	3.2%	$1.8x10^6$	$4.5x10^5$	41

Table 3.3.1 – Comparison of Zhang Model and Jowsey Model

The Zhang model has a length:width:height ratio much larger than that in [16] and this investigation. Additionally, the diffuser length is 41%, one and a half times larger than the other models. As Cooper et al found that the majority of the downforce is due to the flat underbody, the influence of the length of this flat area as well as the diffuser can change the pressure recovery distribution which ultimately changes the downforce distribution. The influence of the length of the diffuser also changes the longitudinal pressure gradient. Cooper et al found that longer diffuser lengths do not allow the pressure recovery on the flat underbody to develop properly before the diffuser inlet. This increases the adverse pressure gradient at, and after the inlet, changing the separation characteristics. These differences could explain the differences observed between the different investigations which make a direct comparison difficult.

The drag coefficient is plotted against diffuser angle in Figure 3.3.4, for the 32mm ride height (h_1/H=0.1032). The drag increases with increasing angle up to 22° above which a reduction is observed before no significant variation between 28° and 30°. This is very similar to the behaviour widely reported for investigations of slant angle by Ahmed [18] Howell [21] and Strachan [56] amongst others.

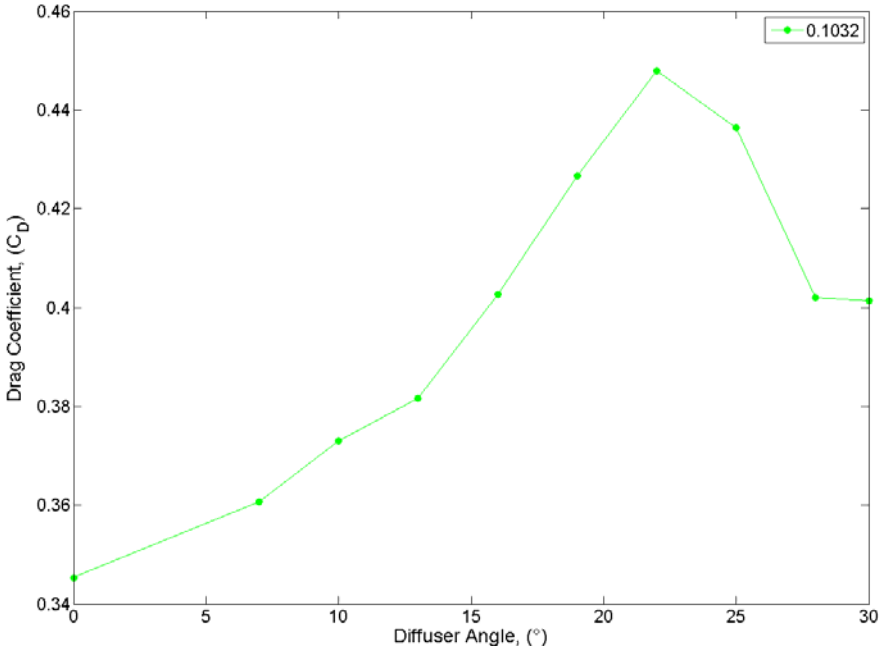

Figure 3.3.4 - Graph of drag coefficient against diffuser angle for 32mm ride height (h_1/H=0.1032)

A typical plot of the C_D vs. slant angle is shown in Figure 3.3.5 [18]. At 0° the flow separates from the top of the slant generating a turbulent wake. As the slant angle is increased, the drag reduces as pressure is recovered increasing base pressure. This is however, accompanied by an increasing contribution from a pair of trailing vortices emanating from the C-pillar after the minimum drag at 12°-14°. The additional contribution to drag from the vortex structure offsets the benefits of maintaining attached flow along the slant and the drag rises. It peaks at 30° with about 15% higher drag than the zero slant. At 30°, the critical angle, the vortex structures burst and drag drops to a consistent value similar to that at 0°.

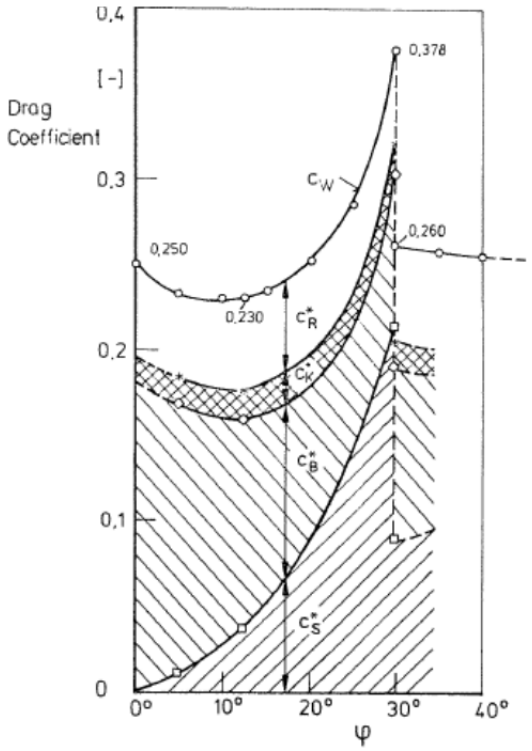

Figure 3.3.5 – Variation of drag with base slant angle for Ahmed model [18]

As the diffuser angle is increased in Figure 3.3.4 the drag increases, however only angles from 7° to 30° have been tested. Cooper et al [16] found that angles below 5° gave a drag reduction over the flat floor (0°) and it is hypothesised that below 7°, the graph would follow a similar pattern to that seen for the fastback variation in Figure 3.3.5. The increase in drag with diffuser angle is consistent with the suggested increase in vortex strength up to the maximum downforce around 13°. This is a similar angle to the minimum drag observed in the fastback. Above the maximum downforce, the increase in drag is attributed to both vortex contribution and separation. The peak drag is seen at 22° (lower than that of the fastback) above which the drag reduces steadily unlike the sudden drop seen in Figure 3.3.5. This suggests that vortex breakdown is gradual rather than

"bursting". At 28° and 30° the drag is at a constant magnitude similar to the fastback variation, but it is higher than the drag of the flat floor (0°) due to the high levels of separation.

The similarities between the drag variation of the fastback and diffuser flows gives confidence that some of the flow mechanisms at work are similar, primarily the influence of the vortex structures. Additionally, the schematic diagrams of back slant flow behaviour [18] and vortex formation [57] created by Ahmed may provide useful information on the possible behaviour of the diffuser flow.

The plane diffuser performance is summarised in the contour plots in Figure 3.3.6 and Figure 3.3.7, presented using non-dimensional diffuser length (N/h_1), which for this set of data is essentially ride height (h_1) as the diffuser length (N) is fixed. The data is plotted in this way to be consistent with other diffuser studies and has the advantage of presenting all the configuration variables (θ, h_1, N) that are altered to be viewed in a single figure. Rear-lift coefficient, as a substitute for the pressure recovery coefficient ($\overline{C_P}$) in conical diffusers [25], is used as used by Cooper et al [16]. This approach highlights more specifically the diffuser contribution.

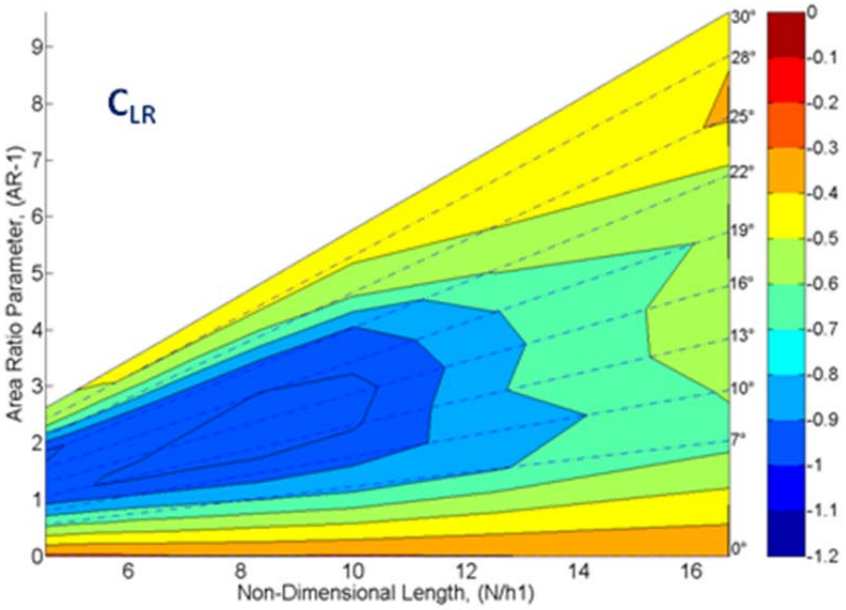

Figure 3.3.6 - Contours of diffuser-based downforce for plane diffuser

The diffuser-based downforce (Figure 3.3.6) shows that for all non-dimensional lengths, as area ratio increases, the downforce passes through an optimum. At different diffuser angles the behaviour can be divided into three regions. The maximum downforce occurs between 13° and 16° and in the optimum region between 10° and 22° the downforce is particularly sensitive to non-dimensional length, with levels of downforce increasing as the non-dimensional length is

reduced. Within the two regions above and below this the diffuser performance is almost independent of non-dimensional length.

When selecting the correct diffuser for a particular application, the balance of lift and drag need to be taken into account. The conventional method for summarising this trade off is to plot the lift-to-drag ratio and Figure 3.3.7 shows this in the form of a contour plot.

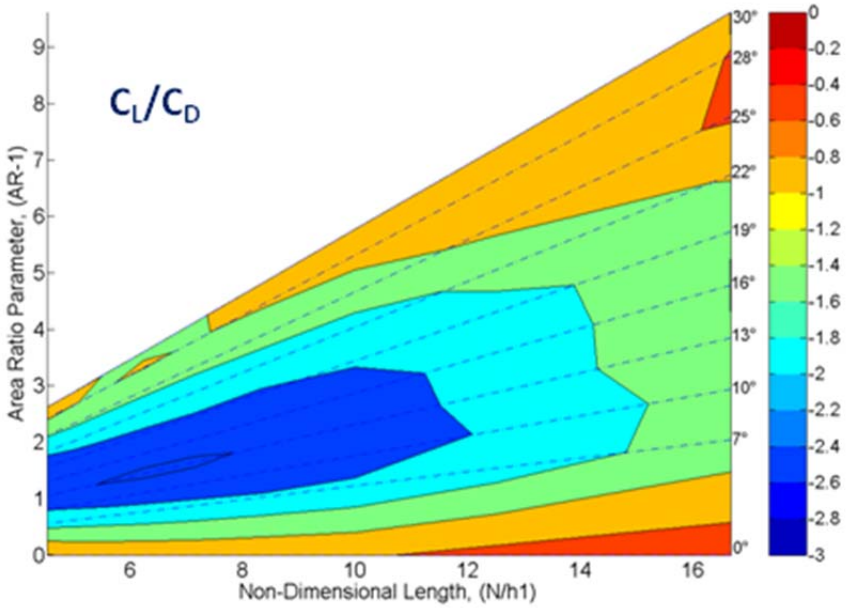

Figure 3.3.7 - Contours of lift/drag ratio for plane diffuser

The lift-to-drag ratio produces a broadly similar plot to the diffuser based downforce, but here the optimum performance region is at 13° compared to the maximum downforce at a slightly higher angle. This suggests that the additional downforce above 13° comes at the expense of an increased induced drag component. Although large amounts of downforce may be advantageous, when considering the overall lift-to-drag performance, the amounts of induced drag produced may, in some applications, outweigh the benefits of the downforce produced. For example, in a racing application, circuits with long straights would be more concerned with the lift-to-drag than a circuit with fewer straights and more corners where downforce is of more importance.

3.4 Pressure Measurements

Pressure measurements were undertaken in order to provide further information regarding the behaviour of the flow as well as to give an indication of the relative downforce contributions from the diffuser and flat underbody. Details of pressure tapping positions can be found in Section 2.1.

3.4.1 Centreline Pressure Distribution

The centreline pressure distributions are compared with previously published data by Cooper et al [16] in Figure 3.4.1. The results compare well with those of Cooper et al showing the same overall pressure distribution. Additionally, the characteristic changes in pressure such as the depression around the lower front edge radius and the depression at the diffuser inlet are observed.

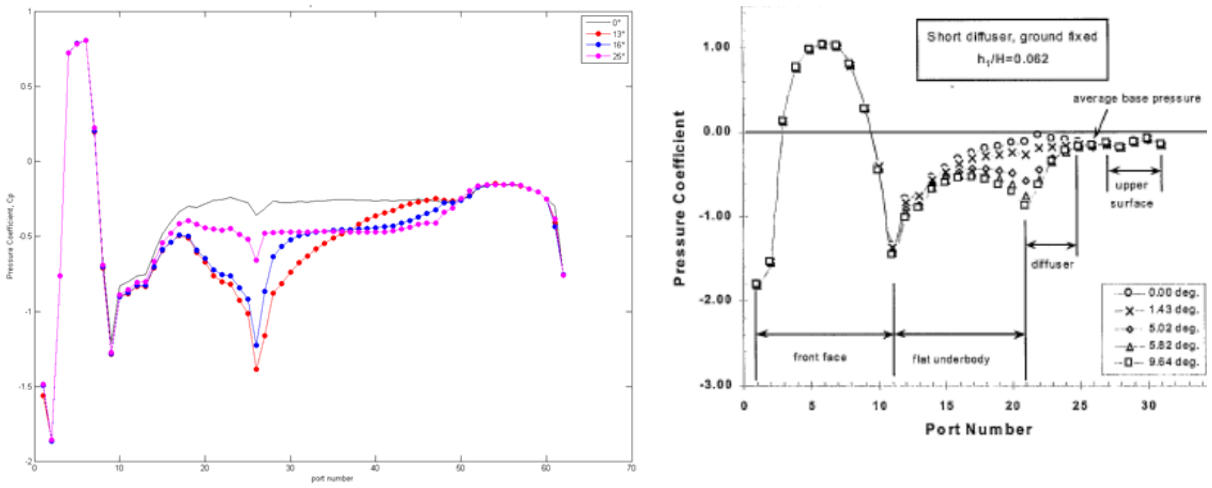

(a) **(b)**

Figure 3.4.1(a) and (b) – Pressure coefficient vs. port number for (a) Plane diffuser at 20mm and (b) Cooper distribution

Although data was collected for all configurations, for clarity only pressure results for a select range of diffuser angles and ride heights will be presented. The angles chosen (0°, 13°, 16° and 25°) represent those of particular interest based on the force measurements, as part of one of four flow regimes. The 0° flat floor configuration was chosen as a reference for the effect of ground simulation only. The 13° angle was chosen as it is a "low angle" that is assumed to be largely attached and producing the highest levels of downforce. The 16° angle, a "mid angle" is assumed to be partially separated but with large levels of downforce and 25° diffuser is a "high angle" performing poorly and assumed to be largely separated.

Figure 3.4.2 shows the pressure distributions for the chosen diffuser angles against non-dimensional model length, with the diffuser inlet shown at x/L=0.75. The flat floor (0°), shown in Figure 3.4.2a shows that the general variation in pressure is similar for all ride heights. The change in pressure at the second tapping on the front edge radius suggests that the front stagnation is moving with ride height. After the suction peak at the lower front edge radius there

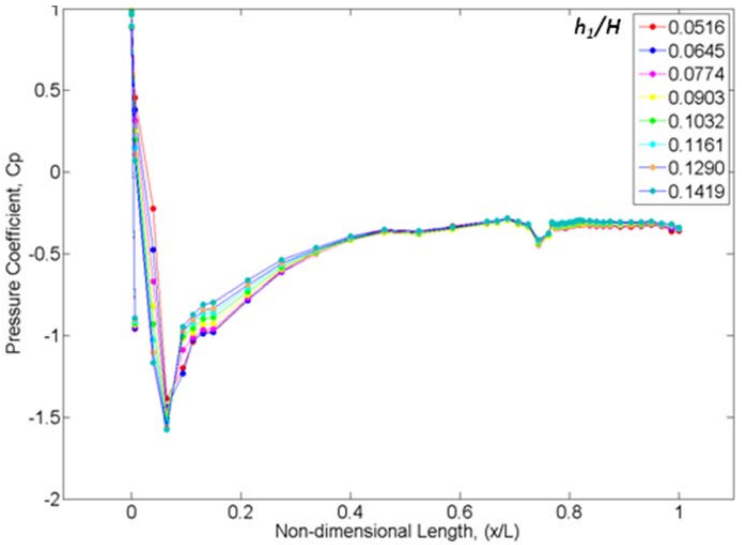

(a) – 0°

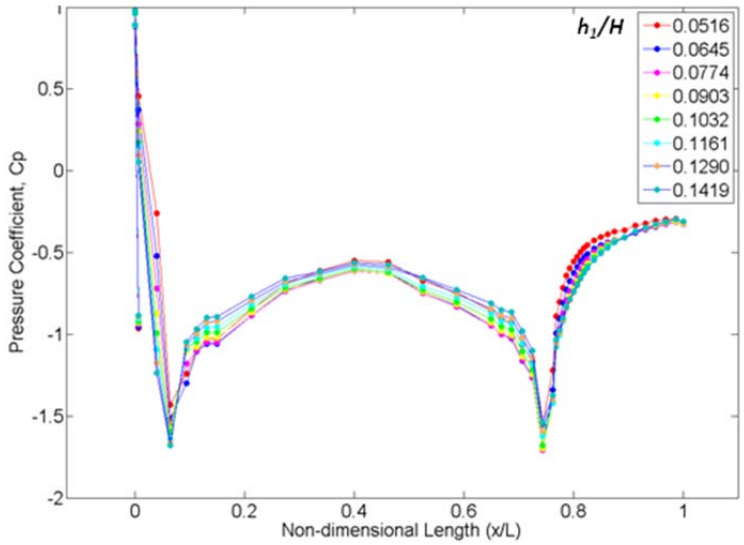

(b) – 13°

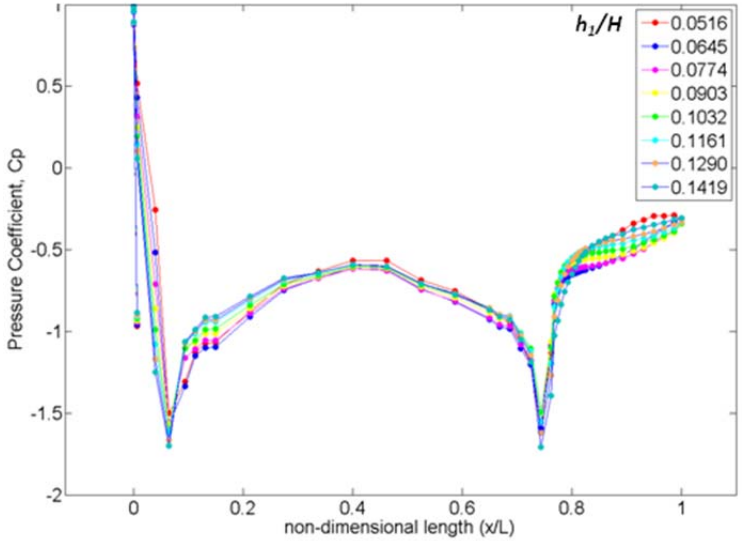

(c) – 16°

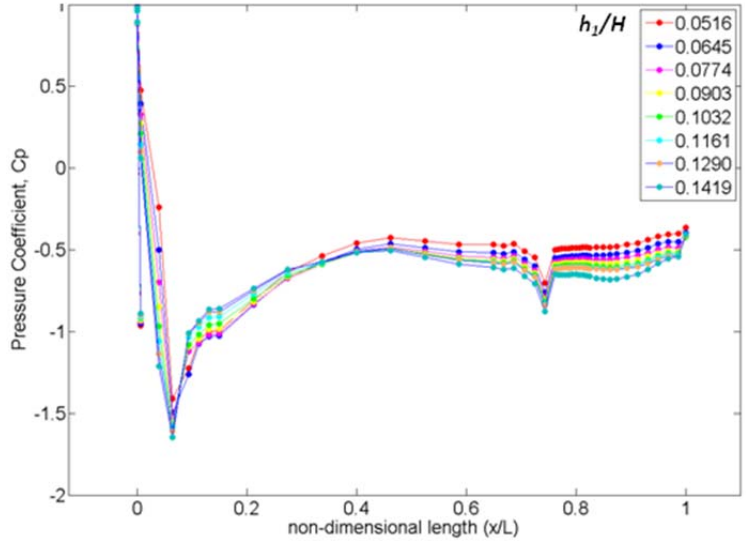

(d) – 25°

Figure 3.4.2 – Comparison of centreline pressure distribution for plane diffuser at different diffuser angles

is a change in the pressure recovery such that as the ride height increases the pressure recovery increases, reducing the downforce. The distribution at diffuser inlet and through the diffuser is relatively flat and consistent through the ride heights. As the flat floor has no 'diffuser pumping' or 'upsweep', the downforce observed in Figure 3.3.1 is due to ground interaction only and the distribution in Figure 3.4.2 – are representative of this ground interaction.

Diffuser angles 13° , 16° and 25° (Figure 3.4.2 – b, c & d) all show the same characteristic distribution around the front face of the model with a front stagnation point that moves towards the ground as the ride height is reduced, identified by Figure 3.4.3. The underbody flow accelerates around the lower radius of the front face producing a significant depression. Around x/L=0.1 there is evidence of a small separation bubble just after the lower front edge radius. This was identified by Cooper et al [16] in a more pronounced way and was attributed to the strong adverse pressure gradient around the front radius. Forward of x/L=0.4 the flat underbody pressures become increasingly negative as the ride height reduces and the pressure recovery is suppressed as in the flat floor case. Downstream of x/L=0.4 the underbody pressures are dependent on the diffuser pumping at the diffuser inlet (x/L=0.75). Decreasing the ride height increases the area ratio, which increases the diffuser pressure recovery. As the base pressure is fixed, the pressure recovery is seen as the characteristic depression at the diffuser inlet. The distributions in Figure 3.4.2 are consistent with those observed by Cooper et al [16].

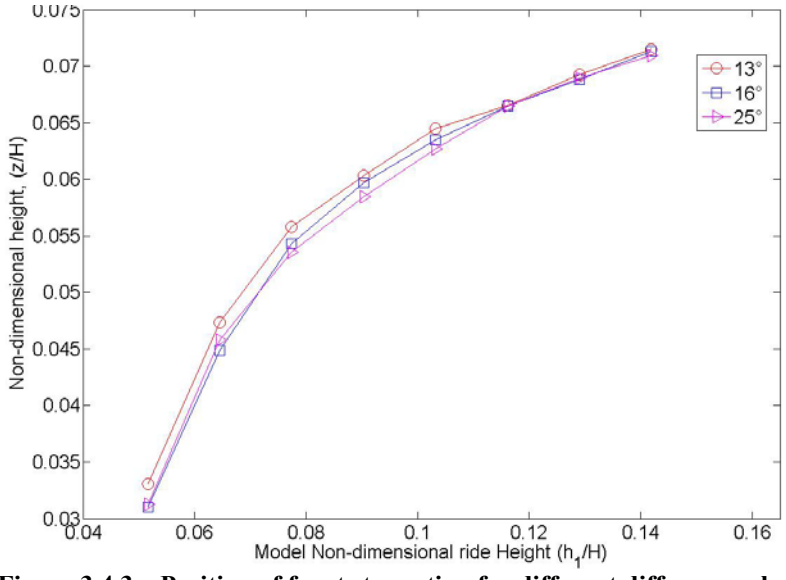

Figure 3.4.3 – Position of front stagnation for different diffuser angles

The pressure recovery (x/L=0.75-1) within the 13° diffuser (Figure 3.4.2 – b) is close to ideal for all ride heights suggesting it is largely attached. As ride height is reduced, the depression at inlet is intensified (more negative pressure coefficient) giving rise to increases similar to that seen in

Zhang et al [14]. At 16° (Figure 3.4.2 – c), the pressures indicate a probable separation occurring just downstream of the diffuser inlet at x/L=0.79 shown by the plateau region similar to that seen in separation of simple aerofoils in [49]. The force measurements (Figure 3.3.1) support this as the increased drag in the 16° diffuser compared with the 13° is assumed to be attributed to separation rather than drag associated with increase in vortex strength because the downforce magnitudes for the two configurations are similar. Further downstream of the inlet the pressure recovery continues to base pressure as the flow reattaches. As the ride height is increased, the adverse pressure gradient is reduced and the flow is less susceptible to separation at the inlet. The reattachment point at which the pressure recovery continues appears at x/L=0.875 for ride heights above h_1/H=0.0903. At 25° (Figure 3.4.2 – d) the separation point has moved upstream and occurs at inlet, with the diffuser largely separated at all ride heights, reducing its ability to recover pressure effectively. This is confirmed by the large reduction in lift and drag coefficient in Figure 3.3.1. A small depression at inlet occurs as the flow is locally accelerated and the downforce gains over the flat floor configuration are due to the upsweep and ground interaction mechanisms rather than diffuser pumping.

Some further insight into the diffuser performance is gained by plotting a range of diffuser angles at fixed ride height. This is seen in Figure 3.4.5 where the pressure distributions for 0°, 13°, 16° and 25° diffusers are plotted against each other for specific ride heights. At all ride heights the flat floor (0°) exhibits the highest pressures though the pressure coefficients are negative, producing downforce due to interaction with the ground. The area between the 0° distribution and each of the other diffuser angles represents the 'diffuser pumping' contribution as described by Cooper et al [17].

At all ride heights the 13° and 16° configurations have a basic shape that is consistent with the ground effect and diffuser pumping effects discussed previously. At the lowest ride height, the 13° diffuser shows a pressure recovery in the diffuser flow that is close to ideal while there is some separation and reattachment at 16°. It is however, noted that the maximum suction occurs around the diffuser inlet and is greater at 16° and the suction around the model leading edge radius is deepened indicating increased underbody flow. As the ride height is increased, the 16° diffuser experiences increased growth of the separation bubble, reducing its initial pressure recovery capability while the 13° continues with almost ideal pressure recovery and greater diffuser pumping. At the highest ride height the 16° angle has greater diffuser pumping and more gradual pressure recovery, increasing the downforce.

The 25° diffuser has much higher pressures than the lower angles as the diffuser is now largely stalled. The pressures are, however, significantly lower than those of the flat floor suggesting the diffuser is still working in some form. There is some depression locally at the diffuser inlet and while the pressures suggest the diffuser is stalled, there is some pressure recovery near the exit. This results in an underfloor depression that exceeds that of the flat floor and may be attributed to the underbody upsweep.

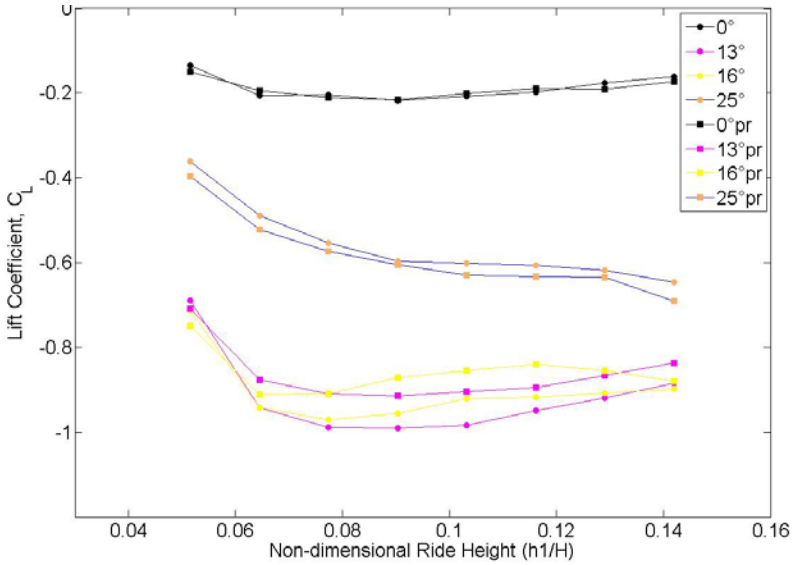

Figure 3.4.4 – Pressure- and force-based lift coefficients for 13°, 16° and 25° diffusers

From these centreline pressure distributions, area weighted pressure based lift coefficients have been calculated and are plotted against non-dimensional ride height alongside the corresponding force distributions. All diffuser angles show very similar trends between the force and pressure measurements. However, the magnitudes of the coefficients depend on the angle range the configuration lies in. The flat floor and 25° diffuser exhibits almost identical magnitudes between force and pressures whereas the 13° and 16° diffusers show a marked difference, with the pressures under predicting the downforce levels. This can be attributed to the fact that surface pressure measurements cannot fully describe the mechanisms at work and do not take into account any change in distribution across the width of the diffuser. As the vortex structures are assumed to be strongest in the 13° and 16° diffusers and their influence is primarily at the outer edges of the diffuser, this would not be shown in the centreline measurements and hence the downforce magnitudes are under predicted. As the flat floor has no vortex structure and the 25° diffuser is assumed to have only a weak structure, their influence on the pressures is small and hence the centreline measurements predict the downforce levels relatively accurately.

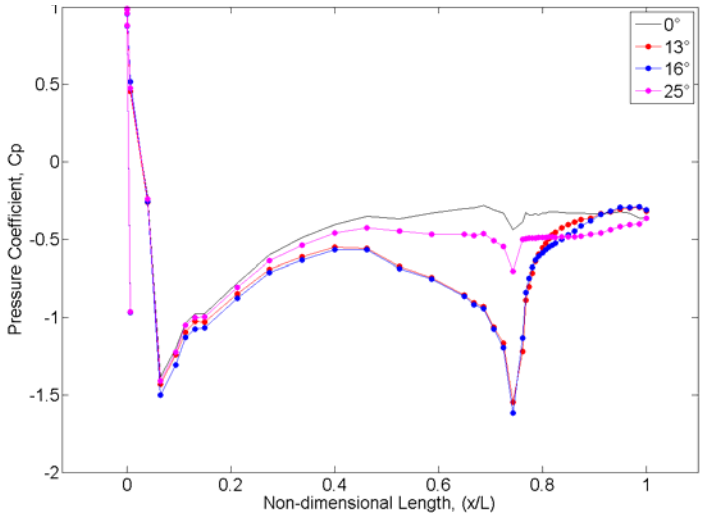

(a) – h_1/H=0.0516 (16mm)

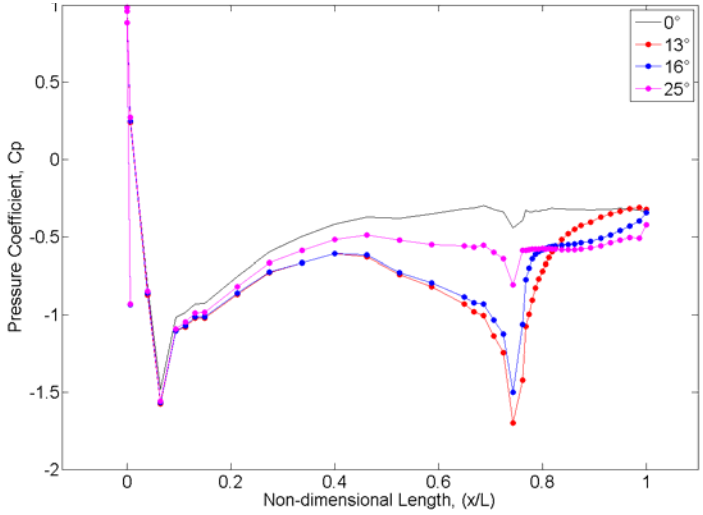

(b) – h_1/H=0.0903 (28mm)

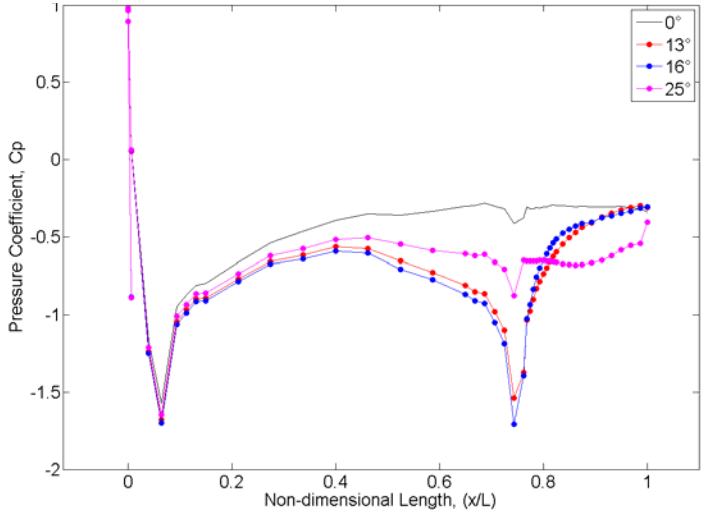

(c) – h_1/H=0.1419 (44mm)

Figure 3.4.5 – Comparison of the pressure distribution for the flat floor and plane diffusers at 13°, 16°, and 25°

3.4.2 Area Pressure Maps

To explore the three-dimensional aspects of the flow, pressure measurements across the width of the diffuser were taken as described in Section 2.1. The following figures show contour plots generated from this pressure data with a template of diffuser configuration superimposed to aid interpretation. The plots begin just upstream of the diffuser inlet (x/L=0.75) and show an area of half the model width covering half the diffuser channel, the centreline at (y/L=0). The endplates (x/L=0.25) are shown for clarity. The area map pressure tappings are identified on the figures as a circle.

Three diffuser angles are presented (13°, 16° and 25°) in Figure 3.4.6 at three ride heights (h_1/H=0.0516, h_1/H=0.0903 and h_1/H=0.1419). The 13° diffuser shows areas of low pressure at the inlet (x/L==0.75) corresponding to the diffuser pumping depression observed in the centreline pressure distributions in Figure 3.4.2. Low pressures are also seen near the endplates (y/L=0.25) at the location of the vortex structures identified by [22] and [13]. At the exit of the diffuser the contours show pressures close to base pressure.

As the ride height is increased the areas of low pressure around the diffuser inlet and endplate region increase due to increased diffuser pumping and stronger vortex structures, which is confirmed by the increased downforce and drag (Figure 3.3.1 and Figure 3.3.2) and more negative depression observed in the centreline pressures (Figure 3.4.2). At the highest ride height, results show slightly reduced low pressure regions suggesting a weaker vortex structure present and reduced inlet depression (Figure 3.4.2) resulting in lower downforce (Figure 3.3.1 and Figure 3.3.2). Additionally, the contours are more widely spaced suggesting a more gradual pressure recovery as highlighted in (Figure 3.4.2).

Increasing the diffuser angle to 16° shows only relatively small differences compared to the 13° diffuser, similar variations are observed but with slightly different diffuser pumping at the inlet. These differences identified correlate with the differences observed in the force (Figure 3.3.1 and Figure 3.3.2) and centreline pressure measurements (Figure 3.4.2).

As the diffuser angle is increased further to 25°, a transition in behaviour is observed. The diffuser no longer exhibits the strong pressure recovery seen at smaller angles, suggesting that vortex breakdown may have occurred causing a small amount of asymmetry in the flow as

observed in the surface flow visualisations in [14]. This is consistent with the large reductions in downforce and drag observed in (Figure 3.3.1 and Figure 3.3.2).

As the ride height is increased the asymmetry remains but reduced pressures around the inlet are observed suggesting a partial attempt at pressure recovery. However, the diffuser is still assumed to be largely stalled and the improvement observed is more likely due to a less adverse pressure gradient as the ride height is increased.

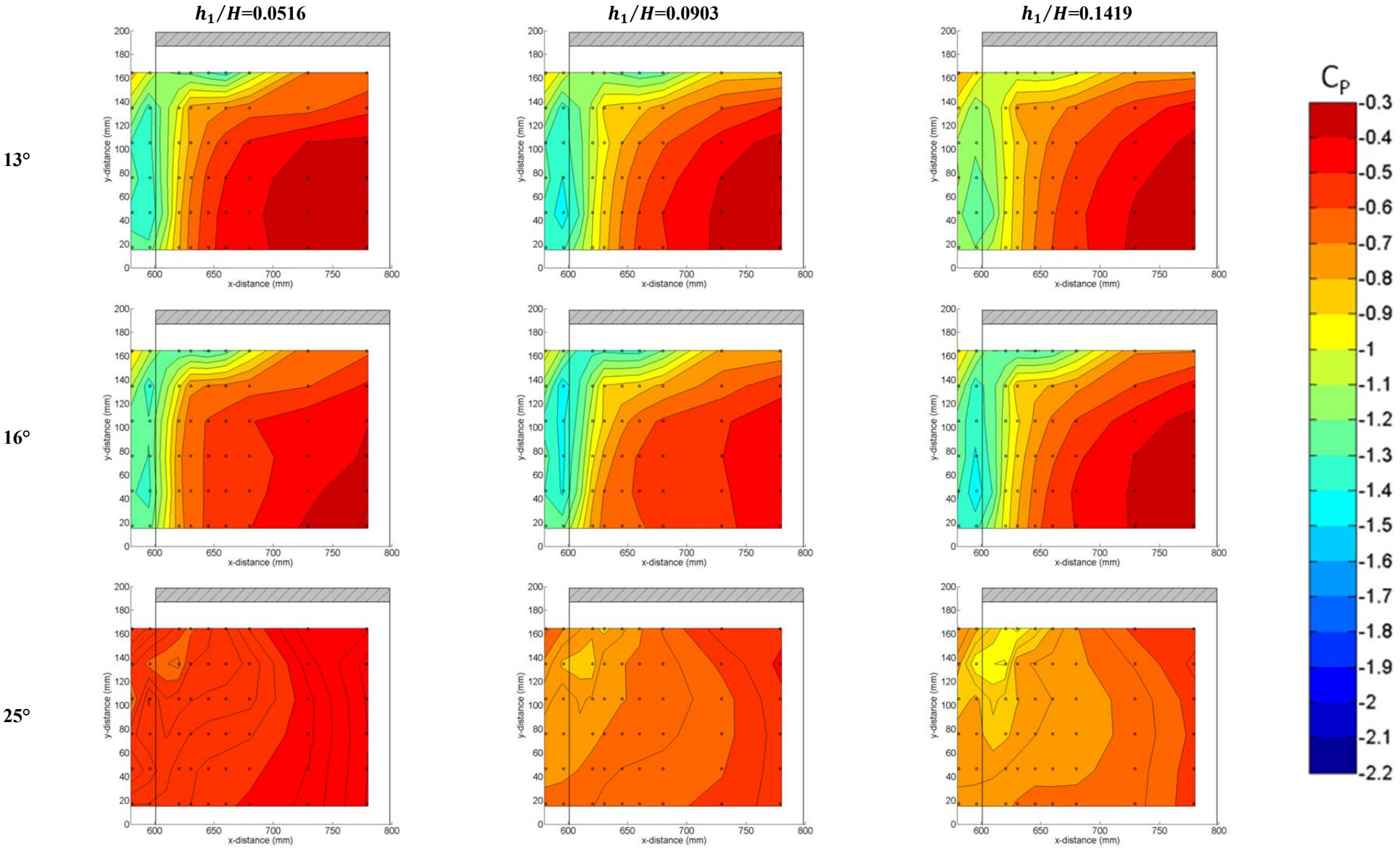

Figure 3.4.6 – Comparison of plane diffuser pressure contour maps at 13°, 16° and 25° diffuser angles

3.5 PIV Measurements

In order to gain further information regarding the flow mechanisms at work in the diffuser, Particle Image Velocimetry (PIV) measurements were taken to provide sets of vector-based flow images. The advantage of using PIV is it is a non-intrusive technique, although time consuming to initially set-up correctly.

The set-up (Figure 3.5.1) utilised a light sheet at the diffuser exit plane with the camera located in a box protecting it from the seeded flow, mounted to the floor at the rear of the tunnel working section. The seeding system was placed at the entry to the working section, close to the floor to enable seeding to travel underneath the model easily. As the laser sheet is just downstream of the model, reflections from the model itself are not a problem but reflections do occur at the floor. This was reduced by masking this area at the camera. It was also found that the usual location of the seeding rake in the settling chamber did not provide sufficient quantities of seeding at the model's diffuser exit, particularly close to the floor. This was rectified by mounting the seeding rake close to the floor at the working section inlet.

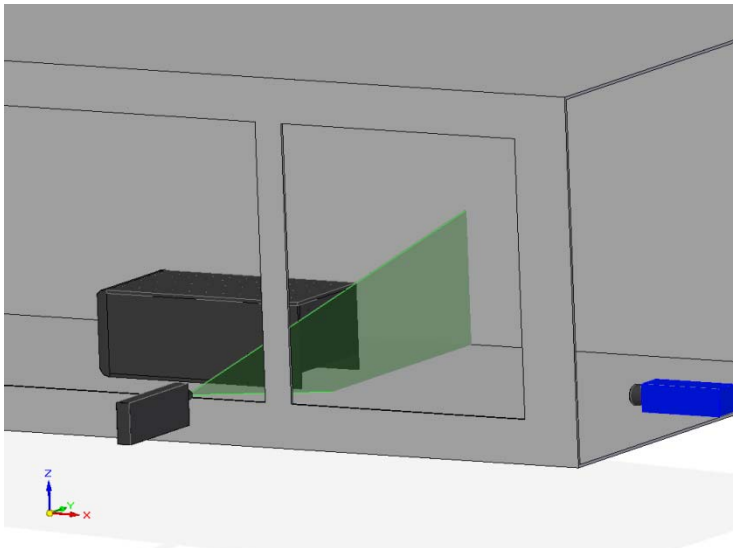

Figure 3.5.1 – Schematic of PIV experimental set-up

Making through plane PIV measurements produces some particular problems in acquiring high quality source images. If the through plane velocity is assumed to be approximately free-stream ($40ms^{-1}$) and the laser sheet is 4mm thick, then the fluid transits the sheet in 100μs. To ensure that the two images in a pair contain the same seeded particles, a relatively short inter-frame time is therefore required. However, if the in plane velocities are relatively low, a longer inter-

frame time may be required to generate sufficient particle shift. The inter-frame time chosen here is 10μs because of the high through plane velocity but this produces a relatively small particle shift of approximately +/- 2pixels on a final interrogation cell of 32x32. The time averaged velocity field at the exit plane of a 13° diffuser is shown in Figure 3.5.2 with vorticity contours in the background.

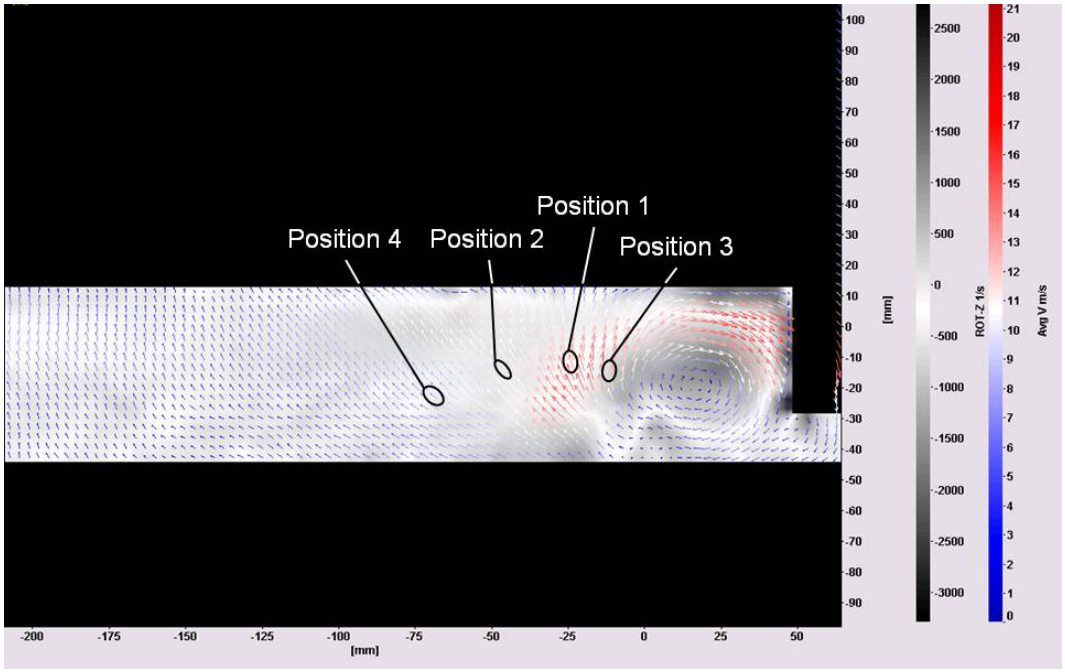

Figure 3.5.2 – Position of vectors for error analysis (shown in average vector plot)

The time averaged data are the average of 1000 instantaneous vector fields. As the mean velocity converges with the increasing number of samples the method of Hollis [36] is used to determine the convergence of the mean. Four positioned vectors were used, locations shown in Figure 3.5.2 and the statistical convergence is illustrated in Figure 3.5.3-Figure 3.5.6. With 1000 samples the 99% confidence limit represents approximately ±2% of the mean velocity but in general the accuracy will depend on the local turbulence intensity.

For all four vector positions, the averages of the results from averaging subsets of image pairs fell within the expected 99% confidence interval for the number of images pairs included in each subset. This is a consequence of the spatial averaging inherent in the PIV technique, where each instantaneous vector is computed from the average particle displacements within an interrogation cell. This gives confidence on the accuracy of the PIV data collected and presented here.

Although all four vector positions fall within the 99% confidence band, the spread of samples is not identical and highlights the turbulent behaviour of the flow in different regions investigated. The variation in deviation in Positions 1 and 3 is less than that observed in Positions 2 and 4. Position 1 (Figure 3.5.3) and 3 (Figure 3.5.5) are in the region of the diffuser where the vortex creates strong structured flows, whereas Position 2 (Figure 3.5.4) and 4 (Figure 3.5.6) are in the regions where the flow may be expected to be less structured and more prone to high levels of separation and asymmetry at large diffuser angles.

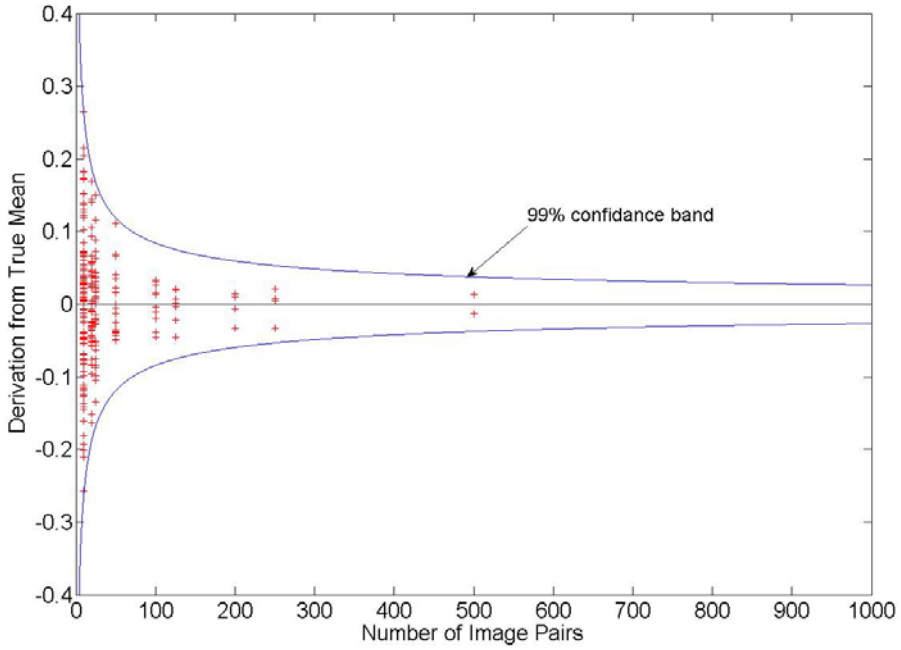

Figure 3.5.3 – Deviation from true mean of the velocity vector in position 1 with 99% confidence band

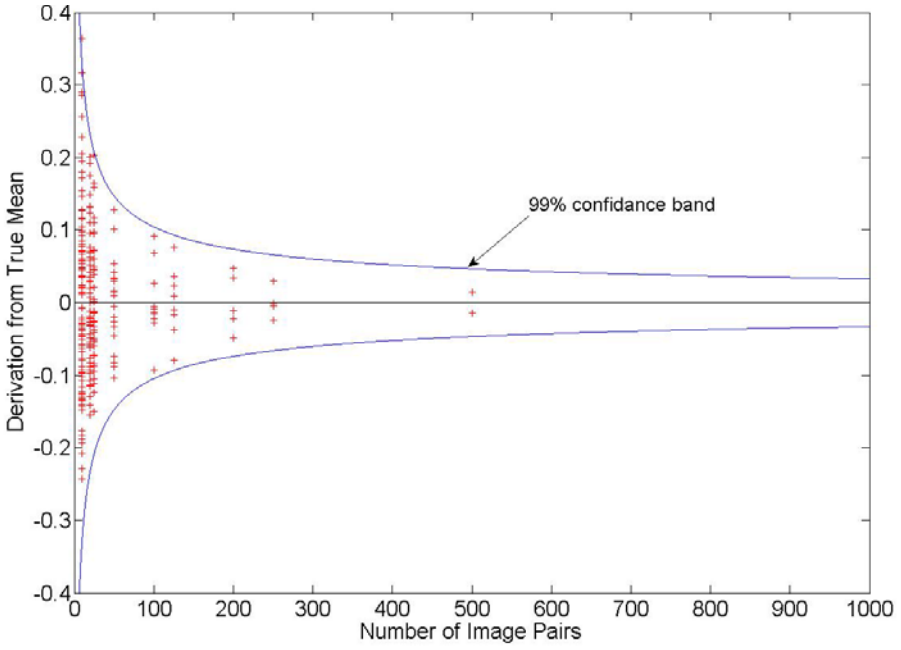

Figure 3.5.4 – Deviation from true mean of the velocity vector in position 2 with 99% confidence band

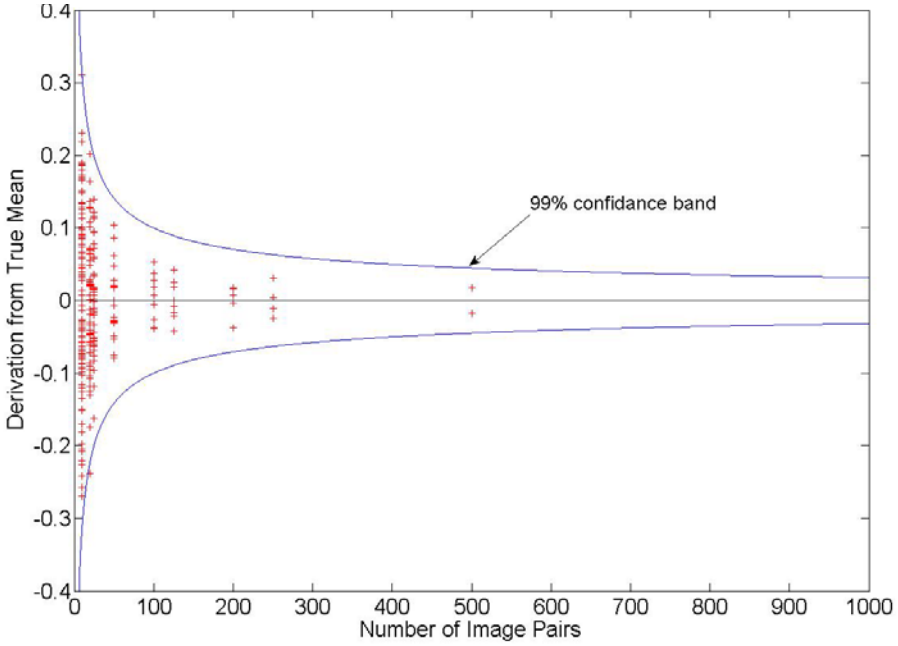

Figure 3.5.5 – Deviation from true mean of the velocity vector in position 3 with 99% confidence band

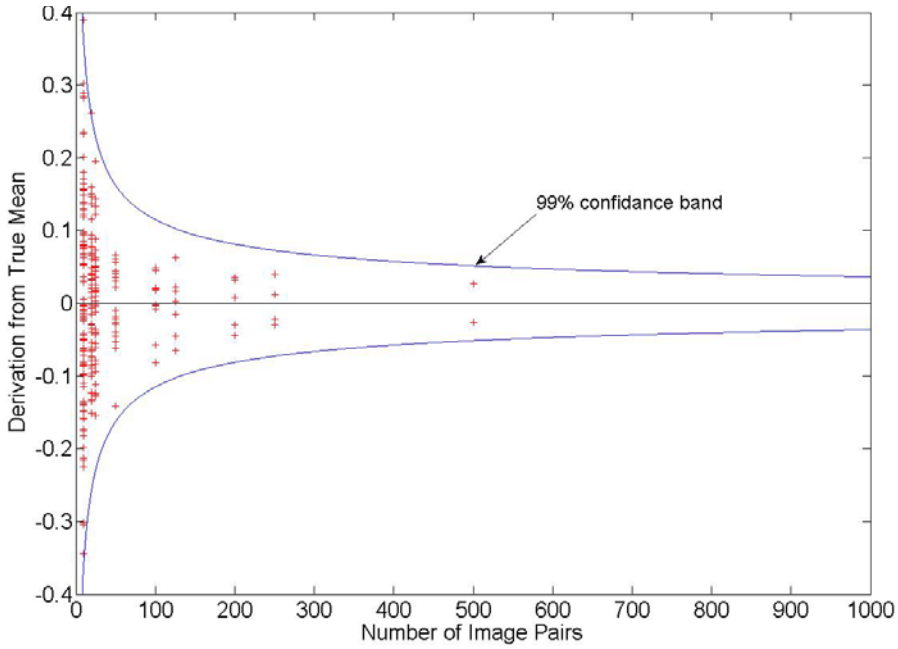

Figure 3.5.6 – Deviation from true mean of the velocity vector in position 4 with 99% confidence band

The PDF function for the 19° diffuser is shown in Figure 3.5.7 for the V_xV_y velocity components. The two components (V_x and V_y) are used for improved statistics [31] over using just a single component. Figure 3.5.7a shows the complete velocity distribution and is similar to the acceptable distribution in Figure 2.2.11. The $\overline{V_{0.5}}$ and $\overline{V_1}$ distributions are shown in Figure 3.5.7b and c. These represent the histogram of the decimal places of the velocity components that essentially "cuts the integer value", i.e. V_xV_y=2.13px is V_xV_y=0.13 for $\overline{V_1}$. The $\overline{V_{0.5}}$ histograms are mapped to a value 1-V (where V>0.5px) giving a better estimation of the peak locking effect. Neither shows a strong U-shaped distribution and hence gives confidence to the

data quality. Additionally, peak lock parameters were found to be 0.032 where a peak lock factor of <0.1 indicates an acceptable peak locking effect [31].

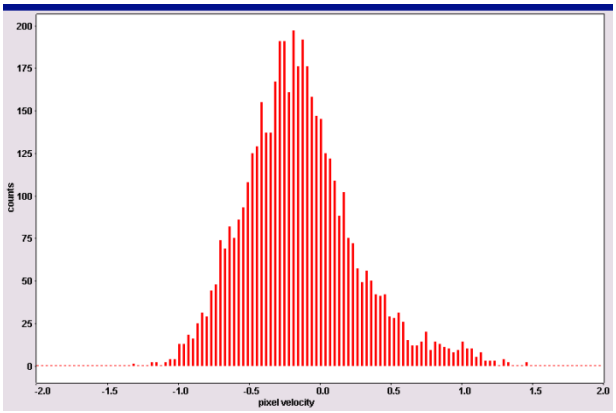

(a) Complete velocity distribution

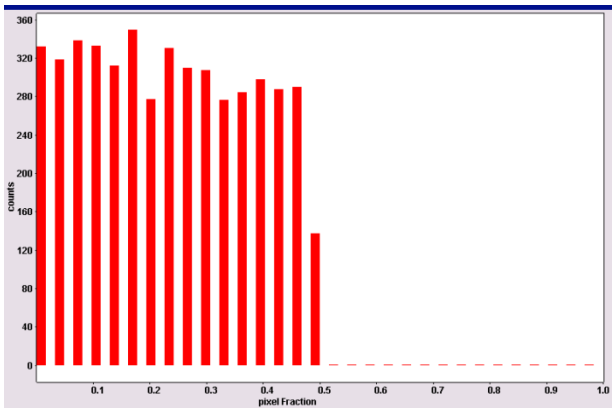

(b) $\overline{V_{0.5}}$ histogram

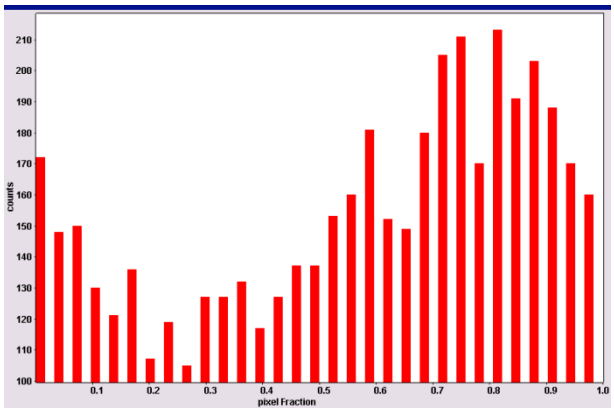

(c) $\overline{V_1}$ histogram

Figure 3.5.7 – Probability Density Function for 19° diffuser

An example of a raw image pair is shown in **Error! Reference source not found.** and highlights the movement of the seeded particles and the brighter second image with larger reflections. From these raw images the vector plots were created.

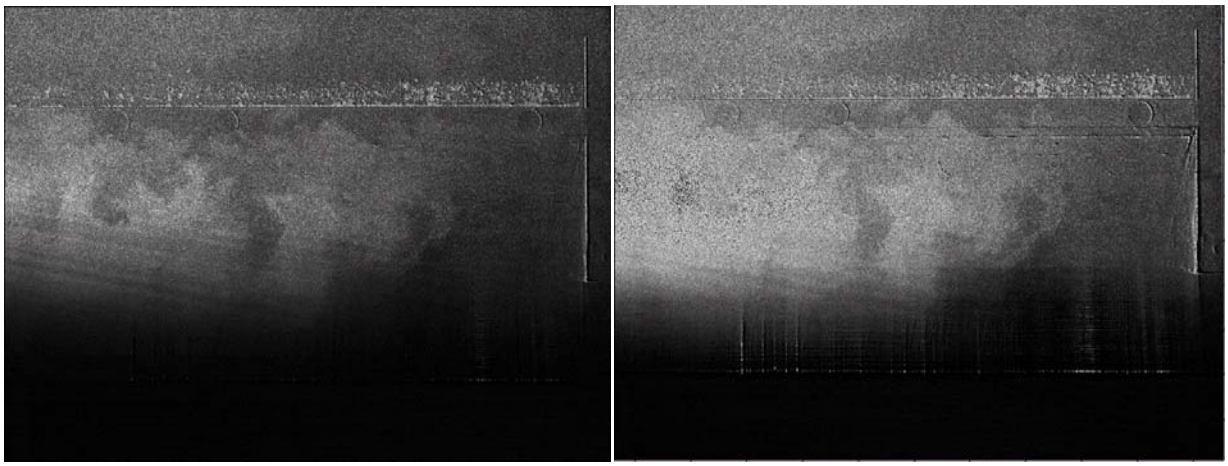

Figure 3.5.8 – Example of PIV raw images pair for 19° diffuser at h_1/H=0.1419

Finally, the most important parameter to analyse initially in the vector plots is the number of first choice vectors. This determines the quality of the data based on a variety of factors including seeding quality and filtering parameters set by the user in the correlation function. It is advised that the number of first choice vectors should be in the region of 95% or higher to assure good quality data. The circumstances where a non-first choice vector would be chosen depends upon the statistics generated from the post processing(as described in Section 2.2.3.3), such as the median filter. This calculates a median vector from the eight surrounding vectors. It then compares the middle vector to this median vector ± deviation of the neighbouring vectors. The vector is rejected if it fails the criteria set out in Equation 2.2.4, after which a second choice vector would be chosen and the process repeated to ensure it too passes the median filter criteria. **Error! Reference source not found.** shows vector choice data for the 19° diffuser with the vectors coloured by vector choice; 1st choice = red, 2nd choice = green, 3rd choice = blue, 4th choice = magenta and filled/smoothed = yellow. The plot shows that the majority of the plot is coloured red as 1st choice. The 2nd choice / 3rd choice/ filled vectors are in the regions near the floor where both seeding and reflection caused problems and hence impair the images and reduce the quality of the velocity data.

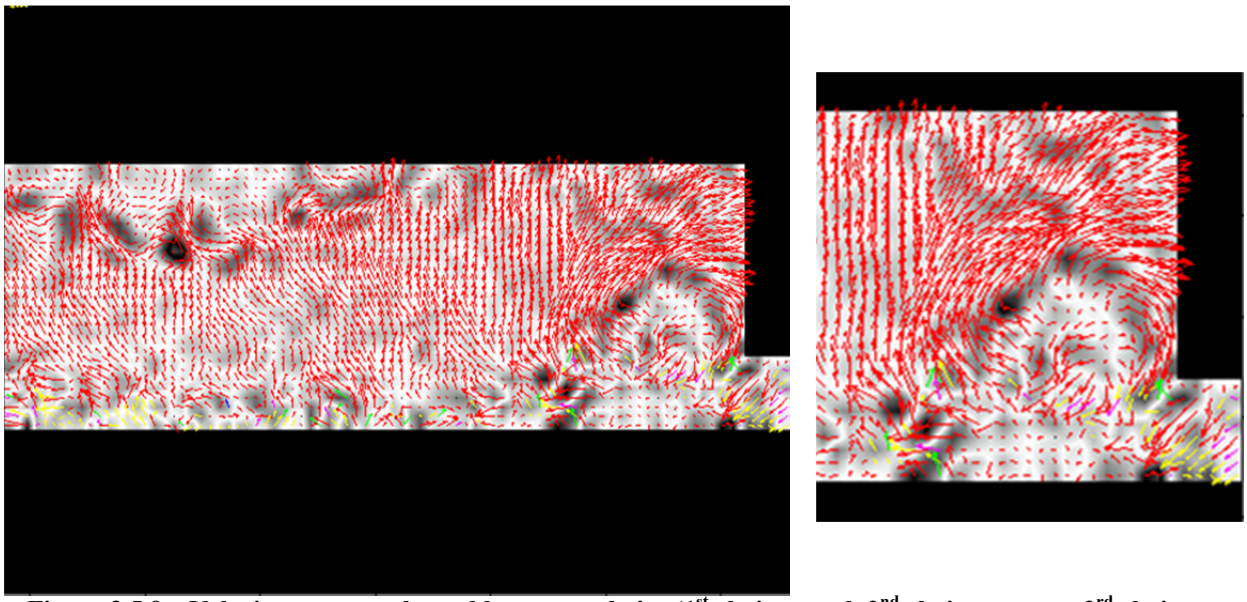

Figure 3.5.9 – Velocity vectors coloured by vector choice (1st choice = red, 2nd choice = green, 3rd choice = blue, 4th choice = magenta and filled/smoothed = yellow)

PIV data was not collected for all diffuser angles and ride heights but concentrated on 13°, 16° and 25° angles as seen in Section 3.4. However, due to the similarity in behaviour of the 13° and 16° diffusers, 19° was also examined as a transitional angle between the attached and separated regimes. The time-averaged vector plots are shown in Figure 3.5.11 - Figure 3.5.14 for these angles at a ride height of 28mm (h_1/H=0.0903). The plots comprise ~70% of the model width

viewed from behind (shown schematically in Figure 3.5.10) and show velocity vectors with rotational velocity in the background. The measurement plane is 10mm behind the rear face of the model equating to the thickness of the calibration plate. The scaling is the same for all of the figures to allow an accurate comparison to be made and is based on the extreme values across all configurations.

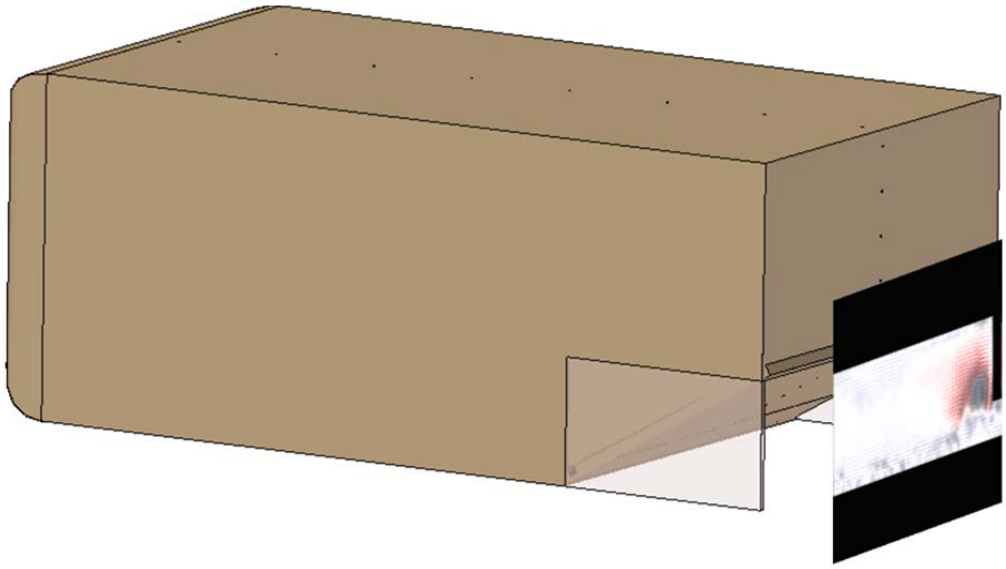

Figure 3.5.10 – Schematic of vector plots on CAD geometry

Results for the 13° diffuser angle are shown in Figure 3.5.11 and show the clear presence of a vortex structure in a position next to the end plates, similar to that observed in the area pressure maps (Figure 3.4.6). The endplates constrain the vortex structure preventing it from dissipating so that it is fed along the length under the endplate and covers the whole height of the diffuser but only ¼ of its width. The rest of the diffuser is dominated by flow coming off the vortex structure and additionally the presence of upwash (described by [16] as a downforce generating mechanism) is shown by the velocity vectors around the centreline pointing toward the diffuser plate. From these vector plots it is assumed that the flow is largely symmetrical about the model centreline.

When the diffuser angle is increased to 16° the vortex structure is slightly larger but in a similar position to the 13° diffuser however the flow towards the centre emanating from the vortex has a higher velocity and affects a larger proportion of the flow. Flow moving underneath the endplates and the upwash is still present in similar proportions as the 13° diffuser. The main difference is that the flow near the diffuser plate surface (particularly close to the centreline) shows slower vectors than those observed previously suggesting that the flow is slowing down and either recovered from a previous separation occurrence or on the verge of separating. The

centreline pressures (Figure 3.4.5) and area maps (Figure 3.4.6) show that the 16° diffuser has an initial sharp pressure recovery after the inlet (approximately x/L=0.8) followed by a plateau region before recovery to base pressure. This could explain the vector distribution observed and the reduction in downforce between 13° and 16°.

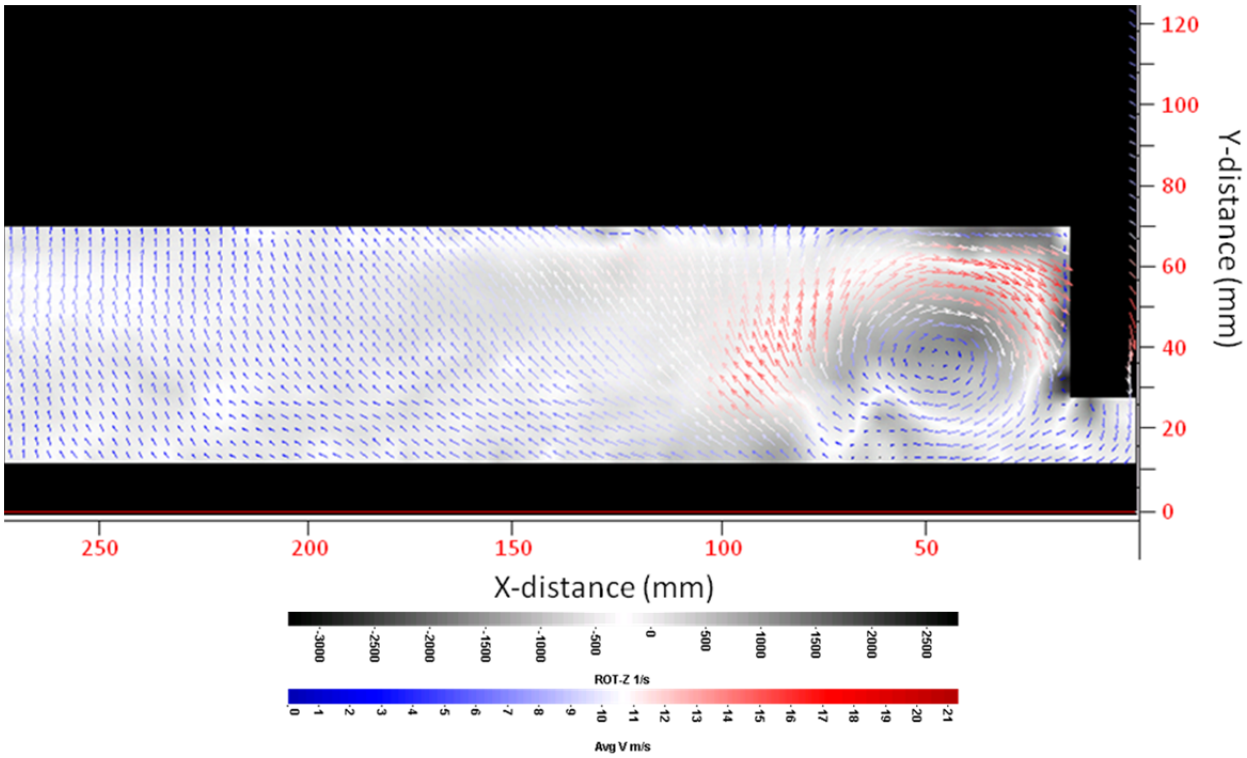

Figure 3.5.11 – Time-averaged vector plot for 13° at h_1/H=0.0903

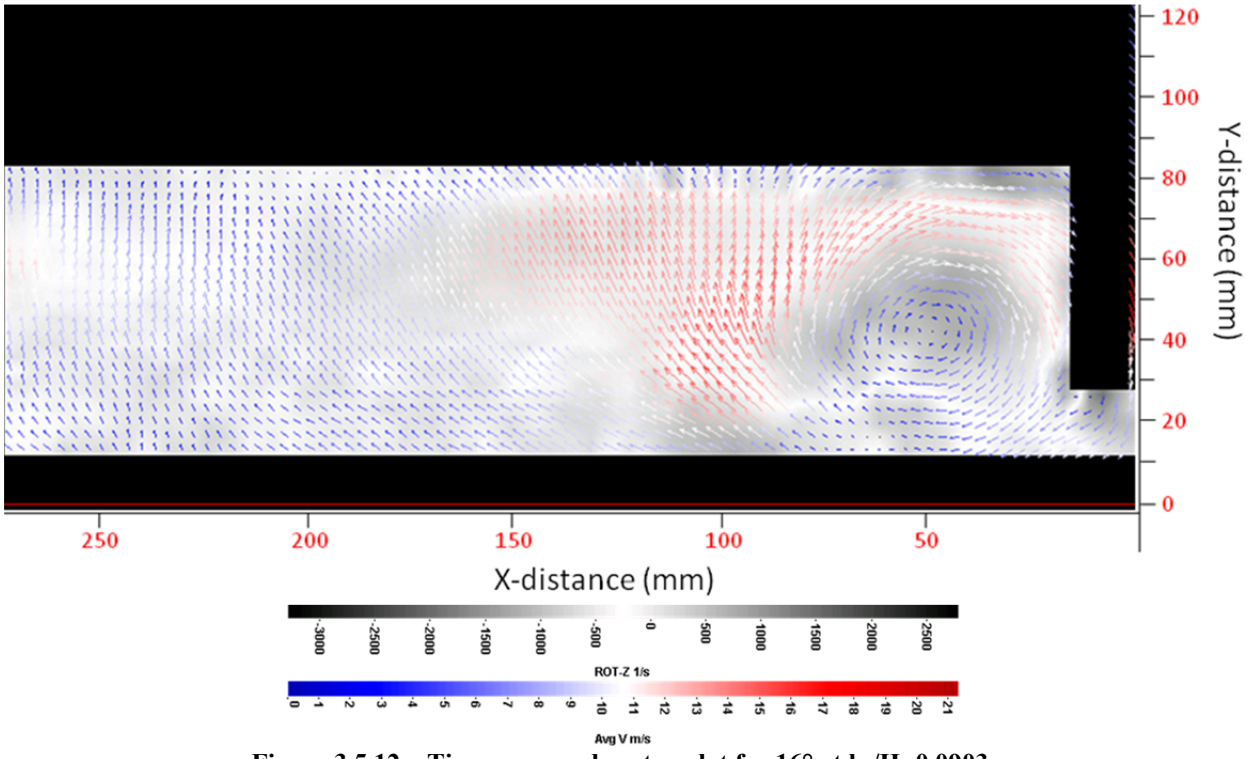

Figure 3.5.12 – Time-averaged vector plot for 16° at h_1/H=0.0903

Increasing the diffuser angle further to 19°, the main low pressure core of the vortex is again in a similar size and position to the lower angles but the shedding from the vortex affects a larger area with higher velocity vectors. The location of the vortex is reasonably constant relative to the floor and endplate so consistent with the thought it is being fed by flow under the endplate.

The upwash and inflow from under the end plates are still present in similar magnitudes however the major difference is the presence of a separation. This occurs near the diffuser plate surface and is symmetrical about the diffuser centreline as shown by the slow velocity vectors travelling towards the floor. Flow is drawn into this separated region suggesting why a decrease in downforce and an increase in drag is observed in the force measurements.

The greatest change in flow behaviour is seen with the 25° diffuser where a much weaker vortex is observed with lower velocity vectors; however the core is again in a similar position to the other diffuser angles. This suggests that flow is still being entrained under the endplates, (confirmed by areas of low pressure in Figure 3.4.6), but that due to the adverse pressure gradient in the diffuser and consequent separation, the vortex is weaker. There are no obvious signs of an upwash occurring as the majority of the flow shows separation. The flow from the vortex structure is drawn into the separated region. This explains the dramatic loss in downforce and increase in drag seen in the force measurements. However, the separated region appears to be relatively symmetrical about the diffuser centreline which is different to that observed in the area pressure maps (Figure 3.4.6) where asymmetry is observed.

The previous images are all acquired at a single ride height, in the following figures the results for the 19° diffuser at 28mm ($h_1/H=0.0903$) and 44m ($h_1/H=0.1419$) are compared. Increasing the ride height increases the vortex strength as shown by the increase in velocity and rotational velocity of the vectors as well as shifting the vortex core position towards the endplates. This is assumed to be due to the increased diffuser pumping contribution (identified by increase in depression at the inlet in Figure 3.4.2), and consequently increased inflow feeding the vortex. Additionally, the separated region reduces with increasing ride height which explains the decrease in drag observed in the force measurements (Figure 3.3.2). These observations are representative of changes in ride height for other angles.

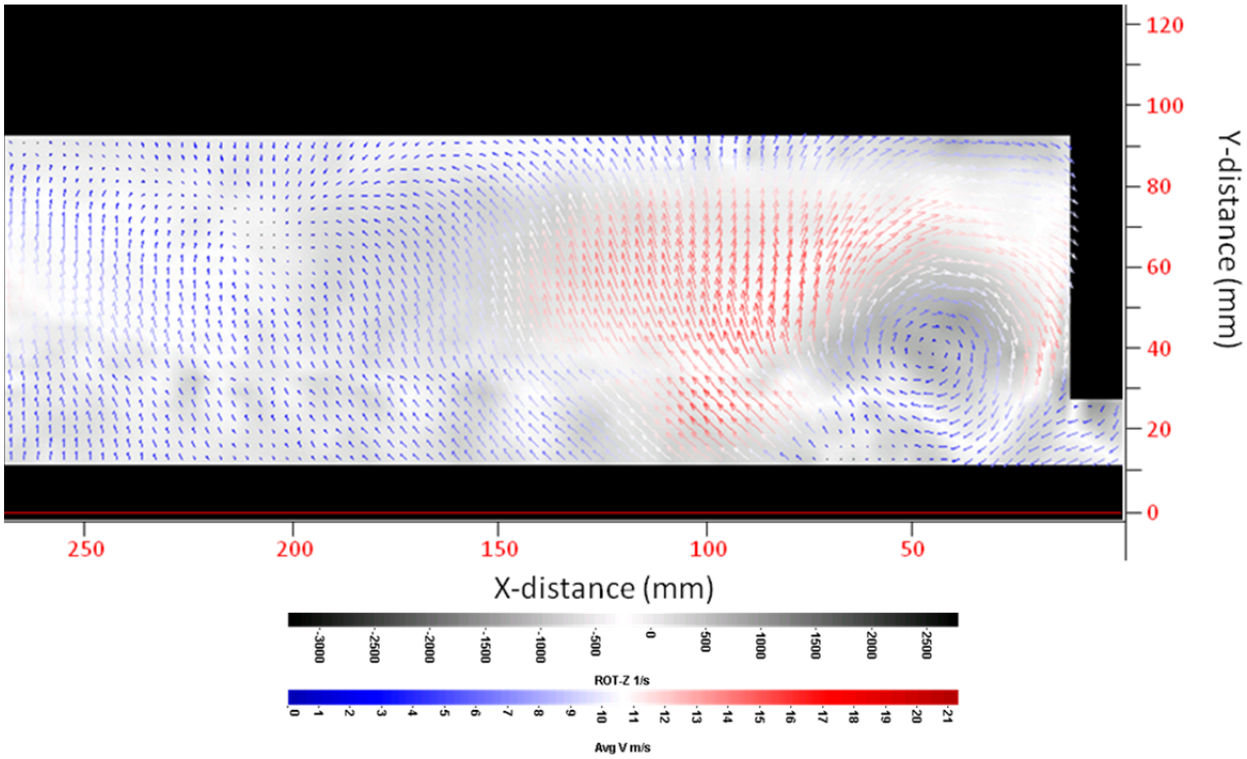

Figure 3.5.13 – Time-averaged vector plot for 19° at h_1/H=0.0903

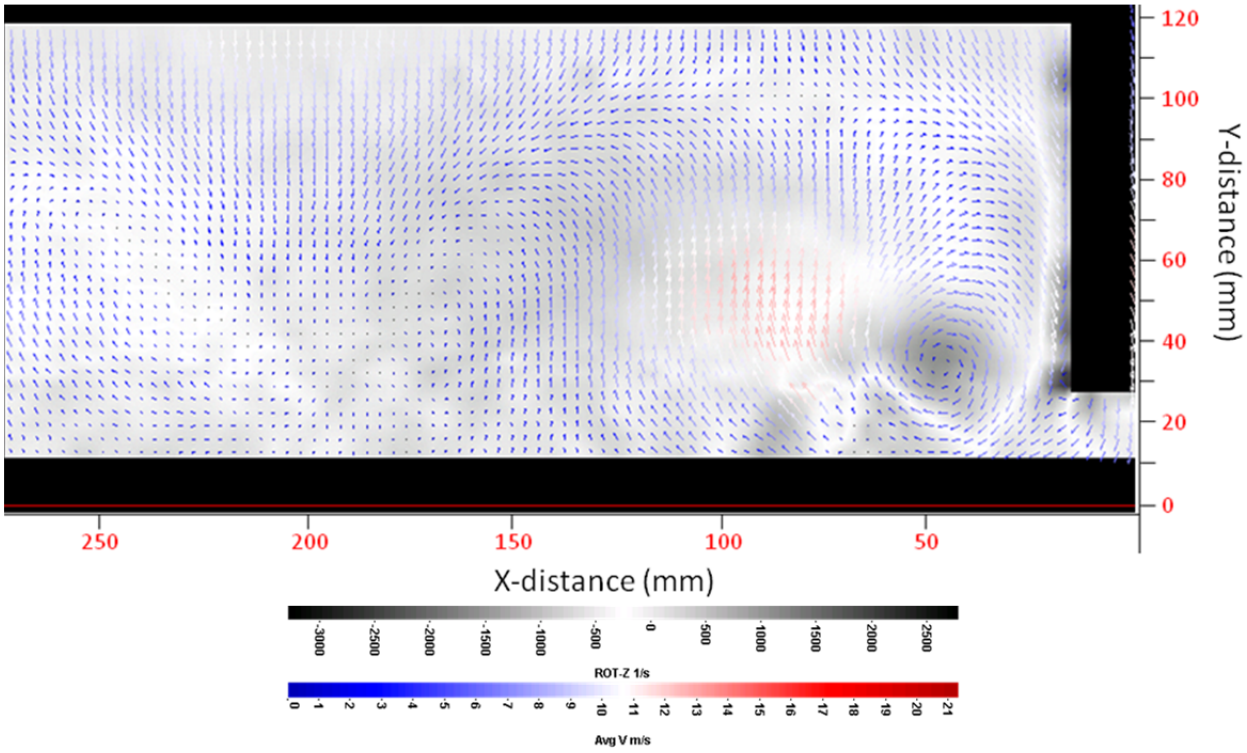

Figure 3.5.14 – Time-averaged vector plot for 25° at h_1/H=0.0903

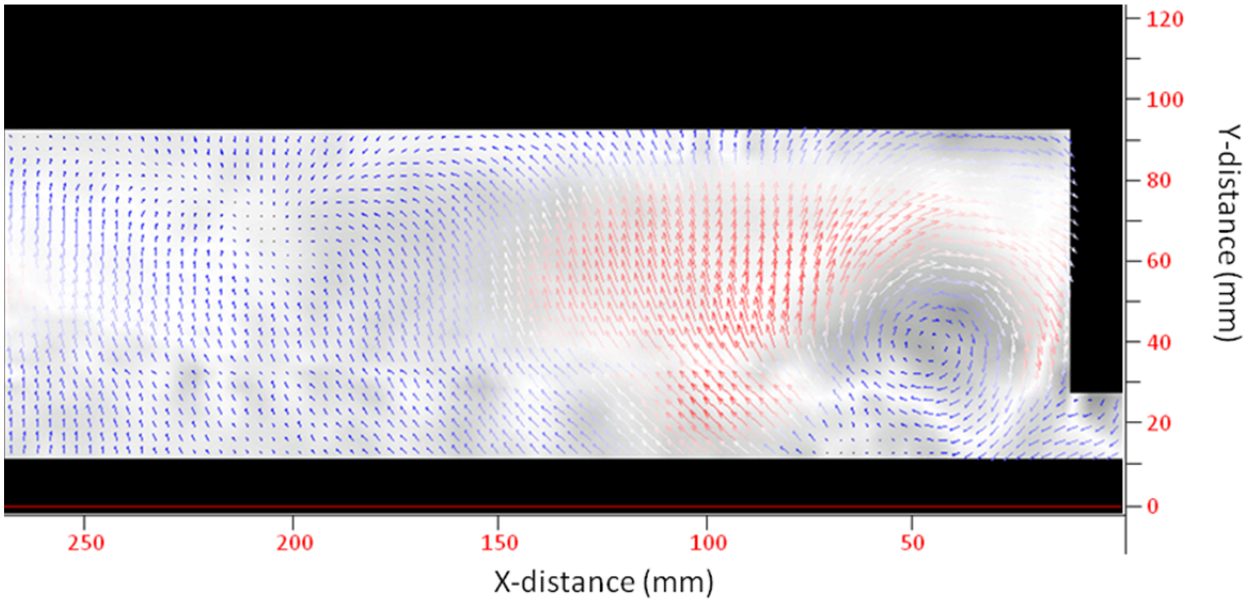

(a) - h_1/H=0.0903

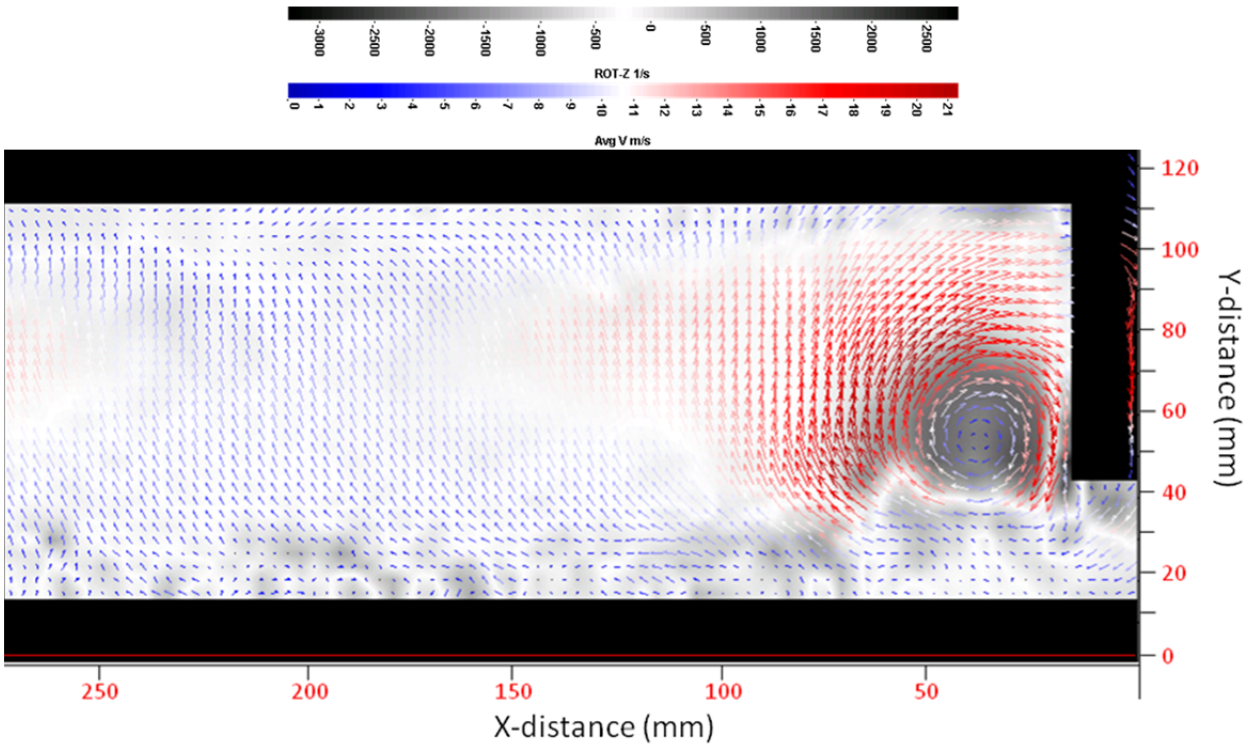

(b) - h_1/H=0.1419

Figure 3.5.15 – Time-averaged vector plot for 19° at h_1/H=0.0903 and h_1/H=0.1419

Chapter 4 - Multi-channel Diffuser Performance

It has been observed in conical diffusers ([25], [51], [52], [53], [54], [55]) that vanes and splitters can provide improved performance through the constraint of separation and increased three-dimensional flow. While the single-channel plane diffuser is effective, this conical diffuser behaviour suggests that the use of multiple channels could provide improved performance and usability. In the following sections the multi-channel diffusers (two-, three- and four-channel) will be presented, providing information on the performance changes observed when compared with the plane diffuser and offering suggestions as to why these changes occur. Results of force, pressure and PIV will be presented and compared with the baseline plane diffuser to establish the differences in performance and the reason for these variations.

4.1 Reynolds Number Sensitivity

Figure 4.1.1 shows the lift variation with Reynolds number for two-, three- and four-channel diffusers. The general trend is the same for all diffuser configurations with little or no C_L variation after a Reynolds number of 2.0 $x10^6$. As all tests are run at 40ms^{-1} (Reynolds number of approximately 2.25 $x10^6$) this confirms that this is a suitable velocity to ensure flow similarity. Additionally, results suggest that increasing the number of diffuser channels reduces the Reynolds sensitivity of the model as the general trend tends towards a flatter distribution as the number of channels increases and transitory angles as seen in the plane diffuser variation is not observed for multi-channel diffusers.

Plotting the same C_L data as a function of diffuser angle (Figure 4.1.2) the trends are similar to those seen for the plane configuration. However, for a fixed diffuser angle less variation in lift

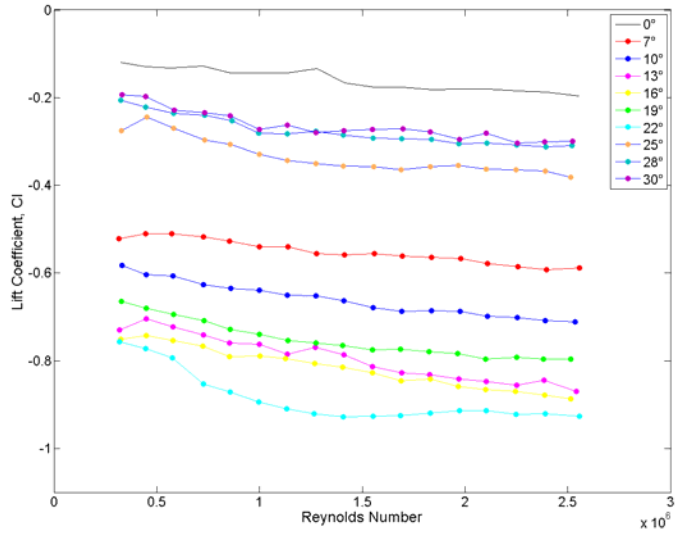

(a) – Dual-channel Diffuser

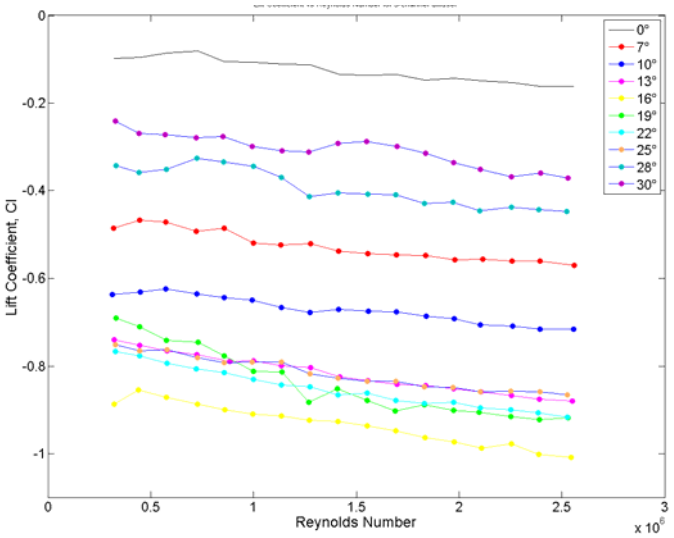

(b) – Three-channel Diffuser

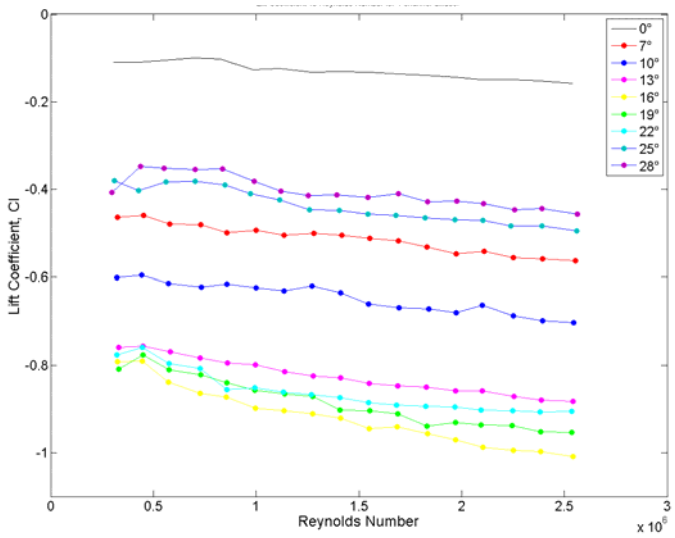

(c) – Four-channel Diffuser

Figure 4.1.1 – Graph of lift coefficient against Reynolds number for multiple channel diffusers

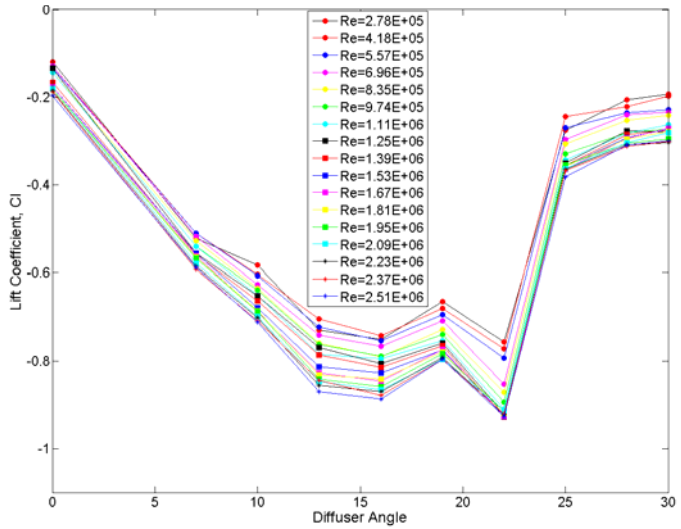

(a) – Dual-channel Diffuser

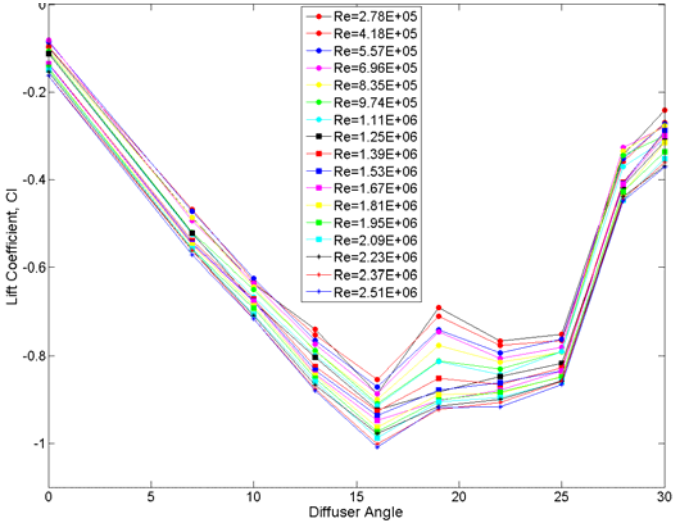

(b) – Three-channel Diffuser

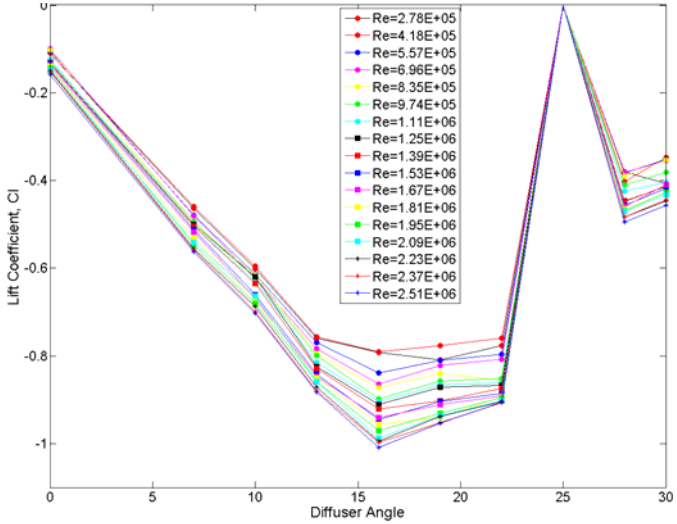

(c) – Four-channel Diffuser

Figure 4.1.2 – Graph of lift coefficient vs. diffuser angle for each Reynolds number for multiple channel diffusers

coefficient is observed in the multi-channel diffusers and the relationship becomes more consistent. This is particularly true at large angles where large variation was seen in the plane diffuser. Around the critical angle at 22° the results show each configuration lining up on each other, which is more pronounced as the number of channels is increased. This confirms that Reynolds number sensitivity is reduced as the number of channels is increased.

4.2 Yaw Sensitivity

Figure 4.2.1 shows the lift and drag variation for 10° and 28° diffusers, these angles were chosen for ease of comparison with the plane diffuser where they represented a high and low angle with differing performance.

At 10° diffuser angle, no real change in distribution is observed as the number of channels is increased. This suggests that the mechanisms at work are not largely affected with the presence of splitter plates. Increasing the angle to 28°, changes in variation are observed. The drag coefficient appears relatively independent of yaw angle irrespective of diffuser configuration.

The maximum lift coefficient occurs at a higher yaw angle as the number of channels is increased, but the difference between the minimum and maximum lift coefficient decreased as the number of channels increases. This could be due to an increase in cross-flow feeding the vortex structure and increasing downforce at large yaw angles.

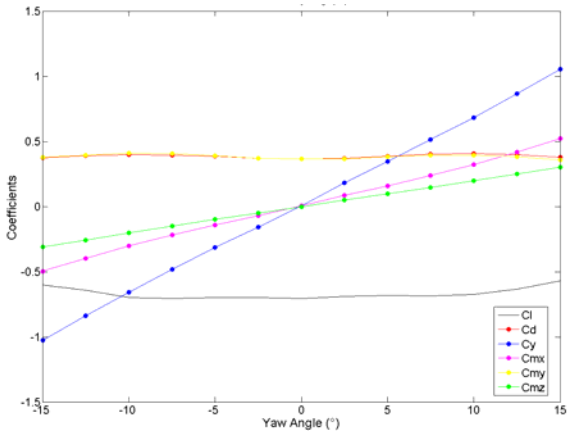

10°

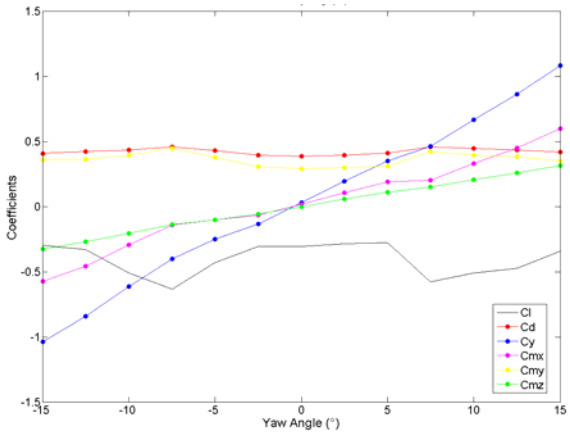

28°

(a) – Two-channel diffuser

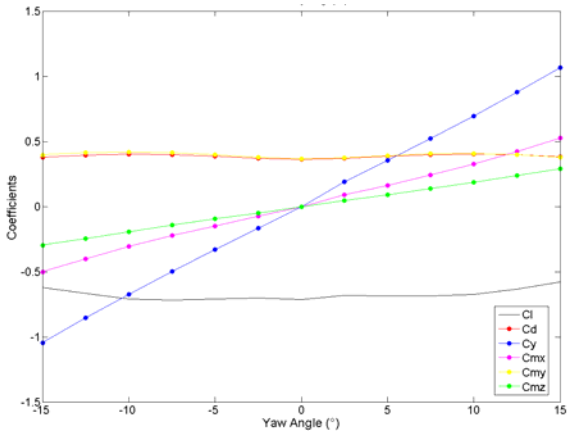

10°

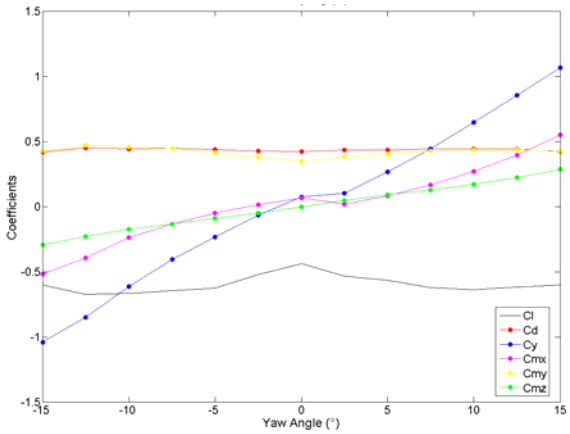

28°

(b) – Three-channel diffuser

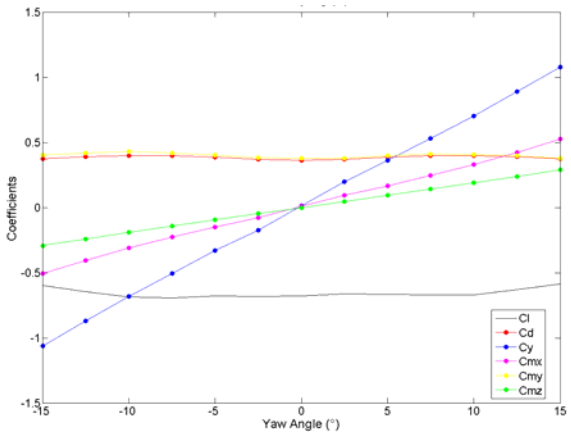

10°

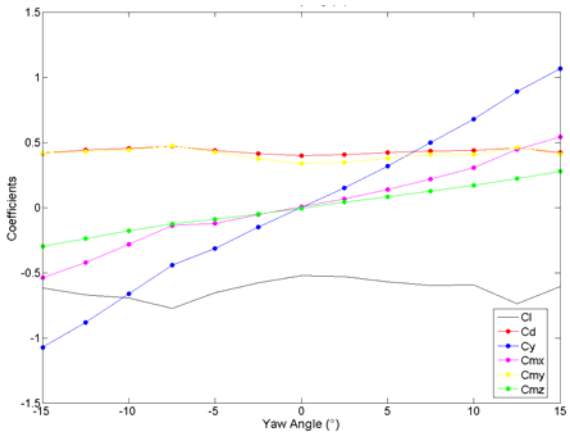

28°

(c) – Four-channel diffuser

Figure 4.2.1 - Graph of coefficients against yaw angle for 10° and 28° multiple-channel diffusers configurations

4.3 Multi-channel Diffuser Force Measurements

In the following section the multi-channel diffuser results are presented and compared with the plane diffuser. For clarity, the results comparing the diffuser configurations are plotted in three groups; low angles (0°-13°), mid angles (16°-19°) and high angles (22°-30°). These regions were chosen to represent angles that were assumed in the plane diffuser to be fully attached (low angles), partially separated (mid angles) and largely separated (high angles). It was thought that if the presence of splitters was to improve performance as suggested by conical diffuser work [25], then these regions would help identify the performance as the number of channels increased.

At small diffuser angles (Figure 4.3.2a) all four diffuser configurations exhibit similar trends; as the number of channels is increased, the downforce is reduced marginally. As these small angles are assumed to be largely attached in the plane configuration, the division into an increased number of channels has no advantage in promoting improved diffuser flow. The small reductions arise because the channel splitters reduce the active area of the diffuser. Examining this further, the multiple-channel configurations actually produce greater downforce per unit area, as shown in Figure 4.3.1, where the lift coefficients are corrected for diffuser area. As the number of channels is increased, downforce magnitudes also increase, with a more pronounced effect as the diffuser angle is increased. At 13°, this increased downforce performance with multiple-channels is seen in the non-area-corrected coefficients (Figure 4.3.2(a)) with a slight downforce improvement observed, particularly at low ride heights. As Chapter 3 showed that the plane diffuser is largely attached, the improvement must be due to an improvement in one of the downforce mechanisms rather than any changes in the separation characteristics, because a drag reduction is observed whereas increased vortex strength and associated downforce improvement would be expected to increase the drag

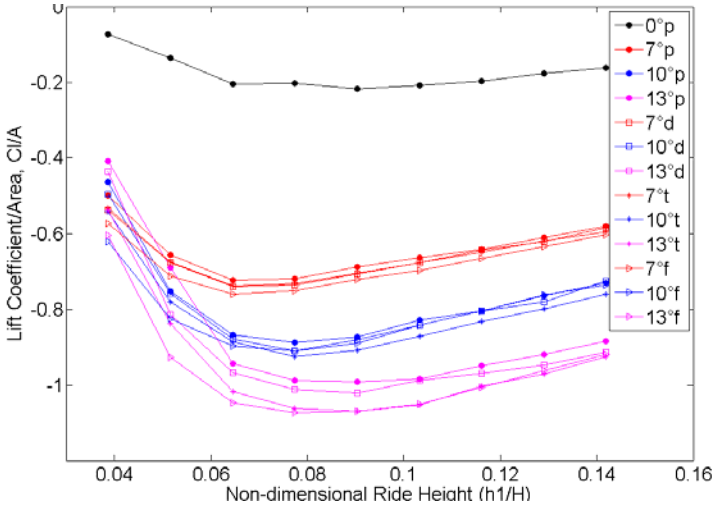

Figure 4.3.1 – Area-corrected lift coefficient for plane and multi-channel diffusers for low angles

At mid-range angles (Figure 4.3.2b) the differences between the plane and multi-channel diffusers is more pronounced. While the trends are the same, splitting the diffuser gives an improvement in the downforce due to an increase in the diffuser pumping contribution. As separation was present in the plane diffuser (Figure 3.4.5), increased diffuser pumping results in an increase in the vortex strength. This is due to increased pressure difference causing flow to travel underneath the endplates therefore increasing vortex strength. This phenomenon is similar to that seen in [13] where a change in the diffuser pumping due to a change in ride height resulted in an increase in vortex strength. This increased vortex strength can aid flow attachment and improve the downforce [18]. In these mid-range diffuser angles the total downforce is increased by 13% compared with the optimum plane diffuser, significantly extending the performance envelope.

At the largest angles (Figure 4.3.2c) the difference between the configurations is much larger, with the multiple-channel diffusers working much more efficiently than the plane diffuser does. This improvement is attributed to reduced levels of separation, due to the presence of the splitter plates.

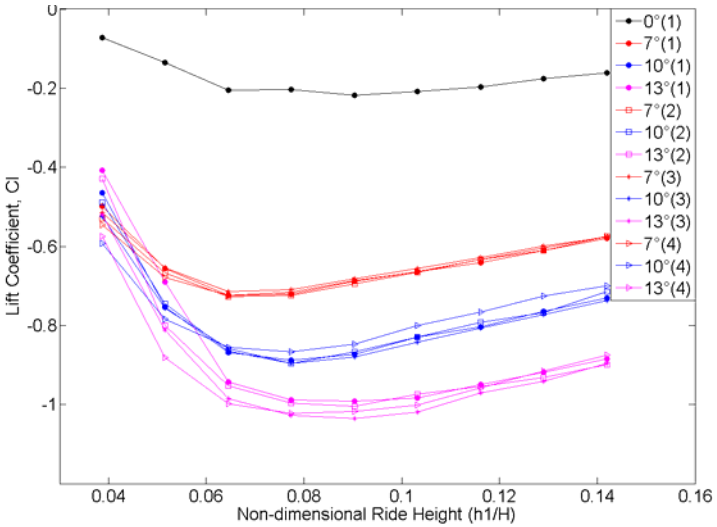

(a) – Low angles

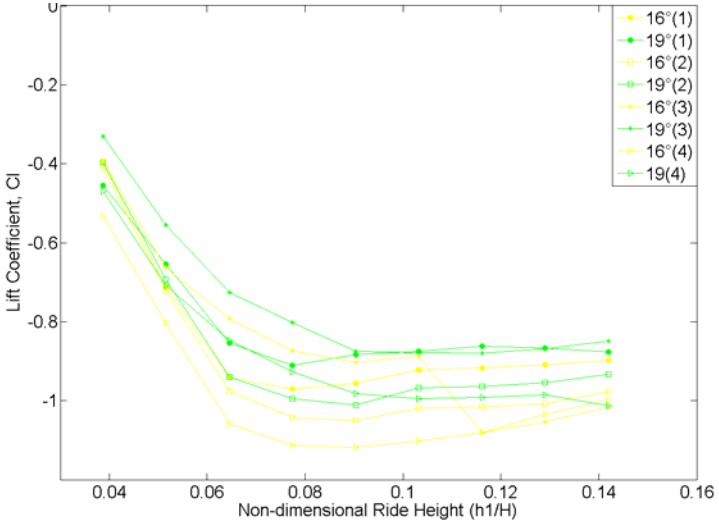

(b) – Mid-angles

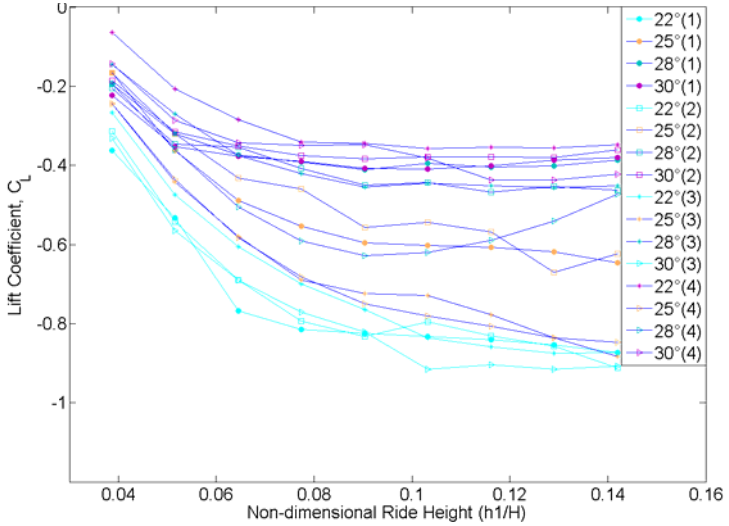

(c) – High angles

Figure 4.3.2 - Graph of lift coefficient against non-dimensional ride height for multi-channel diffuser

The contour plots of diffuser-based downforce for the plane and multi-channel diffusers are shown in Figure 4.3.3. The multi-channel diffusers exhibit the same general trend as seen in the plane diffuser with downforce passing through an optimum as the area ratio parameter increases for a fixed non-dimensional length.

It can be seen that as the number of channels is increased the optimum range of angles increases, which could be due to a reduced adverse pressure gradient with the presence of splitter plates. The maximum downforce angles are consistently between 13° and 22°, however, the magnitudes of downforce produced at these angles increases in the multi-channel configurations. Additionally, as the number of channels is increased, the configurations become less sensitive to change in ride height (i.e. passing through fewer contours) particularly at low to mid angles.

The change in performance between the plane and multi-channel configurations is calculated by subtracting the plane diffuser data from the multi-channel diffuser data as expressed in Equation 4.3.1. The resulting contour plots are shown in Figure 4.3.4 and a more negative contour highlights an increase in downforce.

$$\Delta C_L = C_{L(two-channel)}(\alpha) - C_{L(plane)}(\alpha) \qquad \textbf{Equation 4.3.1}$$

For all multiple-channel diffusers, much of the figures show little or no performance improvement with the changes sufficiently small (±0.05) not to have a significant effect on road vehicle handling [40], although the gains might be considered important in the ongoing development of a race car. However, in some parts of the figures, the changes are much greater than this. In the two-channel diffuser (Figure 4.3.4a) there are much larger gains, up to C_L= 0.125 at mid-range to large angles for a small range of area ratios and ride heights. For the three-channel diffusers (Figure 4.3.4b) improvements are observed at high area ratios, predominantly at an angle of 25°, where the improvement is between 0.15 and 0.20. The four-channel diffuser (Figure 4.3.4c) produces the greatest performance improvement covering two distinct regions; one of high area ratios and high ride heights and the other of medium area ratios and low ride heights. In these areas the downforce is increased by up to 0.20. An improvement of 0.15-0.20 represents a 5-7% improvement for an F1 car with an overall lift coefficient of C_L= -3 and should be viewed in the context of typically 6-10% [8] improvement over a full race season.

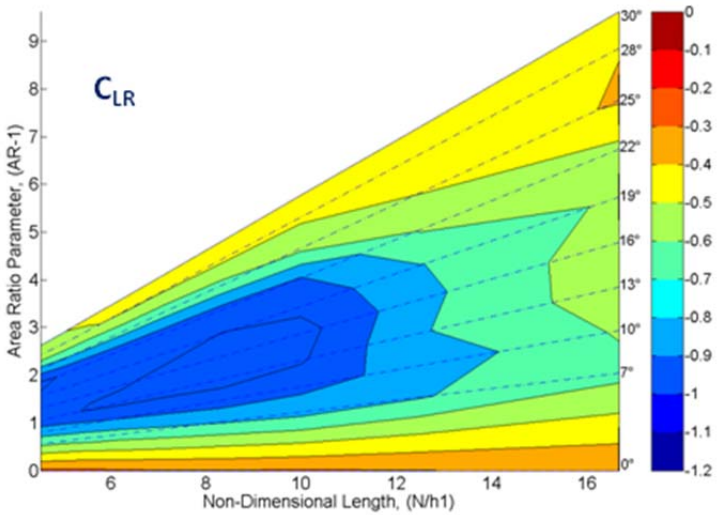

(a) – Plane Diffuser

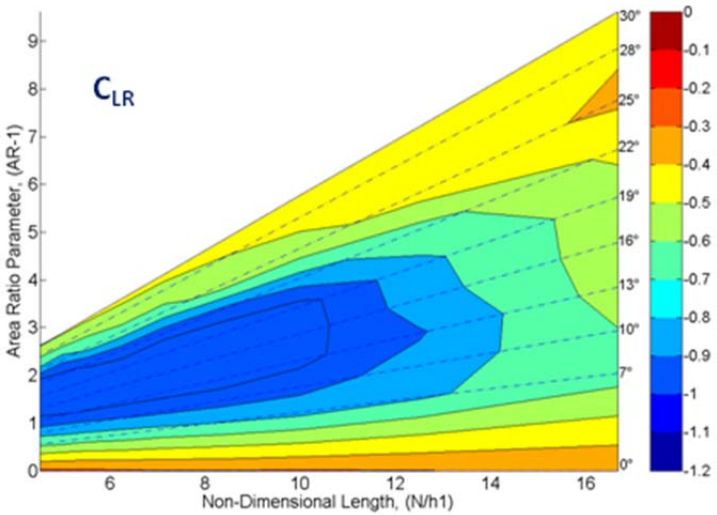

(b) – Dual-channel Diffuser

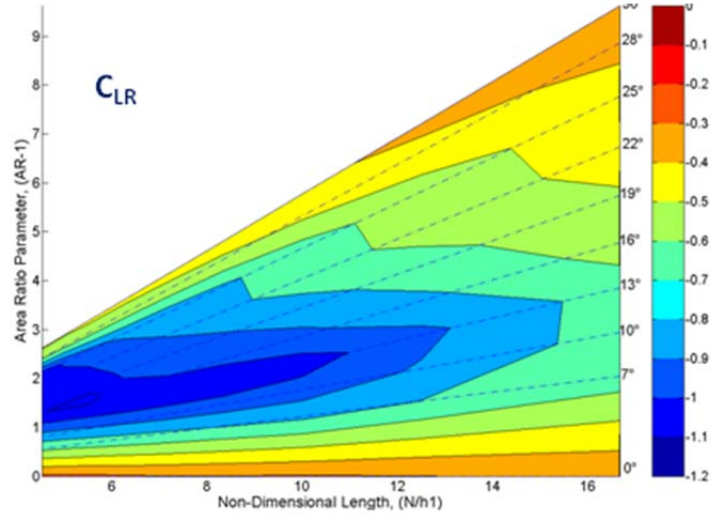

(c) – Three-channel Diffuser

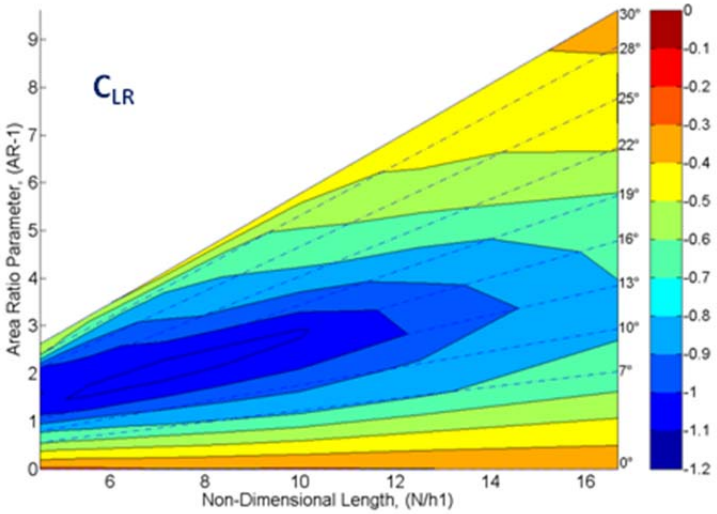

(d) – Four-channel Diffuser

Figure 4.3.3 - Contours of diffuser-based downforce for all diffuser configurations

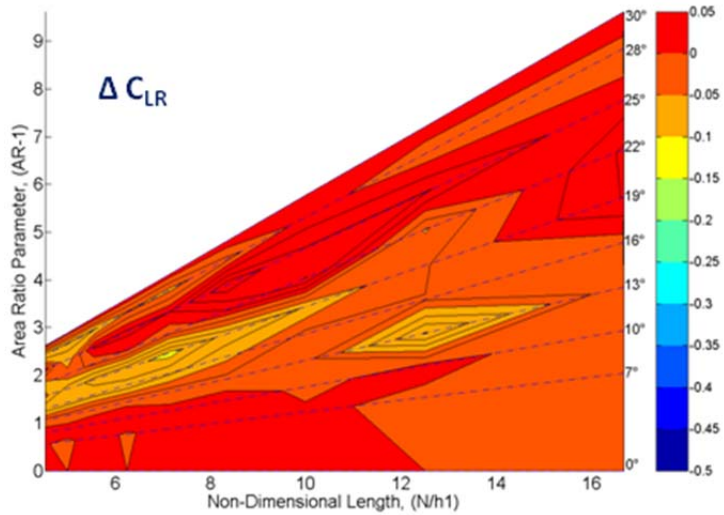

(a) – Dual-channel Diffuser

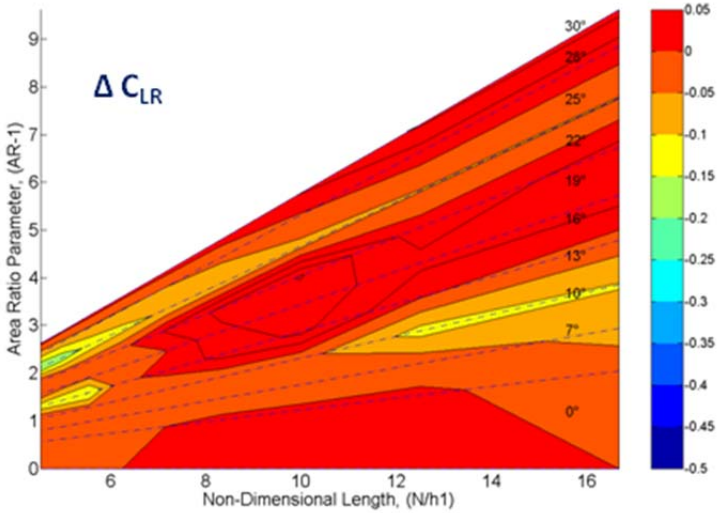

(b) – Three-channel Diffuser

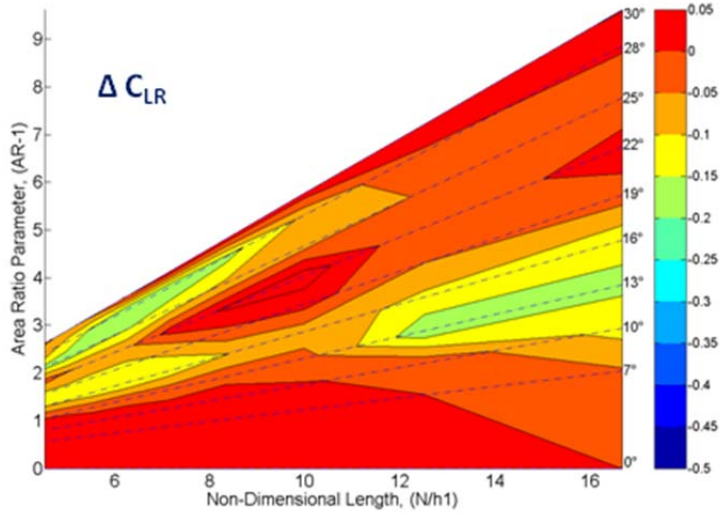

(c) – Four-channel Diffuser

Figure 4.3.4 - Contours of difference in diffuser-based downforce between plane and dual-channel diffusers

Although downforce production is of utmost importance, particularly in a motorsport application, increased amounts of downforce generally result in increased drag. As with the lift coefficient, the difference in drag coefficient (ΔC_D) was used to highlight the difference using Equation 4.3.2.

$$\Delta C_D = C_{D(multi-channel)}(\alpha) - C_{D(plane)}(\alpha) \qquad \textbf{Equation 4.3.2}$$

The contour plots of difference in drag coefficient are presented in Figure 4.3.5 and are similar to Figure 4.3.4 most of the plot shows changes in drag of ±0.01 between the diffusers. This magnitude of drag reduction is significant in the development of road vehicles, although larger changes in drag are observed. The two-channel diffuser (Figure 4.3.5a) has an increase in drag coefficient seen at high angles (22° to 30°) and high ride heights (low non-dimensional lengths) which may be attributed to an increased vortex drag component consistent with the increase in downforce in this region. A reduction in drag (ΔC_D=-0.01 or more) is seen in regions of high (and very low) angles at mid to high ride heights. This may be due to reduced levels of flow separation due to the presence of splitter plates.

The three- and four-channel diffusers (Figure 4.3.5b & c) show more pronounced changes. An increase in drag is observed at high angles and high ride heights, as observed in the two-channel configuration. A marked improvement however is seen across nearly all ride heights at angles between 16° and 30°, with a drag reduction up to ΔC_D=-0.05. This could be due to reduced levels of flow separation, despite an increase in vortex drag through improved downforce.

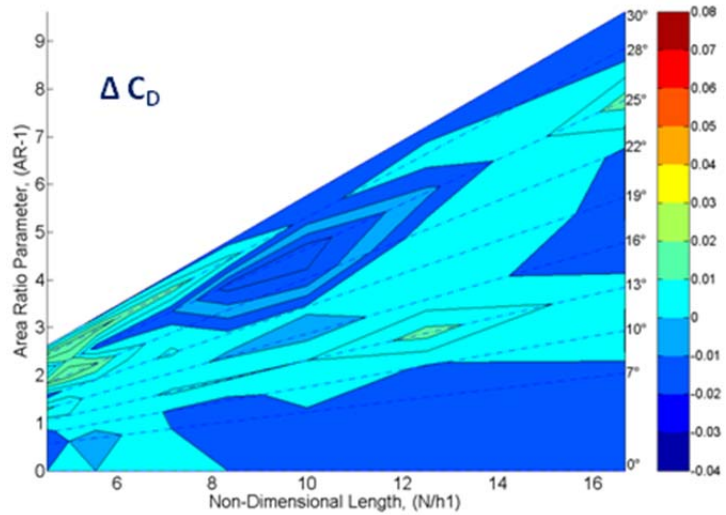

(a) – Dual-channel Diffuser

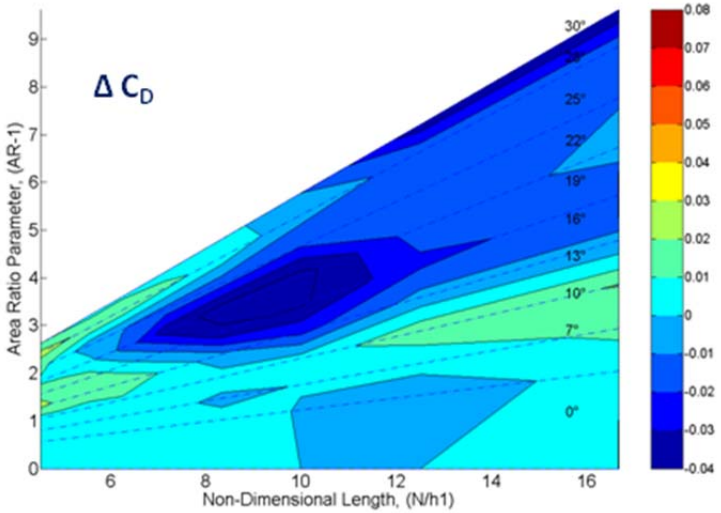

(b) – Three-channel Diffuser

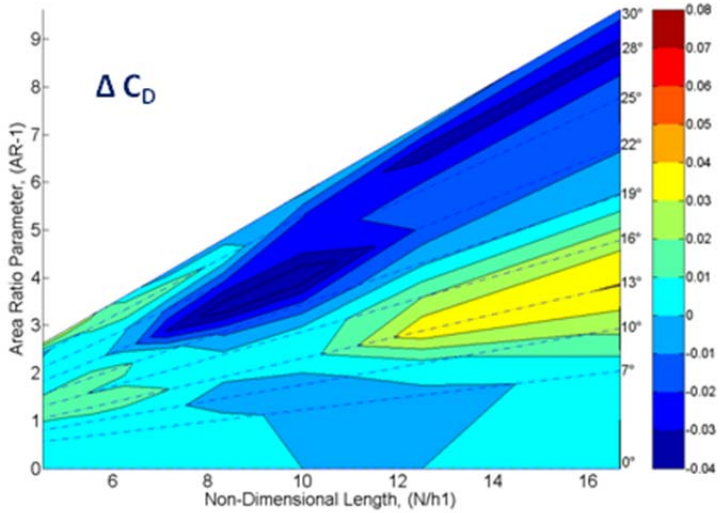

(c) – Four-channel Diffuser

Figure 4.3.5 - Contours of difference in drag between plane and dual-channel diffusers

Although it is important to consider overall drag of each configuration, a more relevant term in automotive aerodynamic design is the lift-to-drag ratio, monitoring the best compromise for a particular set of requirements. Figure 4.3.6 depicts the contours of lift-to-drag ratio for all four diffuser configurations. It shows that all multi-channel configurations exhibit the same general trend observed with the plane diffuser, of increase in area ratio parameter resulting in downforce passing through an optimum. The optimum angle regions are similar for all configurations, generally between 10° and 22°, with the exception of the two-channel diffuser. Additionally, it is seen that as the number of diffuser channels is increased the configurations become less sensitive to change in ride height.

Continuing the approach of presenting the 'change' in performance, the lift-to-drag ratio results are shown in Figure 4.3.7. Because the results deal primarily with downforce, and therefore negative C_L, the more negative the values are the most efficient.

It was identified that, for the two- and three-channel diffusers, the improvement is limited to distinct regions; the two-channel (Figure 4.3.7.a) improvement is seen at 16°-19° at high ride heights, while the three-channel (Figure 4.3.7.b) improvement occurs between 22° and 28° and between 10° and 16° at low ride heights. The four-channel diffuser (Figure 4.3.7.c) shows large improvements in the majority of the configurations. The gains occur mainly at large angles and high ride heights although improvement is seen at the mid-range angles which have not been identified in other configurations. These regions of performance improvement occur where the plane diffuser begins to be compromised by the onset of separation, as identified in Figure 4.3.2. These findings would support the suggestion that increasing the number of channels in the diffuser increases the diffuser's ability to withstand an adverse pressure gradient (longitudinally and radially). This results in less separated flow (lower drag) and more attached flow leading to increased downforce.

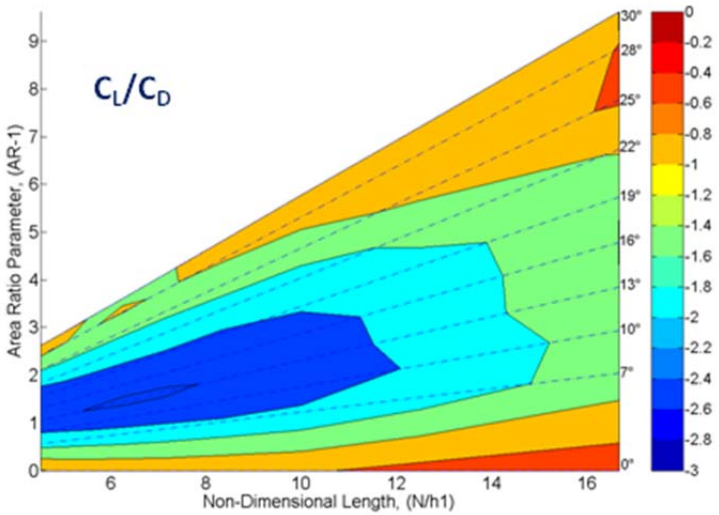

(a) – Plane Diffuser

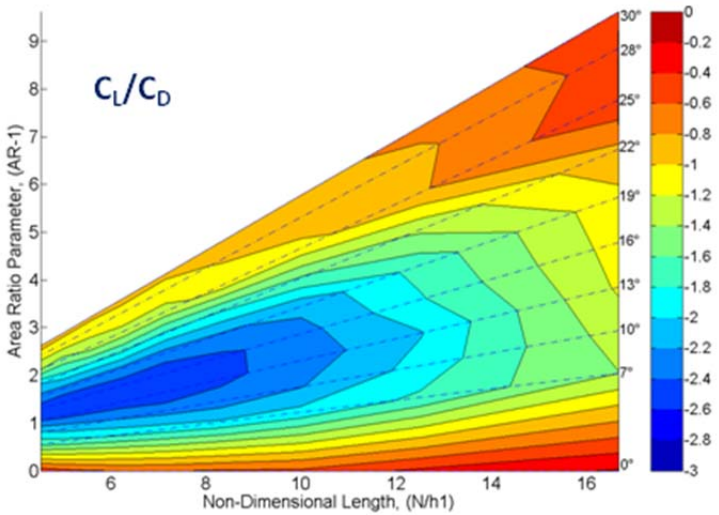

(b) – Dual-channel Diffuser

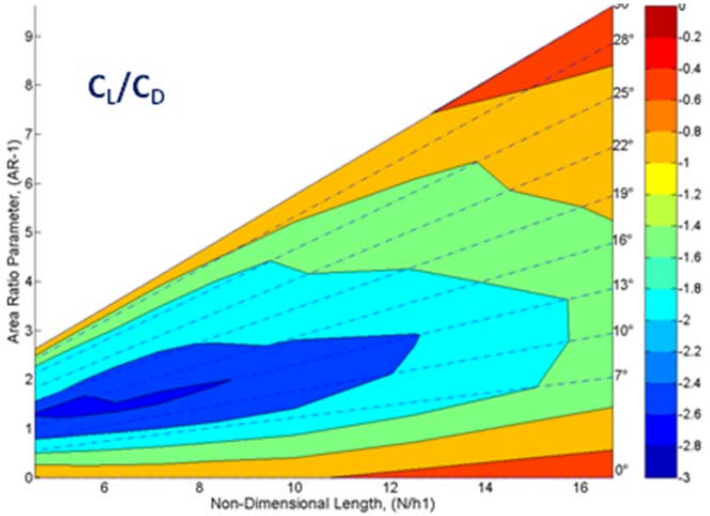

(c) – Three-channel Diffuser

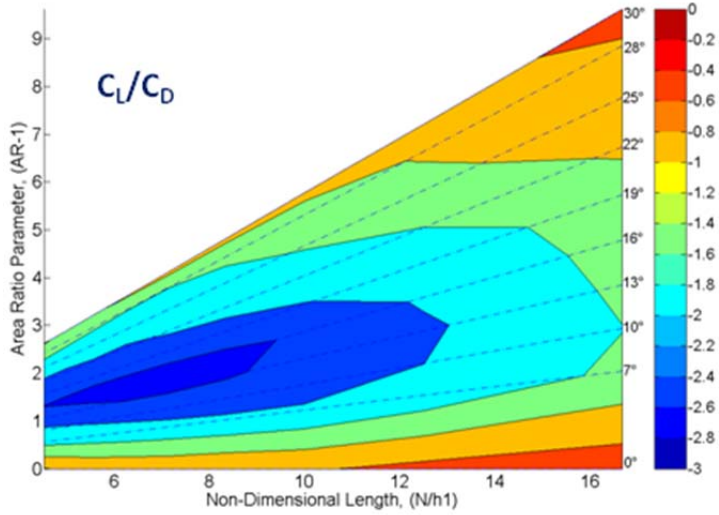

(d) – Four-channel Diffuser

Figure 4.3.6 - Contours of lift-to-drag ratio for all diffuser configurations

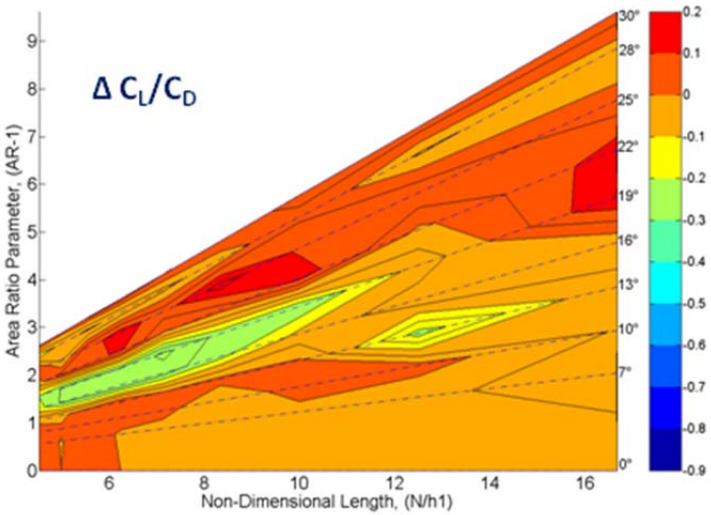

(a) – Dual-channel Diffuser

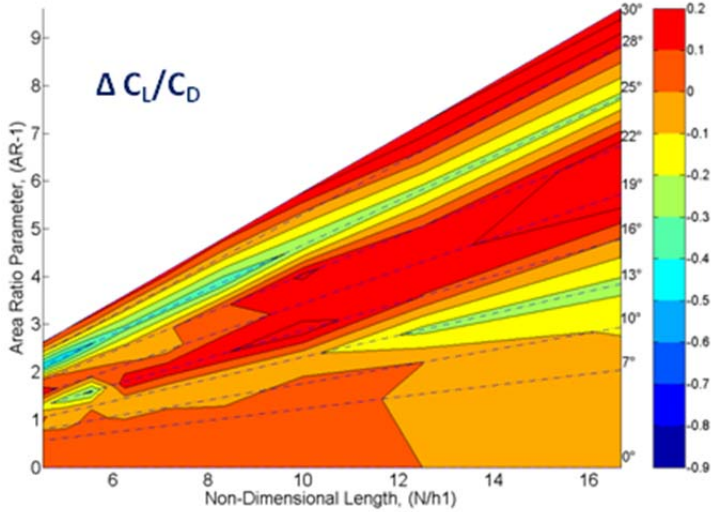

(b) – Three-channel Diffuser

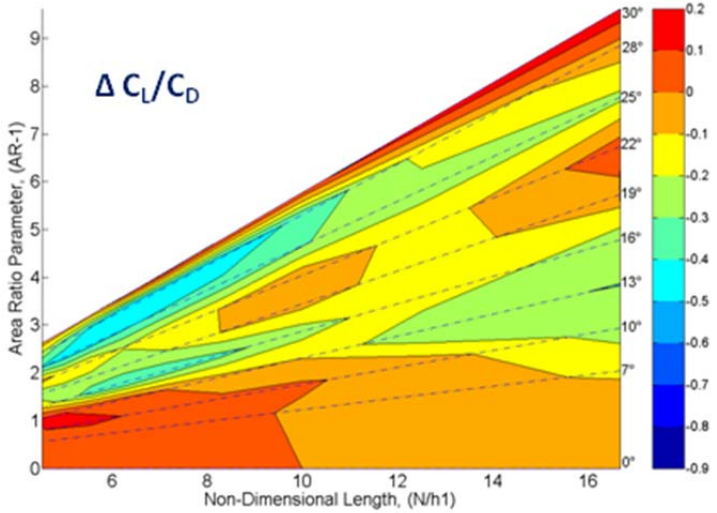

(c) – Four-channel Diffuser

Figure 4.3.7 - Contours of difference in lift-to-drag between plane and multi-channel diffusers

4.4 Multi-channel Diffuser Pressure Measurements

The following pressure measurements were taken at the centreline of one channel in each configuration as described in Section 2.1. Using the plane-channel configuration as a baseline distribution, comparisons should provide information as to changes in pressure recovery between configurations and therefore downforce distribution.

Figure 4.4.1 shows the diffuser channel centreline pressure distributions for the plane- and multi-channel diffuser for three angles at h_1/H=0.0903. The general trend is similar for all diffuser angles; a stagnation point at the front face of the model, acceleration around the lower front edge followed by a pressure recovery along the flat underbody before the characteristic depression at the diffuser inlet and recovery to base pressure. This suggests that the general behaviour of the diffusers (at the centreline) does not change dramatically when the width is changed (i.e. by the presence of the splitters). The primary differences observed are in the two regions of the flat underbody, where the plane diffuser has the lowest underbody pressures and in the diffuser where the greatest changes are observed. The largest of which is seen in the 25° diffuser where a marked improvement in pressure recovery is observed for the three- and four-channel diffusers, consistent with the force measurement in Section 4.3.

These results are useful for the general trend of pressure distribution, however, because the channel centrelines are at diffuser positions laterally across the model, it makes direct comparisons difficult. For this reason in Figure 4.4.2 measurements of channel centreline are plotted for the 13° diffuser with the corresponding lateral position on the plane diffuser.

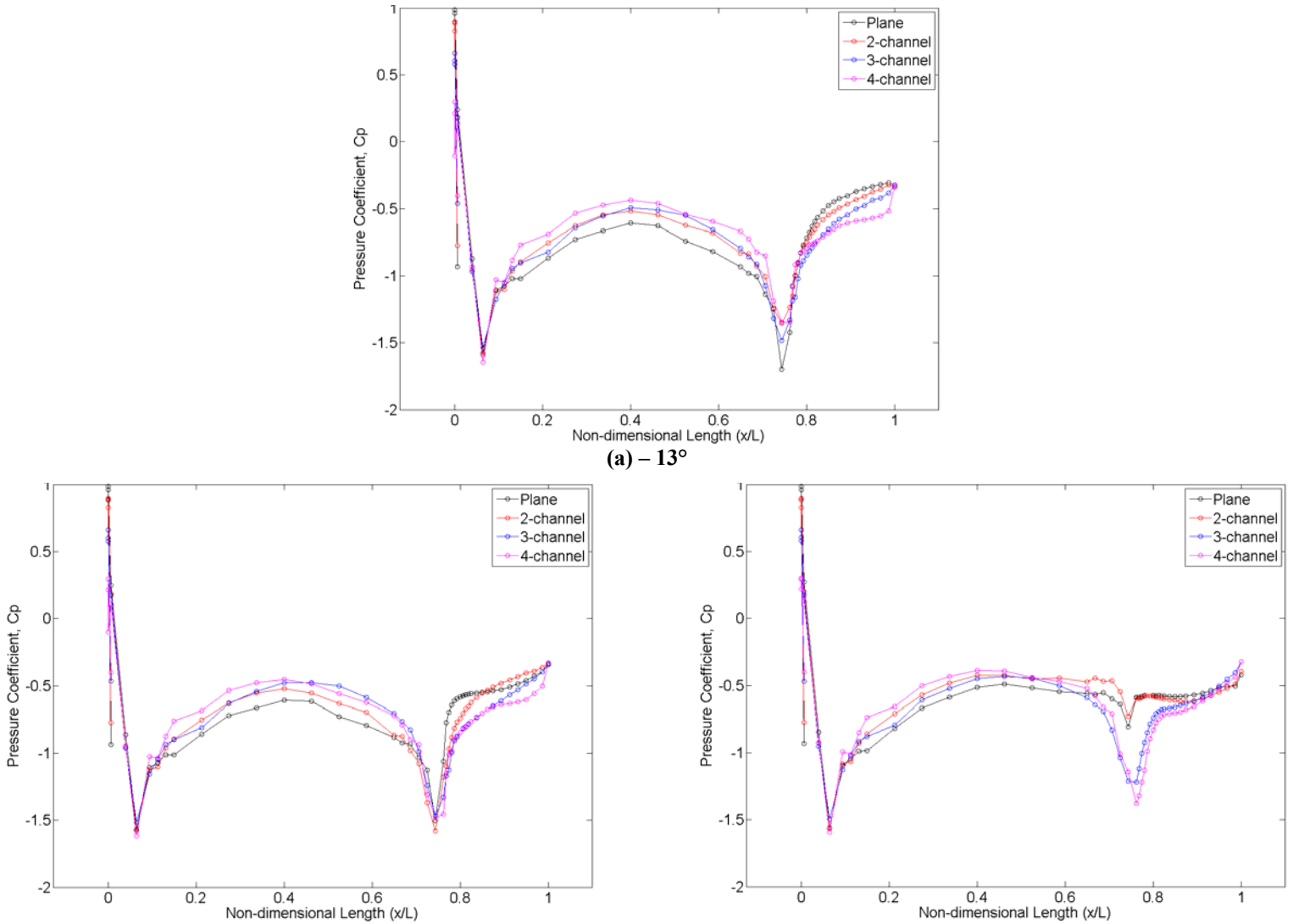

(a) – 13°

(b) – 16°

(c) – 25°

Figure 4.4.1 – Channel centreline pressure distributions for all diffuser configurations at 28mm ($\frac{h_1}{H}$ =0.0903)

At a fixed ride height, it can be seen that for the multi-channel configurations the pressure distributions are very similar to the corresponding plane pressure distributions around the front edge and flat underbody where little or no difference is observed. The primary differences are from the diffuser inlet at x/L=0.65 onwards. In this region, as the number of channels is increased the greater the differences between the plane and multi-channel configurations, such that the multiple channels have greater inlet depression and improved pressure recovery compared to the corresponding plane diffuser. This is due to different positions and influence of the vortex structure present in the multiple diffusers.

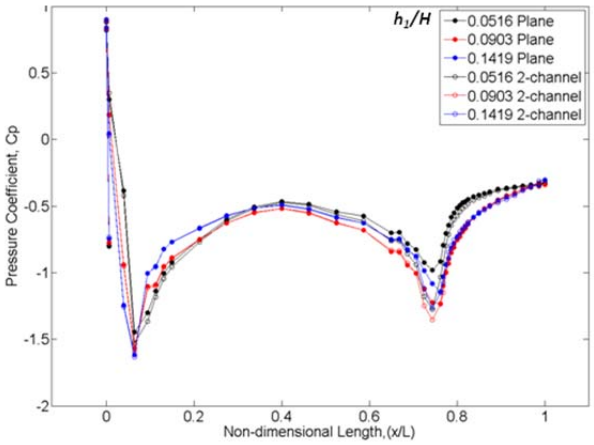

(a) - Two-channel

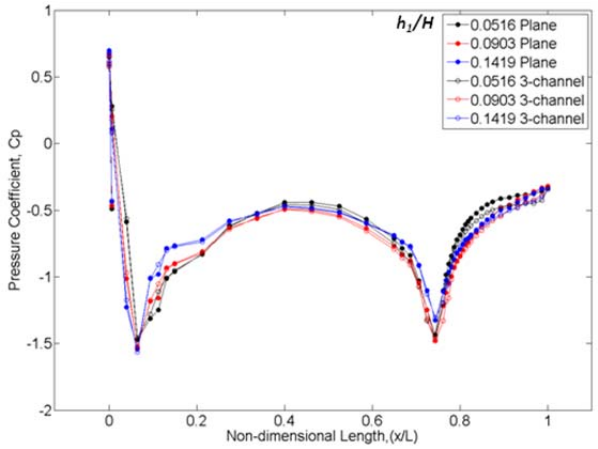

(b) - Three-channel

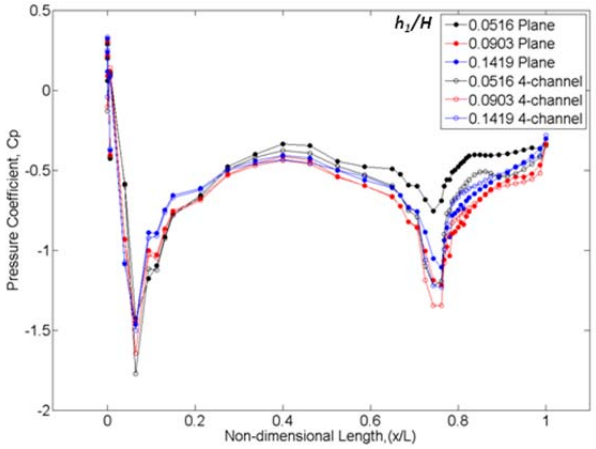

(c) - Four-channel

Figure 4.4.2 – Channel centreline pressure distributions multi-channel centreline and plane equivalent at 13°

The centreline pressure data gives an overall view of the typical distribution, but are less useful for the multiple-channel configurations because the centreline of the model in some configurations, is the location of a splitter plate and the centreline of each channel is in a different lateral location. Pressure data for the multi-channel and plane diffuser configurations are therefore presented in the following figures in the form of contour plots. The plots begin just upstream of the diffuser inlet (x/L=0.75) and show an area of half the model width, which

therefore covers a different number of channels in each configuration; half in the plane diffuser, one in the two-channel diffuser, one and a half in the three-channel diffuser and two channels in the four-channel diffuser. The endplates (y/L = 0.25) and splitter plates (y/L=0, y/L=0.114 and y/L=0.152) are shown in the figure for clarity and the pressure tapping positions are shown in the figures as open circles. Three diffuser angles, (namely 13°, 16° and 25°), are presented at a single ride height of h_1/H=0.090 (28mm). The 13°data (Figure 4.4.3) all show areas of low pressure at the inlet (x/L=0.75) corresponding to the diffuser pumping depression observed in the centreline pressure distributions (Figure 4.4.1). Low pressures are also seen near the end plates (y/L=0.25) at the location of the vortex structures. At the exit of the diffuser the pressure is close to base pressure.

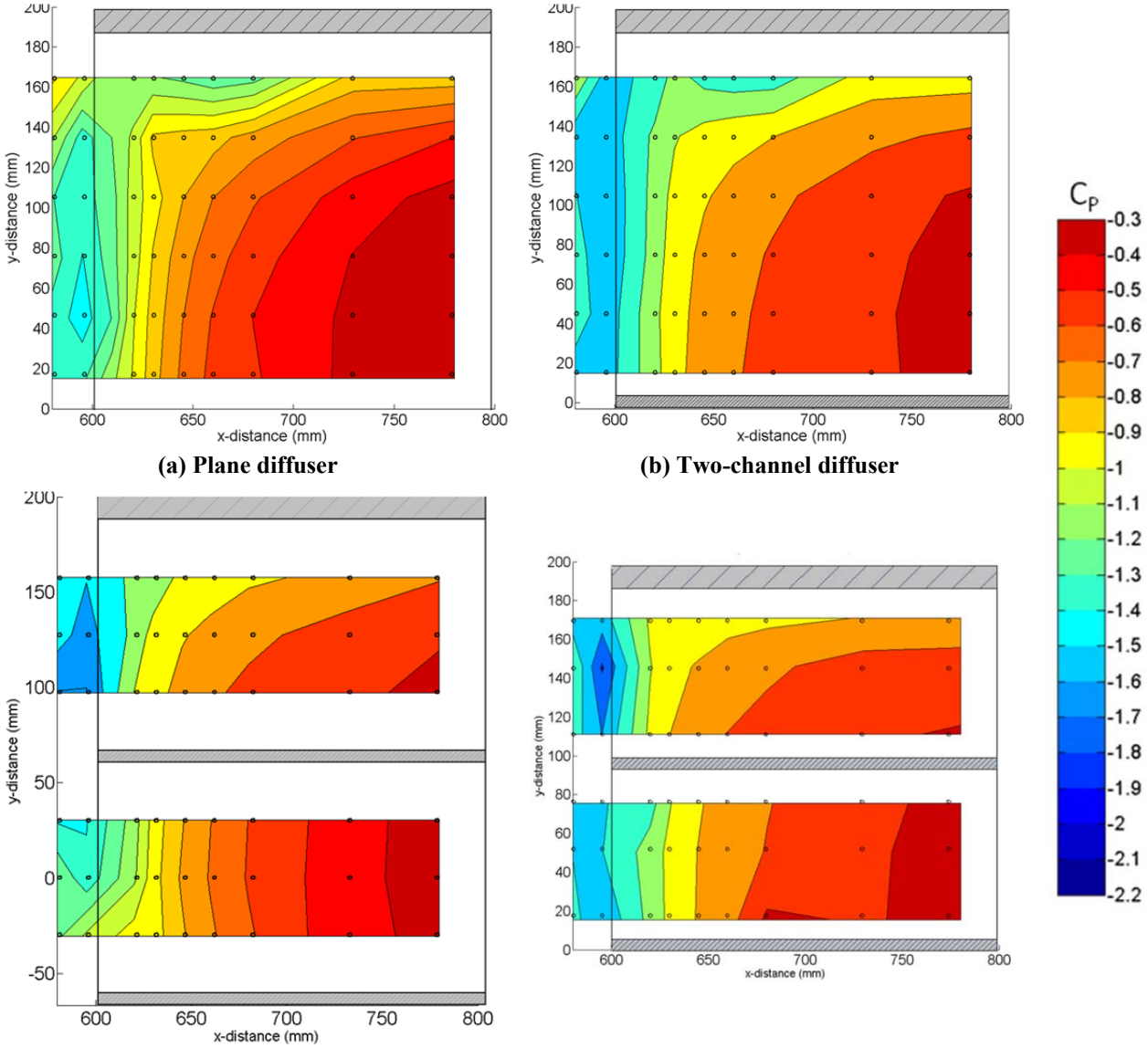

(a) Plane diffuser **(b) Two-channel diffuser**

(c) Three-channel diffuser **(d) Four-channel diffuser**

Figure 4.4.3 – Contours of pressure coefficient for all 13° diffusers at h1/H=0.0903 (28mm)

The plane (Figure 4.4.3a) and two-channel diffuser (Figure 4.4.3b) show very similar distributions, the primary difference being that lower pressures at the inlet are observed in the two-channel from an increased diffuser pumping component. This results in greater inflow into the diffuser channel 'feeding' the vortex structure, shown by lower endplate region pressures. The presence of the splitter plate gives lower pressures at the inlet and end plate region. In reference [14], surface flow visualisation showed S-shaped lines to be more pronounced as the vortices increased in strength, with areas of lower pressure observed around the end plates similar to that seen here. Therefore, it is assumed that the splitter plates help to increase the vortex strength by constraining it into a smaller diffuser channel, similar to the containment of separation seen in conical diffusers with vanes and splitters [25]. The strengthening of the vortex structures makes them more resistant to breakdown and aid attachment resulting in a higher downforce magnitude. As the non-dimensional length is increased, the number of contours passed through is reduced showing a more gradual pressure recovery and greater downforce, confirmed by the force measurements (Figure 4.3.2) which gave a 1.4% improvement for this configuration.

The three- and four-channel configurations each show an inside and outside diffuser channel (Figure 4.4.3c and d). In both cases the outside channels perform better with greater diffuser pumping at the inlet, the three-channel exhibiting the greatest diffuser pumping of all configurations. This increase in diffuser pumping results in stronger vortex structures which are then constrained due to the decreased channel width. The combination of increased diffuser pumping and upwash results in the increase in downforce observed in the force measurements of 4.4% and 2.7% for the three- and four-channel diffusers respectively. The inside channel for the three and four-channel diffusers have similar distributions to the equivalent position on the plane and two-channel configurations respectively, despite the presence of the splitter plates. This suggests that these distributions are independent of the presence of vortex structures and therefore affected primarily by upsweep component and pressure gradient such that if separation occurs it is likely to occur in this region.

Increasing the diffuser angle to 16° (Figure 4.4.4) shows only relatively small differences compared to the 13° diffusers; similar variations are observed but with less diffuser pumping at inlet. The two-channel diffuser has greater diffuser pumping than the plane diffuser leading to increased vortex strength, which is identified by lower pressures in the endplate region. The centreline pressure measurements (Figure 3.4.2) identified separation in the plane configuration, however the increase in vortex strength in the two-channel diffuser aids flow attachment giving a more gradual pressure recovery and a 10% improvement in downforce.

The three- and four-channel diffusers (Figure 4.4.4c and d) perform better than the plane diffuser with much greater diffuser pumping at the inlet in both the inside and the outside channels. The lower pressures and more gradual pressure recovery than the plane and two-channel equivalent suggests reduced separation or adverse pressure gradient. The increased diffuser pumping in the outside channel has the same effect as was observed at 13° but additionally the vortices help reduce or even eliminate the separation observed in the plane diffuser. This improvement in performance is shown by the force measurements where an increase of up to 17% in downforce is observed. This change around the critical angle is important because it demonstrates the potential to extend the performance envelope close to the plane diffuser optimum.

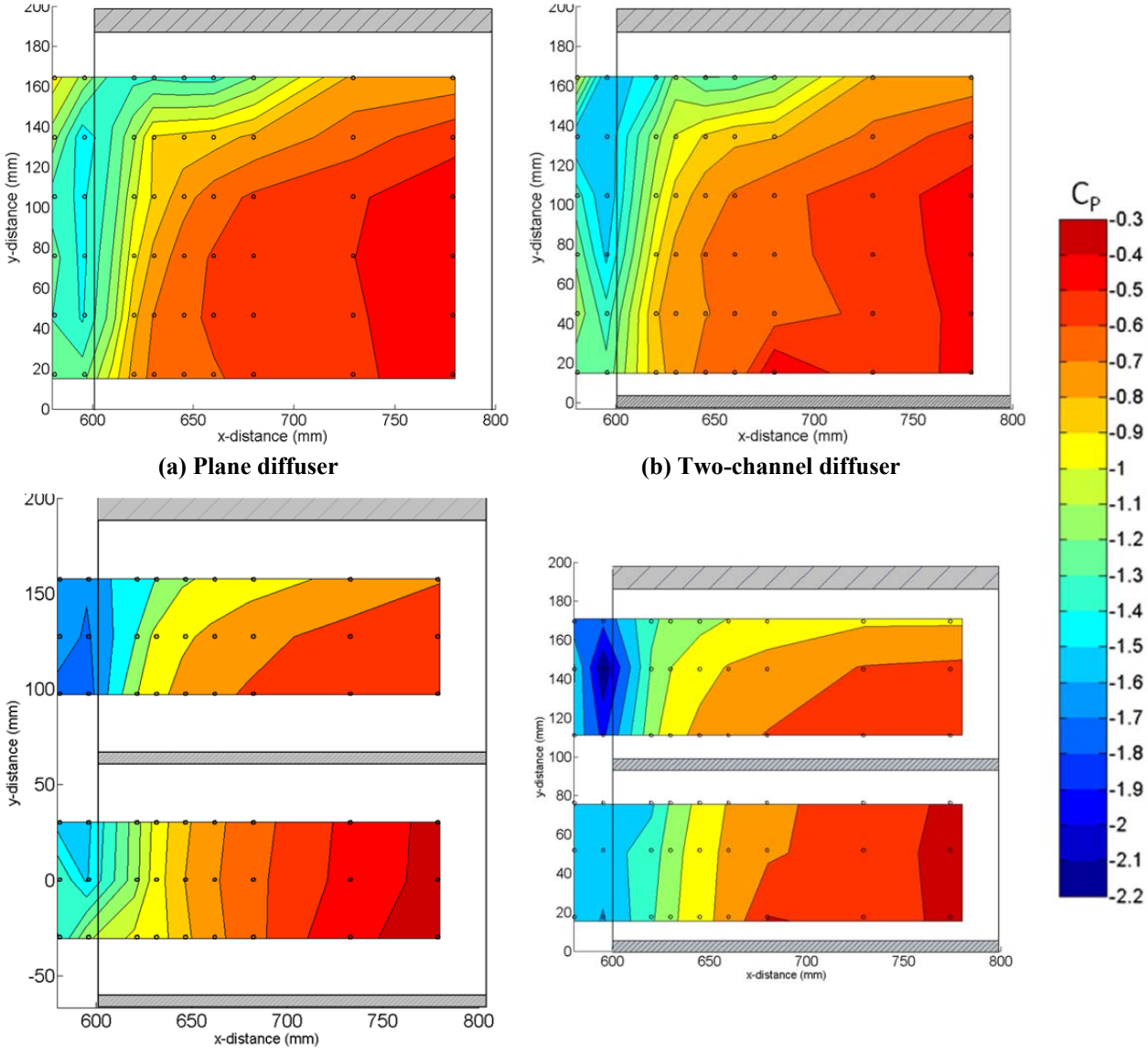

(a) Plane diffuser **(b) Two-channel diffuser**

(c) Three-channel diffuser **(d) Four-channel diffuser**

Figure 4.4.4 - Contours of pressure coefficient for all 16° diffusers at h1/H=0.0903 (28mm)

As the diffuser angle is increased further to 25°, a transition in behaviour between configurations is observed. The plane and two-channel diffusers (Figure 4.4.5a and b) no longer exhibit the strong pressure recovery seen at smaller angles, suggesting that vortex breakdown may have occurred, causing a small amount of asymmetry in the flow as observed by [13]. This is consistent with the large reductions in the downforce and drag observed in Figure 4.3.2.

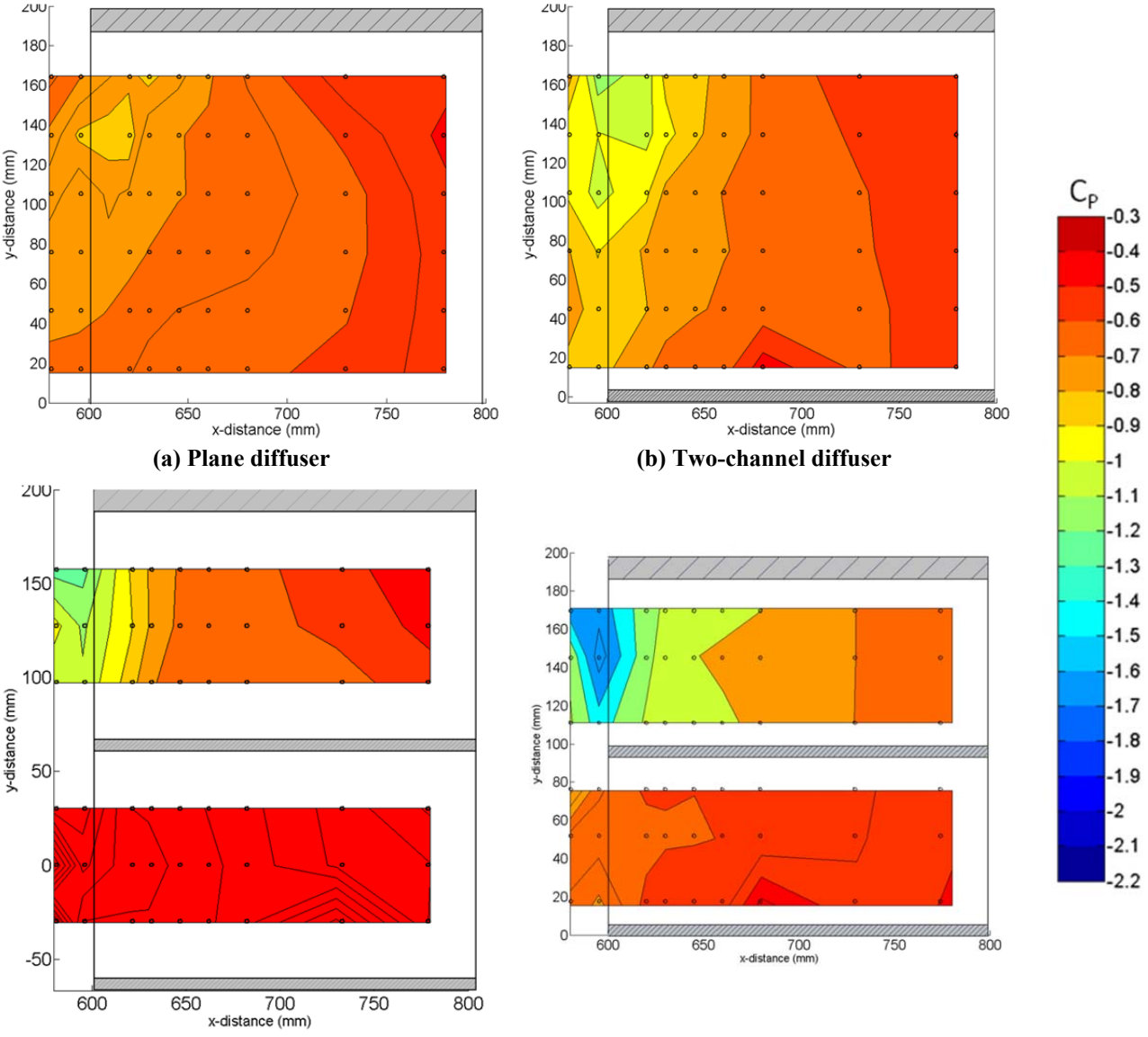

(a) Plane diffuser **(b) Two-channel diffuser**

(c) Three-channel diffuser **(d) Four-channel diffuser**

Figure 4.4.5 - Contours of pressure coefficient for all 25° diffusers at h1/H=0.0903 (28mm)

As the number of channels is increased, the asymmetry disappears and the three and four-channel diffusers (Figure 4.4.5c and d) perform much better. The inside channels appear to remain completely stalled shown by the flat distributions of channel centreline pressures in Figure 4.4.6. The improvement in the downforce comes from the outside channels, which show similar characteristics to those for smaller angles, with strong diffuser pumping and gradual pressure

recovery to base pressure. Unlike the plane diffuser at 25°, the three and four-channel configurations show the presence of vortex structures, albeit weaker than those at smaller angles. The presence of splitter plates makes the configurations less susceptible to flow separation leading to increased diffuser pumping and vortex strength and hence improved downforce. This is confirmed by the force measurements which give 21% and 26% increase in the downforce. It must be noted that although a performance improvement is observed with the three and four-channel configurations, the levels of downforce produced remain relatively low.

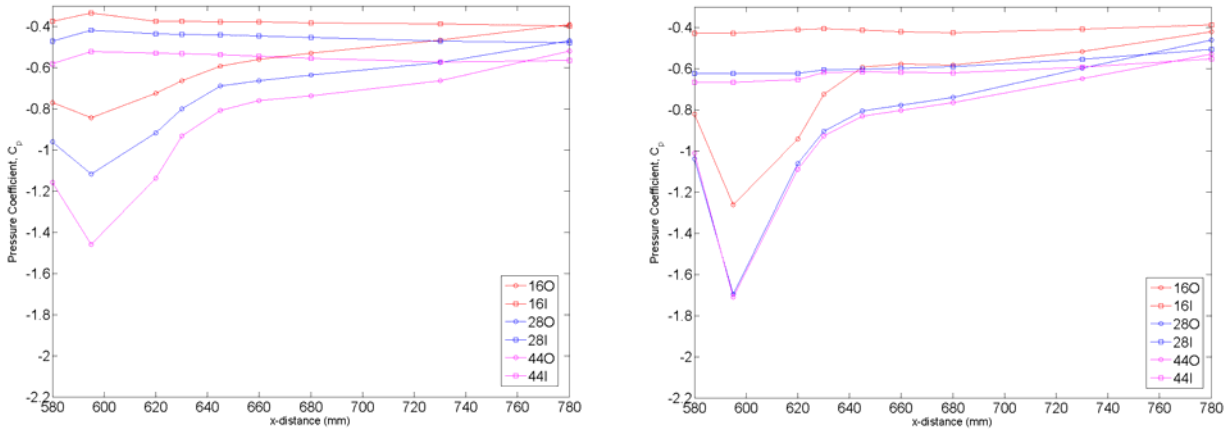

(a) Three-channel diffuser **(b) Four-channel diffuser**

Figure 4.4.6 – Pressure distribution for inside and outside channels diffusers at h_1/H=0.0903 (28mm)

4.5 PIV Measurements

The multiple-channel diffusers have shown to have advantages in downforce generation in the mid to high ranges, predominantly at higher ride heights. The downforce improvement in these regions were as high as C_L=0.20. The pressure measurements demonstrate that these improvements came from an increase in diffuser pumping contribution and more gradual pressure recovery; most likely due to a stronger vortex structure. Therefore, the PIV measurements were undertaken to further investigate the changes in flow behaviour and the impact on performance. The configurations will be compared against the plane diffuser results at each of the angles (13°, 16°, 19° and 25°) at a fixed ride height of 28mm (h_1/H=0.0903).

The 13° diffuser results are shown in Figure 4.5.1. The two-channel diffuser (Figure 4.5.1a) shows a similar velocity distribution to the plane diffuser (Figure 3.5.11) with the vortex core present in a position near to the endplates. There is a small increase in vortex strength in the two-channel diffuser (shown by increased rotational velocity), consistent with the force measurements where the two-channel diffuser showed both higher downforce and drag than the plane diffuser. Additionally, the velocity distribution shows some asymmetry (particularly on the left of the splitter plate) unlike the symmetrical distribution in the plan configuration.

Increasing the number of diffuser channels to three (Figure 4.5.1b) shows an increase in vortex strength over the plane and two-channel diffusers. This is again consistent with the force results where an increase in downforce and drag is observed, corresponding to the increase in vortex strength. Here the velocity distribution appears to be symmetrical about the model centreline.

The four-channel configuration (Figure 4.5.1c) shows the greatest change in behaviour of all the configurations. Although the general behaviour is similar to the plane diffuser (Figure 3.5.11), there is now a small vortex structure present in the inside channel formed by crossflow coming underneath the splitter plate from the main vortex in the outside channel. The main vortex is stronger and in a similar position to the plane diffuser. This is consistent with the force measurements as an increase in both downforce and drag is observed.

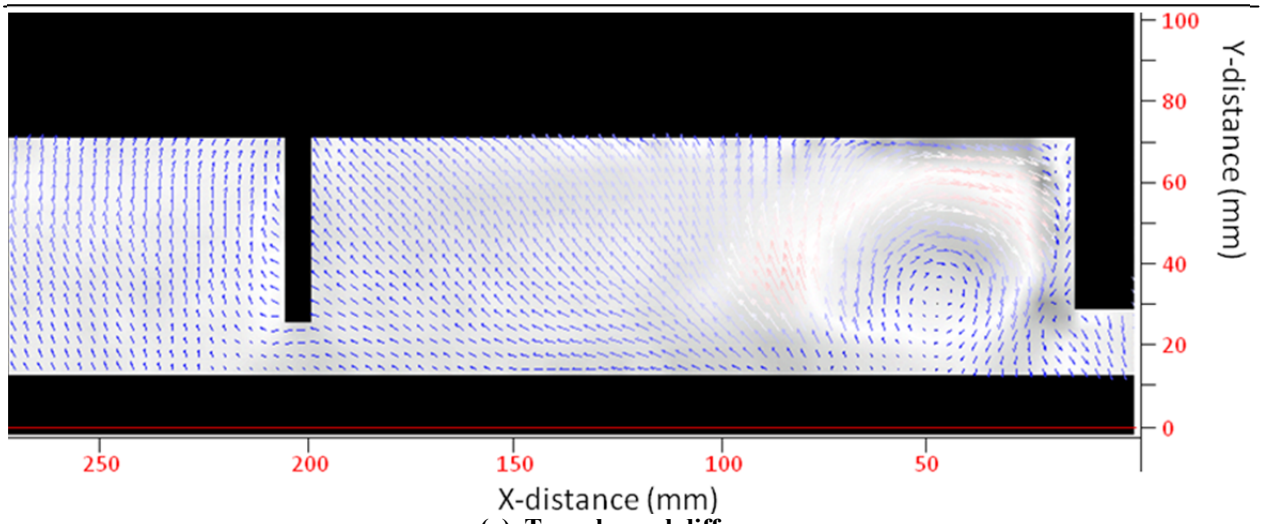

(a) Two-channel diffuser

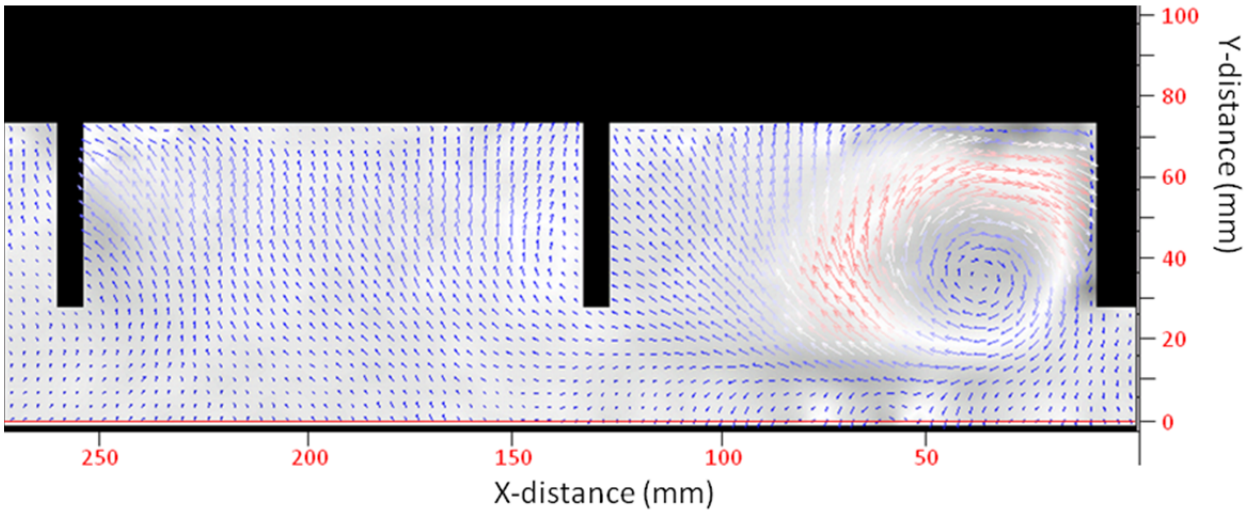

(b) Three-channel diffuser

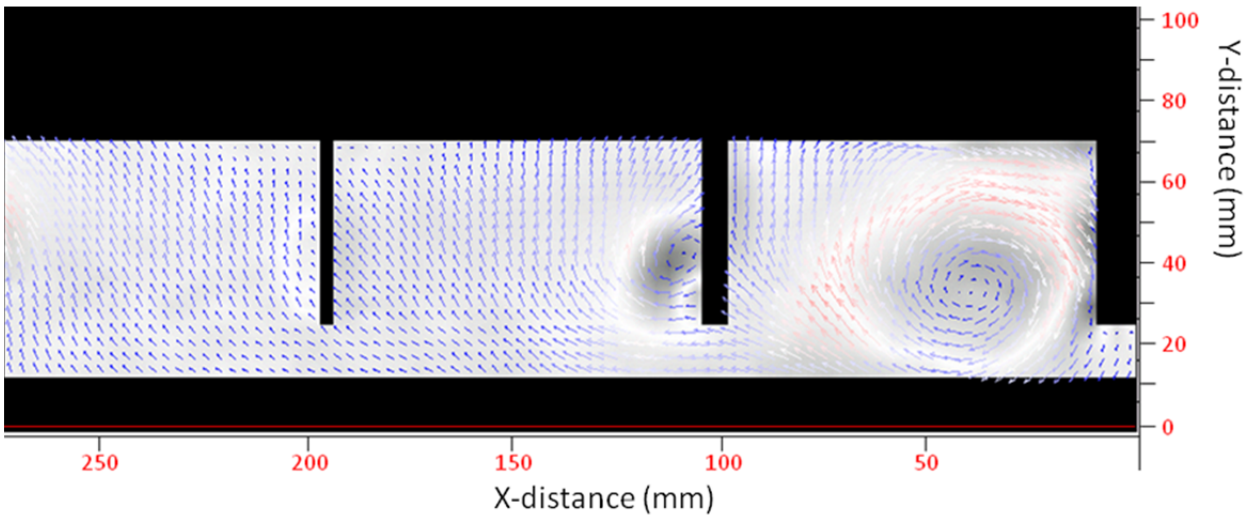

(c) Four-channel diffuser

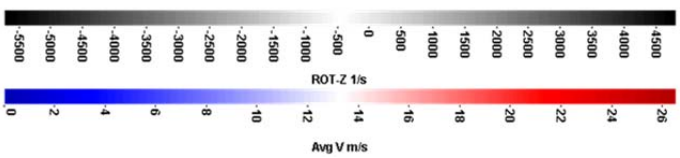

Figure 4.5.1 – Time-averaged vector plot coloured by velocity and rotational velocity in the background for 13° (a) two-channel, (b) three-channel and (c) four channel diffusers at h_1/H=0.0903

The position of the vortex core of the 13° diffusers is shown in Figure 4.5.2. It shows that increasing the number of diffuser channels does not significantly change the position of the vortex core. However, as the ride height is increase, the core position moves towards the endplate. This is consistent with the increased diffuser pumping observed in the area pressure measurements (Figure 4.4.3 - Figure 4.4.5) leading to increased vortex strength, shifting the core towards the end plate.

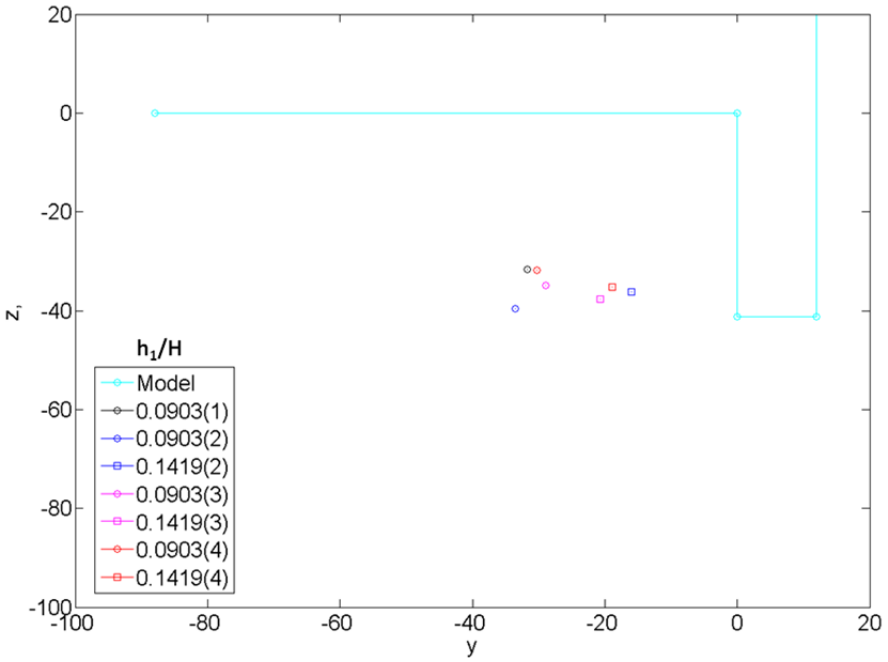

Figure 4.5.2 – Vortex core position for 13° multi-channel diffusers at h_1/H=0.0903 and h_1/H=0.1419

Increasing the diffuser angle to 16° shows that the two-channel configuration (Figure 4.5.3a) has similar velocity distribution to the plane diffuser (**Error! Reference source not found.**) but with an increase in both vortex strength and upwash components. This is consistent with the force measurements where a 10% and 0.15% increase in downforce and drag were observed. The increased vortex strength can also be seen in the pressure maps (Figure 4.4.4) where lower inlet pressures were recorded.

The three-channel 16° diffuser (Figure 4.5.3b) has a velocity field largely similar to the three-channel 13° configuration but with reduced vortex strength resulting in a 13% decrease in downforce. Comparing the three-channel diffuser with the plane diffuser highlights that the vortex position is similar but stronger in the three-channel configuration. However, the force measurements showed a reduction in downforce of 6% and a 2% increase in drag. This may be attributed to the fact that the centre channel appears to recover little pressure and has no presence of a vortex structure in the pressure maps in (Figure 4.4.4). The adverse pressure

gradient may be too great to enable the centre channel to recover pressure without the presence of crossflow in the channel, essentially acting as a 2-dimensional diffuser, explaining the reduction in downforce.

Similar velocity fields are again observed between the 13° and 16° four-channel diffusers with increased strength in both the main and secondary vortex structures at 16°. The increase of the secondary vortex is assumed to be due to larger, stronger main vortex and increased upwash resulting in a 10% increase in downforce and a 5% increase in drag. Comparison with the plane diffuser shows that the 16° four-channel diffuser has an increase in vortex strength giving a 17% and 1% increase in drag and downforce respectively. This increase in vortex strength is caused by the increased diffuser pumping observed in the pressure maps (Figure 4.4.4) highlighted by lower pressures at the diffuser inlet. This aids flow attachment and suppress the small separations observed along the diffuser centreline in the plane diffuser in Figure 4.4.1.

The position of the vortex core for the 16° diffusers is shown in Figure 4.5.4 and similar to the results for the 13° diffusers, it shows that as the number of channels is increased the vortex core position stays relatively constant. Again, as the ride height is increased the core moved towards the endplate.

Increasing the diffuser angle further to 19° brings about a change in the behaviour of the flow. The two-channel diffuser (Figure 4.5.6a) exhibits largely similar velocity distribution to that of the 16° two-channel diffuser, but with increased vortex strength and the onset of separation characterised by the downward facing vectors around the model centreline. This results in a decrease in downforce of 3% and a 6% increase in drag. When compared to the 19° plane diffuser, the 19° two-channel has greater vortex strength but less separation around the centreline, with a 15% downforce and 1% drag increase. This confirms that the presence of splitter plates helps to suppress the separation resulting in improved attachment and subsequently improved downforce. This is due to the constraining of the vortex structures, helping improve their strength and aiding in the creation of upwash in the diffuser; similar to the downwash observed to aid attachment in fastback aerodynamics [57].

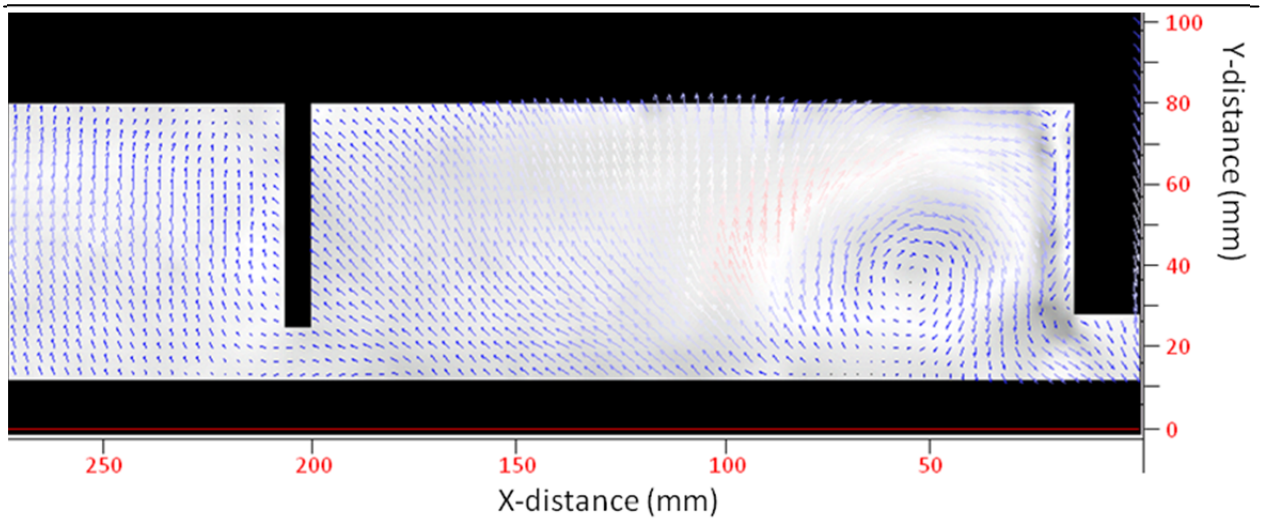

(a) Two-channel

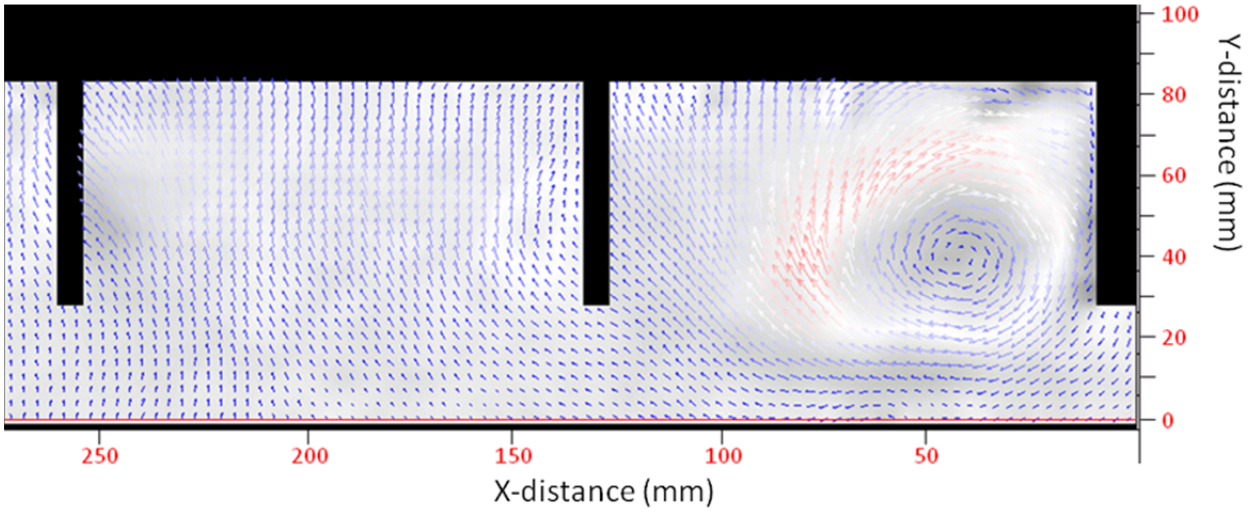

(b) Three-channel

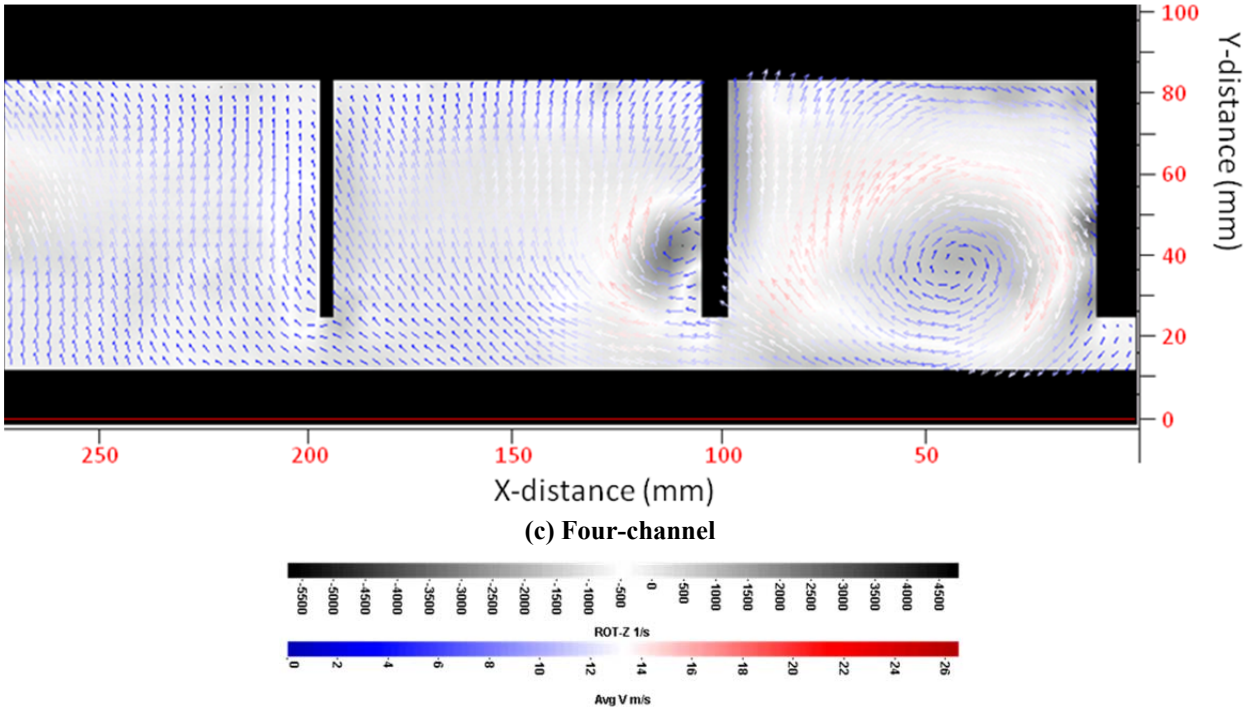

(c) Four-channel

Figure 4.5.3 – Time-averaged vector plot coloured by velocity and rotational velocity in the background for 16° (a) two-channel, (b) three-channel and (c) four channel diffusers at h1/H=0.0903

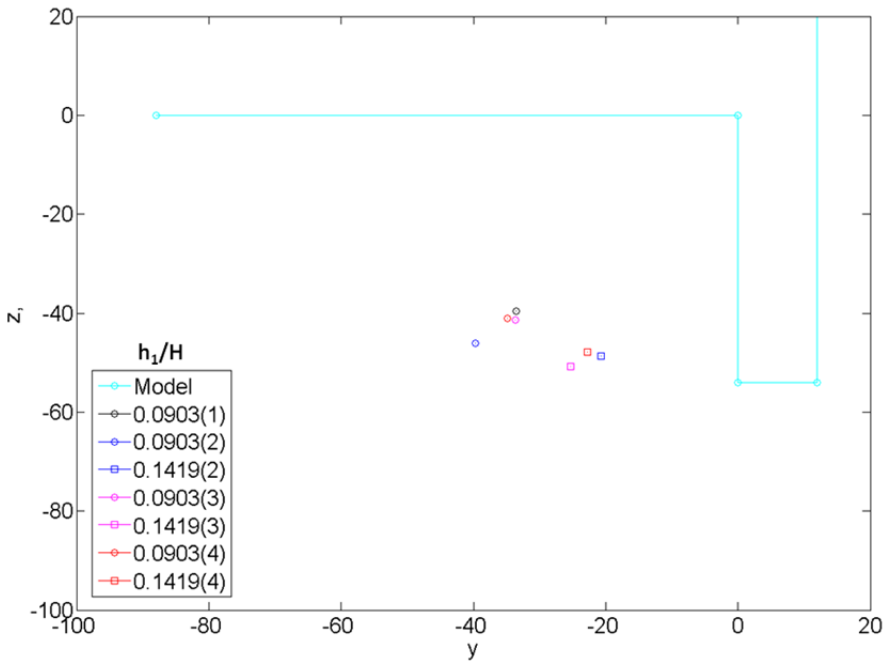

Figure 4.5.4 – Vortex core position for 16° multi-channel diffusers

At 19°, the three-channel diffuser (Figure 4.5.6b) has a much stronger vortex than the three-channel 16° diffuser, however separation has now occurred at the diffuser plate of the centre channel. This could be caused by lack of crossflow in the centre channel, resulting in it acting more like a 2-dimensional diffuser and therefore less able to withstand the high adverse pressure gradient present at 19°. This would account for the 3% decrease in downforce and 1% drag increase. When compared to the 19° plane diffuser, the vortex is still much stronger but the separated region is now much larger in the three-channel configuration. This results in a 1% downforce and 2% drag decrease attributed to little or no downforce being produced in the centre channel.

A small change in behaviour is seen for the four-channel diffuser (Figure 4.5.6c) at 19°. The main vortex has increased in strength compared to the 16° four-channel configuration but the secondary vortex is much less prominent and there are small signs of separation occurring at the diffuser plate surface, giving a 12% reduction in downforce and 5% increase in drag. Compared to the 19° plane diffuser, the four-channel has much stronger vortex structures and less separation explaining the 11% increased in downforce.

Figure 4.5.5 compared the vortex core positions for all 19° diffuser configurations. Unlike the lower angles at $h_1/H=0.0903$, as the number of channels is increased the vortex core is shifted towards the endplate. This is thought to be due to increasing vortex strength as the number of

channels is increased. If the vortex is being fed by flow under the endplate, as the vortex strength increases it moves towards the feeding point. Increasing the ride height provides the vortex with more flow under the endplate and a consequently stronger vortex and less separation with increased diffuser channels, shifting the core even closer to the endplate. The four-channel cores are in an almost identical position, suggesting it may be at its maximum strength in its configuration.

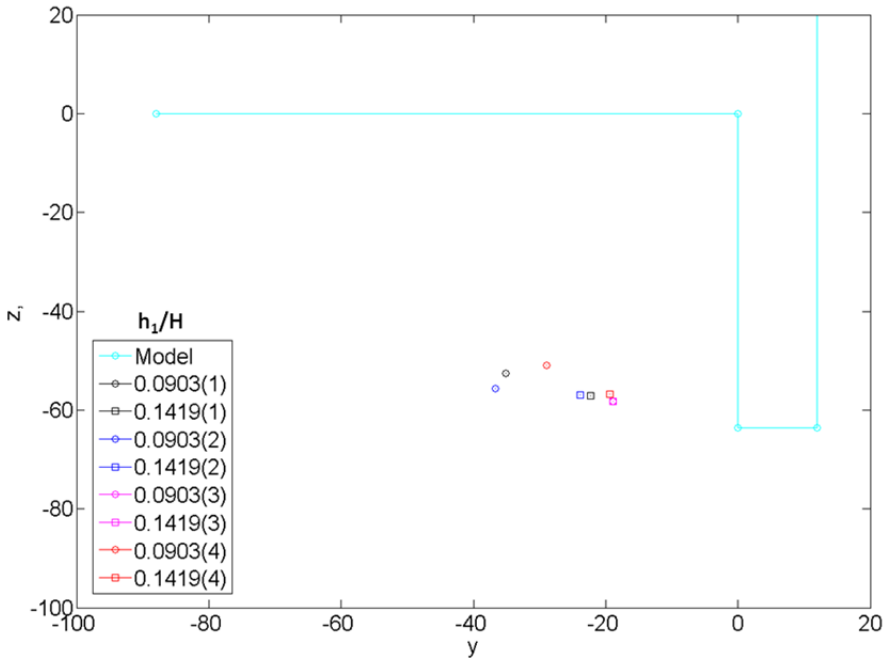

Figure 4.5.5 – Vortex core position for 19° multi-channel diffusers

The size and position of the separated region in the diffusers is shown schematically in Figure 4.5.7, created by using a line search of zero velocity in the vector images. The figures show the same region as the PIV images, with x=0 the edge of the endplate, x=-200 the model centreline and y=0 the diffuser plate surface. It should also be noted that the point at which separation would be expected to propagate is at the centreline of the model at the diffuser surface.

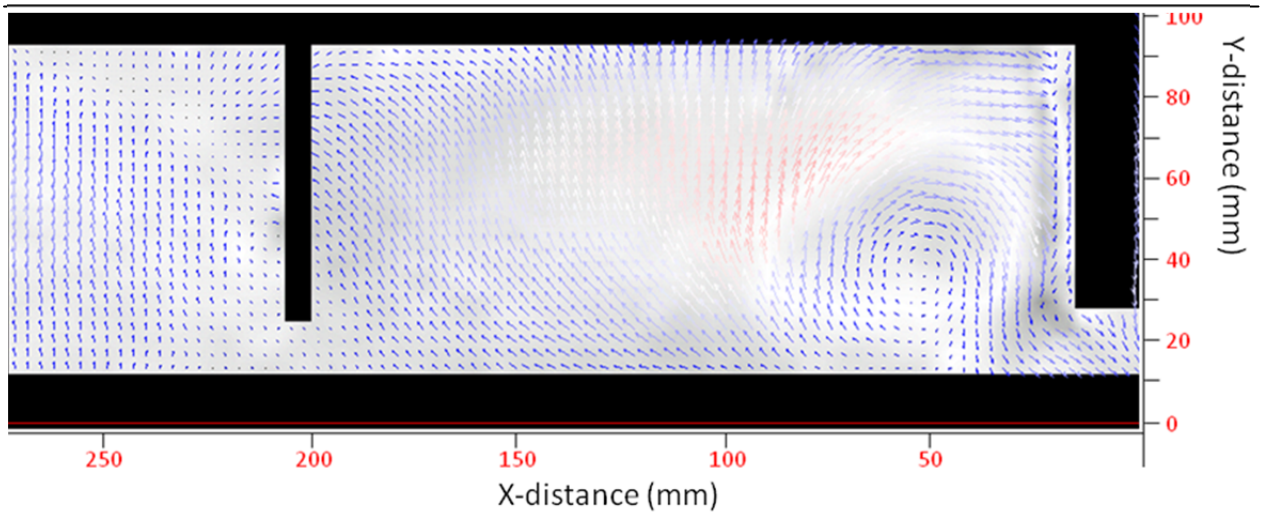

(a) Two-channel

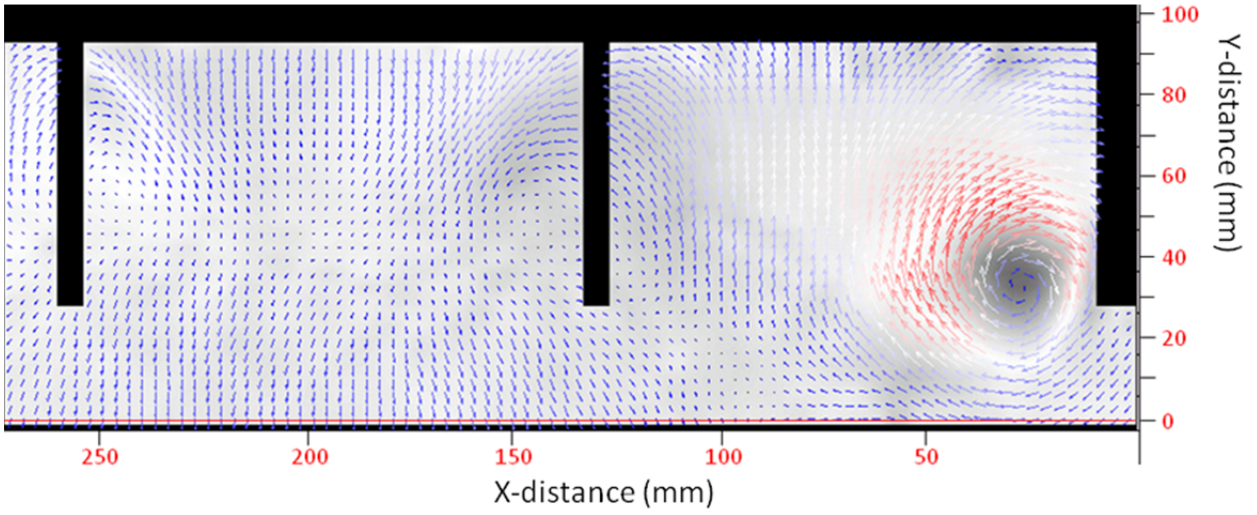

(b) Three-channel

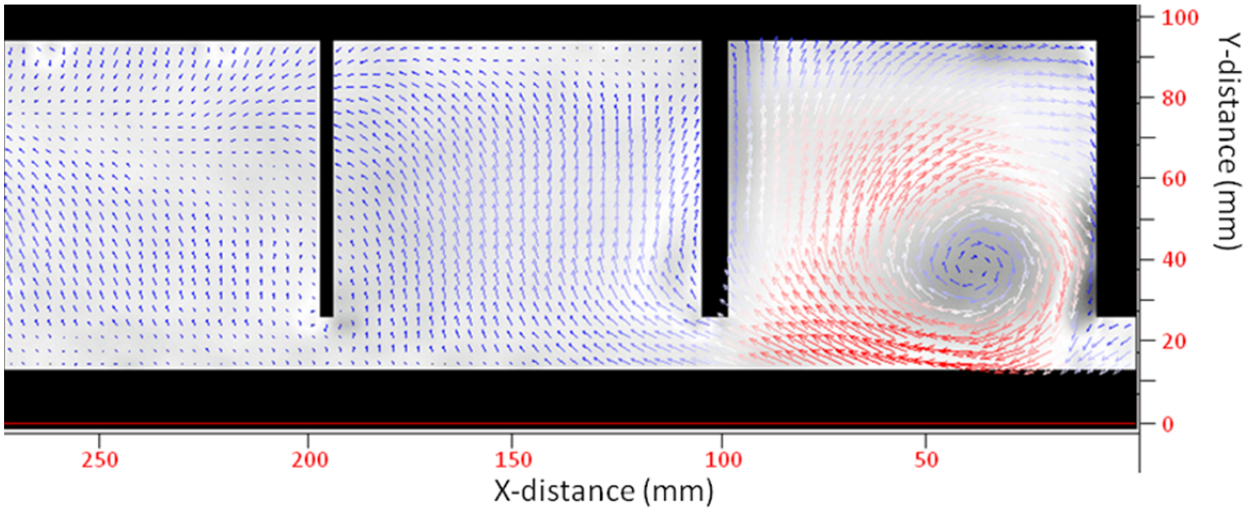

(c) Four-channel

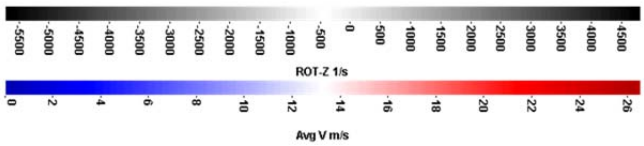

Figure 4.5.6 – Time-averaged vector plot coloured by velocity and rotational velocity in the background for 19° (a) two-channel, (b) three-channel and (c) four channel diffusers at h1/H=0.0903

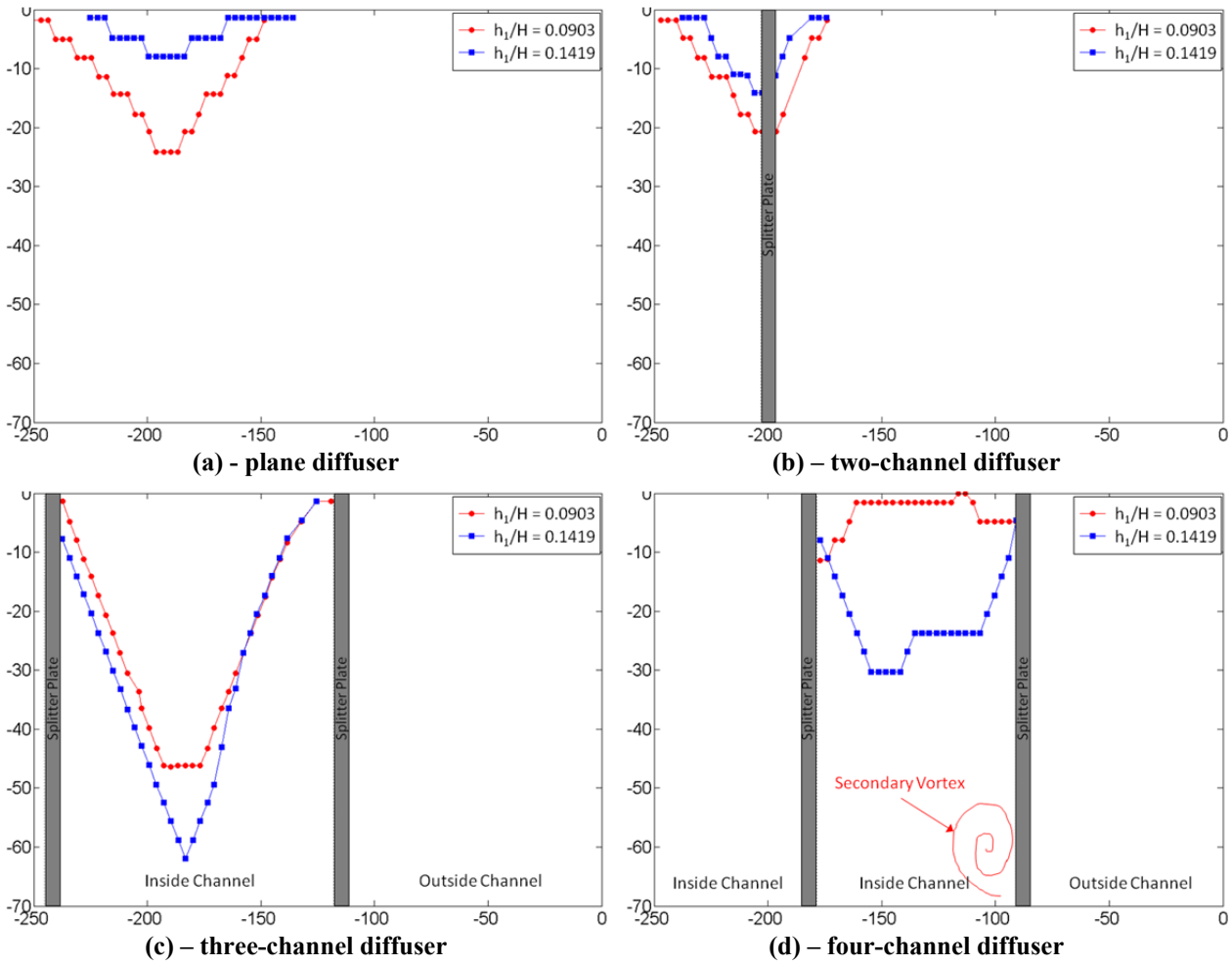

(a) - plane diffuser **(b) – two-channel diffuser**

(c) – three-channel diffuser **(d) – four-channel diffuser**

Figure 4.5.7 – Separation for 19° multi-channel diffusers

For both the plane (Figure 4.5.7a) and two-channel (Figure 4.5.7b) diffusers the separated region occurs relatively symmetrically at the centreline of the model and reduces as the ride height is increased due to increased vortex strength. The two-channel has lower levels of separation than the plane diffuser, across almost half the width, due to the presence of the splitter plate and its consequent influence on increasing the vortex strength and upwash.

The three- (Figure 4.5.7c) and four-channel (Figure 4.5.7d) diffusers do not show any signs of separation in their outside channels due to the strong vortex structures present in smaller channel areas than the other configurations. However, separation is present on the inside channels of both diffusers, assumed to be due to the lack of strong vortex structures and crossflow. The stepped variation seen in the four-channel diffuser at h_1/H= 0.1419 (44mm) is thought to be due to the presence of the secondary vortex structure observed in the vector images.

By far the greatest variation is observed with the 25° diffusers where two different flow regimes appear to exist as identified in the force and pressure measurements. For the two-channel diffuser (Figure 4.5.8a) increasing the diffuser angle from 19° to 25° results in a stronger vortex structure but a much larger region of separation and very little upwash, highlighted by the extreme reduction in downforce of 45%. When compared to the 25° plane diffuser the 25° two-channel has a slightly stronger vortex although the force measurements show a small reduction in downforce of 7% and 1% decrease in drag.

The 25° three-channel diffuser (Figure 4.5.8b) exhibits a weaker vortex than seen in the 19° diffuser and a greater area of separated flow, confirmed by a severe reduction in downforce of 17% and a small increase in drag of 1%. When compared to the 25° plane diffuser, the three-channel diffuser has a slightly stronger vortex structure and smaller region of separated flow which results in an increase in downforce of 21% and 3% decrease in drag. However, it should be noted that although there is a substantial improvement in performance over the plane diffuser it is largely due to the poor performance of the plane diffuser and not an outstanding performance by the three-channel. To put it into context, the 25° three-channel diffuser produces less downforce than the plane 13° diffuser.

The four-channel diffuser (Figure 4.5.8c) has the greatest performance of all the 25° diffusers. When compared to 19° four-channel diffuser it has a much weaker vortex structure and the inner channel appears to be completely separated with no upwash as was observed at 19°. This is confirmed by the reduction of 24% in downforce and 2% reduction in drag. Comparison with the 25° plane diffuser, the four-channel offers a 26% increase in downforce and a 2% reduction in drag. This is due to a better balanced flow; with increased vortex strength but less separation.

The vortex core position for the 25° diffusers is presented in Figure 4.5.9 and shows that at $h_1/H=0.0903$ (28mm) the position for the three- and four-channel diffusers is closer to the end-plate than the plane and two-channel diffusers, consistent with the increased diffuser pumping and increased vortex strength. As the ride height is increased the core positions move closer together and towards the end-plate, suggesting an increase in vortex strength with increasing ride height.

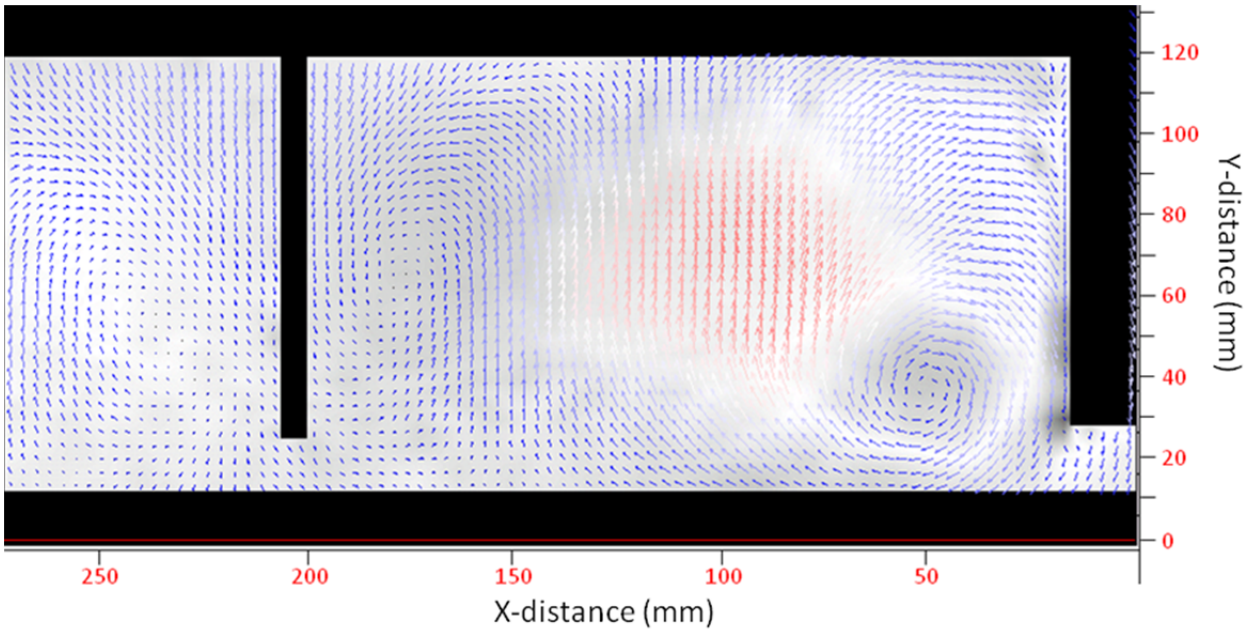

(a) Two-channel

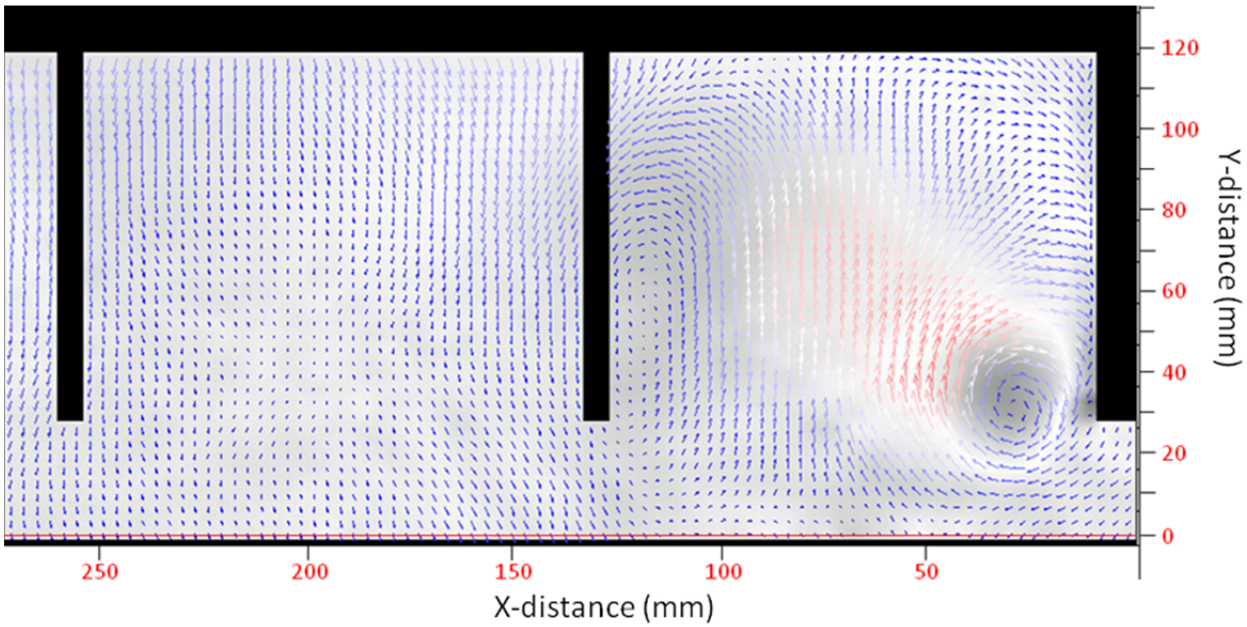

(b) Three-channel

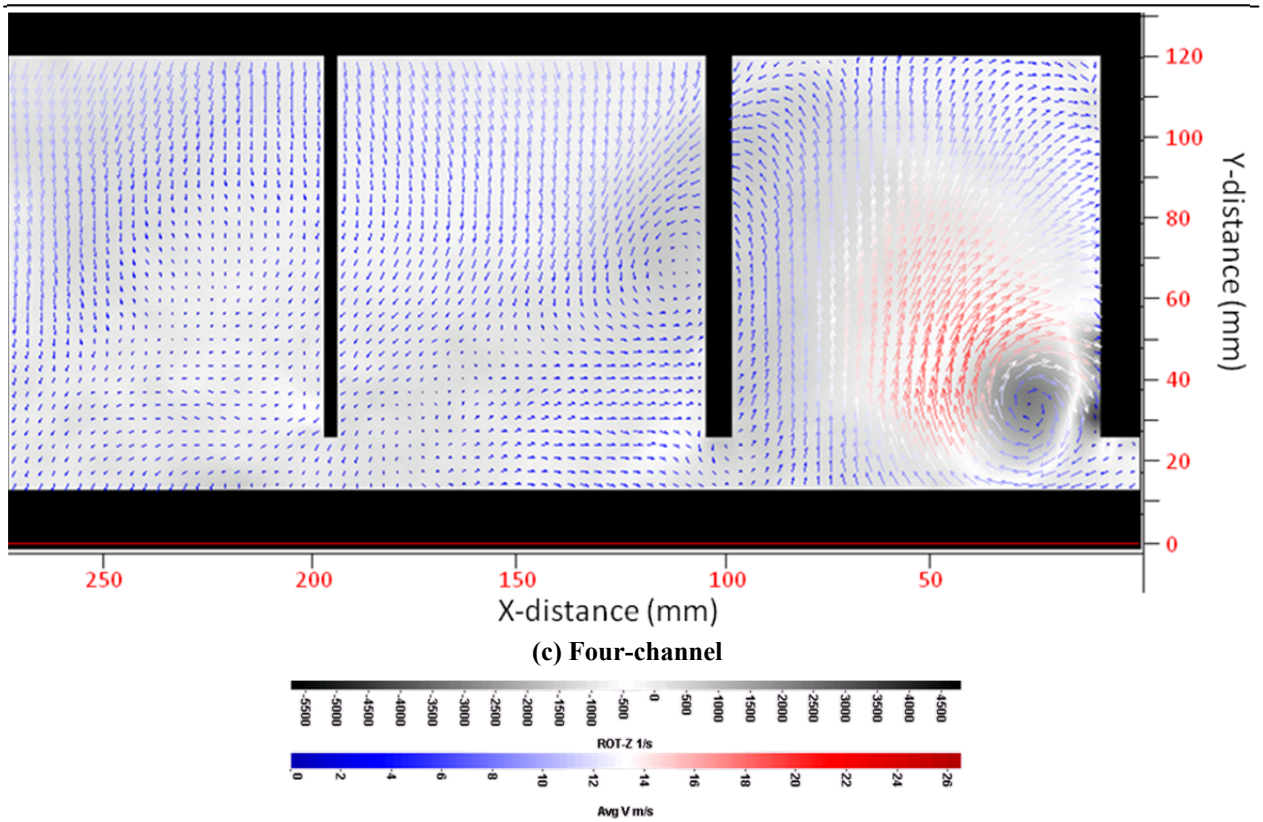

(c) Four-channel

Figure 4.5.8 – Time-averaged vector plot coloured by velocity and rotational velocity in the background for 25° (a) two-channel, (b) three-channel and (c) four channel diffusers at h_1/H=0.0903

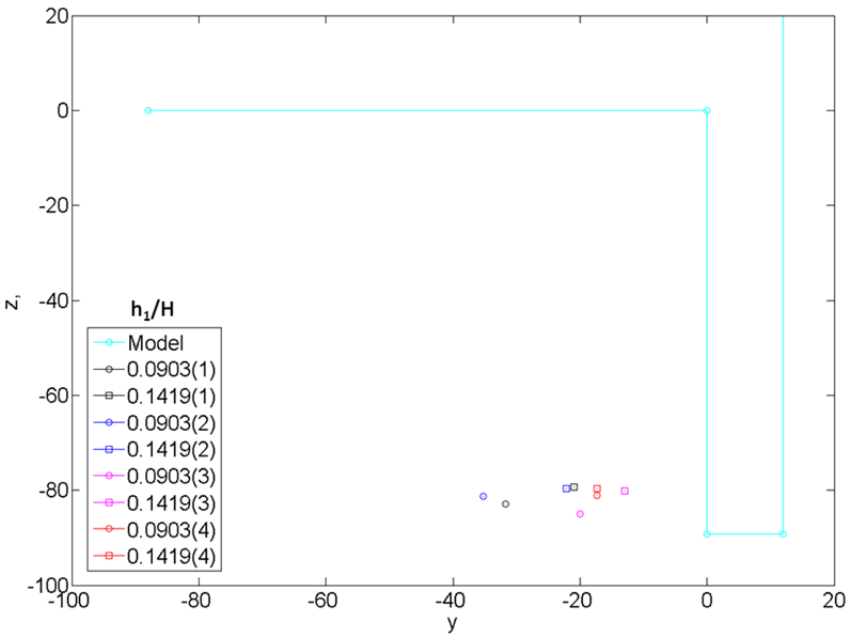

Figure 4.5.9 – Vortex core position for 25° multi-channel diffusers

Chapter 5 - Conclusions

An investigation into the performance of plane and multi-channel automotive underbody diffusers has been carried out using force, pressure and PIV measurements. Ten diffuser angles and eight ride heights were investigated for plane, two-channel, three-channel and four-channel diffuser configurations.

The plane diffuser showed similar trends in lift and drag to published data with increased downforce and drag with decreasing ride height to a maximum followed by a sharp decrease in downforce due to ground proximity. The optimum angle for downforce generation was found to be between 13° and 16°. Above 16°, the downforce levels are reduced with a corresponding increase in drag. The centreline pressure distributions indicate that above 13°, local separation occurs at the diffuser inlet and that at 25° and above, the diffuser is completely stalled although it continues to generate downforce through the mechanism of upsweep.

The PIV data confirmed the presence of a vortex structure and underbody upwash in the diffuser with a relatively symmetrical flow field for all configurations. As the diffuser angle was increased the vortex core remained in a similar position each time but increased signs of separation were observed at the diffuser surface, in the same configurations where reduction in downforce and increase in drag were seen in the force measurements. At 25°, the vortex was much weaker with large separated region which was symmetrical about the diffuser centreline, contrary to the findings of Zhang et al [14]. Increasing the ride height resulted in increased vortex strength and reduced levels of separation attributed to increased diffuser pumping contribution.

The multiple-channel diffusers showed similar trends in the lift and drag to the plane diffuser and for angles of 13° and above, the multiple-channel configurations show an improved downforce production with the percentage gains increasing with increasing diffuser angle. For the mid-range angles (16°-19°) where the degree of separation is small, the multiple-channel configurations show large improvements in the downforce with minimal increase in the drag. In this range the total downforce is increased by 13% compared with the optimum plane diffuser, significantly extending the performance envelope. The pressure maps indicate that the gains occur through improved diffuser pumping and pressure recovery in both the inner and outer channel. Above 19°, large improvements in performance are observed compared with the plane configuration, particularly for three- and four-channel set-ups. However, the levels of downforce produced remain relatively low. The pressure data indicates that the gains arise from improved pressure recovery in the outer channels.

The PIV studies showed that all the multi-channel diffusers showed similar flow field distributions, with the presence of a vortex structure (in the outer channel), and separation present at higher diffuser angles. The vortex core remained in a similar position regardless of configuration, moving towards the endplate with increasing ride height, attributed to an increase in vortex strength fed from flow under the endplates. The 25° three- and four-channel diffusers had the vortex core closer to the endplates than the plane and two-channel configurations, due to reduced separation and increased diffuser pumping. In the two-channel diffuser, the presence of splitter plates helps to suppress separation resulting in improved attachment and subsequent improved downforce due to constraining of vortex structures, improving the upwash similar to the downwash in fastback aerodynamics [57]. The splitter plates have a similar effect in the three- and four-channel diffusers in the outside channel, but the inside channel(s) have high levels of separation present; acting more like a two-dimensional diffuser. The most interesting result showed that the four-channel diffuser had developed a “secondary vortex” in the inside channel, emanating from flow off the main vortex in the outside channel. This explains the considerable improvements observed in the four-channel performance.

Overall, the use of multiple channel diffusers have shown that there are merits in their application and that they significantly increase the performance envelope especially at high diffuser angles.

Chapter 6 - Further Work

The work described here gives a firm foundation of the fundamentals involved in the use of an automotive underbody diffuser. However, further investigations could be performed to increase the knowledge of the influence of certain parameters or how the diffuser itself interacts with other aerodynamic devices.

6.1 Additional PIV Measurements

The PIV measurements collected in this study have been extremely important in aiding the understanding of the mechanisms involved in the behaviour of underbody diffusers. Further PIV data taken at the inlet and along the length of the diffuser would provide additional information not previously able to be collected. Data from these two measurement planes may be able to capture the separation and stall effects, especially at higher diffuser angles.

6.2 New Geometries

Published work by ESDU [25] investigated the use of several different geometries used in conical diffusers. These included the use of partial length splitters as well as curved vanes and splitters, similar to those used in racing applications. Further investigation of the effects of these geometries used in automotive underbody diffusers would be advantageous.

6.3 Interaction with Aerodynamic Components

There is some published work on the interaction of diffusers with other aero components but a full set of measurements including PIV data would aid in the understanding of how the diffuser characteristics (diffuser pumping, ground interaction and upsweep) are changed by the presence of these components. The types of tests would include interaction with components such as wheels, front and rear wings.

Additionally, some previous investigations [47] has examined the effect of other vehicle proximity to the overall lift and drag of a vehicle but the specific influence that another vehicle has on the flow development and performance of the diffuser would be useful to investigate.

References

[1] The Official Chaparral Website (www.ChaparralCars.com)

[2] Formula One World Championship Limited, 2003-2012 (www.FormulaOne.com)

[3] Henry, A., "Brabham: The Grand Prix Cars", Autocourse, 1985

[4] Jones, B., "The Ultimate Encyclopaedia of Formula One", Book People, 1996

[5] Dorgham, M.A., "Impact of Aerodynamics on Vehicle Design", International Journal of Vehicle Design, Technological Advances in Vehicle Design Series SR3, 1983

[6] Toyota Prius Specification (www.Toyota.com/prius-hybrid/specs.html)

[7] Regulation (EC) No. 433/2009 of the European Parliament and of the Council of 23rd April 2009 – Setting emission performance standards for new passenger cars as part of the Community's integrated approach to reduce CO2 emissions from light-duty vehicles.

[8] Wright, P., "Formula 1 Technology", SAE International, 2001

[9] Barnard, R.H., "Road Vehicle Aerodynamic Design", Mech Aero, 2001

[10] Katz, J., "New Directions in Race Car Aerodynamics", Robert Bentley Inc., 1995

[11] Hucho, W-H., "Aerodynamics of Road Vehicles", 4th Edition, SAE International, 1998

[12] Faul, R., "Ein Rennwagen steht im Windkanal", Automobil Revue, No. 41, Berne October 1980,

[13] Zhang,X., Senior,A., Ruhrmann,A., "Vortices behind a bluff body with an upswept aft section in ground effect", International Journal of Heat and Fluid Flow, Vol.25, 2003

[14] Senior, A., Zhang,X., "The force and pressure of a diffuser-equipped bluff body in ground effect", Journal of Fluids Engineering (Transactions of the ASME), Vol.123, 2001

[15] Ruhrmann,A.; Zhang,X., "Influence of diffuser angle on a bluff body in ground effect", Journal of Fluids Engineering (Transactions of the ASME), Vol.125, 2003

[16] Cooper, K. R.; Bertenyi, T.; Dutil, G.; Syms, J. and Sovran, G., "SAE 980030 - The Aerodynamic Performance of Automotive Underbody Diffusers", SAE International, 1998

[17] Cooper, K. C.; Syms, J. and Sovran, G., "SAE 2000-01-0354 - Selecting Automotive Diffusers to Maximise Underbody Downforce", SAE International, 2001

[18] Ahmed, S., Ramm, G., Faltin, G., "840300 - Some Salient Features of the Time-Averaged Ground Vehicle Wake", SAE International, 1984

[19] Sovran, G., "The Kinematic and Fluid-Mechanic Boundary Conditions in Underbody Flow Simulation", CNR–Pininfarina Workshop on Wind Tunnel Simulation of Ground Effect, 1994

[20] Cooper, K., Fediw, A., Wlodarski, S., "Development of a Moving Ground System for Study of Vehicle Aerodynamics", Loughborough Vehicle Aerodynamics Conference, 1994

[21] Howell, J.P., "The Influence of Ground Simulation on the Aerodynamics of Simple Car Shapes with an Underfloor Diffuser", Loughborough Vehicle Aerodynamics Conference, 1994

[22] George, A.R., Donis, J., "Flow Patterns, Pressures and Forces in the Underside of Idealised Ground Effect Vehicles", Proceedings of the ASME Fluids Engineering Division Symposium on Aerodynamics of Transportation II, Vol. 7 Dec., 1983

[23] George, A.R., "Aerodynamic Effects of Shape, Camber, Pitch on Ground-vehicle Bodies", ASME Journal of Fluids Engineering, Vol. 103, Dec. 1981

[24] Cogotti, A., "980031 – A Parametric Study on the Ground Effect of a Simplified Car Model", SAE International, 1998

[25] ESDU, "76027 – Introduction to Design and Performance Data for Diffusers", ESDU International Ltd, 1976

[26] Breslouer, O.J., George, A.R., "2008-01-0326 - Exploratory studies of forces and flow structures on a bluff body with variable diffuser and wheel configurations", SAE International, 2008

[27] Newnham, P.S., Passmore, M.A., Baxendale, A., "On the effect of turbulence on lift, drag and yaw sensitivity of a generic vehicle model with a variable backlight angle", 6th MIRA International Vehicle Aerodynamics Conference, 2006

[28] Passmore, M.A., "Ground Vehicle Aerodynamics", Loughborough University Department of Aeronautical and Automotive Engineering

[29] SAE Standard J1252 – Truck and Bus Aerodynamics and Fuel Economy Committee, 1979-2012, SAE International

[30] Miniature Electronic Pressure Scanners – Manual, Chell Instruments, 2007

[31] Product Manual – FlowMaster 1105011-4, LaVision GmbH, 2007

[32] User Manual – Aerosol Generator PIVPart45-M Series, PIVTech GmbH

[33] Turbulent Flow Instrumentation Cobra Probe Manual

[34] Keane, R. and Adrian, R.J.– "Optimisation of Particle Image Velocimeters; Part I: Double Pulsed Systems", Measurement Science and. Technology, Vol.1, pp.1202-1215, 1990

[35] Chen, J. and Katz, J., "Elimination of peak-locking error in PIV analysis using the correlation mapping method", Measurement Science and Technology, Vol. 16, pp1605-1618, 2005

[36] Hollis,D., "Particle Image Velocimetry in Gas Turbine Combustor Flowfields", PhD Thesis Loughborough University, 2004.

[37] Hoffman, R., "Contribution of Aerodynamics and Thermal Management to Automotive Fuel Economy", 6th FKFS Conference on Progress in Vehicle Aerodynamics and Thermal Management, October 2007

[38] Data from full-scale tests performed at MIRA, December 2009 (See Apprendix1)

[39] Data from full-scale tests performed at MIRA, December 2008 (See Apprendix2)

[40] Jeff Howell (ex Head of Aerodynamics, Rover Group and Jaguar Land Rover) - private communication 2008.

[41] Johl, G., Passmore, M. and Render, P., "Design methodology and performance of an indraft wind tunnel", The Aeronautical Journal, pp465, 2004

[42] Howell, J., and Le Good, G., "1999-01-0651 - The influence of aerodynamic lift on high speed stability", SAE International, 1999

[43] Le Good, G.M., and Passmore, M.A., "Real world drag measurements versus laboratory tests", Vehicle Performance and Refinement - Autotech 93 Conference, Seminar 24, IMechE Automobile Division, 1993

[44] Dominy, J.A., and Dominy, R.G., "Aerodynamic influences on the performance of the grand prix racing car", Proceedings of the Institute of Mechanical Engineers, Vol. 198D, No.7, pp87, 1984

[45] Dominy, R.G., "Aerodynamics of grand prix cars", Proceedings of the Institute of Mechanical Engineers, Vol. 206, No.7, pp267, 1984

[46] Barnard, R.H. and Vaughan, H., "The aerodynamic tuning of a group c sports racing car", Journal of Wind Engineering and Industrial Aerodynamics, Vol. 22, pp279-289, 1986

[47] Howell, J., "Catastrophic lift forces on racing cars", Journal of Wind Engineering and Industrial Aerodynamics, Vol. 9, pp145-154, 1981

[48] Sims-Williams, D.B. and Duncan, B.D., "2003-01-1315 - The Ahmed model unsteady wake: experimental and computational analyses", SAE International, 2003

[49] Tani, I., "Low-speed flows involving bubble separation", Progress in Aerospace Sciences, Vol. 5, pp70-103, 1964

[50] Mahon, S., Zhang, X. and Gage, C., "Evolution of edge vortices underneath a diffuser equipped bluff body", 12th International Symposium on Applications of Laser Techniques to Fluid Mechanics, 2004

[51] ESDU, "73024 – Performance of conical diffusers in incompressible flow", ESDU International Ltd, 1973

[52] ESDU, "74015 – Performance in incompressible flow of plane-walled diffusers with single-plane expansion", ESDU International Ltd, 1974

[53] ESDU, "75026 – Performance of circular annular diffusers in incompressible flow", ESDU International Ltd, 1975

[54] ESDU, "76027 – Introduction to design and performance data for diffusers", ESDU International Ltd, 1976

[55] ESDU, "72011 – Flow through a sudden enlargement of area in a duct", ESDU International Ltd, 1974

[56] Strachan, R.K., Knowles, E.K., Lawson, N.J.,"The vortex structure behind an Ahmed reference model in the presence of a moving ground plane", Experiments in Fluids, 2007, Vol. 42, pp659-669

[57] Ahmed, S.R., "An Experimental study of the wake structure of typical automobile shapes", Journal of Wind Engineering and Industrial Aerodynamics, 1981, Vol. 9, pp49-62

Appendix A – Data from full-scale testing of Ford Focus performed at MIRA, December 2009

FILE	T1	07Dec2009@08:33:02	User data																		
FIRM	LOUGHBOROUGH UNI																				
VEHI	FORD																				
MAKE	FOCUS																				
MODL																					
TYPE	GROUP ONE																				
CNFG	1																				
OALN	4365																				
WIDT	1784																				
HEIG	1495																				
WBAS	2630																				
FTRK	1520																				
RTRK	1515																				
FTRM	0																				
RTRM	0																				
MRFX	0																				
MRFZ	0																				
VPOX	0																				
VPOY	0																				
HBLR	0.8																				
SCAL	100																				
BLFE	NO																				
GBHT	0																				
MODE	NORMAL																				
UNITFM	N.m																				
UNITWS	m/s																				
Run/Cfg	Wind_m/s	Deg	FA.Sqm	CD	CY	CL	CMX	CMY	CMZ	CYF	CYR	CLF	CLR	XCP	Lift	Drag	Pitch	Side	Yaw	Roll	Amb.DegC	Amb.mBar
WEIGHT	(kg:T/F/R)	(Lb:T/F/R)	1340.8	808.9	531.9	2956	1783.3	1172.7														
CofG	(+=fwd. mm/ft)	272	0.89																			
1/ 1	26.67	0	2.32	0.341	0.013	0.149	0.004	0.002	-0.004	0.003	0.01	0.076	0.072	0	151.5	352.9	5.4	13.5	-10	9.8	6.9	991
2/ 1	26.86	0	2.32	0.341	0.011	0.144	0.003	0.004	-0.004	0.002	0.009	0.076	0.068	0	148.7	358.8	11.7	11.7	-9.8	8.5	6.4	991
3/ 1	27.2	0	2.32	0.341	0.011	0.142	0.003	0.005	-0.004	0.002	0.009	0.076	0.066	0	150.9	368.3	13.2	11.9	-10.7	9.1	6.2	991
4/ 1	27.26	2.5	2.32	0.345	0.103	0.155	0.021	0.002	0.023	0.074	0.029	0.08	0.075	22.1	164.9	374.3	6.6	109.3	63.6	60	6.2	991
5/ 1	27.24	5	2.32	0.356	0.2	0.183	0.042	-0.003	0.048	0.148	0.052	0.089	0.094	23.8	194.5	384.7	-7.3	212.7	133.3	118.5	6.2	991
6/ 1	27.15	7.5	2.32	0.363	0.305	0.21	0.066	-0.002	0.068	0.22	0.085	0.103	0.107	22.1	222.5	389.8	-6.1	323	188.1	184.7	6.3	991
7/ 1	27.11	10	2.32	0.379	0.409	0.273	0.091	-0.009	0.085	0.289	0.119	0.128	0.145	20.8	287.4	405.7	-23.9	430.5	235.9	252.8	6.4	991
8/ 1	26.94	12.5	2.32	0.398	0.499	0.354	0.113	-0.015	0.107	0.357	0.143	0.162	0.192	21.4	368.3	420	-41.4	519.3	292.6	310.2	6.6	991
9/ 1	26.88	15	2.32	0.402	0.589	0.406	0.135	-0.009	0.124	0.419	0.17	0.194	0.212	21.1	419.7	421.7	-24.9	609.8	337.9	368.5	6.6	991
10/ 2	27.42	0	2.32	0.328	0.01	0.109	0.003	0.008	-0.003	0.002	0.008	0.062	0.046	0	116.4	357.3	22.6	10.2	-7.8	7.6	8.1	990
11/ 3	27.41	0	2.32	0.343	0.01	0.179	0.003	0.012	-0.004	0.001	0.009	0.101	0.078	0	191.5	373.3	32.7	10.3	-11.7	7.3	8	990
12/ 4	27.51	0	2.32	0.321	0.01	0.119	0.003	0.018	-0.003	0.003	0.008	0.077	0.042	0	127.9	351.5	49.9	11	-7.2	7.5	8.5	989
13/ 5	27.5	0	2.32	0.32	0.009	0.055	0.003	-0.054	-0.003	0.001	0.007	-0.026	0.081	0	59.2	349.2	-151.9	9.4	-8.8	7.1	8.8	989
14/ 6	27.48	0	2.32	0.353	0.006	-0.032	0.002	-0.023	-0.002	0.001	0.005	-0.039	0.007	0	-34.7	384.7	-64.6	6.4	-6.7	5.9	8.6	989
15/ 7	27.48	0	2.32	0.348	0.009	-0.022	0.002	-0.018	-0.003	0.002	0.007	-0.029	0.007	0	-24.1	379.2	-50.3	9.5	-7.9	5.7	8.7	989
16/ 8	27.56	0	2.32	0.352	0.007	-0.012	0.003	-0.005	-0.002	0.001	0.005	-0.011	-0.001	0	-12.8	385.5	-13.7	7	-5.2	7.5	8.9	989
17/ 9	27.6	0	2.32	0.354	0.003	-0.015	0.001	0.002	-0.001	0.001	0.002	-0.006	-0.009	0	-16.6	388.2	4.4	3.5	-2.1	4.2	9.1	988
18/ 10	27.56	0	2.32	0.354	0.005	-0.018	0.001	0.001	-0.002	0	0.005	-0.008	-0.01	0	-19.1	387.2	2.5	5.4	-6	3.8	8.8	989
19/ 11	27.74	0	2.32	0.343	0.005	0.004	0.002	0.005	-0.001	0.002	0.003	0.007	-0.003	0	4.6	380.3	13.5	5.4	-2.4	4.8	9	988
20/ 12	27.67	0	2.32	0.343	0.006	0.004	0.001	0.003	-0.001	0.002	0.004	0.005	-0.001	0	4.1	377.8	7.6	6.2	-3.2	3.8	9.1	988
21/ 13	27.58	0	2.32	0.34	0.007	0.001	0.001	-0.002	-0.001	0.003	0.004	-0.002	0.002	0	0.6	372.1	-5.1	7.5	-2.4	2.5	9.4	988
22/ 14	27.65	0	2.32	0.346	0.007	-0.006	0.001	0.004	0	0.004	0.003	0.001	-0.007	0	-7	380.1	12	7.7	0.7	2.8	9.3	988
23/ 15	27.6	0	2.32	0.316	0.013	0.096	0.003	-0.04	-0.003	0.004	0.009	0.008	0.088	0	103.3	346.4	-113.9	14	-7.7	9.2	9.4	988
24/ 16	27.62	0	2.32	0.322	0.007	0.033	0.001	-0.015	-0.001	0.003	0.004	0.002	0.031	0	36.1	353.2	-41.8	7	-1.5	3.5	9.3	987
25/ 17	27.61	0	2.32	0.322	0.006	0.034	0.001	-0.015	0	0.002	0.003	0.002	0.032	0	37	352.9	-43.1	6	-1.3	2.4	9.5	987
26/ 18	27.62	0	2.32	0.328	0.003	0.027	0.001	-0.009	-0.003	-0.001	0.005	0.005	0.023	0	29.6	359.3	-25.8	3.6	-8.3	4.1	9.6	987
27/ 19	27.66	0	2.32	0.328	0.011	0.05	0.002	0.001	0.001	0.007	0.005	0.026	0.024	0	54	359.8	3.2	12.3	3.1	4.6	9.7	987

FILE	T1	07Dec2009@12:25:29	User data																		
FIRM	LOUGHBOROUGH UNI																				
VEHI	FORD																				
MAKE	FOCUS																				
MODL																					
TYPE	GROUP TWO																				
CNFG	1																				
OALN	4365																				
WIDT	1784																				
HEIG	1495																				
WBAS	2630																				
FTRK	1520																				
RTRK	1515																				
FTRM	0																				
RTRM	0																				
MRFX	0																				
MRFZ	0																				
VPOX	0																				
VPOY	0																				
HBLR	0.8																				
SCAL	100																				
BLFE	NO																				
GBHT	0																				
MODE	NORMAL																				
UNITFM	N.m																				
UNITWS	m/s																				
Run/Cfg	Wind_m/s	Deg	FA.Sqm	CD	CY	CL	CMX	CMY	CMZ	CYF	CYR	CLF	CLR	XCP	Lift	Drag	Pitch	Side	Yaw	Roll	Amb.DegC	Amb.mBar
WEIGHT	(kg:T/F/R)	(Lb:T/F/R)	1340.7	808.8	531.9	2955.7	1783	1172.6														
CofG	(+=fwd. mm/ft)	272	0.89																			
1/ 1	27.36	0	2.32	0.34	0.012	0.147	0.003	0.004	-0.005	0.001	0.011	0.077	0.07	0	155.2	365.7	10.1	12.4	-13.3	8.3	9	986
2/ 1	27.4	0	2.32	0.34	0.013	0.146	0.003	0.004	-0.005	0.001	0.011	0.077	0.069	0	155.1	366.8	11.3	13.3	-13.4	8.3	8.5	986
3/ 1	27.41	-2.5	2.32	0.348	-0.092	0.169	-0.019	-0.001	-0.028	-0.074	-0.018	0.083	0.086	30.6	179.8	376	-3	-98.1	-79	-53.2	8.3	986
4/ 1	27.37	-5	2.32	0.352	-0.193	0.179	-0.041	0	-0.051	-0.148	-0.045	0.089	0.089	26.6	189.7	380.1	-0.1	-205.2	-143.7	-113.2	8.3	986
5/ 1	27.39	-7.5	2.32	0.358	-0.294	0.2	-0.062	0.001	-0.074	-0.221	-0.073	0.102	0.099	25.1	213	386.1	4	-312.2	-206	-174.7	8.4	986
6/ 1	27.33	-10	2.32	0.371	-0.399	0.236	-0.085	0.001	-0.093	-0.292	-0.107	0.119	0.117	23.3	249.2	398.1	2.5	-422.2	-258.6	-237.2	8.4	986
7/ 1	27.22	-12.5	2.32	0.388	-0.505	0.301	-0.11	-0.003	-0.11	-0.362	-0.142	0.147	0.154	21.8	315.5	412.9	-9.4	-529.3	-303.1	-302.7	8.6	986
8/ 1	27.13	-15	2.32	0.398	-0.589	0.362	-0.131	-0.002	-0.131	-0.426	-0.163	0.179	0.183	22.3	377.2	420	-5.3	-613.4	-359.5	-358.8	8.7	986
9/ 2	27.58	0	2.32	0.331	0.011	0.12	0.003	0.009	-0.004	0.001	0.01	0.069	0.051	0	128.1	359.6	25.6	12.3	-12.3	7.5	10.1	985
10/ 3	27.54	0	2.32	0.321	0.007	0.095	0.002	0.017	-0.002	0.001	0.005	0.065	0.031	0	101.7	348.9	47.6	7	-5.6	6.2	9.9	985
11/ 4	27.51	0	2.32	0.328	0.014	0.17	0.004	0.021	-0.005	0.003	0.012	0.106	0.064	0	181.1	355.5	59.7	15.1	-12.7	11	9.8	985
12/ 5	27.56	0	2.32	0.319	0.009	0.119	0.003	0.018	-0.003	0.002	0.007	0.078	0.042	0	127.7	346.6	50.5	9.8	-7.3	7.8	10	985
13/ 6	27.61	0	2.32	0.319	0.007	0.035	0.002	-0.035	-0.001	0.002	0.005	-0.017	0.053	0	38	347.8	-98.7	7.7	-4.2	5.9	10.3	985
14/ 7	27.59	0	2.32	0.328	0.005	0.012	0.002	-0.026	-0.001	0.001	0.004	-0.019	0.032	0	13	356.8	-71.8	5.5	-3.5	7	10.2	985
15/ 8	27.58	0	2.32	0.338	0.006	-0.007	0.002	-0.018	-0.001	0.002	0.004	-0.022	0.015	0	-7.6	367.5	-50.9	6.1	-3.4	5.9	10.4	985
16/ 9	27.58	0	2.32	0.331	0.008	0.012	0.002	-0.012	-0.002	0.002	0.006	-0.006	0.019	0	13.1	359.4	-35	8.3	-5.6	6.3	10.5	985
17/ 10	27.61	0	2.32	0.33	0.01	0.047	0.003	0.016	-0.003	0.002	0.008	0.039	0.008	0	50.4	359.3	44.6	10.3	-8.9	8.2	10.2	985
18/ 11	27.67	0	2.32	0.33	0.009	0.047	0.003	0.015	-0.003	0.002	0.008	0.038	0.008	0	50.5	361.5	42.5	10.1	-8.5	8.9	10.2	986
19/ 12	27.62	0	2.32	0.332	0.008	0.027	0.002	-0.002	-0.004	0	0.008	0.011	0.015	0	28.4	361.5	-5.3	8.9	-11.2	5.9	10.5	985
20/ 13	27.63	0	2.32	0.328	0.009	0.024	0.003	-0.005	-0.004	0	0.009	0.007	0.017	0	25.9	358	-13	9.2	-12.1	7.4	10.5	985
21/ 14	27.63	0	2.32	0.326	0.007	0.02	0.003	-0.009	-0.003	0	0.007	0.001	0.018	0	21.3	356	-24	7.4	-9.7	7.3	10.5	985
22/ 15	27.63	0	2.32	0.334	0.005	0.01	0.002	-0.011	-0.004	-0.002	0.007	-0.006	0.016	0	11.2	364	-31.3	5.7	-11.9	4.7	10.5	986
23/ 16	27.55	0	2.32	0.325	0.008	0.021	0.003	-0.009	-0.004	0	0.008	0.002	0.019	0	22.6	352.9	-24.6	8.4	-10.9	7.7	10.2	986
24/ 17	27.59	0	2.32	0.325	0.01	0.008	0.003	-0.003	-0.005	0	0.01	0.001	0.007	0	8.5	353.5	-9.1	11.1	-14.6	9.4	10.4	986
25/ 18	27.76	0	2.32	0.325	0.009	0.011	0.003	-0.003	-0.005	-0.001	0.01	0.003	0.008	0	12.3	358.2	-7.3	10.2	-15.1	9.9	10.5	986
26/ 19	27.21	0	2.32	0.311	0.011	0.03	0.003	-0.011	-0.004	0.001	0.01	0.004	0.027	0	31.5	330.9	-31.4	11.9	-12.2	8.8	9.9	987

FILE	T1	08Dec2009@07:50:55	User data																		
FIRM	LOUGHBOROUGH UNI																				
VEHI	FORD																				
MAKE	FOCUS																				
MODL																					
TYPE	GROUP THREE																				
CNFG	1																				
OALN	4365																				
WIDT	1784																				
HEIG	1495																				
WBAS	2630																				
FTRK	1520																				
RTRK	1515																				
FTRM	0																				
RTRM	0																				
MRFX	0																				
MRFZ	0																				
VPOX	0																				
VPOY	0																				
HBLR	0.8																				
SCAL	100																				
BLFE	NO																				
GBHT	0																				
MODE	NORMAL																				
UNITFM	N.m																				
UNITWS	m/s																				
Run/Cfg	Wind_m/s	Deg	FA.Sqm	CD	CY	CL	CMX	CMY	CMZ	CYF	CYR	CLF	CLR	XCP	Lift	Drag	Pitch	Side	Yaw	Roll	Amb.DegC	Amb.mBar
WEIGHT	(kg:T/F/R)	(Lb:T/F/R)	1340.6	808.9	531.8	2955.6	1783.2	1172.4														
CofG	(+=fwd. mm/ft)	272	0.89																			
1/ 1	27.15	0	2.32	0.341	0.009	0.144	0.003	0.005	-0.004	0	0.008	0.078	0.067	0	154.1	369.3	15.1	9.4	-11.5	7.9	7.2	1004
2/ 1	27.03	0	2.32	0.342	0.011	0.139	0.003	0.008	-0.005	0.001	0.01	0.078	0.061	0	147.7	368.9	23.5	11.7	-13.4	9.1	6.5	1004
3/ 1	27.11	0	2.32	0.341	0.011	0.142	0.003	0.007	-0.005	0.001	0.01	0.078	0.063	0	151.5	370.2	20.9	11.6	-13.3	9.5	6.2	1004
4/ 1	26.53	17.5	2.32	0.406	0.673	0.461	0.154	0.007	0.142	0.479	0.194	0.238	0.223	21.2	472.2	421.1	19.5	689	383.7	415	6	1005
5/ 1	26.42	20	2.32	0.417	0.748	0.547	0.173	0.012	0.164	0.538	0.21	0.286	0.261	22	555.2	429.5	33.3	759.8	439.1	461.1	6.1	1005
6/ 1	26.31	22.5	2.32	0.429	0.837	0.591	0.189	0.028	0.179	0.597	0.24	0.324	0.267	21.4	594.6	437.8	74.9	842.2	473.2	501.3	6.2	1004
7/ 1	26.18	25	2.32	0.435	0.913	0.625	0.205	0.035	0.193	0.649	0.264	0.347	0.278	21.1	622.8	439.4	91.2	909.7	504.5	536	6.3	1004
8/ 1	26	27.5	2.32	0.431	0.996	0.62	0.219	0.035	0.2	0.697	0.298	0.345	0.275	20	609	428.6	91.2	977.9	515.3	564.9	6.4	1004
9/ 1	25.77	30	2.32	0.432	1.059	0.598	0.232	0.026	0.207	0.736	0.323	0.325	0.273	19.5	576.3	421.6	66.8	1020.7	524.4	587.4	6.6	1004
10/ 2	26.79	0	2.32	0.333	0.009	0.123	0.003	0.006	-0.004	0.001	0.008	0.068	0.055	0	127.7	351.7	17.2	9.8	-9.8	8.9	7.7	1004
11/ 3	27.34	0	2.32	0.342	0.009	0.181	0.002	0.013	-0.004	0.001	0.009	0.103	0.077	0	195.1	375.7	36.8	10.2	-11.7	6.3	7.9	1004
12/ 4	26.89	0	2.32	0.333	0.011	0.168	0.004	0.015	-0.004	0.001	0.01	0.099	0.069	0	175.4	353.4	41.9	11.9	-12.3	9.7	8.2	1004
13/ 5	27.46	0	2.32	0.324	0.008	0.108	0.003	0.012	-0.003	0.001	0.007	0.066	0.042	0	117.9	358.4	34.1	8.3	-8.5	7.8	8.2	1004
14/ 6	27.52	0	2.32	0.32	0.006	0.095	0.003	0.014	-0.002	0.001	0.005	0.062	0.033	0	103.8	355	41.2	7	-6.2	8	8.4	1004
15/ 7	27.58	0	2.32	0.318	0.006	0.067	0.002	-0.006	-0.002	0.001	0.005	0.027	0.04	0	73.1	354.1	-18.2	6.6	-5.5	5.5	8.9	1003
16/ 8	27.51	0	2.32	0.318	0.003	0.044	0.001	-0.021	-0.003	-0.001	0.005	0.001	0.043	0	48.4	352.5	-60.1	3.3	-8.5	3.9	8.7	1003
17/ 9	27.55	0	2.32	0.318	0.005	0.044	0.003	-0.018	-0.004	-0.001	0.007	0.004	0.04	0	48	353.9	-53	5.9	-11.3	8	8.6	1004
18/ 10	27.55	0	2.32	0.331	0.003	0.037	0.002	0.003	-0.003	-0.002	0.005	0.022	0.016	0	40.6	368	8.9	2.9	-10	6.8	8.9	1004
19/ 11	27.53	0	2.32	0.311	0.007	0.083	0.002	-0.004	-0.003	0.001	0.006	0.038	0.045	0	90.9	345.2	-10.7	7.5	-7.9	6.2	9	1003
20/ 12	27.53	0	2.32	0.309	0.009	0.083	0.002	-0.006	-0.003	0.001	0.008	0.036	0.047	0	90.3	343.1	-16.9	9.5	-9.8	5.8	9	1003
21/ 13	27.55	0	2.32	0.307	0.007	0.077	0.002	-0.011	-0.004	-0.001	0.008	0.027	0.049	0	83.6	341.7	-31.3	7.5	-12.1	6	8.9	1004
22/ 14	27.57	0	2.32	0.307	0.006	0.075	0.002	-0.014	-0.004	-0.001	0.007	0.024	0.051	0	81.6	340.8	-39.4	6.7	-12.1	5.4	9.4	1003
23/ 15	26.96	0	2.32	0.304	0.009	0.07	0.002	-0.012	-0.005	0	0.009	0.023	0.046	0	72.8	324	-31.6	9.1	-12.5	6.7	8.9	1003
24/ 16	27.58	0	2.32	0.304	0.007	0.074	0.002	-0.012	-0.005	-0.001	0.008	0.025	0.049	0	80.7	339.1	-35.3	7.6	-13.1	6.9	9	1003
25/ 17	27.6	0	2.32	0.304	0.009	0.068	0.003	-0.01	-0.005	-0.001	0.01	0.024	0.044	0	74.6	339	-28.1	9.5	-15.4	8.4	9	1003
26/ 18	27.54	0	2.32	0.308	0.011	0.07	0.004	-0.009	-0.006	0	0.012	0.026	0.044	0	76.2	340.5	-25.2	12.3	-17	10.1	9.8	1003
27/ 19	27.54	0	2.32	0.304	0.008	0.07	0.003	-0.01	-0.005	-0.001	0.009	0.025	0.045	0	75.8	337.1	-29.1	9.1	-15.1	9.4	9.5	1003
28/ 20	27.6	0	2.32	0.295	0.006	0.109	0.002	-0.024	-0.005	-0.002	0.008	0.03	0.079	0	119.4	328.4	-70.3	7	-14.4	6	9.5	1003
29/ 21	27.53	0	2.32	0.306	0.008	0.065	0.003	-0.007	-0.006	-0.001	0.01	0.025	0.04	0	70.5	339	-20.6	9.2	-16	9.2	9.6	1003
30/ 22	27.56	0	2.32	0.299	0.008	0.083	0.003	-0.015	-0.005	-0.001	0.009	0.027	0.056	0	90.3	331.7	-41.6	8.8	-14.5	7.9	9.7	1003
31/ 23	27.52	0	2.32	0.3	0.008	0.083	0.001	-0.015	-0.005	-0.001	0.009	0.027	0.057	0	90.5	331.4	-42.6	8.5	-13.8	4.3	9.8	1003
32/ 24	27.56	0	2.32	0.295	0.007	0.076	0.002	-0.024	-0.002	0.002	0.005	0.014	0.062	0	82.3	327.4	-68.4	7.4	-4.7	5.5	10	1003
33/ 25	27.51	0	2.32	0.297	0.006	0.076	0.002	-0.024	-0.002	0.001	0.005	0.015	0.062	0	82.9	328.3	-67.4	6.4	-6.1	5.4	9.7	1003
34/ 26	27.53	0	2.32	0.296	0.007	0.078	0.002	-0.014	-0.002	0.001	0.005	0.025	0.053	0	84.7	327.6	-40.5	7.1	-5.9	5	9.8	1003
35/ 27	27.62	0	2.32	0.296	0.005	0.074	0.001	-0.014	-0.002	0.001	0.004	0.023	0.051	0	80.9	329.5	-39.9	4.9	-5	3.5	10	1003

FILE	T1	08Dec2009@13:12:18	User data																			
FIRM	LOUGHBOROUGH UNI																					
VEHI	FORD																					
MAKE	FOCUS																					
MODL																						
TYPE	GROUP FOUR																					
CNFG	1																					
OALN	4365																					
WIDT	1784																					
HEIG	1495																					
WBAS	2630																					
FTRK	1520																					
RTRK	1515																					
FTRM	0																					
RTRM	0																					
MRFX	0																					
MRFZ	0																					
VPOX	0																					
VPOY	0																					
HBLR	0.8																					
SCAL	100																					
BLFE	NO																					
GBHT	0																					
MODE	NORMAL																					
UNITFM	N.m																					
UNITWS	m/s																					
Run/Cfg	Wind_m/s	Deg	FA.Sqm	CD	CY	CL	CMX	CMY	CMZ	CYF	CYR	CLF	CLR	XCP	Lift	Drag	Pitch	Side	Yaw	Roll	Amb.DegC	Amb.mBar
WEIGHT	(kg:T/F/R)	(Lb:T/F/R)	1340.6	808.2	532.3	2955.4	1781.8	1173.6														
CofG	(+=fwd. mm/ft)	271	0.89																			
1/ 1	27.43	0	2.32	0.339	0.013	0.14	0.004	0.004	-0.003	0.003	0.009	0.074	0.065	0	150.4	370.6	12.4	13.5	-8.5	10.6	10	1003
2/ 1	27.43	0	2.32	0.34	0.012	0.144	0.004	0.003	-0.003	0.003	0.009	0.075	0.069	0	155.1	372.9	8.9	12.9	-8.3	10.3	9.2	1003
3/ 1	27.36	0	2.32	0.339	0.013	0.147	0.004	0.001	-0.003	0.003	0.01	0.075	0.072	0	158.3	370.7	3.8	13.9	-9.5	10.5	8.9	1003
4/ 1	26.83	-17.5	2.32	0.42	-0.656	0.467	-0.147	-0.006	-0.155	-0.483	-0.173	0.228	0.239	23.6	483.4	440.5	-15.8	-679.7	-422.1	-399.9	8.8	1003
5/ 1	26.76	-20	2.32	0.426	-0.74	0.536	-0.167	0.004	-0.173	-0.543	-0.197	0.272	0.264	23.4	551.8	444.8	11.4	-762.9	-469.3	-451.9	8.9	1003
6/ 1	26.68	-22.5	2.32	0.432	-0.835	0.588	-0.187	0.016	-0.186	-0.604	-0.232	0.31	0.278	22.3	601.8	447.7	43.1	-854.8	-500.4	-502.6	8.9	1003
7/ 1	26.61	-25	2.32	0.44	-0.908	0.647	-0.2	0.019	-0.2	-0.654	-0.254	0.342	0.305	22	657.8	453.7	49.7	-923.6	-534.5	-536.4	9.1	1003
8/ 1	26.52	-27.5	2.32	0.431	-1.002	0.679	-0.218	0.022	-0.209	-0.71	-0.292	0.362	0.317	20.9	686	441.2	59.1	-1012.6	-555.8	-578.1	9.2	1003
9/ 1	26.36	-30	2.32	0.418	-1.102	0.672	-0.236	0.019	-0.215	-0.766	-0.337	0.355	0.317	19.5	670.6	423	49.1	-1100.1	-563.4	-620.4	9.3	1003
10/ 2	27.57	0	2.32	0.326	0.009	0.113	0.003	0.01	-0.001	0.003	0.006	0.066	0.046	0	122.3	359.9	28.4	9.9	-3.9	9.1	10.7	1002
11/ 3	26.94	0	2.32	0.332	0.015	0.156	0.004	0.011	-0.003	0.005	0.01	0.089	0.067	0	162	349.6	29.3	15	-6.9	11.3	10.5	1002
12/ 4	26.9	0	2.32	0.344	0.014	0.198	0.003	0.021	-0.003	0.004	0.01	0.12	0.078	0	205.2	361.2	56.8	14.4	-7.8	8.4	10.3	1003
13/ 5	27.01	0	2.32	0.321	0.014	0.053	0.004	-0.055	-0.002	0.005	0.009	-0.029	0.082	0	55.3	340.3	-151.5	14.5	-6.2	9.7	10.8	1002
14/ 6	27.62	0	2.32	0.316	0.01	0.035	0.003	-0.052	-0.001	0.003	0.006	-0.035	0.069	0	37.6	350.3	-149.2	10.7	-4.3	8.3	10.8	1002
15/ 7	27.57	0	2.32	0.317	0.015	0.074	0.004	-0.012	-0.003	0.005	0.01	0.025	0.049	0	80.2	350.4	-33.8	15.8	-7.5	11	10.7	1002
16/ 8	27.56	0	2.32	0.312	0.016	0.104	0.004	-0.003	-0.003	0.005	0.011	0.049	0.055	0	112.6	344.3	-9.3	17	-8.6	10	10.7	1002
17/ 9	27.63	0	2.32	0.311	0.02	0.132	0.004	-0.01	-0.004	0.006	0.014	0.056	0.076	0	144.5	345.4	-28.8	21.8	-11.9	10.7	10.6	1002
18/ 10	27.59	0	2.32	0.308	0.017	0.131	0.004	-0.013	-0.003	0.006	0.012	0.053	0.078	0	142.3	341.5	-35.8	19	-9.1	10.3	10.6	1002
19/ 11	27.58	0	2.32	0.312	0.018	0.146	0.003	-0.016	-0.003	0.006	0.012	0.057	0.089	0	158.8	344.8	-45	19.1	-8	8.8	10.9	1002
20/ 12	27.68	0	2.32	0.32	0.005	0.057	0	0.005	0	0.002	0.003	0.034	0.024	0	62.6	356.3	14.1	5.6	-0.2	1.4	10.7	1002
21/ 13	27.5	0	2.32	0.319	0.005	0.059	0.001	0.002	0	0.003	0.002	0.032	0.027	0	63.8	350.3	7	5.7	0.9	2.7	10.6	1002
22/ 14	27.57	0	2.32	0.305	0.01	0.101	0.002	-0.023	-0.002	0.003	0.007	0.027	0.074	0	109.4	337.1	-66.6	10.7	-5.6	5.1	10.6	1002
23/ 15	27.56	0	2.32	0.305	0.004	0.1	0.001	-0.015	-0.001	0.002	0.003	0.035	0.065	0	108.2	336.7	-42.9	4.8	-1.5	3.3	10.6	1002
24/ 16	27.47	0	2.32	0.314	0.002	0.066	0	-0.003	0	0.001	0.001	0.03	0.035	0	70.8	344.6	-7.1	2.2	0.5	0.1	10.8	1002
25/ 17	27.45	0	2.32	0.313	0.001	0.06	0	-0.001	0.001	0.001	0	0.029	0.031	0	64.2	343.3	-2.4	1.4	1.5	0.7	10.7	1002
26/ 18	27.59	0	2.32	0.31	0.006	0.069	0.001	-0.004	-0.001	0.002	0.004	0.03	0.039	0	75	342.7	-12.2	6.7	-2.6	3.7	10.7	1002

FILE	T1	09Dec2009@08:31:50	User data																			
FIRM	LOUGHBOROUGH UNI																					
VEHI	FORD																					
MAKE	FOCUS																					
MODL																						
TYPE	GROUP FIVE																					
CNFG	1																					
OALN	4365																					
WIDT	1784																					
HEIG	1495																					
WBAS	2630																					
FTRK	1520																					
RTRK	1515																					
FTRM	0																					
RTRM	0																					
MRFX	0																					
MRFZ	0																					
VPOX	0																					
VPOY	0																					
HBLR	0.8																					
SCAL	100																					
BLFE	NO																					
GBHT	0																					
MODE	NORMAL																					
UNITFM	N.m																					
UNITWS	m/s																					
Run/Cfg	Wind_m/s	Deg	FA.Sqm	CD	CY	CL	CMX	CMY	CMZ	CYF	CYR	CLF	CLR	XCP	Lift	Drag	Pitch	Side	Yaw	Roll	Amb.DegC	Amb.mBar
WEIGHT	(kg:T/F/R)	(Lb:T/F/R)	1340.6	808.5	532.2	2955.5	1782.3	1173.2														
CofG	(+=fwd. mm/ft)	271	0.89																			
1/ 1	27.18	0	2.32	0.342	0.013	0.144	0.004	0.004	-0.004	0.002	0.011	0.076	0.068	0	154.4	373.1	11	14.3	-12.2	10.1	8	1011
2/ 1	27.17	0	2.32	0.341	0.012	0.145	0.003	0.003	-0.004	0.002	0.01	0.076	0.07	0	156.4	372.8	9.1	13.1	-10.5	8.9	7.4	1011
3/ 2	27.3	0	2.32	0.319	0.009	0.12	0.003	-0.045	-0.004	0	0.009	0.015	0.105	0	129.9	352.1	-128.6	10.1	-11.9	9.9	7.9	1011
4/ 3	27.38	0	2.32	0.334	0.012	0.142	0.004	-0.005	-0.004	0.002	0.01	0.066	0.076	0	155.1	370.6	-15.5	13.2	-12.4	11.3	7.8	1011
5/ 4	27.35	0	2.32	0.327	0.013	0.161	0.004	0.017	-0.004	0.003	0.01	0.098	0.063	0	175.3	361.6	49.6	14	-10.4	10.9	8.4	1010
6/ 5	27.45	0	2.32	0.319	0.009	0.119	0.003	0.017	-0.003	0.002	0.007	0.077	0.042	0	130.6	355.7	49.5	10.2	-7.6	8.8	8.4	1010
7/ 6	27.41	0	2.32	0.321	0.01	0.1	0.003	-0.004	-0.003	0.002	0.008	0.046	0.054	0	109.2	355.1	-12	11.4	-7.9	9.6	8.7	1010
8/ 7	27.45	0	2.32	0.318	0.004	0.072	0.002	-0.026	-0.001	0.001	0.003	0.01	0.062	0	79	353.3	-75.4	4.2	-3.7	6.1	8.6	1010
9/ 8	27.42	0	2.32	0.328	0.007	0.057	0.003	0.011	-0.003	0.001	0.006	0.04	0.017	0	62.2	363.1	32.6	8	-7.8	7.9	9	1010
10/ 9	27.41	0	2.32	0.323	0.009	0.02	0.003	-0.017	-0.002	0.003	0.006	-0.007	0.027	0	21.8	357.5	-47.3	10	-5	7.4	9.3	1010
11/ 10	27.4	0	2.32	0.325	0.012	0.06	0.004	0.012	-0.004	0.003	0.01	0.042	0.018	0	65.2	358.6	33.9	13.5	-10.3	10.1	9.5	1010
12/ 11	27.47	0	2.32	0.325	0.009	0.058	0.003	0.015	-0.003	0.002	0.007	0.044	0.014	0	63	360.2	42.2	9.6	-7.3	9.2	9.5	1010
13/ 12	27.5	0	2.32	0.322	0.015	0.082	0.003	0.02	-0.002	0.005	0.01	0.06	0.021	0	89.1	357.4	56	16.2	-6.6	9	9.7	1010
14/ 13	27.51	0	2.32	0.318	0.013	0.081	0.003	0.017	-0.002	0.004	0.008	0.057	0.024	0	88.5	353.3	48.2	13.7	-6.4	10	9.6	1010
15/ 14	27.46	0	2.32	0.319	0.014	0.075	0.003	0.012	-0.002	0.005	0.009	0.05	0.025	0	81.2	353.1	35.7	15.3	-6.1	9.9	9.6	1010
16/ 15	27.4	0	2.32	0.318	0.017	0.078	0.003	0.011	-0.001	0.008	0.009	0.049	0.028	0	84.3	350.9	30.1	18.5	-1.8	8.3	9.8	1010
17/ 16	27.44	0	2.32	0.315	0.015	0.071	0.003	0.01	-0.001	0.006	0.008	0.046	0.026	0	77.6	348.5	28	16.2	-2.9	10	10	1010
18/ 17	27.48	0	2.32	0.314	0.016	0.074	0.003	0.009	0	0.007	0.008	0.046	0.028	0	81	348.5	26.2	17.1	-1.2	9.6	10.1	1010
19/ 18	27.43	0	2.32	0.312	0.015	0.08	0.003	0.007	0	0.007	0.008	0.047	0.033	0	86.4	344.7	20.4	16.2	-1.2	8.5	10.2	1010
20/ 19	27.49	0	2.32	0.311	0.014	0.093	0.003	0.013	-0.001	0.006	0.007	0.06	0.034	0	101.7	344.8	37.6	15.2	-1.5	8.3	10.3	1010
21/ 20	27.46	0	2.32	0.311	0.012	0.052	0.002	-0.02	0	0.006	0.006	0.006	0.045	0	56	343.9	-56.3	12.8	-0.9	6.9	10.3	1010
22/ 21	27.53	0	2.32	0.301	0.009	0.036	0.002	-0.042	-0.001	0.004	0.005	-0.023	0.06	0	39.7	335.3	-119.4	9.8	-2.2	5.5	10.2	1010
23/ 22	27.56	0	2.32	0.308	0.012	0.049	0.003	-0.023	-0.002	0.004	0.008	0.001	0.047	0	53.3	343	-66.4	13.1	-5.6	7.8	10.2	1010

Appendix B – Data from full-scale testing of Ford Mondeo performed at MIRA, December 2008

FILE	T1	08Dec2008@08:42:12	User data																			
FIRM	LOUGHBOROUGH UNI																					
VEHI	GROUP 1																					
MAKE	FORD																					
MODL	MONDEO 2.0LTR PETROL																					
TYPE	HATCH BACK																					
CNFG	1																					
OALN	4795																					
WIDT	1830																					
HEIG	1475																					
WBAS	2845																					
FTRK	1575																					
RTRK	1585																					
FTRM	0																					
RTRM	0																					
MRFX	0																					
MRFZ	0																					
VPOX	0																					
VPOY	0																					
HBLR	0.8																					
SCAL	100																					
BLFE	NO																					
GBHT	0																					
MODE	NORMAL																					
UNITFM	N.m																					
UNITWS	m/s																					
Run/Cfg	Wind_m/s	Deg	FA.Sqm	CD	CY	CL	CMX	CMY	CMZ	CYF	CYR	CLF	CLR	XCP	Lift	Drag	Pitch	Side	Yaw	Roll	Amb.DegC	Amb.mBar
WEIGHT	(kg:T/F/R)	(Lb:T/F/R)	1440.2	825.9	614.4	3175.2	1820.7	1354.4														
CofG	(+=fwd. mm/ft)	209	0.69																			
1/ 1	27.62	0	2.4	0.329	-0.011	0.221	-0.003	0.005	0.001	-0.005	-0.006	0.116	0.105	0	259.9	394.5	18.2	-13.1	2.7	-10.6	3.4	1020
2/ 1	27.66	0	2.4	0.328	-0.011	0.22	-0.003	0.005	0.001	-0.005	-0.006	0.115	0.105	0	260.6	394.8	17	-13.4	2.3	-11.6	3	1020
3/ 1	27.58	5	2.4	0.333	0.172	0.253	0.033	0.007	0.047	0.134	0.039	0.133	0.12	27.5	297.7	399.3	22.8	202.9	158.7	111.8	2.7	1021
4/ 1	27.51	10	2.4	0.341	0.356	0.326	0.071	0.018	0.094	0.272	0.083	0.181	0.145	26.6	381.9	406.2	59.6	416.7	314.8	237.1	2.8	1021
5/ 1	27.32	15	2.4	0.349	0.513	0.46	0.102	0.031	0.148	0.404	0.109	0.261	0.199	28.8	530.8	409.8	102	592.5	484.8	334.1	2.8	1021
6/ 2	27.73	0	2.4	0.333	-0.012	0.236	-0.003	0.016	0.001	-0.005	-0.007	0.134	0.103	0	279.7	401.6	52.6	-14.4	3.3	-11.2	4	1020
7/ 3	27.67	0	2.4	0.329	-0.012	0.234	-0.003	0.016	0.001	-0.005	-0.007	0.133	0.101	0	275.4	394.5	52.7	-14.3	3	-10	4	1020
8/ 4	27.69	0	2.4	0.323	-0.009	0.218	-0.002	0.006	0	-0.005	-0.005	0.115	0.103	0	256.9	388.6	20.8	-10.9	0	-8.4	4.2	1019
9/ 5	27.68	0	2.4	0.323	-0.005	0.166	-0.002	0.035	-0.001	-0.004	-0.001	0.118	0.048	0	195.1	387.7	116.5	-6.1	-4.5	-5.7	4.5	1019
10/ 6	27.68	0	2.4	0.327	-0.006	0.184	-0.002	0.025	-0.001	-0.004	-0.002	0.118	0.067	0	217	391.7	84.7	-6.8	-3.7	-6.8	4.6	1019
11/ 7	27.62	0	2.4	0.333	-0.009	0.211	-0.003	-0.012	0.001	-0.004	-0.005	0.093	0.118	0	247.4	396.8	-40.4	-10.8	1.7	-9.1	4.4	1019
12/ 8	27.66	0	2.4	0.33	-0.01	0.177	-0.003	-0.036	0.002	-0.003	-0.007	0.053	0.124	0	208	393.9	-118.8	-11.3	6.7	-10.2	5	1019
13/ 9	27.71	0	2.4	0.317	-0.006	0.122	-0.002	-0.009	0	-0.003	-0.003	0.052	0.07	0	144	379.8	-29.5	-6.6	0.5	-6.6	5.2	1019
14/ 10	27.65	0	2.4	0.324	-0.005	0.125	-0.002	-0.008	0	-0.003	-0.002	0.055	0.071	0	146.5	387.2	-26.8	-5.8	-1.6	-6.6	5	1019
15/ 11	27.68	0	2.4	0.317	-0.001	0.137	0	-0.011	-0.003	-0.003	0.003	0.057	0.08	0	160.7	377.9	-38.2	-0.8	-9.5	-0.9	5.5	1018
16/ 12	27.65	0	2.4	0.315	-0.001	0.141	0	-0.01	-0.004	-0.004	0.003	0.061	0.08	0	165.3	375.4	-32	-1	-12.6	0.8	5.5	1018
17/ 13	27.63	0	2.4	0.319	-0.005	0.123	-0.002	-0.01	0	-0.003	-0.002	0.052	0.071	0	143.3	379.1	-32.5	-6.2	-0.8	-6.1	5.6	1018
18/ 14	27.6	0	2.4	0.319	-0.005	0.124	-0.002	-0.01	0	-0.003	-0.002	0.052	0.072	0	144.2	378.5	-33.7	-5.3	-1.2	-5.2	5.7	1018
19/ 15	27.68	0	2.4	0.316	-0.006	0.121	-0.002	-0.013	0	-0.003	-0.003	0.047	0.074	0	141.5	376.4	-44.2	-6.5	0.4	-6.8	5.7	1018
20/ 16	27.66	0	2.4	0.315	-0.004	0.114	-0.002	-0.018	0	-0.002	-0.002	0.039	0.075	0	133.6	374.9	-59.3	-4.5	0.1	-5.4	5.7	1018
21/ 17	27.65	0	2.4	0.315	-0.005	0.128	-0.002	-0.01	0	-0.002	-0.003	0.054	0.074	0	148.9	374.3	-32.1	-5.7	0.9	-6.2	6.2	1017
22/ 18	27.64	0	2.4	0.32	-0.004	0.117	-0.002	-0.016	-0.001	-0.002	-0.001	0.042	0.075	0	136.8	380.3	-54.6	-4.3	-2	-6	6	1017
23/ 19	27.67	0	2.4	0.327	-0.006	0.119	-0.002	-0.025	0.001	-0.002	-0.004	0.035	0.085	0	139.2	388.2	-83.3	-6.8	2.8	-6.9	6.2	1017
24/ 20	27.68	0	2.4	0.316	-0.005	0.12	-0.002	-0.014	0	-0.002	-0.002	0.047	0.074	0	140.5	376.4	-45.3	-5.6	-0.2	-5.9	6.1	1017
25/ 21	27.61	0	2.4	0.335	-0.012	0.085	-0.003	0.03	0.003	-0.003	-0.009	0.073	0.013	0	98.8	395.1	99.4	-13.4	9.4	-11	6.7	1017
26/ 22	27.71	0	2.4	0.311	-0.001	0.136	0.001	-0.014	-0.003	-0.004	0.003	0.054	0.082	0	159.2	369.9	-46.1	-1.2	-10.3	2.3	6.6	1017

FILE	T1	08Dec2008@12:33:12	User data																			
FIRM	LOUGHBOROUGH UNI																					
VEHI	GROUP 1																					
MAKE	FORD																					
MODL	MONDEO 2.0LTR PETROL																					
TYPE	HATCH BACK																					
CNFG	1																					
OALN	4795																					
WIDT	1830																					
HEIG	1475																					
WBAS	2845																					
FTRK	1575																					
RTRK	1585																					
FTRM	0																					
RTRM	0																					
MRFX	0																					
MRFZ	0																					
VPOX	0																					
VPOY	0																					
HBLR	0.8																					
SCAL	100																					
BLFE	NO																					
GBHT	0																					
MODE	NORMAL																					
UNITFM	N.m																					
UNITWS	m/s																					
Run/Cfg	Wind_m/s	Deg	FA.Sqm	CD	CY	CL	CMX	CMY	CMZ	CYF	CYR	CLF	CLR	XCP	Lift	Drag	Pitch	Side	Yaw	Roll	Amb.DegC	Amb.mBar
WEIGHT	(kg:T/F/R)	(Lb:T/F/R)	1440.1	825.5	614.7	3175	1819.8	1355.2														
CofG	(+=fwd. mm/ft)	208	0.68																			
1/ 1	27.68	0	2.4	0.33	-0.011	0.222	-0.003	0.004	0.001	-0.004	-0.006	0.115	0.107	0	258.2	391.7	14.1	-12.3	3.3	-10	6.4	1016
2/ 1	27.66	0	2.4	0.33	-0.01	0.221	-0.003	0.005	0.001	-0.005	-0.006	0.115	0.106	0	257.9	392.2	16.3	-11.8	1.8	-9.9	5.7	1016
3/ 2	27.77	0	2.4	0.321	-0.009	0.215	-0.003	0.005	0	-0.004	-0.005	0.112	0.103	0	251.4	382.7	16.3	-10.7	0.8	-8.5	6.8	1015
4/ 2	27.7	0	2.4	0.321	-0.007	0.215	-0.002	0.005	0	-0.004	-0.003	0.112	0.103	0	251.3	382	15	-8.1	-0.9	-6.7	6.1	1016
5/ 3	27.75	0	2.4	0.33	-0.011	0.232	-0.003	0.015	0	-0.005	-0.006	0.131	0.101	0	271.2	392.9	49	-12.8	1.2	-10.7	6.9	1015
6/ 4	27.78	0	2.4	0.321	-0.008	0.224	-0.002	0.013	0	-0.005	-0.004	0.125	0.099	0	262.1	382.6	43.4	-9.6	-1.4	-7.7	6.9	1015
7/ 5	27.73	0	2.4	0.327	-0.009	0.159	-0.003	-0.036	0.002	-0.002	-0.007	0.044	0.115	0	185.4	388.6	-118.1	-10.8	7.7	-9.7	7	1015
8/ 6	27.77	0	2.4	0.324	-0.008	0.159	-0.002	-0.053	0.003	-0.001	-0.007	0.026	0.132	0	185.5	386.3	-176.4	-9.5	8.9	-8.1	7	1015
9/ 7	27.77	0	2.4	0.324	-0.006	0.19	-0.002	0.022	-0.001	-0.004	-0.002	0.117	0.073	0	222.2	386.3	73.8	-7.1	-2.6	-7	6.8	1015
10/ 8	27.66	0	2.4	0.327	-0.002	0.159	-0.001	0.039	-0.002	-0.003	0.001	0.118	0.04	0	184.2	386.6	128.8	-2.4	-6.7	-4.7	6.8	1015
11/ 9	27.65	0	2.4	0.321	-0.005	0.101	-0.002	-0.016	0	-0.002	-0.003	0.035	0.066	0	116.6	378.7	-52	-5.7	0.8	-6.7	7.2	1015
12/ 10	27.75	0	2.4	0.322	-0.005	0.113	-0.002	-0.003	0	-0.002	-0.003	0.053	0.06	0	131.6	381.3	-10.3	-6.1	0.7	-7.8	7.6	1014
13/ 11	27.72	0	2.4	0.321	-0.004	0.111	-0.002	-0.013	0	-0.002	-0.002	0.042	0.069	0	128.5	380.6	-43.9	-4.8	0.8	-6.4	7.3	1015
14/ 12	27.81	0	2.4	0.307	-0.005	0.115	-0.002	-0.003	0	-0.002	-0.003	0.054	0.061	0	134.8	365.9	-11.6	-6.3	1	-6.7	7.6	1014
15/ 13	27.82	0	2.4	0.301	-0.006	0.111	-0.002	-0.006	0	-0.003	-0.004	0.049	0.062	0	130.2	360.5	-21.2	-7.5	1.2	-7.8	7.2	1015
16/ 14	27.73	0	2.4	0.303	-0.005	0.112	-0.002	-0.007	0	-0.003	-0.003	0.049	0.063	0	130.6	359.1	-24.1	-6.4	0.5	-6.8	7.4	1014
17/ 15	27.66	0	2.4	0.302	-0.006	0.106	-0.002	-0.011	0.001	-0.002	-0.003	0.042	0.064	0	123.1	356.5	-35.7	-6.4	1.7	-6.6	7.7	1014
18/ 16	28.04	0	2.4	0.304	-0.004	0.124	-0.002	-0.013	0	-0.003	-0.002	0.049	0.075	0	147.5	369.1	-44.5	-5.1	-1.6	-6.3	7.6	1014
19/ 17	27.93	0	2.4	0.305	0	0.124	-0.001	-0.014	-0.002	-0.002	0.002	0.048	0.077	0	146.8	367.8	-48.4	-0.1	-6	-2.4	7.1	1014

FILE	T1	09Dec2008@07:29:53	User data																		
FIRM	LOUGHBOROUGH UNI																				
VEHI	GROUP 1																				
MAKE	FORD																				
MODL	MONDEO 2.0LTR PETROL																				
TYPE	HATCH BACK																				
CNFG	1																				
OALN	4795																				
WIDT	1830																				
HEIG	1475																				
WBAS	2845																				
FTRK	1575																				
RTRK	1585																				
FTRM	0																				
RTRM	0																				
MRFX	0																				
MRFZ	0																				
VPOX	0																				
VPOY	0																				
HBLR	0.8																				
SCAL	100																				
BLFE	NO																				
GBHT	0																				
MODE	NORMAL																				
UNITFM	N.m																				
UNITWS	m/s																				
Run/Cfg	Wind_m/s	Deg	FA.Sqm	CD	CY	CL	CMX	CMY	CMZ	CYF	CYR	CLF	CLR	XCP	Lift	Drag	Pitch	Side	Yaw	Roll	Amb.DegC	Amb.mBar
WEIGHT	(kg:T/F/R)	(Lb:T/F/R)	1440.2	825.6	614.6	3175.2	1820.2	1355														
CofG	(+=fwd. mm/ft)	208	0.68																			
1/ 1	27.54	0	2.4	0.33	-0.01	0.223	-0.003	0.005	0	-0.005	-0.005	0.117	0.106	0	260.8	393.7	17.4	-11.6	1.4	-9.3	3.2	1019
2/ 1	27.55	0	2.4	0.332	-0.009	0.223	-0.003	0.006	0	-0.004	-0.005	0.117	0.106	0	261.9	396.2	18.5	-10.7	0.2	-8.8	2.7	1019
3/ 1	27.54	-2.5	2.4	0.333	-0.088	0.231	-0.017	0.006	-0.027	-0.071	-0.017	0.122	0.109	30.8	269.8	396.8	20.9	-102.5	-89.8	-57.6	3.2	1019
4/ 1	27.52	-5	2.4	0.332	-0.18	0.252	-0.036	0.009	-0.051	-0.141	-0.039	0.134	0.117	28.3	294.2	394.8	28.7	-210.3	-169.4	-121.1	3	1019
5/ 1	27.59	-7.5	2.4	0.331	-0.27	0.282	-0.055	0.012	-0.075	-0.21	-0.059	0.153	0.129	28	331.4	396.9	41	-316.9	-252	-182.9	2.9	1019
6/ 1	27.61	-10	2.4	0.338	-0.356	0.324	-0.071	0.016	-0.1	-0.278	-0.078	0.178	0.146	28.2	381.2	404.7	52.8	-419.1	-335.9	-238.8	3.1	1019
7/ 1	27.55	-12.5	2.4	0.345	-0.443	0.386	-0.088	0.022	-0.124	-0.346	-0.097	0.215	0.171	28	452.5	411.7	72.9	-519.2	-414.2	-293.8	3.1	1019
8/ 1	27.48	-15	2.4	0.35	-0.52	0.466	-0.103	0.03	-0.151	-0.412	-0.109	0.263	0.203	29.1	543.2	414.6	100.1	-605.8	-501.4	-342.5	3.3	1019
9/ 1	27.62	0	2.4	0.332	-0.01	0.223	-0.003	0.005	0	-0.005	-0.005	0.116	0.106	0	260.4	394.6	16.6	-11.5	0.9	-9.1	4.9	1018
10/ 1	27.65	0	2.4	0.33	-0.009	0.223	-0.002	0.005	0	-0.005	-0.004	0.116	0.107	0	261.4	394.4	15.8	-10.6	-0.4	-8.2	4.3	1018
11/ 1	27.31	15	2.4	0.349	0.514	0.459	0.102	0.03	0.147	0.405	0.11	0.259	0.2	28.7	527	407.6	96.9	590.1	481.2	332.3	3.9	1019
12/ 2	27.74	0	2.4	0.326	-0.009	0.222	-0.002	0.007	-0.001	-0.005	-0.003	0.117	0.104	0	261.3	391.7	22.3	-10.2	-2.9	-8.1	4.7	1018
13/ 3	27.73	0	2.4	0.334	-0.015	0.241	-0.004	0.02	0.001	-0.006	-0.008	0.14	0.101	0	283.6	401	66.4	-17.3	3.3	-13.9	4.8	1018
14/ 4	27.69	0	2.4	0.329	-0.012	0.238	-0.003	0.022	0	-0.006	-0.006	0.141	0.097	0	279.4	393	72.7	-14.5	1.1	-10.9	5	1018
15/ 5	27.69	0	2.4	0.325	-0.008	0.208	-0.002	-0.007	-0.001	-0.005	-0.003	0.097	0.111	0	244.1	388.5	-22.9	-9.3	-1.9	-7.6	5.3	1018
16/ 6	27.87	0	2.4	0.323	-0.007	0.189	-0.002	-0.028	0	-0.003	-0.004	0.067	0.122	0	224.4	390.5	-93.4	-8.7	1.5	-7.2	5.7	1017
17/ 7	27.81	0	2.4	0.318	-0.008	0.132	-0.002	0.003	0.001	-0.003	-0.005	0.068	0.063	0	155.3	382.9	9	-9.4	2.8	-7.2	5.8	1017
18/ 8	27.77	0	2.4	0.319	-0.006	0.153	-0.002	-0.009	0	-0.003	-0.003	0.068	0.085	0	179.7	382.8	-29.5	-7	-0.2	-6.6	5.7	1017
19/ 9	27.82	0	2.4	0.316	-0.006	0.152	-0.002	-0.011	0	-0.003	-0.003	0.065	0.087	0	179.4	381.4	-37	-7.3	1.1	-7.3	5.4	1017
20/ 10	27.77	0	2.4	0.31	-0.006	0.161	-0.002	0.008	0	-0.003	-0.003	0.088	0.073	0	188.8	370.7	25.4	-7.4	0.5	-7.6	6.2	1017
21/ 11	27.74	0	2.4	0.302	-0.004	0.146	-0.001	-0.004	-0.001	-0.003	-0.001	0.07	0.077	0	171.5	361.1	-11.8	-4.5	-2.9	-3.2	6.3	1017
22/ 12	27.76	0	2.4	0.302	-0.005	0.126	-0.001	0.009	-0.001	-0.003	-0.001	0.071	0.054	0	147.4	362	28.5	-5.7	-3.3	-3.7	6.1	1017
23/ 13	27.84	0	2.4	0.302	-0.003	0.13	-0.001	0.007	-0.001	-0.002	-0.001	0.072	0.058	0	153.8	363.3	24.3	-3.8	-2.4	-4.1	6.2	1017
24/ 14	27.81	0	2.4	0.3	0	0.12	0	-0.005	-0.001	-0.001	0.001	0.055	0.065	0	140.9	360.3	-18	-0.1	-4.1	-0.6	6.5	1016
25/ 15	27.78	0	2.4	0.301	-0.003	0.112	-0.001	-0.018	-0.001	-0.002	-0.001	0.038	0.074	0	131.2	360.1	-58.7	-3.3	-1.9	-3.8	6.6	1016
26/ 16	27.85	0	2.4	0.299	0.005	0.139	0.001	0.002	-0.001	0.001	0.004	0.071	0.067	0	163.7	359.8	6.9	6.3	-4	3.6	6.5	1016
27/ 17	27.82	0	2.4	0.304	0.01	0.147	0.002	0.009	-0.003	0.002	0.008	0.083	0.064	0	172.4	364.1	30.8	11.7	-9.8	8.2	6.7	1016
28/ 18	27.83	0	2.4	0.293	0.001	0.105	0	-0.022	-0.001	-0.001	0.001	0.031	0.075	0	124.1	352.2	-74.3	0.7	-3.3	0.1	6.7	1016
29/ 19	27.81	0	2.4	0.296	-0.001	0.108	0	-0.019	-0.001	-0.001	0	0.034	0.073	0	126.8	355.3	-65.2	-0.6	-1.8	-1.2	6.1	1017

FILE	T1	09Dec2008@12:22:27	User data																		
FIRM	LOUGHBOROUGH UNI																				
VEHI	GROUP 4																				
MAKE	FORD																				
MODL	MONDEO 2.0LTR PETROL																				
TYPE	HATCH BACK																				
CNFG	1																				
OALN	4795																				
WIDT	1830																				
HEIG	1475																				
WBAS	2845																				
FTRK	1575																				
RTRK	1585																				
FTRM	0																				
RTRM	0																				
MRFX	0																				
MRFZ	0																				
VPOX	0																				
VPOY	0																				
HBLR	0.8																				
SCAL	100																				
BLFE	NO																				
GBHT	0																				
MODE	NORMAL																				
UNITFM	N.m																				
UNITWS	m/s																				
Run/Cfg	Wind_m/s	Deg	FA.Sqm	CD	CY	CL	CMX	CMY	CMZ	CYF	CYR	CLF	CLR	XCP	Lift	Drag	Pitch	Side	Yaw	Roll	Amb.DegC	Amb.mBar
WEIGHT	(kg:T/F/R)	(Lb:T/F/R)	1440.2	825.1	615.1	3175.1	1819	1356.1														
CofG	(+=fwd. mm/ft)	207	0.68																			
1/ 1	27.81	0	2.4	0.328	-0.011	0.221	-0.003	0.005	0	-0.005	-0.006	0.115	0.105	0	258.1	390.8	16.7	-12.5	1.3	-9.3	7.1	1014
2/ 1	27.79	0	2.4	0.328	-0.011	0.221	-0.003	0.005	0	-0.005	-0.005	0.116	0.106	0	259.5	392.2	17.2	-12.4	0.6	-9.7	6.4	1014
3/ 1	27.79	2.5	2.4	0.329	0.072	0.229	0.013	0.005	0.026	0.062	0.01	0.12	0.11	35.9	269.2	393.8	16.4	84.4	86.2	44.5	6.1	1014
4/ 1	27.75	7.5	2.4	0.331	0.263	0.282	0.052	0.013	0.07	0.202	0.061	0.154	0.128	26.7	330.2	394.8	42.1	307.9	233.9	174.5	6	1014
5/ 1	27.61	12.5	2.4	0.344	0.436	0.385	0.086	0.025	0.121	0.339	0.097	0.217	0.168	27.7	446.3	405.8	81.1	505.8	398.6	285.2	6	1014
6/ 2	27.87	0	2.4	0.32	-0.009	0.215	-0.002	0.004	0	-0.004	-0.005	0.112	0.103	0	252.7	383	13.6	-10.3	0.4	-7.1	7.3	1014
7/ 3	27.82	0	2.4	0.332	-0.015	0.24	-0.004	0.017	0.002	-0.006	-0.009	0.137	0.103	0	281.2	396	56.7	-17.5	6.1	-12.3	7.3	1014
8/ 4	27.92	0	2.4	0.319	-0.01	0.223	-0.002	0.01	0	-0.005	-0.005	0.122	0.101	0	262.4	383.3	34	-11.9	-0.2	-7.5	7.4	1014
9/ 5	27.85	0	2.4	0.31	-0.009	0.217	-0.002	0.012	0	-0.005	-0.004	0.12	0.097	0	254.6	371.5	38.4	-10.9	-0.8	-6.3	7.2	1014
10/ 6	27.94	0	2.4	0.299	-0.008	0.139	-0.001	-0.065	-0.001	-0.005	-0.004	0.004	0.134	0	163.8	359.4	-218.1	-9.8	-1.8	-4.9	7.5	1013
11/ 7	27.97	0	2.4	0.297	-0.007	0.077	-0.001	-0.029	-0.001	-0.005	-0.002	0.01	0.067	0	91.1	358.5	-97.2	-8	-4.2	-4.4	7.4	1013
12/ 8	27.93	0	2.4	0.309	-0.01	0.108	-0.002	-0.006	-0.001	-0.006	-0.004	0.047	0.06	0	126.7	371.4	-21.5	-12.1	-3.2	-7.1	7.6	1014
13/ 9	28.12	0	2.4	0.303	-0.01	0.094	-0.002	-0.024	0	-0.005	-0.005	0.023	0.071	0	112.6	369.7	-80.8	-12.3	-0.5	-7.4	7.5	1014
14/ 10	27.93	0	2.4	0.307	-0.007	0.044	-0.001	-0.005	-0.001	-0.005	-0.002	0.017	0.027	0	51.9	369	-15.9	-7.8	-5	-3.8	7.8	1014
15/ 11	27.94	0	2.4	0.3	-0.01	0.083	-0.002	-0.024	0	-0.005	-0.005	0.018	0.065	0	97.5	360.9	-79	-11.2	-0.6	-6.4	7.8	1014
16/ 12	27.86	0	2.4	0.305	-0.013	0.101	-0.003	-0.028	0.002	-0.005	-0.008	0.022	0.078	0	118	364.9	-93.2	-15.7	5.2	-8.8	7.7	1014
17/ 13	27.8	0	2.4	0.297	-0.004	0.085	-0.001	-0.018	-0.001	-0.002	-0.001	0.025	0.061	0	99.8	353.5	-60.1	-4.2	-1.7	-4.9	7.7	1014
18/ 14	27.84	0	2.4	0.296	-0.004	0.092	-0.002	-0.016	0	-0.002	-0.002	0.03	0.062	0	107.8	354.3	-51.9	-4.7	-1.2	-5.5	7.5	1014
19/ 15	27.82	0	2.4	0.299	-0.004	0.082	-0.002	-0.01	-0.001	-0.003	-0.001	0.031	0.051	0	95.9	357.1	-32.3	-4.3	-2.5	-5.4	7.3	1015